Studies of Diffractive Jet-Gap-Jet Events using $\sqrt{s} = 13.6$ TeV ATLAS Data

Pragati Patel

Institute of Nuclear Physics
Polish Academy of Sciences

2025

Supervisor: prof. dr hab. Janusz Chwastowski
Co-supervisor: dr Maciej Trzebiński

Declaration

I declare that the thesis is original except for the source materials explicitly acknowledged and that as a whole or in part of has not been previously submitted for the degree.

I also acknowledge that I have read and understood the Rules on Handling Student Academic Dishonesty and the Regulations of the Student Discipline of the Institute of Nuclear Physics Polish Academy of Sciences.

Foreword

I did my PhD in a very interesting era. From one side, the LHC delivered a significant amount of luminosity – in the so-called Run 1 ATLAS experiment recorded 5.08 fb^{-1} of proton-proton data at $\sqrt{s} = 7$ TeV and 21.3 fb^{-1} at $\sqrt{s} = 8$ TeV [1]. Run 2 was even more fruitful with 147 fb^{-1} recorded at $\sqrt{s} = 13$ TeV. Such an amount of data made a promise of progress in understanding Nature. On the other hand, this was also the time of the COVID-19 pandemic, which significantly complicated our lives. The scientific work was not an exception – just to mention the one-year delay of the LHC re-start.

My PhD journey started in January 2021, when I joined the team formed within the project "Studies of Hard Diffractive Production with the ATLAS Experiment" (NCN, Sonata Bis) led by Dr. Maciej Trzebiński. My subject was to perform the diffractive jet-gap-jet analysis using data recorded by the ATLAS detector.

My first task was to become a member of the ATLAS Collaboration. The qualification project was concentrated on the studies of the LHC beam optics for diffractive measurements using the ATLAS Forward Proton (AFP) detectors. One year later, in March 2022, I was qualified as the ATLAS Author – signing all publications and being allowed to represent Collaboration on a public forum, *e.g.* during the conferences.

My collaborative work for ATLAS was not finished at this moment. During my PhD studies I spent quite some time (0.34 FTE[1]/year in years 2022–2024) being the on-call expert (24/7 detector operation), taking part in the detector hardware maintenance and re-installation and continuing work on the general performance studies within the "Proton Combined Performance" group. My engagement resulted in being the co-author of 270 ATLAS publications[2] and representing ATLAS during the following international conferences and workshops:

- LHCFPWG 2021: LHC Forward Physics Meeting, *Towards Run 4 – HL-LHC Optics Studies for ATLAS Roman Pots*, CERN, Switzerland, 14-15 December 2021,

[1] FTE – Full Time Equivalent. In ATLAS, the FTE equal to 1 is normalized to 243 workdays.
[2] Following Inspires; access: 13/03/2025.

- DIS2022 XXIX: International Workshop on Deep-Inelastic Scattering and Related Subjects, *Overview of ATLAS forward proton detectors for LHC Run 3 and plans for the HL-LHC*, Santiago de Compostela, Spain, 2-6 May 2022,

- LHCFPWG 2024: LHC Forward Physics July 2024 Workshop, *AFP - summary of data-taking + plans for 2024/2025*, CERN, Switzerland, 15–16 July 2024.

Finally, my work was not only devoted to the current ATLAS detector maintenance, performance studies or data analysis. I was also involved in the High-Luminosity LHC upgrade – I did the optics feasibility studies for ATLAS and ALICE. Partial results were presented during:

- EMMI workshop: Forward Physics in ALICE 3, *Studies of forward proton trajectories in vicinity of IP2 for the HL-LHC optics*, Heidelberg, Germany, 18–20 October 2023,

- XXX Cracow EPIPHANY Conference on Precision Physics at High Energy Colliders, *HL-LHC Optics – Feasibility Studies for: ATLAS, ALICE and LHCb*, Krakow, Poland, 8–12 January 2024.

These results were published in Acta Physica Polonica B Proc. Suppl. 17, 5-A30 (2024) [2].

Regarding the analysis, the original concept was to look at the special data sets collected by ATLAS during the 2017 campaigns. Unfortunately, these data "suffered" from many problems (*c.f.* P. Erland thesis [3]), making the diffractive analyses extremely challenging. In light of Run 3 data, the decision was to base diffractive jet-gap-jet measurement on the 2022 data sample, a subject of this PhD dissertation.

Chapter 1 introduces the basic theoretical concepts used in this thesis. Dedicated sections are devoted to the description of hard diffractive processes, especially jet-gap-jet and diffractive jet-gap-jet.

Chapter 2 contains a brief description of the experimental setup used to "produce" (LHC accelerator) and measure the events (ATLAS detector). Main ATLAS

sub-detectors are briefly described, focusing on features later used in the data analysis. A bit more details are given in the case of the ATLAS Forward Proton detectors since these devices are unique to measure scattered protons, which are the signature of diffractive events.

Properties of data collected by the ATLAS detector during so-called LHC Run 2 and 3 are given in Chapter 3. After a brief justification of the sample selection, the properties of the dataset used in this analysis (ATLAS run number 428770) are described in detail. This includes LHC optics, AFP detector settings, Good Run List and collected luminosity.

The Next Chapter is devoted to the description of Monte Carlo samples used for the presented studies. An extended discussion is devoted to a gap formation and properties of generated jet events.

Since the presented diffractive jet analysis is the first of such type using ATLAS AFP Run 3 data, a lot of dedicated performance studies had to be done beforehand. Details of trigger efficiency and reconstruction features of protons, tracks, vertices, clusters and jets (including custom-made Jet Energy Scale) are given in Chapter 5.

With all the performance studies done, data was analysed to identify signatures of jet-gap-jet, single diffractive jet and single diffractive jet-gap-jet processes. The details of event selection and the obtained fiducial cross-sections are given in Chapter 6.

The observed issues and "features" are summarised in Chapter 7, which also contains some recommendations for the future analyses of such (and similar) types.

Acknowledgments

Making an analysis of data collected by the ATLAS experiment is practically not possible to be done by a single person in a timescale of a PhD preparation. Even putting apart the huge effort needed to record and reconstruct the data, a significant amount of performance work is needed. Especially to obtain the "reconstructed proton object" which is relatively new in ATLAS and unique for the analyses with forward proton detectors.

The global performance efforts were coordinated by the group conveners: S. Clawson and M. Lewicki (and R. Staszewski and P. Newman in the past). AFP data quality studies (Good Run List) were done by T. Mlinarevic, P. Fiedler and V. Lysenko. A dedicated quality recommendations for run 428770 were prepared by M. Trzebiński. Precise luminosity for that run was computed by E. Sanzani and A. Sbrizzi. The data format (STDM6) was prepared by M. Lewicki. Monte Carlo samples were generated by M. Lewicki (ND and SD JJ) and M. Trzebiński (JGJ). Analysis-specific tasks described in this thesis were done in collaboration with Colleagues from the Proton Combined Performance group. Trigger analysis, optics and transport parametrization were prepared by M. Trzebinski. Low-level SiT efficiency studies were done by S. A. Javier Val and M. Trzebinski. AFP local alignment for 2022 data was done by R. Staszewski and F. Ozturk. Global alignment was obtained by S. Clawson, W. Stanek-Maslowska and T. Mroz. Run 3 pot rotation studies described in the appendix were done based on a similar but slightly simpler Run 2 analysis by M. Trzebiński.

Data selection criteria and performance studies presented in this PhD were based on the experience of the Run 2 single diffractive jet analysis team composed of: M. Trzebinski, P. Erland, S. J. Arbiol Val, K. Cerny, M. Lewicki, V. Sothlignam, R. Staszewski, M. Tasevsky and the Author. Run 3 (diffractive) jet-gap-jet analysis presented in this thesis was based on the Single Diffractive Jet analysis done in collaboration with M. Trzebinski, M. Lewicki, M. Campanelli, S. J. Arbiol Val and Y. He, with the Author being the main analyser.

My work was supported by the National Science Centre (NCN, Poland) grant No. UMO-2019/34/E/ST2/00393.

Streszczenie

Zbadanie właściwości procesu produkcji układu dżet-przerwa-dżet jest bardzo interesujące zarówno z punktu widzenia eksperymentu jak i teorii. Po dokonaniu pierwszych obserwacji opartych o dane zgromadzone przez detektory CDF oraz D0 [4, 5] na akceleratorze Tevatron pomiar został przeprowadzony z wykorzystaniem danych zgromadzonych przez eksperymenty na LHC. Dla przykładu, pierwsza publikacja Współpracy ATLAS na ten temat oparta była o weto na obecność dżetu w tak zwanej przerwie w pseudopospieszności [6]. Z kolei Współpraca CMS opublikowała wynik pomiaru procesu tzw. dyfrakcyjnej produkcji dżet-przerwa-dżet [7]. Należy jednak nadmienić, że pomiary te, wykonane przy energiach w układzie środka masy 7 oraz 13 TeV, były obarczone dużą niepewnością. Ponadto, proces produkcji układu dżet-przerwa-dżet w procesie z podwójną wymianą Pomeronu, postulowany w Ref. [8], nie został nigdy zmierzony. Powyższe fakty stanowią mocną podstawę i motywację dla wykonania pomiaru procesu produkcji dżetów z przerwą w pseudopospieszności używając danych dostarczonych przez LHC przy energii zderzeń $\sqrt{s} = 13.6$ TeV.

Analiza przestawiona w niniejszej dysertacji została oparta o dane zebrane podczas jednego ze specjalnych naświetlań detektora ATLAS na LHC wykonanych w 2022 roku. Ustawienia punktu pracy akceleratora skutkowały średnim prawdopodobieństwem oddziaływania proton-proton podczas przecięcia się wiązek na poziomie 0.05. Bazując na doświadczeniach z analizy danych zebranych przy energii 13 TeV, taki zestaw danych (w tym wypadku ATLAS run 428770) powinien zapewnić dużą czystość próbki. Dodatkowo scałkowana świetlność wynosząca prawie 30 nb^{-1} daje nadzieję na wykonanie obserwacji o dużej znaczności statystycznej.

Sygnaturą procesu dżet-przerwa-dżet jest obecność co najmniej dwóch dżetów odseparowanych od siebie tak zwaną przerwą w pseudopospieszności. Eksperymentalnie, taka przerwa definiowana jest jako brak widocznej w detektorze aktywności (zrekonstruowanych śladów lub energii powyżej pewnego poziomu) w danym obszarze pseudopospieszności. W przypadku procesu dyfrakcyjnej produkcji dżet-przerwa-dżet sygnaturą jest dodatkowo obecność protonu rozproszonego pod małym kątem. Proton taki po oddziaływaniu poruszą się

wewnątrz rury próżniowej akceleratora i może zostać zarejestrowany przy użyciu dedykowanych detektorów. W niniejszym przypadku są to detektory ATLAS Forward Proton (AFP).

Niniejsza rozprawa została skomponowana w następujący sposób. Pierwszy rozdział stanowi krótkie wprowadzenie do chromodynamiki kwantowej potrzebnej do zrozumienia procesu produkcji dżetów z przerwą w pseudopospieszności. Rozdział 2 zawiera krótki opis akceleratora LHC, który dostarczył danych do omawianego pomiaru. Szczególny nacisk został położony na opis otoczenia punktu oddziaływania eksperymentu ATLAS, który jest kluczowy do zrozumienia kinematyki rozproszonych protonów. Rozdział ten zawiera również opis aparatury użytej do pomiarów – detektora ATLAS. Oprócz zwyczajowego opisu „centralnej" części eksperymentu koniecznej do rekonstrukcji dżetów oraz przerwy w pseudopospieszności, obszerniej omówione zostały zagadnienia poświęcone pomiarowi rozproszonych protonów w detektorach AFP.

Rozdział 3 poświęcony jest rozważaniom na temat wyboru odpowiedniej próbki danych do analizy. Znaczna jego część jest poświęcona opisowi własności, w szczególności jakości, zebranych danych. Natomiast własności odpowiednich próbek Monte Carlo są pokrótce przedstawione w rozdziale 4.

Najobszerniejszą część rozprawy stanowi rozdział 5, w którym w szczegółach zostały opisane aspekty rekonstrukcji obiektów użytych w analizie: dżetów, przerwy w pośpieszności definiowanej w opartciu o zrekonstruowane ślady jak i klastry w kalorymetrach, protonów.

Rozdział rozpoczyna się analizą wydajności trygerów użytych do selekcji przypadków. W przypadku analizy niedyfrakcyjnej – bez tagowanego protonu – argumentowana jest konieczność połączonego użycia dwóch trygerów, w zależności od pędu poprzecznego wiodącego dżetu. Jest to podyktowane użyciem na poziomie trugera czynników skalujących (prescale) oraz efektywności zastosowanych algorytmów trygerowych. W przypadku procesów dyfrakcyjnej produkcji, rekomendowane zostało użycie trygera opartego o obecność protonu w detektorze AFP oraz dżetu. Tryger ten, pomimo niewydajności związanej z tagowaniem protonu, wynoszącej 91.25 ± 0.29 oraz 45.92 ± 0.13 w zależności o tego czy proton jest po stronie A czy C detektora ATLAS, oferuje zapis największej ilości przypadków.

Rozdział 5 zawiera również obszerną dyskusję na temat kalibracji oraz wydajności rekonstrukcji detektora AFP. Szczególnie interesująca jest oczekiwana precyzja odwikłania energii protonu, która wynosi $\delta\xi/\xi \approx 1\%$. Nie mniej ważna jest akceptancja detektora AFP, która pozwala na zarejestrowanie protonów które straciły pomiędzy 0.03 a 0.09 swojej początkowej energii. Duża cześć rozdziału została poświęcona rekonstrukcji „centralnych" obiektów takich jak ślady cząstek naładowanych, energia deponowana w kalorymetrze oraz dżety. W szczególności, w przypadku tej ostatniej, konieczne było wykonanie dedykowanej kalibracji.
Mając opracowane charakterystyki kluczowych obiektów, możliwe było rozpoczęcie analizy danych pod kątem poszukiwania przypadków z przerwą w pseudopospieszności. Opis ten stanowi treść rozdziału 6. Na początek, na bazie wygenerowanych próbek Monte Carlo, przeprowadzone zostały rozważania różnych definicji przerwy w pseudopospieszności. Na ich podstawie przeprowadzona została selekcja przypadków w danych eksperymentalnych. Wymaganie obecności co najmniej dwóch dżetów o pędzie poprzecznym co najmniej 30 GeV oraz 20 GeV, mających pseudopospieszność przynajmniej $|\eta| > 1.5$, znajdujących się w przeciwnych hemisferach ($\eta^{J1} \times \eta^{J2} < 0$) oraz przerwy w pseudopospieszności zdefiniowanej jako brak zrekonstruowanych śladów oraz klastrów o sumie energii większej niż 2 GeV w obszarze $|\eta| < 1$, poskutkowało wyłonieniem 234 przypadków-kandydatów o sygnaturze dżet-przerwa-dżet. Uwzględniając świetlność wynoszącą 29.65 ± 0.44 nb^{-1}, przekrój czynny został oszacowany na:

$$\sigma^{fid}_{ND\ JGJ} = 7.9 \pm 0.5 \text{ nb}.$$

Rozdział 6 zawiera również opis selekcji dyfrakcyjnych przypadków produkcji dżetów, która w świetle opisywanej analizy dżet-przerwa-dżet stanowi krok pośredni do identyfikacji przypadków z tagowanym protonem. Selekcja przypadków została oparta o wymagania dżetów o odpowiednim pędzie poprzecznym (min. 30/20 GeV), ograniczeniu na liczbę zrekonstruowanych wierzchołków oraz związki kinematyczne pomiędzy energią zdeponowaną w kalorymetrze oraz odwikłaną z położenia protonu w AFP. Po zastosowaniu powyższych wymagań, zaobserwowano 4011 oraz 1328 przypadków z protonem tagowanym odpowiednio po stronie A oraz C. Analiza oparta o próbki Monte Carlo sugeruje obecność znacznej

domieszki tła pochodzącego od przypadków niedyfrakcyjnych. Należy jednak nadmienić, że może one zostać zredukowane po zaadresowaniu zaobserwowanych problemów z rekonstrukcją wierzchołka oddziaływania.
Złożenie selekcji opisanych powyżej zaowocowało wyłonieniem kandydatów o sygnaturze dyfrakcyjnej produkcji dżet-przerwa-dżet z pojedynczym tagowaniem protonu. W analizowanej próbce danych znaleziono 7 takich przypadków, co przekłada się na oszacowanie przekroju czynnego na poziomie:

- $\sigma^{fid}_{SD\ JGJ,\ A} = 0.19 \pm 0.08$ nb dla protonu tagowanego po stronie A,
- $\sigma^{fid}_{SD\ JGJ,\ C} = 0.15 \pm 0.10$ nb dla protonu po stronie C.

Właściwą cześć rozprawy kończy podsumowanie otrzymanych wyników wraz z wykazem rekomendacji odnośnie przyszłej analizy danych. Ponadto, w dodatkach obszernie opisane zostały techniczne aspekty studiów wydajności wykonanie podczas doktoratu: zagadnienie znalezienia tzw. „prawdziwej'' optyki LHC oraz wpływ efektu rotacji stacji AFP na odwikłanie energii protonu. Ostatni załącznik stanowi krótki opis studiów wykonanych na potrzeby potencjalnego użycia „rzymskich garnków" na akceleratorze High Luminosity LHC.

Table of Contents

Chapter 1

Introduction

Diffraction was always an important part of the studies performed in the particle physics experiments. This is also true in the LHC era. Both theoreticians and experimentalists work on various aspects of diffractive measurements. For example, during the last 10 years, around 70 publications containing the words 'diffraction' and 'LHC' were posted yearly on arXiv. Unfortunately, despite many studies, this field still has many mysteries. Clearly, there is a strong need and place for input from the LHC data.
This work is devoted to one aspect of diffractive physics: the production of jets with a rapidity gap[1] between them. Such events, called jet-gap-jet, should allow interesting tests of theoretical predictions. Moreover, the jet-gap-jet topology produced in the single diffractive and the double Pomeron exchange processes is poorly known – the latter was never measured experimentally. However, before going into the details of the analysis, a brief introduction to the theory and phenomenology of the process should be given.

1.1 Standard Model of Particle Physics

The epitome of our understanding of the fundamental constituents of matter and their inherent traits is represented in the "Standard Model of Particle Physics" (SM). This mathematically rigorous framework, derived through a synthesis of experimental evidence and theoretical reasoning, has provided predictions regarding the existence of particles and their interactions. In the current state of scientific knowledge, as recorded within the framework of this thesis, there are recognised to be four primary forces that operate within the Universe, namely the "strong interaction", the "weak interaction", "electromagnetism", and "gravity". These forces are accountable for the interactions between the fundamental, point-like particles that compose the matter present in the Universe. Among these four, the Standard Model (SM) encompasses all but gravity[2]. The lack of the latter does not spoil the description since it is much weaker than the other three to impact

[1] A gap is a space in rapidity without particles. Experimentally, it is defined as a space without reconstructed objects.

[2] Some theories postulate that the phenomenon of gravity can be accounted for through the exchange of a hypothetical, massless, neutral, spin-2 particle referred to as the "graviton".

high-energy physics experiments.

The Standard Model outlines two broad categories of particles; see Fig. 1.1. *Fermions* possess a half-integral spin and include both *leptons* (such as electrons) and *quarks*. The second category of particles, so-called *bosons*, is characterised by the integral spin. The three fundamental interactions described by the SM being mediated by spin-1 bosons; the strong interactions by gluons, weak by $W^{\pm}$ and Z, and electromagnetic by γ. The spin-0 Higgs boson H [9, 10] is responsible for imparting mass to other elementary particles. The quarks collectively form *baryons*, such as protons and neutrons and *mesons* (pions, kaons, ...). Baryons and leptons comprise all visible matter in the Universe.

Standard Model is a gauge theory with a non-abelian gauge group expressed as:

$$G_{SM} = SU(3)_C \times SU(2)_L \times U(1)_Y, \tag{1.1}$$

where strong interaction is represented by $SU(3)_C$ with C subscript denoting the conserved colour charge, and having 8 generators.

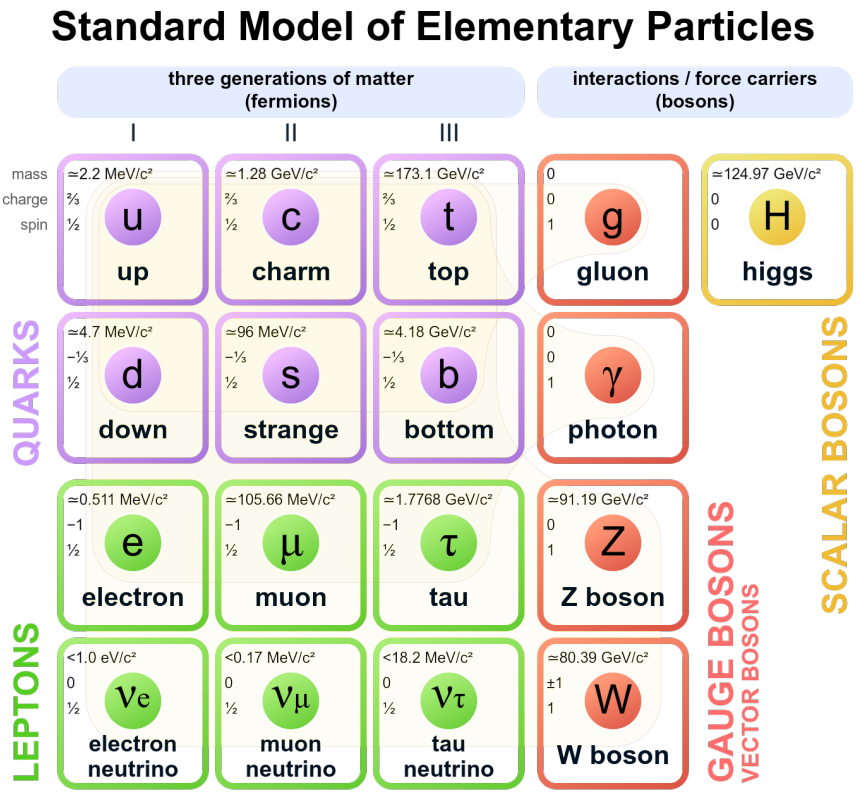

Figure 1.1: Particle content of Standard Model of particle physics. From [11].

The subscript L in the $SU(2)_L$ group indicates that it only acts on the left-handed particles or the right-handed anti-particles, and the conserved quantity corresponding to the group is weak isospin, T_3, with 3 generators. The Y subscript

of $U(1)_Y$ group represents the conserved weak hypercharge and has one generator.

Quarks can carry one of three colour charges, usually named red, green and blue, whereas gluons carry the colour and anti-colour, which gives them the ability to self-interact. The $SU(3)_C$ symmetry is unbroken and remains at low-energy scales. In contrast, the remaining gauge symmetry of the SM breaks down as the Higgs field reaches its ground state, thus generating gauge invariant masses for the weak gauge bosons in the process:

$$SU(2)_L \times U(1)_Y \rightarrow U(1)_Q. \tag{1.2}$$

Presently, the EM interactions are described by the quantum electrodynamics, which is based on the $U(1)_Q$ symmetry. The conserved quantity corresponding to this symmetry is the electric charge given as $Q = T_3 + Y$. The gauge field corresponding to $SU(3)_C, SU(2)_L$ and $U(1)_Y$ are $G^{\alpha}_{\mu}, W^{a}_{\mu}$ and B_{μ} field tensors. Lagrangian for SM can be expressed as the sum of these three terms:

$$\mathcal{L}_{SM} = \mathcal{L}_{gauge} + \mathcal{L}_{fermions} + \mathcal{L}_{Higgs}, \tag{1.3}$$

with the Lagrangian for gauge boson defined as,

$$\mathcal{L}_{gauge} = -\frac{1}{4}(B_{\mu\nu}B^{\mu\nu} + W^{a}_{\mu\nu}W^{a\mu\nu} + G^{a}_{\mu\nu}G^{\alpha\mu\nu}). \tag{1.4}$$

The gauge field strength tensors are defined as:

$$\begin{aligned} B_{\mu\nu} &= \partial_\mu B_\nu - \partial_\nu B_\mu, \\ W^{a}_{\mu\nu} &= \partial_\mu W^{a}_{\nu} - \partial_\nu W^{a}_{\mu} + g\epsilon^{abc}W^{b}_{\mu}W^{c}_{\nu}, \\ G^{\alpha}_{\mu\nu} &= \partial_\mu G^{\alpha}_{\nu} - \partial_\nu G^{\alpha}_{\mu} + g_s f^{\alpha\beta\gamma}G^{\beta\gamma}_{\mu\nu}, \end{aligned} \tag{1.5}$$

where $f^{\alpha\beta\gamma}$ and ϵ^{abc} are the structure constants for $SU(3)_C$ and $SU(2)_L$ group, respectively. The g_s and g are the dimensionless coupling constants quantifying the strength of the interaction corresponding to $SU(3)_C$ and $SU(2)_L$ symmetry groups, respectively.

The Lagrangian for fermions is given by:

$$\mathcal{L}_{fermions} = \psi i\gamma^{\mu}D_{\mu}\psi, \tag{1.6}$$

where ψ denotes the fermion field, γ^{μ} – the gamma matrices and D_μ is the most general form of the covariant derivative described as:

$$D_\mu = \partial_\mu - ig_s G^{\mu}_{\alpha}t^{\mu}_{\alpha} - igW^{\mu}_{a}t^{a}_{L} - ig'B_\mu Y, \tag{1.7}$$

where t_c^α and t_L^α are the generators of the $SU(3)_C$ and $SU(2)_L$ groups, respectively. The dimensionless coupling constant, g', represents the strength of the interaction related to the $U(1)_Y$ symmetry group.

No explicit mass term for particles is present in $\mathcal{L}_{gauge}$ and $\mathcal{L}_{fermions}$ because they would not be gauge invariant. Therefore, they predict massless particles, contrary to the experimental evidence of massive particles.

The Higgs mechanism solves the issue of massless particles predicted by the gauge invariance by breaking the underlying symmetry of $SU(2)_L \times U(1)_Y$ as in Eq. 1.2, thus giving rise to the mass term in the SM Lagrangian for gauge bosons and fermions.

The Electro-Weak Symmetry Breaking (EWSB) is a process of $SU(2)_L \times U(1)_Y$ symmetry breaking into $U(1)_Q$ symmetry, by introducing an $SU(2)_Y$ doublet of complex scalar fields called the Higgs Field, with the weak hypercharge Y_Φ:

$$\Phi = \begin{pmatrix} \phi^+ \\ \phi^0 \end{pmatrix}, \quad Y_\Phi = \frac{1}{2} \tag{1.8}$$

to the existing SM Lagrangian which acts as an $SU(3)_C$ colour singlet. Thus, the Lagrangian describing the Higgs sector is given by

$$\mathcal{L}_{Higgs} = (D^\mu \phi)^\dagger (D_\mu \phi) - V(\phi) - \mathcal{L}_{Yukawa} \tag{1.9}$$

where the Yukawa interaction between the scalar Higgs fields and the fermions is described by $\mathcal{L}_{Yukawa}$ and the Higgs potential is defined as:

$$V(\phi) = \mu^2 \Phi^\dagger \Phi - \lambda (\Phi^\dagger \Phi)^2. \tag{1.10}$$

To make the potential bounded from below, ensuring a stable vacuum $\lambda > 0$ is required. Since $\lambda = 0$ results in no symmetry breaking, λ is assumed to be positive. For $\mu^2 > 0$, the potential has its minimum at $|\phi| = 0$, and there is no scope for spontaneous symmetry breaking (SSB). However, for $\mu^2 < 0$, the potential does not have a minimum at $|\phi| = 0$ and corresponds to SSB.

Higgs field can be written as a unitary gauge to minimise the scalar degree of freedom as:

$$\Phi(x) = \frac{1}{\sqrt{2}} \begin{pmatrix} 0 \\ \nu + H \end{pmatrix}, \tag{1.11}$$

where ν is the Vacuum Expectation Value (VEV) of the real Higgs field H. From Eq. 1.10, the Higgs potential reaches its minimum for $\phi^\dagger \phi = -\frac{\mu^2}{2\lambda}$. Thus, VEV is defined as:

$$\nu = \sqrt{-\frac{\mu^2}{\lambda}} \quad \text{where} \quad \mu^2 < 0. \tag{1.12}$$

Substituting this into the expression of $\mathcal{L}_{Higgs}$ given by Eq. 1.9 gives rise to a mass term and an interaction term for bosons in SM Lagrangian. Except for photon, γ, which remains massless. The mass term for the spin 0 scalar Higgs boson is also obtained. After $SU(2)_L \times U(1)_Y$ symmetry is broken, the electric charge, e, is a conserved quantity. After EWSB, the gauge fields of $SU(2)_L \times U(1)_Y$ group mix to yield the physical states corresponding to the weak boson ($W_\mu^\pm$ and Z_μ) and a photon (A_μ):

$$W_\mu^\pm = \frac{1}{\sqrt{2}}(W_\mu^1 \mp iW_\mu^2), \tag{1.13}$$

$$Z_\mu = \cos\theta_W W_\mu^3 - \sin\theta_W B_\mu, \tag{1.14}$$

$$A_\mu = \sin\theta_W W_\mu^3 + \cos\theta_W B_\mu, \tag{1.15}$$

where θ_W is a weak mixing angle defined as:

$$\cos\theta_W = \frac{g}{\sqrt{g^2 + g'^2}} \quad \text{and} \quad \sin\theta_W = \frac{g'}{\sqrt{g^2 + g'^2}}, \tag{1.16}$$

where g and g' are the dimensionless coupling constants defined earlier. The masses of gauge bosons are given by:

$$M_W = \frac{1}{2}g\nu, \quad M_Z = \frac{1}{2}\nu\sqrt{g^2 + g'^2}, \quad M_A = 0, \quad M_h = \nu\sqrt{2\lambda}. \tag{1.17}$$

The $\mathcal{L}_{Yukawa}$ term in the SM Lagrangian allows fermions to have mass. Yukawa interaction between the fermions and the Higgs field is described in the Lagrangian as:

$$\mathcal{L}_{Yukawa} = (y_i \bar{\psi}_R \phi^\dagger \psi_L + h.c.), \tag{1.18}$$

where ψ denotes the fermion field, y_i denotes the Yukawa coupling defined as the strength of interaction between the Higgs field and fermions and $h.c.$ denotes the Hermitian conjugate of the previous term. Inserting the Higgs field ϕ of Eq. 1.11 into Eq. 1.18 gives rise to the fermion mass and the interaction term between fermions and the Higgs field.

1.2 Quantum Chromodynamics

Quantum Chromodynamics (QCD) is a non-Abelian gauge theory characterized by the gauge group $SU(3)_C$. It comprehensively describes the strong nuclear force and governs most interactions involving hadrons. The essence of QCD lies in the concept of the *colour charge*, which differentiates between the three types of quarks and the gluons that mediate the strong force between them. This idea serves as the basis for explaining how quarks can coexist inside hadrons without

violating the Pauli exclusion principle.

The concept of the colour charge in QCD brings forth a variety of crucial consequences. Foremost among these is the phenomenon of *colour confinement*, due to which the coloured states of quarks and gluons are not observed in the natural realm but are instead confined to form colourless bound states. These bound states, known as *hadrons*, take the form of either quark-anti-quark pairs (*mesons*, $q\bar{q}$) or combinations of three quarks (*baryons*) that exist in a state of colour neutrality (colour singlet state).

The phenomenon of *hadronisation* dictates how the colourless hadrons are formed out of quarks and gluons confined within them. The confinement arises from the strength of the strong force between quarks and gluons, which becomes increasingly potent at longer distances. This can also be understood through a simplistic illustration of separating a quark-anti-quark pair. As the separation increases, the energy of the colour field also increases. At a certain point, the energy surpasses the rest mass of the pair, which forces the reduction of the system's potential energy, and the colour field collapses and a new $q\bar{q}$ pair is created. The confinement of coloured states manifests in collider experiments as the formation of jets, collimated sprays of hadrons and other particles initiated from the production or scattering of a quark or gluon.

Another important property of QCD is its manifestation of *asymptotic freedom* [12]. This term refers to the observation that at high energy or short distances, the interaction between quarks and gluons becomes increasingly weak, implying a reduction in the strength of the binding force. In essence, this means that quarks within hadrons behave as relatively free particles when probed at sufficiently high energies/scales. This property has far-reaching implications for our understanding of the strong force and serves as the foundation for the perturbative QCD development.

The concept of asymptotic freedom in QCD is rooted in the theory of renormalisation group, which describes the evolution of a physical system as the scale of observation changes. In QCD, the running strong coupling constant $\alpha_s(Q^2)$ [13] is the fundamental quantity that describes the strength of the interaction between quarks and gluons as a function of the energy scale Q. In the leading order, it can be expressed as:

$$\alpha_s(Q^2) \approx \frac{1}{\beta_0 \ln(Q^2/\Lambda^2_{\mathrm{QCD}})}, \tag{1.19}$$

where β_0 represents the leading-order coefficient of the beta function, which dictates the evolution of $\alpha_s(Q^2)$ with the energy scale, Q^2 and Λ_{QCD} signifies the confinement scale. In the perturbative regime, where the energy scale Q is much larger than the Λ_{QCD}, $\alpha_s(Q^2)$ becomes small, leading to a weakly coupled system.

In this regime, perturbative calculations can be performed using the Feynman diagram approach. In this approach, interactions between quarks and gluons are treated as perturbations to the free theory and can be systematically calculated using perturbative methods.

The interactions are represented by the Feynman diagrams, in which each diagram describes a term in the perturbative expansion. The resulting series can be summed up providing predictions for the physical observables in QCD. One should note that such an expansion is typically limited to leading and next-to-leading orders. However, considerable progress has been observed in recent years.

1.3 Parton Model, Structure and Parton Distribution Functions

The structure of hadrons, such as protons and neutrons, can be understood through the Parton Model [14]. The point-like *partons* represent the constituents of hadrons and include quarks and gluons.

In certain interactions, the structure of hadrons can be described by an instantaneous distribution of these partons. For example, the structure of a proton has been extensively studied in deep inelastic lepton-proton scattering (DIS) experiments. Measurements of DIS structure functions allowed determining how the proton's momentum is distributed among the partons.

The momentum distribution functions $f_i(x, Q^2)$ of parton $i = u, d, .., g$ within the proton are called the Parton Distribution Functions (PDFs) and represent the probability density to find a parton of a given type carrying the proton momentum fraction, x, at energy scale Q. In general, the PDFs are solutions of DGLAP[3] evolution equations providing the Q^2 dependence, but only in the perturbative domain. The x-dependence at a given Q^2 cannot be calculated analytically but is rather extracted from the global fits to the data from many experiments [15, 16, 17, 18].

Figure 1.2 shows the PDFs of a proton at two energy scales: $Q^2 = 1.9$ GeV^2 and $Q^2 = 10$ GeV^2. The xu_v and xd_v represent the valence up- and down-quark PDFs, respectively, whereas xS is the sea quark PDF and xg is the gluon one (note the numerical reduction of both xg and xS). The gluon density within the proton grows substantially quicker at small-x values than other parton densities. This distinct pattern becomes apparent at greater energies or resolutions of a probe, allowing the testing of the small-x partons residing within the protons.

[3]Standing for Dokshitzer-Gribov-Lipatov-Altarelli-Parisi.

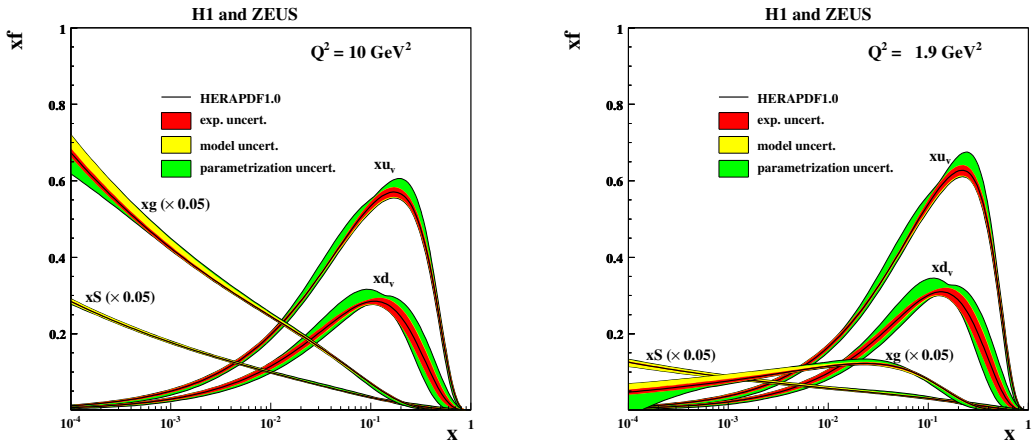

Figure 1.2: The parton distribution function of the proton from HERAPDF1.0 for $Q^2 = 10\ GeV^2$ (left) and $Q^2 = 1.9\ GeV^2$ (right). The sea and gluon PDFs are scaled down by a factor of 20 in both figures. From [18].

1.4 Diffractive Physics

Interactions between protons can be classified as either elastic or inelastic. In the elastic scattering, the protons are scattered at small angles and maintain the same energy as the initial protons, with a small momentum transfer between them. On the contrary, inelastic processes result in the production of new particles and the initial state protons are typically destroyed.

Elastic scattering is a binary process and, owing to its angular properties, the final state protons can be observed in the forward region, *i.e.* at high rapidities. The interaction is mediated by a colourless object: a photon in the case of the electromagnetic process and a Pomeron if the interaction is strong. The latter can be represented at the lowest order as a system of two colour-compensating gluons. The electromagnetic amplitude is accurately calculable within the Quantum Electrodynamics (QED). In case of strong interactions, one typically deals with a non-perturbative regime, a domain of the Regge theory and Regge-inspired phenomenology [19], providing a good description of the so-called nuclear amplitude. One should note the importance of quantum interference for this process.

The total cross-section in the hadron scattering experiments can be classified into three categories: elastic, diffractive and non-diffractive (ND) components. At the LHC energies, the elastic part accounts for about 20% of the total cross-section. The inelastic contribution (diffractive and non-diffractive) is the remaining 80%, out of which 25 - 30% is attributed to the diffractive channels, see for example [20]. Based on the final state topology, diffraction can be further classified into several types:

- **Single Diffraction (SD)**: In this process, one of the initial state protons

remains intact (*i.e.* survives the interaction and does not break up into other particles), while the other one dissociates into a system of particles, X. In case of proton-proton collision, this is represented as:

$$p + p \to p + X. \tag{1.20}$$

- **Double Diffraction (DD)**: Characterised by the feature that both protons dissociate into systems of particles:

$$p + p \to X_1 + X_2. \tag{1.21}$$

- **Central Diffraction (CD)**: both protons (may) remain intact, and a system of particles is produced in the central region. This can be represented as:

$$p + p \to p + X + p. \tag{1.22}$$

All these cases are illustrated in Fig. 1.3, where corresponding Feynman diagrams are shown. The double line represents the colourless object.

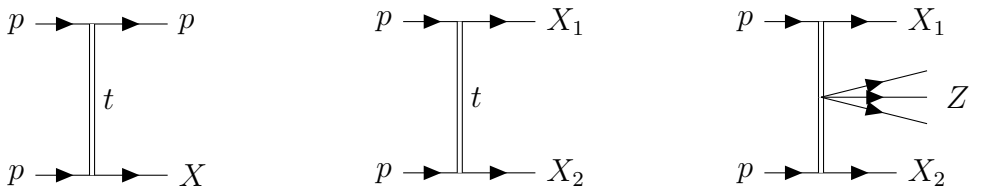

(a) single diffraction (b) double diffraction (c) central diffraction

Figure 1.3: Feynman diagrams of soft diffractive processes.

1.4.1 Kinematics

The kinematics of a two-body scattering process, such as $1 + 2 \to 3 + 4$, can be effectively described using the Mandelstam variables. These are Lorentz-invariant quantities defined as:

- $s = (p_1 + p_2)^2 = (p_3 + p_4)^2$,
- $t = (p_1 - p_3)^2 = (p_2 - p_4)^2$,
- $u = (p_1 - p_4)^2 = (p_2 - p_3)^2$,

where p_1 and p_2 are the four-momenta of the incoming particles and p_3 and p_4 are the four-momenta of the outgoing particles. The Mandelstam variables are

not independent – the following useful relation between them holds:

$$s + t + u = m_1^2 + m_2^2 + m_3^2 + m_4^2, \tag{1.23}$$

where m_i are the masses of the respective particles.
Let's consider Single Diffraction, denoted as $1 + 2 \to 3 + X$. Such a process is usually described by three independent variables: s, t and the invariant mass of the system X, denoted as M_X^2. The latter can be expressed as:

$$M_X^2 = (p_1 + p_2 - p_3)^2. \tag{1.24}$$

A very useful variable is the **relative energy loss** of a scattered proton defined as:

$$\xi \simeq \frac{M_X^2}{s}, \tag{1.25}$$

where $\sqrt{s}$ by definition is the mass of the system of both colliding particles. If the energy of the particles is the same, then

$$\sqrt{s} = 2E_{beam}, \tag{1.26}$$

where E_{beam} denotes the energy of the particles in the colliding beams. The t channel represents the exchange of an intermediate particle between two initial-state particles. In that case, t is the square of the four-momentum transfer carried out by an intermediate particle.
In diffractive events, a prominent signature is the presence of the large rapidity gap, which is a consequence of the colour-neutral nature of the Pomeron exchange and is correlated with ξ:

$$\Delta y \approx \ln \frac{s}{M_X^2} \approx \ln \frac{1}{\xi}. \tag{1.27}$$

1.4.2 Hard Diffraction

Diffractive processes can also be classified into soft and hard diffraction based on the momentum transfer during the interaction:

- **Soft Diffraction** is characterised by a small momentum transfer and an energy scale significantly lower than the standard hadronic scale (less than 1 GeV^2). This part of diffraction is described as non-perturbative and inherits all the complexity of calculations at small momentum transfers. One should note that the description at the beginning of Section 1.4 as well as Feynman diagrams presented in Fig. 1.3, refer only to soft diffractive processes.

- **Hard Diffraction**: involves large momentum transfer and is described

within the framework of perturbative QCD.

Hard diffraction was proposed in Ref. [21], where the authors suggested the existence of the $p + p \to p + X$ process. There, the X system contained two jets with high transverse momentum. This process was experimentally measured by the UA8 experiment at the SPS collider at CERN [22, 23]. The presence of objects having large transverse momentum (p_T) allowed the use of perturbative methods in the calculations. Measurement of the cross-section for single diffractive production of two jets (SD JJ) allows for a determination of the so-called gap survival probability, a quantity introduced to explain differences between the extrapolation of HERA results and the Tevatron measurement [24].

The cross-section for a hard process, as non-diffractive jet production shown in Fig. 1.4[4], can be calculated as a convolution of the Parton Distribution Function with the cross-section for parton-parton interaction:

$$\mathrm{d}\sigma = f_p(x_1, Q^2) \cdot f_p(x_2, Q^2) \cdot \mathrm{d}\sigma_{\mathrm{hard}}(x_1, x_2, Q^2), \tag{1.28}$$

where x_1 and x_2 are the proton momentum fractions carried by the interacting partons, Q is the scale of the process and $f_p(x_1, Q^2)$ and $f_p(x_2, Q^2)$ are the corresponding Parton Distribution Functions [25, 26, 27]. The PDFs are thought to be universal *i.e.*, the same for all processes. The QCD theory accurately predicts how the PDF values change with scale. Therefore, it is possible to measure them at one scale and predict the results at another one.

Diffractive Parton Distribution Function (DPDF) can be factorised into [28]:

$$f_d(x, Q^2, \xi, t) = \Psi_P(\xi, t) \cdot f_P(\beta, Q^2), \tag{1.29}$$

where $\Psi_P(\xi, t)$ is the Pomeron flux, $f_P(\beta, \mu^2)$ denotes the Pomeron partonic structure and $\beta = x/\xi$, where ξ is the proton momentum fraction carried by the Pomeron. To agree with data, there is a need (especially in regions with low values of β and high values of ξ) to consider also the non-diffractive contributions [29]. This is usually done by adding Reggeons [19] and leads to the following formula:

$$f_d(x, Q^2, \xi, t) = \Psi_P(\xi, t) \cdot f_P(\beta, Q^2) + \Phi_R(\xi, t) \cdot f_R(\beta, Q^2). \tag{1.30}$$

The DPDFs obtained in electron-proton scattering can be used to describe proton-proton or proton-antiproton collisions. The cross-section for hard Single Diffrac-

[4]See Section 2.2.1 for the coordinate system definitions, including pseudorapidity (Eq. 2.10).

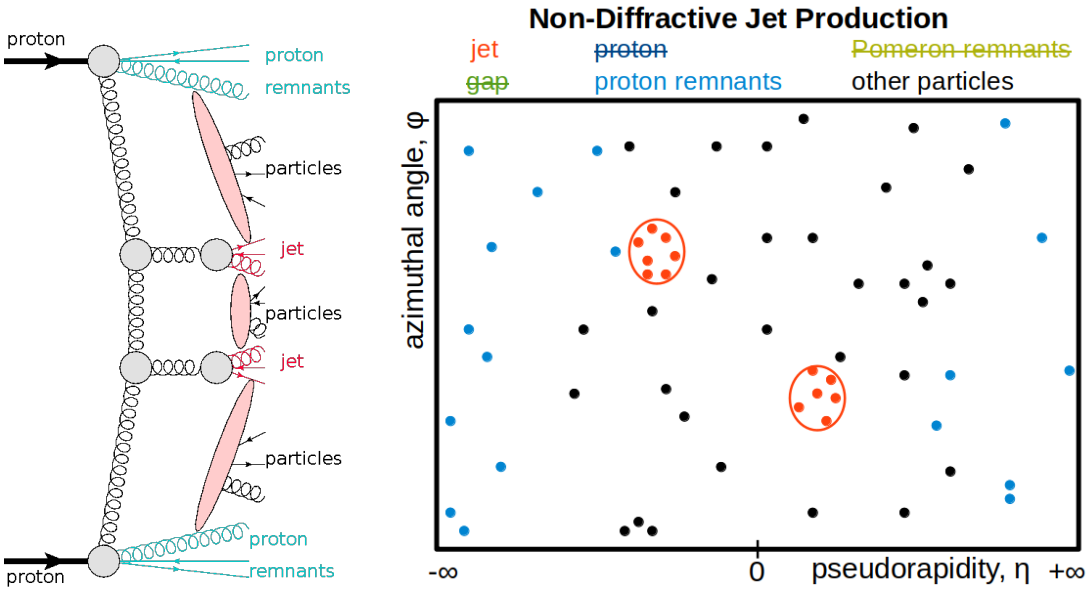

Figure 1.4: **Left:** Feynman diagram of the non-diffractive jet production: two high p_T jets originate from the leading gluons and both protons taking part in the collision are destroyed and hadronize. **Right:** example how the non-diffractive jet event may look in the pseudorapidity-azimuthal angle (η, φ) plane.

tive production (*cf.* Fig. 1.5) can be written as:

$$\mathrm{d}\sigma = S^2 \cdot \Psi(\xi_1, t) \cdot f_P(\beta, Q^2) \cdot f_p(x_2, Q^2) \cdot \mathrm{d}\sigma_{\mathrm{hard}}(x_1, x_2, Q^2) \tag{1.31}$$

and the one for Double Pomeron Exchange (*cf.* Fig. 1.6) is:

$$\mathrm{d}\sigma = S^2 \cdot \Psi(\xi_1, t) \cdot \Psi(\xi_2, t) \cdot f_P(\beta_1, Q^2) \cdot f_P(\beta_2, Q^2) \cdot \mathrm{d}\sigma_{\mathrm{hard}}(x_1, x_2, Q^2). \tag{1.32}$$

In the above equations, there is an additional factor S. It is called the rapidity gap survival probability and takes into account the fact that additional soft interactions between the initial or final state particles could destroy the rapidity gap in proton-(anti-)proton collisions. This factor was introduced following the analysis of the Tevatron data [24]. It was experimentally discovered that the number of hard diffractive events is smaller by a factor of about 10 than the one expected from the extrapolations of the HERA data. The factorisation is argued to be correct because soft interactions happen on much longer time scales than hard ones. Finally, the gap survival probability is expected to depend on the centre-of-mass energy – as $\sqrt{s}$ increases, the gap survival probability tends to decrease. This is because the interactions between the remnants of the particles become stronger, thereby tending to populate the gap [30].

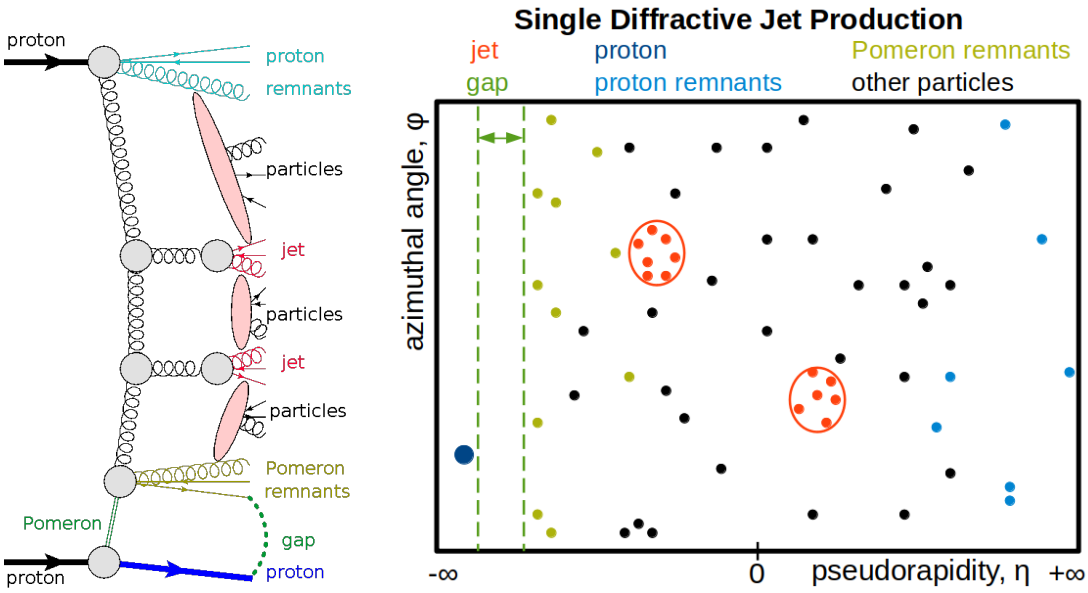

Figure 1.5: **Left:** Feynman diagram of the single diffractive jet production: two high p_T jets originate from the leading gluons, one proton taking part in the collision is destroyed and hadronize but the second one survives and can be measured. **Right:** example how the single diffractive di-jet event may look in the pseudorapidity-azimuthal angle (η, φ) plane.

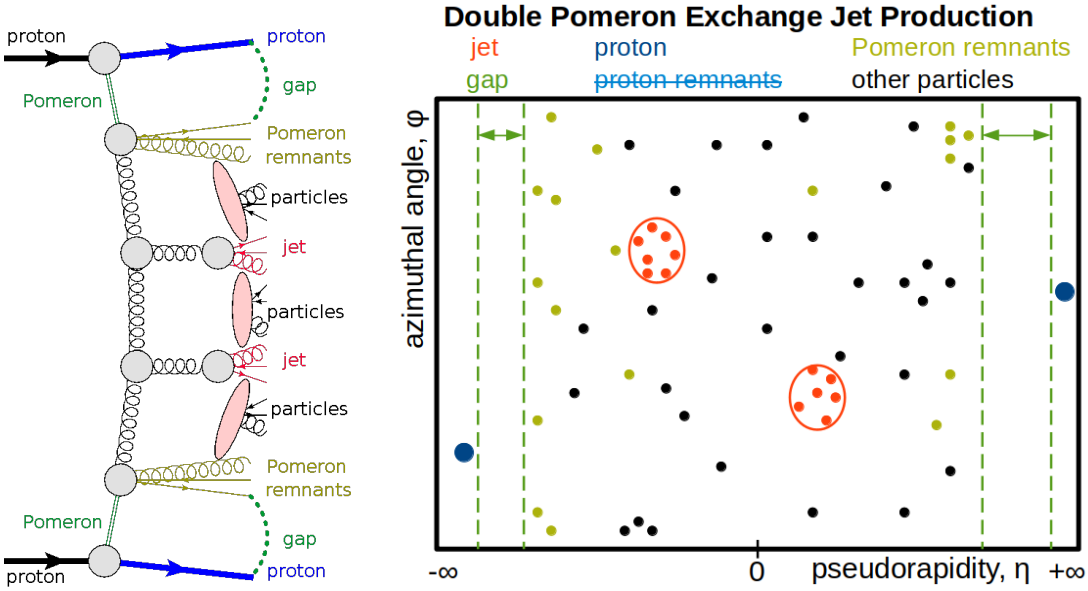

Figure 1.6: **Left:** Feynman diagram of the double Pomeron exchange jet production: two high p_T jets originate from the leading gluons and both colliding protons survive and can be measured. **Right:** example how DPE di-jet event may look in the pseudorapidity-azimuthal angle (η, φ) plane.

1.4.3 Jet-Gap-Jet Production

Interestingly, a colour singlet can be exchanged in the t channel, resulting in a rapidity gap between the two hard jets. Such events, pictured on Fig. 1.7, are called the (non-diffractive) Jet-Gap-Jet (JGJ) production [31, 32].

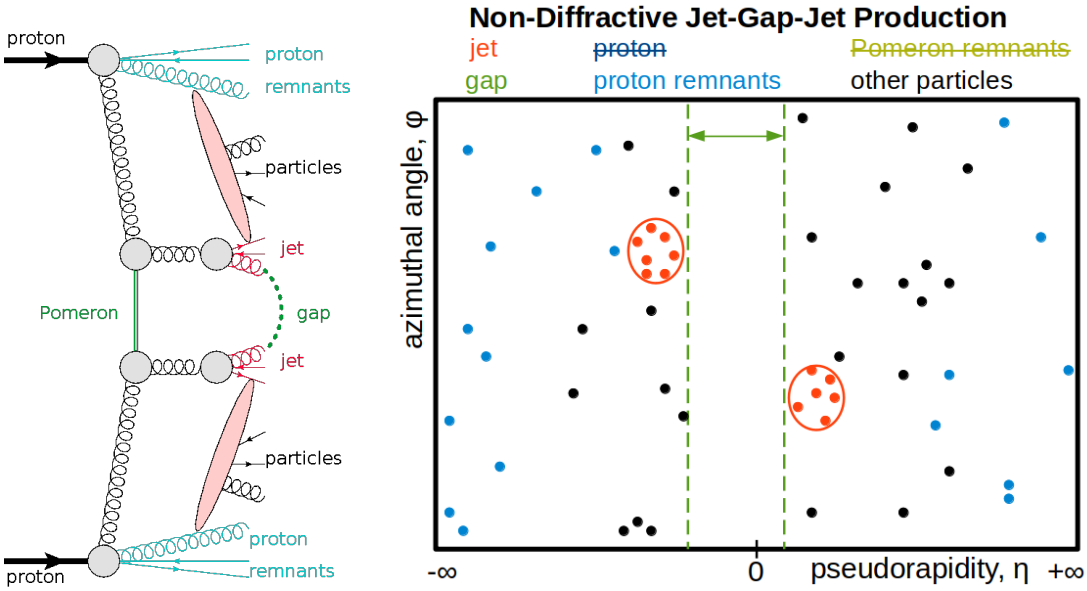

Figure 1.7: **Left:** Feynman diagram of non-diffractive jet-gap-jet production: a rapidity gap is present between two high p_T jets originating from the leading gluons and both protons taking part in the collision are destroyed and hadronize. **Right:** Example of how a non-diffractive JGJ event may look in the pseudorapidity-azimuthal angle (η, φ) plane.

The rapidity interval between the two jets is $\Delta\eta_J = \ln(x_1 x_2 s/(p_{T,1} p_{T,2}))$, where $p_{T,1}$ and $p_{T,2}$ are the transverse momenta of the jets and x_1 and x_2 are their longitudinal momentum fraction with respect to the incident hadrons [33]. At the parton level, the rapidity gap is equal to the rapidity interval between the outgoing partons. Hadronisation resulting in jets reduces the size of the rapidity gap to $\Delta\eta_g$. In the pseudorapidity plane (see Fig. 1.7 right), one will see two jets, protons' remnants spread in the forward direction and empty rapidity-space between the jets.

Jet-gap-jet event is often described by the Balitsky-Fadin-Kuraev-Lipatov (BFKL) framework of QCD [33, 34, 35, 36]. In this formalism, the cross-section for the JGJ process is defined as:

$$\frac{d\sigma_{pp\to XJJY}}{dx_1 dx_2 dp_T^2} = S \cdot f_{eff}(x_1, p_T^2) f_{eff}(x_2, p_T^2) \frac{d\sigma_{gg\to gg}}{dp_T^2}, \tag{1.33}$$

where S is the gap survival probability, f_{eff} are the effective parton density func-

tions and the cross-section formula for gluon-gluon (gg) scattering is given by:

$$d\sigma_{gg\to gg} = \frac{1}{16\pi}|A(\Delta\eta, p_T^2)|^2 dp_T^2. \tag{1.34}$$

The amplitude for gluon-gluon scattering, $A(\Delta\eta, p_T^2)$, is calculated as:

$$\begin{aligned} A(\Delta\eta, p_T^2) =& 16N_c\pi\alpha_s^2 C_F p_T^2 \sum_{p=-\infty}^{\infty} \int \frac{d\gamma}{2i\pi}[p^2 - (\gamma - \frac{1}{2})^2] \exp(\bar{\alpha}\chi_{eff}[2p, \gamma, \bar{\alpha}]\Delta\eta) \\ &\times \left[\frac{1}{(\gamma - \frac{1}{2})^2 - (p - \frac{1}{2})^2}\right] \left[\frac{1}{(\gamma - \frac{1}{2})^2 - (p + \frac{1}{2})^2}\right], \end{aligned}$$

where the complex integral is evaluated along the imaginary axis from $\frac{1}{2} - i\infty$ to $\frac{1}{2} + i\infty$. The summation is carried out over even values of p, termed in the literature as the "conformal spin" [34]. The $\overline{\alpha}(p_T^2) = \frac{\alpha_s(p_T^2)N_c}{\pi}$ is the running coupling constant.

Following [33], the effects of the next-to-leading logarithmic (NLL) BFKL effects can be accounted for in the conformal eigenfunction with an eigenvalue denoted as $\chi_{\text{eff}}(2p, \gamma, \overline{\alpha})$.

The interesting observable to study JGJ dynamics is the fraction of di-jet events produced by hard colour-singlet exchange, f_{CSE}. Such variable, also referred to as the gap fraction, is defined as:

$$f_{CSE} = \frac{N_{CSE\ di-jet}}{N_{all\ di-jet}}, \tag{1.35}$$

where $N_{CSE\ di-jet}$ is the number of di-jet events produced by the hard colour-singlet exchange and $N_{alldi-jet}$ is the number of all di-jet events (dominated by non-diffractive di-jet production). The fraction f_{CSE} can be measured as a function of various parameters, such as the second-leading jet transverse momentum p_{T2}, the pseudorapidity separation between the jets $\Delta\eta_{jj}$ or azimuthal angle between the jets: $\Delta\phi_{jj}$. The ratio offers a distinct advantage as it effectively reduces experimental and theoretical uncertainties by cancelling them. These uncertainties arise from several factors, including the calibration and reconstruction of the jets, proton parton densities or variations in the renormalisation and factorisation scales.

Finally, it should be noted that although the rapidity gaps are expected to occur primarily in the colour singlet exchange processes, they can also be observed in colour triplet (quark) or colour octet (gluon) exchanges as a result of fluctuations. Fortunately, the ratio of such exchanges is expected to decrease sharply with the increasing size of the pseudorapidity gap between the jets. This is due to the

larger phase space for hadronisation, resulting in the increased average particle multiplicity between the jets. Thus, when the rapidity distance between jets is large, the rapidity gap should be due to colour singlet exchange.

1.4.4 Diffractive Jet-Gap-Jet Production

The jet-gap-jet topology is also expected to be produced in the single diffractive and the double Pomeron exchange processes [8]. The first one is shown in Fig. 1.8 and the latter in Fig. 1.9.

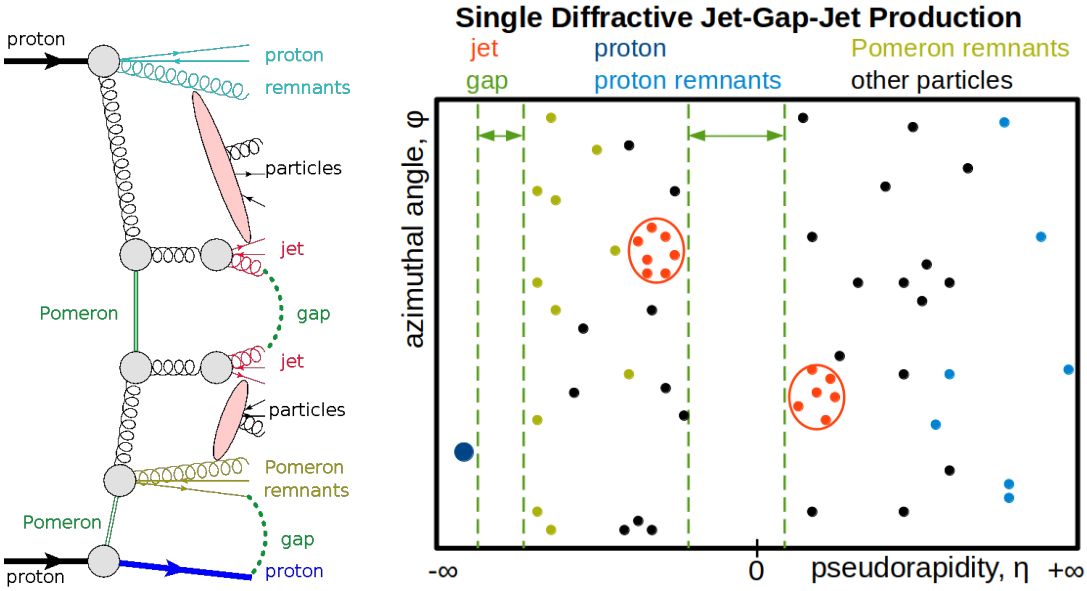

Figure 1.8: **Left:** Feynman diagram of the single diffractive jet-gap-jet production: a rapidity gap is present between two high p_T jets originating from the leading gluons, one proton taking part in the collision is destroyed and hadronize but the second one survives and can be measured. **Right:** Example of how the SD JGJ event may look in the pseudorapidity-azimuthal angle (η, φ) plane.

As argued in Ref. [8], in these configurations, the tests of the BFKL model are expected to be more powerful. This is because the gap fraction (f_{CSE}, *cf.* Eq. 1.35) is defined as a ratio of SD(DPE) JGJ to all SD(DPE) jet events. Therefore, the "penalty" of the gap survival probability applies to both the SD/DPE JGJ and the total SD/DPE cross-sections.

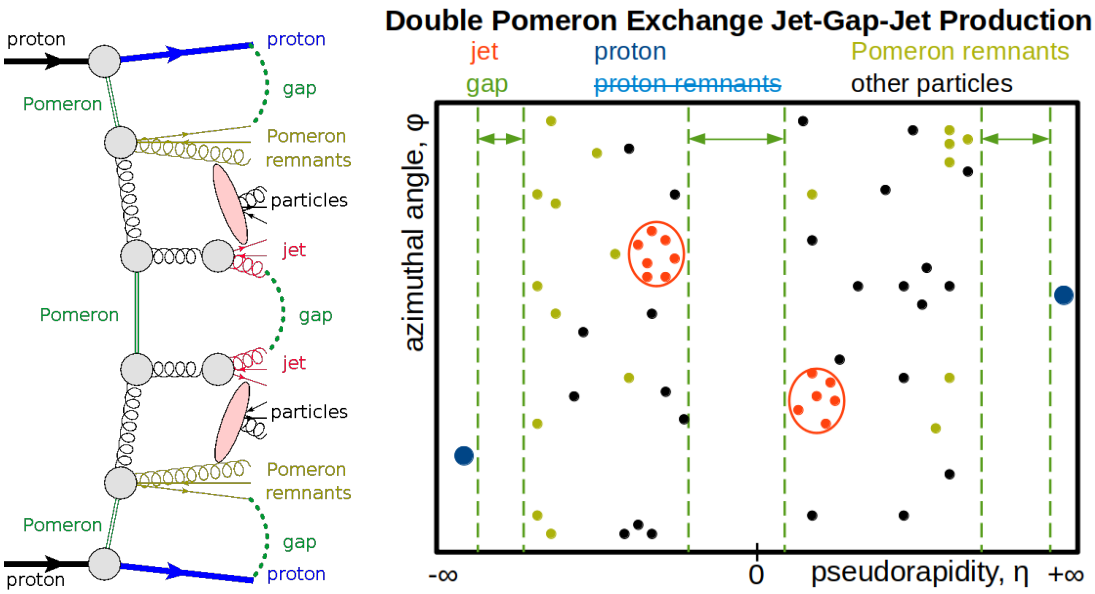

Figure 1.9: **Left:** Feynman diagram of the double Pomeron exchange jet-gap-jet production: a rapidity gap is present between two high p_T jets originating from the leading gluons and both colliding protons survive and can be measured. **Right:** Example of how the DPE JGJ event may look in the pseudorapidity-azimuthal angle (η, φ) plane.

Chapter 2

Experimental Setup

Features of (diffractive) jet-gap-jet events indicate the need for a certain experimental set-up. The data are expected to be delivered by the Large Hadron Collider (LHC). Events can be recorded by any of four major LHC experiments, but in this thesis, the focus will be on data collected by the ATLAS detector. The jets and gap are predominantly expected at relatively small absolute pseudorapidities; therefore "central" parts of ATLAS – the tracker and calorimeter – are important for their measurement. Diffractive protons are expected to be scattered into the beam pipe, escaping even the most forward parts of the ATLAS calorimeter. Special detectors, installed around 210 m from the collision point, were used to register them.
An overview of LHC and ATLAS sub-detectors will be given. Special attention will be paid to the forward proton taggers – the ATLAS Forward Proton (AFP) sub-detector. Since the settings of the LHC magnetic lattice have a crucial impact on the diffractive proton properties, but their description may be too technical for the reader, they are discussed in the Appendices.

2.1 The Large Hadron Collider: An Overview

The Large Hadron Collider (LHC) [37] is the world's largest and most powerful particle accelerator to date, designed to investigate the fundamental properties of matter and the forces that govern the Universe. This section provides a comprehensive technical description of the LHC, focusing on its design, key components, operational challenges and performance parameters. As this thesis uses the data collected during the so-called Run 3 of the LHC, particular attention will be given to the machine's specifications and capabilities during this period.
The LHC, located 50 to 175 meters underground near Geneva, Switzerland, spans a 27-kilometre circular tunnel initially built for the Large Electron-Positron Collider (LEP). Operated by CERN, the LHC accelerates and collides two counter-rotating beams of protons or heavy ions at four key interaction points. These points, each hosting a major experiment, are ATLAS [38], ALICE [39], CMS [40] and LHCb [41]. The beams intersect at these four interaction points, ensuring that both rings maintain equal circumferences, each comprising four inner and

four outer arcs.

Before entering the main LHC ring, the protons undergo a series of acceleration stages, each progressively increasing their energy. The injection chain consists of the linear accelerator Linac 4, the Proton Synchrotron Booster (PSB), the Proton Synchrotron (PS) and the Super Proton Synchrotron (SPS). This chain progressively increases the proton energy from 50 MeV to 450 GeV before injection into the LHC, where they are further accelerated to their final energy of 6.8 TeV per beam. A sketch of the CERN accelerator complex as of 2022 is shown in Figure 2.1.

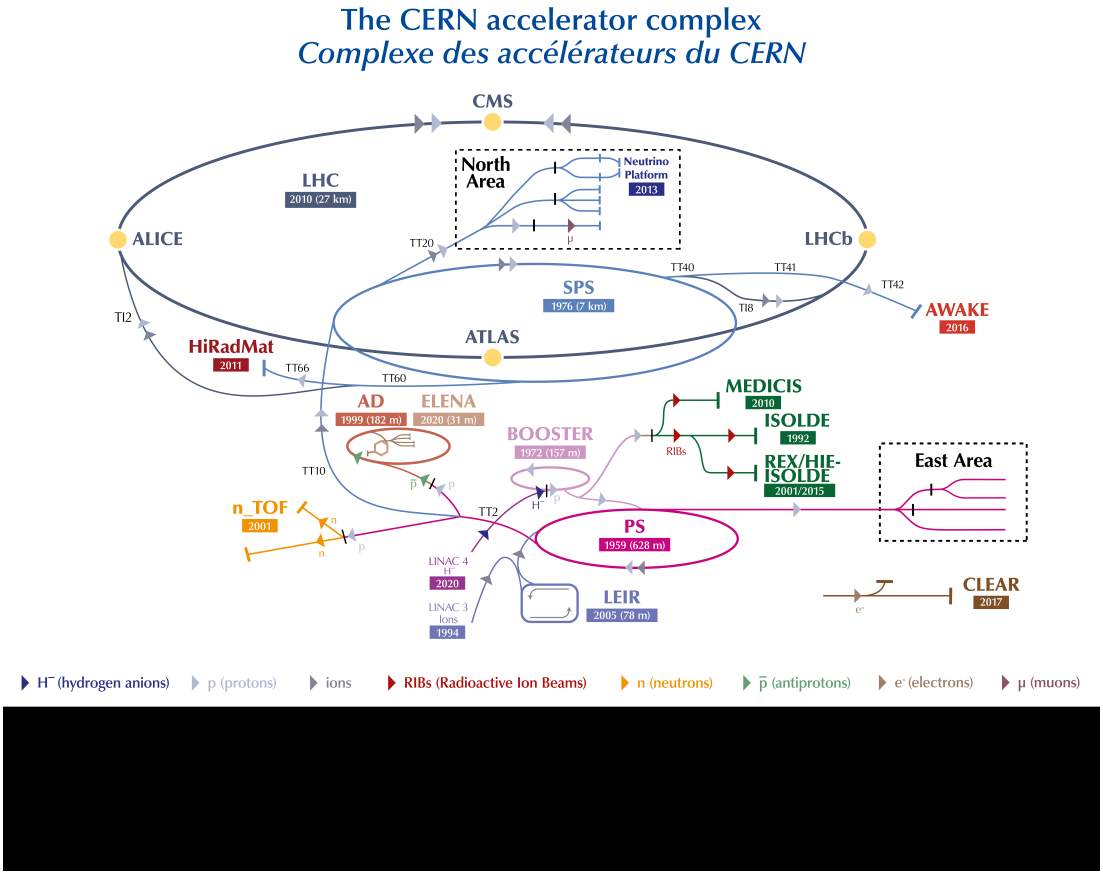

Figure 2.1: A detailed layout of CERN accelerators. Key facilities and experiments are highlighted, along with their commissioning dates. From [42].

In the LHC, the protons are grouped into bunches, each containing approximately 1.15×10^{11} particles. These bunches are spaced at 25-nanosecond intervals, allowing for up to around 2800 bunches per beam. Such tight bunch spacing presents significant challenges for the detector design and data acquisition systems, which must handle high data rates and resolve events occurring in a rapid succession.

In the LHC, the particle acceleration is achieved using 16 radio-frequency (RF) cavities, operating at 400 MHz, housed in four cryomodules. These cavities are cooled to superconducting temperatures to enhance efficiency and are powered

by high-energy klystrons. The RF energy, transmitted via waveguides, creates intense electromagnetic fields within the cavities, each capable of reaching 2 megavolts (MV), totalling 16 MV per beam.
The RF system boosts particle energy from 450 GeV to 6.8 TeV, a 15-fold increase, within about 20 minutes, with particles passing through the cavities over 10 million times. Precise timing at 400 MHz ensures optimal acceleration as the protons with correct energy remain unchanged, while those with slight deviations are adjusted. This helps to preserve the bunch-beam structure and minimises the proton energy spread.

2.1.1 Magnet System and Beam Guidance

The LHC magnet system uses superconducting technology to achieve the high magnetic fields necessary for steering and focusing the high-energy proton beams. The system consists of 1232 dipole magnets for bending the trajectories of the beams, 392 quadrupole magnets for beam focusing and various higher-order magnets for beam corrections. The superconducting dipole magnets, each 14.3 meters long, operate at the field strength of 8.3 Tesla, achieved using NbTi superconducting coils cooled to 1.9 K by superfluid helium. This low temperature is crucial for achieving the high dipole field required to bend the 6.8 TeV proton beams around the 27 km circumference.
The field, B, in the dipole magnets, is related to the proton transverse momentum p_T and the radius of curvature r by:

$$\vec{B} = \frac{p_T}{0.3 \cdot r}, \tag{2.1}$$

where the factor 0.3 accounts for the units (Tesla, GeV/c and meters).
The quadrupole magnets create a magnetic field gradient that increases linearly with distance from the magnet axis, providing a restoring force that keeps particles confined within the beam envelope. It should be noted that the nature of the quadrupole field focuses the beam in one transverse direction and defocuses it in the other. However, as in the case of lenses, one can achieve focusing in both transverse directions by the smart usage of focusing and defocusing elements. The focusing strength k of a quadrupole is given by:

$$k = \frac{1}{B\rho} \cdot \frac{dB}{dx}, \tag{2.2}$$

where $B\rho$ is the magnetic rigidity and dB/dx is the field gradient.
Higher-order magnets (sextupoles, octupoles, *etc.*) are used to correct for the beam imperfections and control various beam dynamics effects. Sextupoles, for

instance, are primarily used for chromaticity correction, while octupoles provide the Landau damping of collective instabilities.

The LHC's beam structure and dynamics are equally critical to its performance. The beam transverse size at the interaction point, σ^*, is a function of several parameters:

$$\sigma^* = \sqrt{\frac{\varepsilon_n \cdot \beta^*}{\beta_L \gamma}}. \tag{2.3}$$

Here, ε_n is the normalised emittance, a measure of the beam's average spread in position and momentum phase space, β^* is the betatron function at the interaction point, which describes the beam's focal properties and β_L and γ are the Lorentz factors, where $\beta_L = v/c$ (v is the particle velocity and c is the speed of light) and $\gamma = 1/\sqrt{(1-\beta_L^2)}$. One should note that in high energy physics β_L and γ are often expressed in terms of beam energy, E, particle momentum, p and particle mass, m: $\beta_L = p/E$ and $\gamma = E/m$.

For the LHC beam energy of 6.8 TeV, β_L is very close to 1 and γ is approximately 7250. The normalised emittance is "designed" to be about 3.5 μm·rad, and the beta function at the interaction point ranges from 1.2 to 0.3 m during the high-luminosity fills. This results in the beam transverse size of approximately 15 μm at the interaction point.

The rate of events due to a process with the cross-section, σ, and for the machine instantaneous luminosity, L, is given by:

$$\frac{dN}{dt} = \sigma \cdot L. \tag{2.4}$$

The instantaneous luminosity is given in units of $\mathrm{cm}^{-2}\cdot\mathrm{s}^{-1}$, and for Gaussian head-on colliding beams with uniformly populated bunches is defined as:

$$L = \frac{N^2 f n_b}{4\pi(\sigma^*)^2}, \tag{2.5}$$

where N is the number of particles per bunch, f is the beam revolution frequency, n_b is the number of bunches per beam, and σ^* is the Gaussian transverse width of the beam at the IP. The LHC-designed luminosity is $10^{34} cm^{-2} s^{-1}$, though the machine has exceeded this value during Run 3.

To mitigate the long-range beam-beam effects and to avoid parasitic collisions of the beams, the LHC employs a crossing angle θ_c of 150-200 μrad at the interaction point. This angle affects the luminosity through a geometric reduction factor [43]:

$$F = \frac{1}{\sqrt{1 + \left(\frac{\theta_c \sigma_z}{2\sigma^*}\right)^2}}, \tag{2.6}$$

where σ_z is the longitudinal bunch length. This factor balances the need for beam separation at parasitic collision points with maximising luminosity at the primary interaction point. The beam-beam interaction is quantified by the tune shift parameter ζ:

$$\zeta = \frac{N r_p}{4\pi\varepsilon_n \beta^*}, \tag{2.7}$$

where r_p is the classical proton radius. At the LHC, the ζ value is typically around 0.0034 per interaction point.

Another important parameter is the pile-up, μ, referring to the multiple proton-proton interactions in a single bunch crossing. The average number of interactions per crossing μ is given by:

$$\mu = \frac{L\sigma_{inel}}{n_b f}, \tag{2.8}$$

where σ_{inel} is the total inelastic cross-section. During Run 3, the LHC operates with μ of 50-60 at ATLAS and CMS collision points, see Fig. 2.2. This introduces significant challenges for the event reconstruction and analysis.

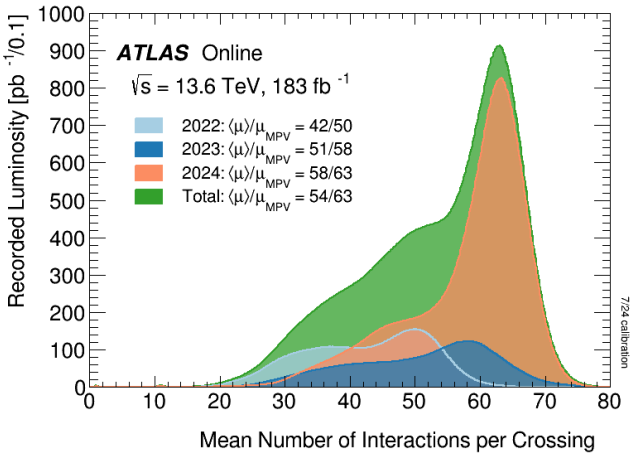

Figure 2.2: The luminosity-weighted distribution of the mean number of interactions per crossing for the 2022–2024 pp collision data at $\sqrt{s} = 13.6$ TeV at the ATLAS interaction point. From [1].

The dynamic aperture, defined as the maximum stable amplitude of particle oscillations, is crucial for long-term beam stability. It is primarily limited by the magnetic field errors in the superconducting magnets, especially at the injection energy where persistent current effects are most pronounced. Maintaining a sufficiently large dynamic aperture requires extensive numerical simulations and careful magnet design and operation.

Operational challenges in the LHC include beam instabilities, electron cloud effects, long-range beam-beam interactions, cryogenic system management and radiation-induced effects. These are addressed through a combination of advanced technologies and operational strategies, including feedback systems, special beam

pipe coatings, optimised bunch spacing, sophisticated cryogenic control systems and the use of radiation-hard electronics.

2.1.2 Operating Parameters

Since 2009, the LHC has been in continuous operation. It works in the so-called runs, which are multi-year periods of roughly continuous data collection. So far, the LHC has had three such run periods. Run 1 was held from 2009 to 2012, Run 2 from 2015 to 2018 and Run 3 since 2022.

During Run 1, the machine was operated at the centre-of-mass energies of 7 and 8 TeV, delivering[1] a total data set of 5.46 fb^{-1} and 22.8 fb^{-1}, correspondingly. This allowed *i.a.* the discovery of the SM Higgs Boson.

After two years of shutdown, Run 2 was started at $\sqrt{s} = 13$ TeV and delivered the data set of 156 fb^{-1}. The beam energy increase together with the reduction of bunch spacing from 50 ns to 25 ns resulted in this dataset being highly practical for searches for new particles.

The beam energy was further increased, resulting in $\sqrt{s} = 13.6$ TeV during Run 3. Up to now, 195 fb^{-1} of data have been delivered, with plans to double the integrated luminosity by the middle of 2026 when the Long Shutdown 3 is expected to start. The progress in luminosity delivery is shown in Fig. 2.3.

2.1.3 Future Plans

In Run 2, the LHC outperformed expectations, delivering higher-than-expected integrated luminosities. So far, Run 3 has also exceeded the expectations. The operation of such a complex machine resulted in many challenges. When I started PhD, Run 3 was planned to be three years long, starting in 2021. Its goal was to accumulate at least 150 fb^{-1} to attain the target of 300 fb^{-1} since the LHC started [44]. COVID-19 resulted in significant complications: Run 3 started in 2022 and is extended until the middle of 2026 to give enough time for the upgrade activities performed in parallel to the data-taking. It is interesting to compare the "old" and "current" LHC schedules – see Fig. 2.4.

Starting from the middle of 2026, the LHC accelerator and experiments aim for major upgrades. This campaign is often referred to as High-Luminosity LHC (HL-LHC). The goal of the HL-LHC is to collect at least 3000 fb^{-1} counting on the increased peak luminosity (due to the upgrades in detectors, cryogenics, triplet shielding *etc.*) and the increased density of the luminous region (due to

[1]The luminosity numbers quoted in this Section are for the ATLAS experiment. CMS collected a similar amount of data, whereas the data-taking condition required by ALICE and LHCb resulted in much smaller integrated luminosities.

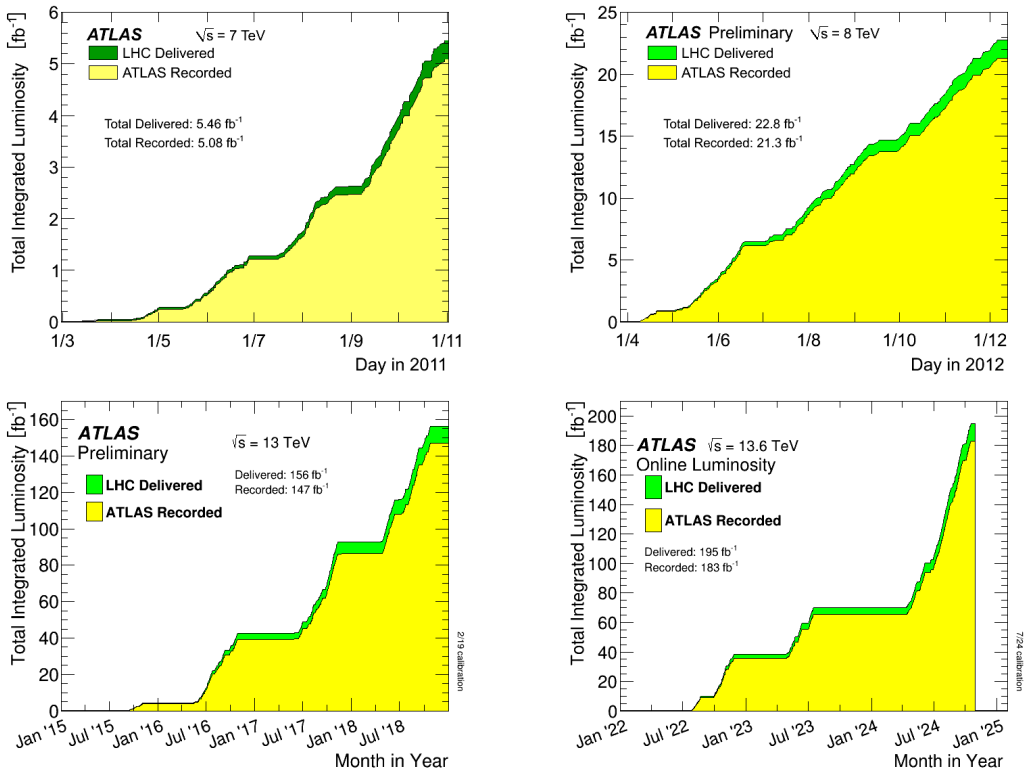

Figure 2.3: Cumulative luminosity versus time delivered to (green) and recorded by ATLAS (yellow) during stable beams and for *pp* collisions for Run 1 (top), Run 2 (bottom left) and Run 3 (bottom right). From [1].

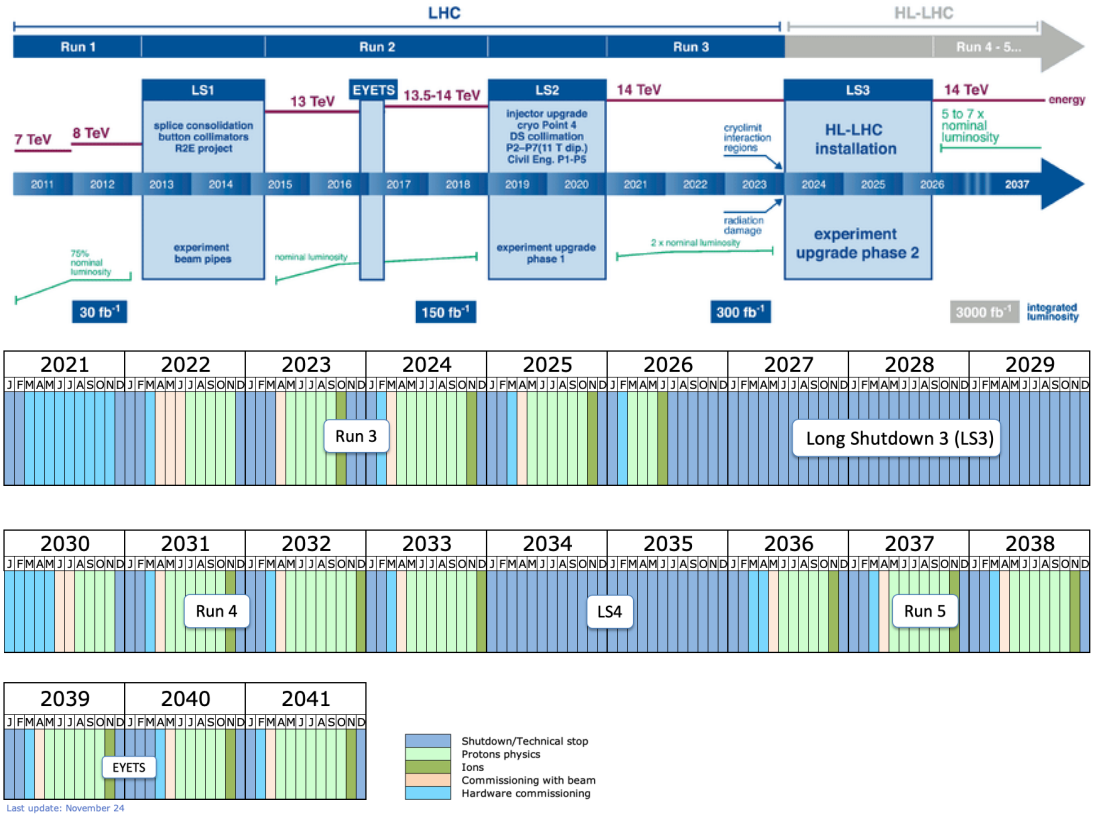

Figure 2.4: "Old" (**top**) and "current" (**bottom**) LHC long-term schedule.

bunch population with small emittance, β^* reduction *etc.*). The HL-LHC relies on an average of 140 to 200 events per crossing.

2.2 The ATLAS Detector: An Overview

The ATLAS (A Toroidal LHC ApparatuS) detector is one of two general-purpose particle detectors at the LHC. With its 45 m length, 25 m diameter and a mass of approximately 7000 tonnes, ATLAS is a complex, cylindrical detector designed to probe a wide range of physics processes at the TeV scale. The detector's architecture comprises several specialised sub-detectors arranged in concentric layers around the interaction point – Figure 2.5.

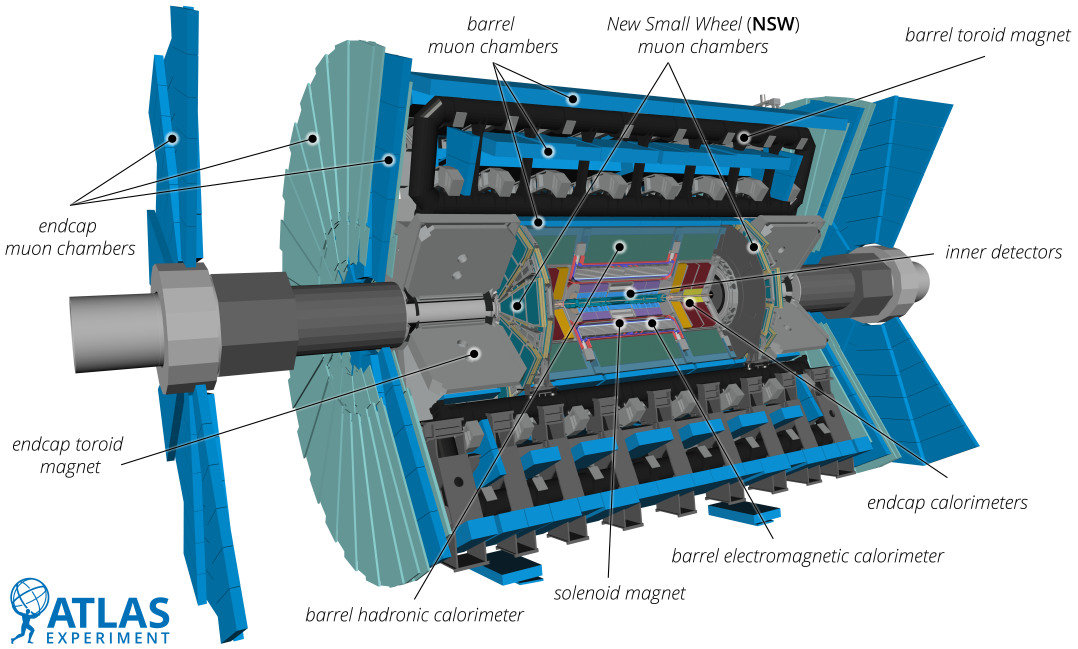

Figure 2.5: Drawing of the ATLAS detector with all its sub-detectors. From [45].

Such design provides nearly 4π solid angle coverage around the collision point, maximising the detector acceptance and enabling comprehensive reconstruction of collision events. At the core of ATLAS lies the Inner Detector, situated closest to the beam pipe. It operates within a 2 T solenoidal magnetic field and is responsible for tracking charged particles, reconstructing their momenta and determining vertex positions with high precision. Surrounding the Inner Detector and solenoid magnet are the calorimeter systems. The electromagnetic calorimeter, based on liquid argon technology, measures the energies of electrons and photons. The hadronic calorimeter, using a combination of scintillating tiles and liquid argon, is optimised for measuring the energies of hadrons. These calorimeters perform particle identification and energy measurements, particularly for jets and missing

transverse energy calculations. The outermost layer of ATLAS is occupied by the Muon Spectrometer, which identifies muons with tracks bent by a toroid magnet system and measures their momenta.

2.2.1 ATLAS Coordinate System

ATLAS uses a right-handed coordinate system with its origin located at the nominal interaction point – the centre of the detector. The z-axis is defined along the beam pipe, with the positive direction pointing towards the A-side[2] of the ATLAS cavern. The x-axis points from the interaction point towards the centre of the LHC ring, while the y-axis points upwards, perpendicular to the LHC plane.

Given the cylindrical symmetry of the detector, cylindrical (r, ϕ, z) and spherical (r, θ, ϕ) coordinates are frequently used in conjunction with the Cartesian system. The radial distance, r, is measured from the beam axis and is defined as $r = \sqrt{x^2 + y^2}$. The azimuthal angle, ϕ, is measured in the transverse, (x, y), plane, starting from the positive x-axis, with $\phi \in [-\pi, \pi]$. It is calculated using the two-argument arctangent function to ensure the correct quadrant:

$$\phi = \arctan 2(y, x). \tag{2.9}$$

The polar angle, θ, is measured from the positive z-axis and ranges from 0 to π. However, in practice, ATLAS predominantly uses pseudorapidity, η, defined as:

$$\eta = -\ln\left[\tan\left(\frac{\theta}{2}\right)\right]. \tag{2.10}$$

Differences in η are invariant under the longitudinal Lorentz boosts, which is particularly useful at the hadron colliders where the centre-of-mass frame of the hard scatter is generally boosted along the beam axis. Particle production is approximately uniform in the central η region at the colliders, making it a natural choice to describe detector acceptance and particle distributions. Figure 2.6 illustrates the ATLAS coordinate system, showing the relationship between various coordinates.

The ATLAS detector is conceptually divided into several regions based on pseudorapidity. The central region, also known as the barrel, covers $|\eta| < 1.4$. The end-cap region extends to $1.4 < |\eta| < 3.2$, while the forward region covers $3.2 < |\eta| < 4.9$. These regions are related to transitions between different detector subsystems or technologies.

[2] A stands for "anti-clockwise", *i.e.* towards the LHCb experiment. C is "clockwise" – towards ALICE.

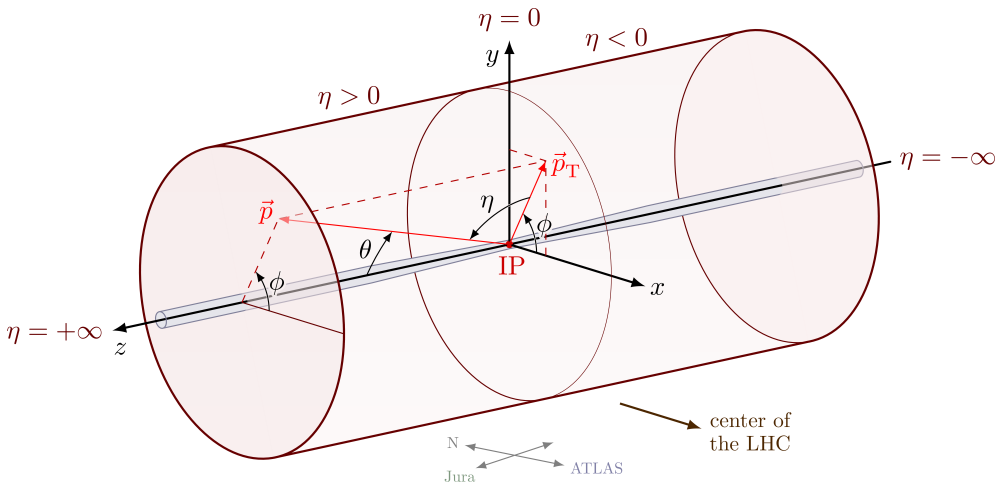

Figure 2.6: Illustration of the ATLAS coordinate system.

In hadron collider physics, transverse quantities are of particular importance due to the unknown longitudinal momentum of the colliding partons. The transverse momentum p_T and transverse energy E_T are defined in the (x, y) plane:

$$p_T = \sqrt{p_x^2 + p_y^2}, \quad E_T = E \sin\theta = E \cosh\eta. \tag{2.11}$$

The angular separation between objects in the detector is typically quantified using ΔR, defined as:

$$\Delta R = \sqrt{(\Delta\eta)^2 + (\Delta\phi)^2}. \tag{2.12}$$

This measure is approximately invariant under longitudinal boosts for relativistic particles and is widely used in jet algorithms and isolation criteria.

2.2.2 Inner Detector

The Inner Detector (ID) [46, 47] is the innermost sub-detector of the ATLAS tracking system, designed to provide high-precision measurements of charged particle trajectories in the intense radiation environment of the LHC. Operating within a 2 T axial magnetic field generated by the central solenoid, the ID enables accurate determination of particle momenta and vertex positions. The ID has a diameter of 2.1 m and a length of 6.2 m, consisting of three main components: the Pixel Detector, the Semiconductor Tracker (SCT) and the Transition Radiation Tracker (TRT).

Each component has a cylindrical barrel region arranged in concentric cylinders around the beam axis and two disk end-caps perpendicular to the beam axis, covering a total pseudorapidity range of $|\eta| < 2.5$. This design ensures comprehensive tracking capabilities across a wide range of angles from the interaction

point. Figure 2.7 shows a sketch of the Inner Detector in the central region, illustrating the concentric arrangement of its components.

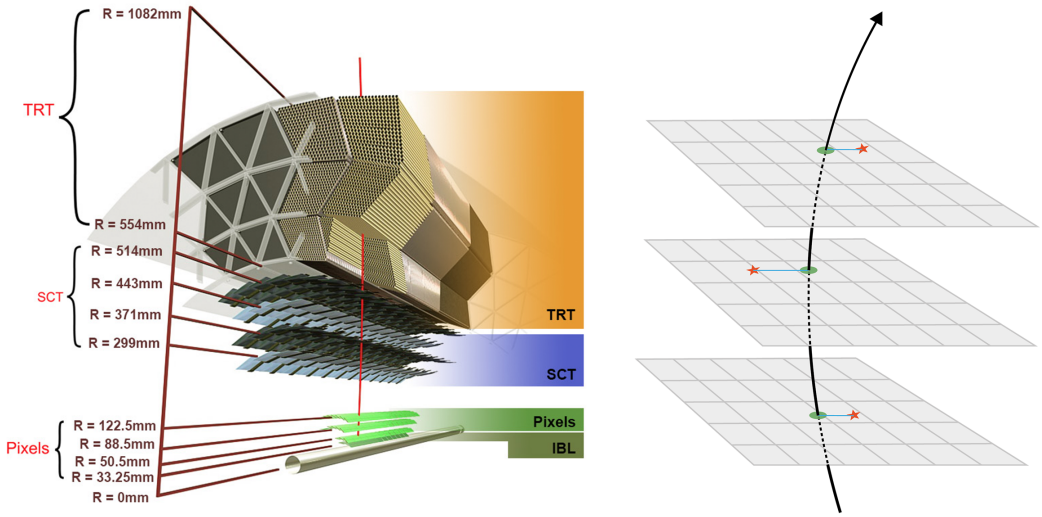

Figure 2.7: **Left:** sketch of the Inner Detector in the central region, showing the concentric arrangement of the Pixel Detector. **Right:** concept of particle trajectory reconstruction. Red stars mark each detector measurement (hit). The fitted track is illustrated with a black arrow. Green dots denote the intersections of the track with each surface. Blue lines indicate the track-to-hit residuals for each layer. From [45].

The combined transverse momentum resolution of the ID is parametrised as:

$$\frac{\sigma(p_T)}{p_T} = 0.05\% \cdot p_T[\text{GeV}] \oplus 1\%. \tag{2.13}$$

This resolution degrades as the transverse momentum of the incoming particle increases, primarily because of the smaller track curvatures at higher momenta. The constant term (1%) represents the effects of multiple scattering, which dominate at lower momenta, while the term proportional to p_T accounts for the intrinsic detector resolution and alignment uncertainties, which become more significant at higher momenta.

2.2.2.1 Pixel Detector

The Pixel Detector, being the innermost component of the ID, provides the highest granularity for the vertex reconstruction and b-tagging. It consists of four-barrel layers and three disks on each end-cap, covering a pseudorapidity range of $|\eta| < 2.5$. The detector layers are arranged concentrically around the beam pipe, with the Insertable B-Layer (IBL) [48] at a radius of 33.25 mm, followed by the B-Layer at 50.5 mm, Layer 1 at 88.5 mm, and Layer 2 at 122.5 mm. This arrangement ensures excellent tracking resolution close to the interaction point.

The Pixel Detector sensors have a nominal pixel size of 50×400 μm^2 ($\phi \times z$) for the three outer layers. The IBL, added during the Long Shutdown 1, features smaller pixels of 50×250 μm^2, providing enhanced resolution. The sensors are 256 μm thick for the outer layers and 200 μm for the IBL.
The cluster positions have the spatial resolution, in transverse direction $R-\phi$, of about 10 μm for the outer layers and 8 μm for the IBL. The z-direction resolution is approximately 115 and 70 μm for the outer layers and IBL, respectively.

2.2.2.2 Semiconductor Tracker (SCT)

The Semiconductor Tracker (SCT) forms the middle component of the ATLAS Inner Detector, surrounding the Pixel Detector. It consists of four-barrel layers and nine disks on each end-cap, covering a pseudorapidity range of $|\eta| < 2.5$. The SCT works according to the same physics principles as the pixel detector but with silicon strips instead of pixels.
In the barrel, the strip pitch is 80 μm, while in the end-caps, it varies from 57 to 94 μm. The SCT barrel layers are positioned at radii of 299, 371, 443 and 514 mm, with the end-cap disks located at distances between 853.8 and 2720.2 mm from the interaction point.
Each SCT module comprises two layers of silicon microstrip sensors. The strips are read out on both sides of the silicon modules which are rotated 40 mrad relative to each other. These two 2D measurements are combined to recreate the incident particle location, enabling both $r-\phi$ and z measurements. The SCT modules have a resolution of 17 μm in the $r-\phi$ plane and 580 μm in the z-direction.

2.2.2.3 Transition Radiation Tracker (TRT)

The Transition Radiation Tracker (TRT) forms the outermost component of the ATLAS Inner Detector. It consists of straw tubes filled with the Xenon-based gas mixture, providing continuous tracking and electron identification capabilities. The TRT covers the pseudorapidity range $|\eta| < 2.0$.
In the barrel region, $|\eta| < 1.0$, the TRT comprises approximately 50,000 straws, each 144 cm long, arranged parallel to the beam axis. The end-cap regions ($1.0 < |\eta| < 2.0$) contain about 320,000 radially oriented straws, each 37 cm long. The straw has a diameter of 4 mm and contains 31 μm thick gold-plated tungsten wire at its centre.
The TRT's dual functionality includes the following:

1. Tracking: Charged particles ionise the gas mixture in the straws. The resulting electrons drift towards the central wire, producing a measurable

signal. This allows continuous tracking with an intrinsic accuracy of about 130 μm per straw.

2. Particle Identification: The spaces between the straws are filled with polymer fibres (barrel) or foils (end-cap) that induce the transition radiation when traversed by relativistic charged particles, dependent on the Lorentz boost. This radiation is absorbed by the Xenon-based gas mixture, producing much larger signals than those from ionisation alone.

The TRT's ability to distinguish between transition radiation and tracking signals allows for efficient electron identification, complementing the energy measurements from the calorimeters. As the transition radiation depends on the particle's Lorentz gamma, the electrons produce many more high-threshold hits along their path than the pions of the same energy, predominantly generating low-threshold hits.
On average, a charged particle with $p_T > 0.5$ GeV and $|\eta| < 2.0$ will traverse about 35 straws, except in the barrel-end-cap transition region ($0.8 < |\eta| < 1.0$), where this number decreases to about 22 straws. This high number of hits per track significantly contributes to the momentum resolution of the Inner Detector, particularly for tracks with $p_T > 1$ GeV.
During LS2, a demonstrator module of the future Inner Tracker (ITk) [49, 50] Strip Detector was installed. While the full ITk upgrade is scheduled for LS3, this prototype allows for testing and validation of the new silicon strip technology in real LHC conditions. The ITk will eventually replace the entire current Inner Detector, providing improved tracking performance to cope with the higher luminosities and radiation levels expected in the High-Luminosity LHC phase. The demonstrator's performance informs the final design and installation strategy for the complete ITk upgrade.

2.2.3 Calorimeter System

After passing the inner detector, particles produced in the collision interact with the dense material of ATLAS calorimeters, initiating cascades of secondary particles. This allows the reconstruction of the original particle's energy.
The ATLAS calorimeter system, illustrated in Figure 2.8, comprises three main components: the electromagnetic calorimeter (ECAL), the hadronic calorimeter (HCAL) and the forward calorimeter (FCAL). This tripartite system covers up to $|\eta| < 4.9$. However, the detector's efficiency is compromised in transition regions due to significant dead material and services (*e.g.* cryostat walls, cabling). These regions occur between the central barrels and end caps at $|\eta| \sim 1.5$ and between the ECAL/HCAL and FCAL at $|\eta| \sim 3.1$ [38].

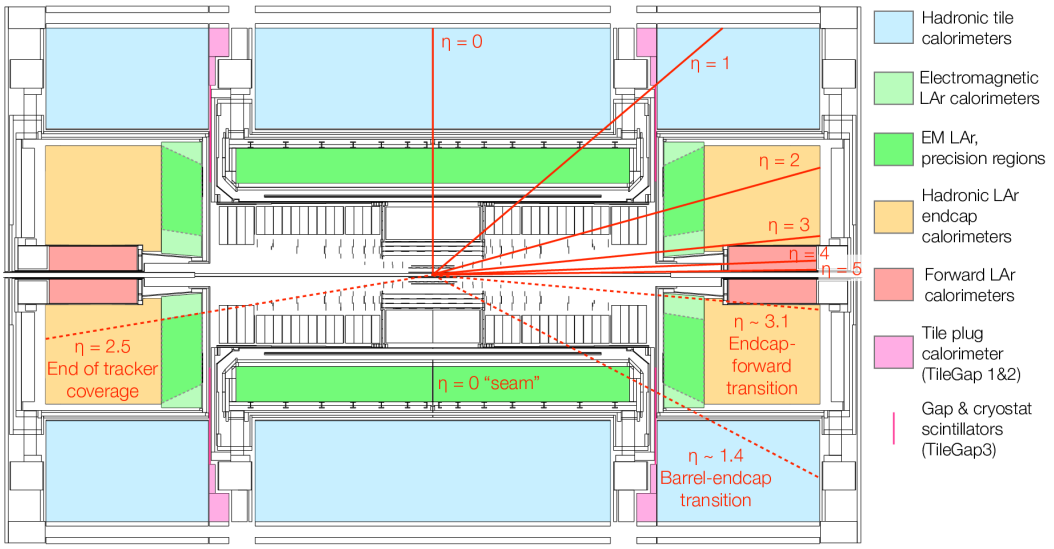

Figure 2.8: Sketch of the ATLAS calorimeter system.

ATLAS employs sampling calorimeters with alternating layers of dense absorber material and active detection media. This design ensures full azimuthal (ϕ) symmetry and coverage around the beam axis. The absorber initiates particle showers, while the active medium generates detectable signals proportional to the deposited energy. The key characteristics of the ATLAS calorimeter subsystems are summarised in Table 2.1.

Table 2.1: Overview of the ATLAS calorimeter system, detailing subsystem types, coverage in pseudorapidity, longitudinal segmentation, granularity and energy resolution. From [51].

Subsystem	Type	Coverage ($\|\eta\|$)	Longitudinal Segmentation	Granularity ($\eta \times \phi$)	Energy Resolution[3] (%)
EM Calorimeter	Barrel (LAr+Pb)	< 1.475	3 samplings	0.003 × 0.1 (S1) 0.025 × 0.025 (S2)	$\frac{10}{\sqrt{E}} \oplus 0.7$
	End-cap (LAr+Pb)	1.375 - 3.2	2 samplings (3 for 1.5 - 2.5)	0.025 × 0.1 0.1 × 0.1	
Presampler	Barrel (LAr)	< 1.52	1 sampling	0.025 × 0.1	-
	End-cap (LAr)	1.5 - 1.8	1 sampling	0.025 × 0.1	
Hadronic Tile	Barrel	< 1.0	3 samplings	0.1 × 0.1	$\frac{52}{\sqrt{E}} \oplus 3$
	Extended barrel	0.8 - 1.7	3 samplings	0.1 × 0.1	
Hadronic LAr	End-cap (LAr+Cu)	1.5 - 3.2	4 samplings	0.1 × 0.1	$\frac{84}{\sqrt{E}} \oplus 3$
Forward (LAr)	EM+Hadronic	3.1 - 4.9	3 samplings	FCal1: ∼0.15 × 0.15 FCal2: ∼0.2 × 0.2 FCal3: ∼0.2 × 0.2	$\frac{94}{\sqrt{E}} \oplus 7.5$

2.2.3.1 Electromagnetic Calorimeter (ECAL)

The electromagnetic calorimeter (ECAL) measures the energy of electrons and photons and contributes to jet energy measurements. It consists of a barrel sec-

tion (EMB) covering $|\eta| < 1.475$ and two end-cap components (EMEC) covering $1.375 < |\eta| < 3.2$. The ECAL is a sampling calorimeter with lead absorber plates and liquid argon (LAr) as the active medium, arranged in an accordion geometry. The accordion structure allows for fast signal collection by placing the readout electrodes close to the active detector material.

The ECAL barrel region is segmented into three compartments with varying granularity. The first layer, closest to the beam pipe, is finely segmented in η with 4 mm wide strips, enabling good separation between prompt photons and $\pi^0 \to \gamma\gamma$ decays. The second compartment, where most of the shower energy is deposited, has the granularity of $\Delta\eta \times \Delta\phi = 0.025 \times 0.025$. The third layer has a coarser granularity of $\Delta\eta \times \Delta\phi = 0.05 \times 0.025$, which captures only the shower tails and thus does not require the same level of fine segmentation.

Lead plates were chosen as the passive medium due to their large electromagnetic cross-section. High-energy electrons and photons primarily interact through bremsstrahlung or pair production, resulting in the generation of an electromagnetic shower. The shower's spatial extent is characterised by the radiation length, X_0, representing the average distance over which a high-energy electron loses all but $1/e$ of its energy. The ECAL's thickness is $\geq 22X_0$ across all regions, ensuring that most electromagnetic showers are fully contained within the calorimeter volume.

In the region $|\eta| < 1.8$, a thin presampler detector (11 mm in the barrel, 5 mm in the end-caps) precedes the ECAL. This LAr layer provides a first sampling of showers, allowing corrections for energy lost in the upstream material such as the inner detector, cryostat walls and solenoid coil.

The transition region between the barrel and end-cap cryostats ($1.37 < |\eta| < 1.52$) suffers from reduced energy resolution and is often excluded in precision measurements. Additional transition regions exist between the outer and inner wheels of the end-cap at $|\eta| = 2.5$ and between the end-cap and forward calorimeter at $|\eta| \approx 3.2$.

During LS2, the LAr calorimeter received an electronics upgrade, with new trigger readout boards installed to provide higher granularity data to the Level-1 trigger system.

2.2.3.2 Hadronic Calorimeter (HCAL)

While the ECAL is designed to contain electromagnetic showers, hadrons typically penetrate further into the detector. The Hadronic Calorimeter (HCAL) measures the energy of hadrons and jets, which can interact both electromagnetically and hadronically with the detector material. The HCAL plays a crucial role in jet reconstruction and missing transverse energy ($E_{\mathrm{T}}^{\mathrm{miss}}$) measurements.

Hadronic showers are characterised by the nuclear interaction length λ, which is typically 5-10 times larger than the radiation length X_0. Consequently, hadronic showers develop over longer distances compared to electromagnetic ones. The HCAL is designed with sufficient depth to contain most hadronic showers, with a thickness of approximately 11λ at $\eta = 0$, including support structures.
The ATLAS HCAL system consists of three main components. The Tile Calorimeter covers the pseudorapidity range $|\eta| < 1.7$ and uses steel as the absorber material and scintillating tiles as the active medium. It is divided into a central barrel region ($|\eta| < 1.0$) and two extended barrels ($0.8 < |\eta| < 1.7$). The Tile Calorimeter has an inner radius of 2.28 m and an outer radius of 4.25 m. The scintillating tiles are read out by wavelength-shifting fibres into photomultipliers. It is segmented into three layers with a granularity of $\Delta\eta \times \Delta\phi = 0.1 \times 0.1$ in the first two layers and 0.2×0.1 in the third layer. Between the barrel and extended barrels, special scintillators are placed to recover energy that would otherwise be lost in these transition regions.
The Hadronic End-Cap calorimeter (HEC) covers $1.5 < |\eta| < 3.2$. It uses copper plates as the absorber material and liquid argon as the active medium. The HEC shares the same cryostats as the EMEC and Forward Calorimeter (FCal). The HEC has a granularity of $\Delta\eta \times \Delta\phi = 0.1 \times 0.1$ for $|\eta| < 2.5$ and 0.2×0.2 for larger $|\eta|$.

2.2.3.3 Forward Calorimeter

The FCal extends the calorimeter coverage to $|\eta| < 4.9$, providing both electromagnetic and hadronic energy measurements in the high-pseudorapidity region. It is approximately 10 interaction lengths long and consists of three modules: the first uses copper as the absorber and is devoted to the electromagnetic measurements, while the other two use tungsten and are designed for hadronic interactions. All modules use liquid argon as the active medium. This compact design, a metal matrix with uniformly spaced longitudinal channels filled with concentric rods and tubes, allows for effective shower containment and fast signal readout in the high-flux forward region.

2.2.4 Muon Spectrometer

The Muon Spectrometer (MS) [52] forms the outermost layer of the ATLAS detector. It is designed to detect and measure the momentum of charged particles, primarily muons, that traverse the inner detectors and calorimeters. The MS extends from a radius of 4.25 m to the full 11 m radius of the detector and provides coverage up to $|\eta| < 2.7$. It operates within the magnetic field generated

by a system of superconducting air-core toroid magnets: a large barrel toroid and two end-cap toroids. This configuration produces a mostly radial magnetic field that bends muon trajectories in the η-direction, allowing for precise momentum measurements independent of the inner detector.

During the Long Shutdown 2, a major upgrade to the muon spectrometer was implemented with the installation of the New Small Wheel (NSW) [53]. The NSW replaces the innermost stations of the end-cap muon tracking system in the region $1.3 < |\eta| < 2.7$. It consists of two new detector technologies: small-strip Thin Gap Chambers (sTGC) and Micromegas (MM), providing improved spatial resolution ($<$100 μm), angular resolution ($\sim$1 mrad), and timing for muon reconstruction. This upgrade enhances the trigger and tracking capabilities in the forward regions, which is crucial for maintaining performance in the high-luminosity environment of the LHC Run 3 and beyond.

The MS has four different types of muon chambers. Monitored Drift Tubes (MDTs) are used for precision tracking measurements in most of the η-range, with Cathode Strip Chambers (CSCs) used in the innermost layer of the end-caps ($2.0 < |\eta| < 2.7$) to withstand higher rates. For triggering and second-coordinate measurements, the Resistive Plate Chambers (RPCs) are used in the barrel region ($|\eta| < 1.05$), while the Thin Gap Chambers (TGCs) are employed in the end-cap regions ($1.05 < |\eta| < 2.4$). This combination of technologies enables the MS to achieve a stand-alone transverse momentum resolution of approximately 10% for 1 TeV muons, and when combined with the inner detector measurements, improves to about $2 - 3\%$ in the same momentum range. The MS not only provides muon identification and momentum measurement but also contributes to the Level-1 trigger system, offering fast event selection for muons across a wide range of transverse momenta.

2.2.5 ATLAS Forward Proton Detector

The ATLAS Forward Proton (AFP) [54] detector system, installed during 2015/2016 (side C) and 2016/2017 (full set) shutdown, extends the physics program of ATLAS. AFP is designed to register the protons scattered at very small angles relative to the beam direction, which emerge intact from collisions and carry 80% to 98% of the initial beam energy.

The AFP stations are located at $\pm$205 m (NEAR) and $\pm$217 m (FAR) from the ATLAS interaction point. Figure 2.9 illustrates the general layout of the AFP detectors and their components.

AFP uses the Roman pot technology. The pots are manoeuvred by a high-precision positioning system consisting of stepper motors and linear variable dif-

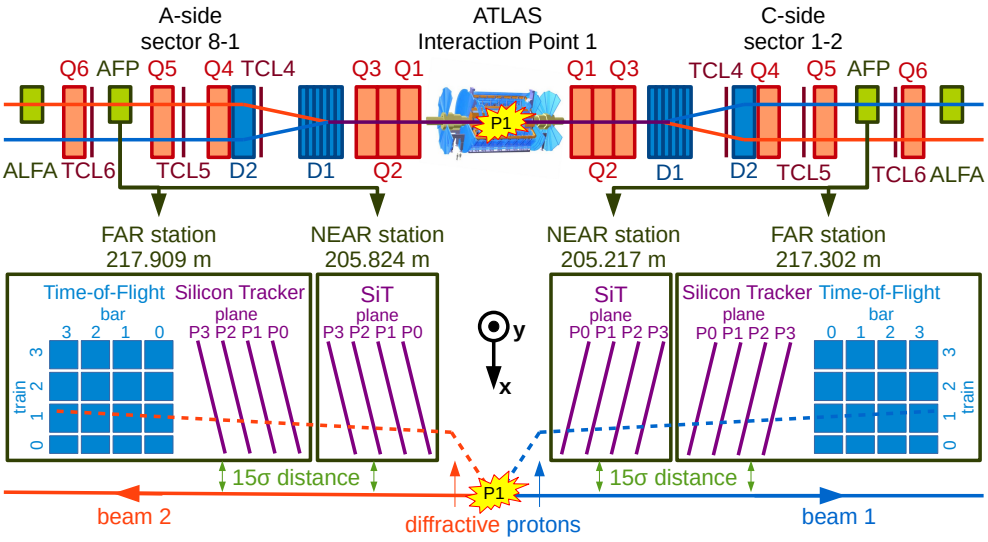

Figure 2.9: Scheme of the AFP detectors around the ATLAS interaction point.

ferential transformers (LVDTs). This system inserts the pots to 2-3 mm of the beam centre during stable conditions and retracts them to 40-45 mm during injection and acceleration. Stepper motors achieve 10 μm positioning precision. Pots are made of stainless steel with beam-facing windows having a thickness of 300 μm, to minimise material interactions with scattered protons. This design enables the AFP to detect protons scattered at very small angles without interfering with normal LHC operations.

2.2.5.1 AFP Silicon Detectors

The AFP Silicon Trackers (SiT) measure the positions of forward-scattered protons with high precision. Located in NEAR and FAR stations, each station houses four planes of 3D silicon pixel sensors, see Fig. 2.10. This dual-station configuration enables improved track reconstruction and momentum resolution compared to a single-station setup.

The SiT uses radiation-hard 3D silicon pixel sensors, a technology chosen for its excellent radiation tolerance and high-speed readout capabilities. The 3D sensor design, featuring columnar electrodes that penetrate the silicon bulk perpendicular to the surface, allows for a shorter charge collection distance than planar sensors. This design results in faster charge collection, improved radiation hardness, and reduced charge trapping effects.

The 3D silicon sensors used in the SiT have an active area of 16.8 mm $\times$ 20.0

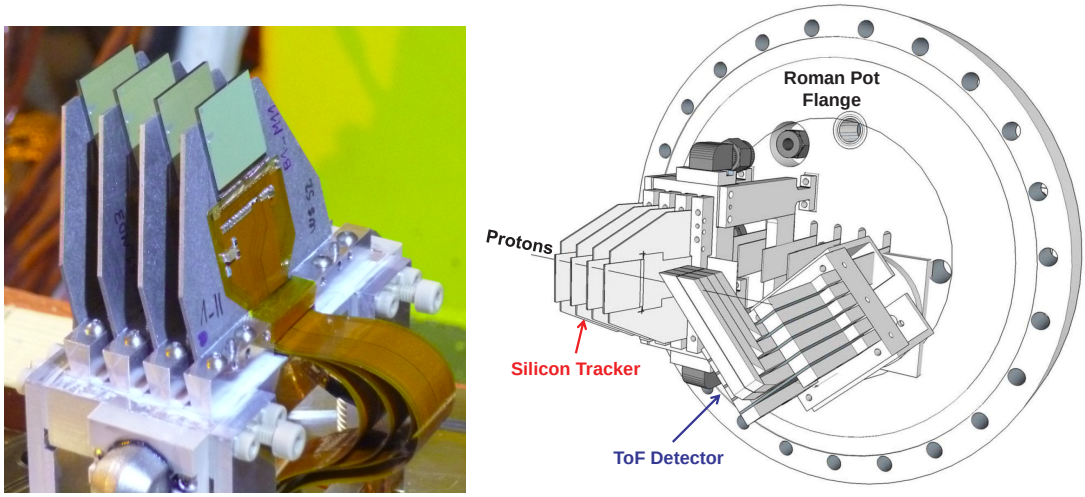

Figure 2.10: **Left**: four AFP Silicon Tracker detectors mounted on the heat exchanger. **Right**: Schematic view of the AFP FAR station, presenting the SiT and ToF modules. The scattered forward proton and the RP flange are also depicted.

mm, with a matrix of 336 × 80 pixels. Each pixel measures 50 μm × 250 μm and is 230 μm thick.

The silicon sensors are read out by FE-I4B front-end chips, originally developed for the ATLAS Insertable B-Layer (IBL). Each FE-I4B chip reads 26,880 independent pixel cells arranged in 80 columns and 336 rows, matching the sensor's pixel matrix. The chip operates at a 40 MHz clock frequency, compatible with the LHC bunch crossing rate. It features a deep buffer architecture, capable of storing up to 5 events simultaneously, which is enough for coping with the hit rates in the AFP.

The four tracking planes in each AFP station are tilted by 14° with respect to the z-axis. This tilting strategy serves two purposes. On one hand, it improves the charge sharing between adjacent pixels, thus improving the position resolution beyond the nominal pixel size, and on the other, it helps to resolve the hit ambiguities in multi-track events. The effective spatial resolution achieved with this configuration is approximately 6 μm in the horizontal direction (x) and 30 μm in the vertical one (y) [55].

To maintain optimal performance in the high-radiation environment near the LHC beams, the SiT modules are cooled to temperatures around −20°C. The cooling system uses a two-phase air circulation system using the so-called vortex tubes, which provides efficient heat removal with minimal material budget. The low-temperature operation mitigates radiation-induced effects in the silicon sensors, such as increased leakage current and charge trapping, ensuring stable performance over extended periods of high-luminosity running.

2.2.5.2 AFP Time-of-Flight Detector

The AFP Time-of-Flight (ToF) detector system is designed to provide precise timing measurements for forward-scattered protons. Installed only in the FAR stations (*cf.* Figs 2.9 and 2.10 right), it helps in background reduction and event selection. The fundamental principle behind background reduction using the ToF system lies in its ability to measure the arrival time of protons with high precision. The ToF system distinguishes between protons originating from the primary interaction of interest and those from pile-up events in the high-luminosity data-taking conditions.

By measuring the time difference between the protons detected in the forward detectors and the collision time at the interaction point, the ToF system effectively determines the z-vertex position of the proton's origin. This timing information, when correlated with the z-vertex position of an event measured by the ATLAS inner tracker, allows for the identification and selection of protons associated with the primary vertex of interest. Protons from the out-of-time pile-up events or beam-induced backgrounds typically have timing signatures inconsistent with that of the primary interaction and can thus be rejected. The measurement concept is shown in Fig. 2.11.

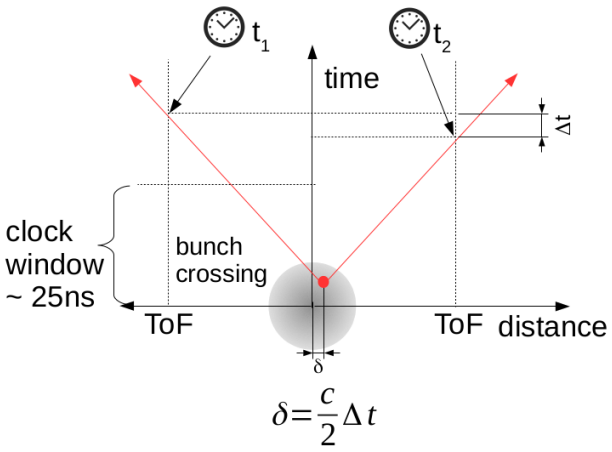

Figure 2.11: Time-of-Flight measurement concept.

The ToF system utilises the Laser-Quartz bar (LQbar) technology. It consists of sixteen L-shaped quartz bars per AFP FAR station. Protons traversing a quartz bar generate Cherenkov radiation, which is guided through the bar via the total internal reflection. The first two layers of bars are 3 mm wide, whereas the last two are larger and have a width of 5 mm. All bars have a total length of 180 mm, with a 90-degree bend. The bars are oriented at a 48-degree angle relative to the beam direction to optimise the Cherenkov light collection.

At the end of each light-guide arm, a micro-channel plate multi-anode photo-

multiplier (MCP-PMT) with 16 channels converts the light signal into an electric pulse. The MCP-PMTs used are radiation-hard and capable of operating in a high-rate environment near the LHC beams.

The system is designed to achieve the timing resolution of O(20 ps), with measurements in 2017 data showing excellent resolutions of 20.2 ± 4.0 ps and 25.7 ± 4.7 ps for the A-FAR and C-FAR stations, respectively [56, 55]. This translates to the expected forward proton z-vertex resolution of 5.5 ± 2.7 mm, which accounts for the smearing due to the unknown y-coordinate of the proton track.

The ToF detector faced efficiency challenges in 2017, with train efficiencies reaching only 6–9% in the A-FAR station and 3–5% in the C-FAR station. These low efficiencies were attributed to insufficient high-voltage and exceeded lifetimes of the PMTs, which were only expected to last 2-4 months under operating conditions.

Despite these challenges, the ToF system's potential for background reduction remains significant. Simulations presented in Fig 2.12 show that the timing measurements can reduce the combinatorial backgrounds by a factor of a few, depending on the pile-up conditions and the timing resolution achieved.

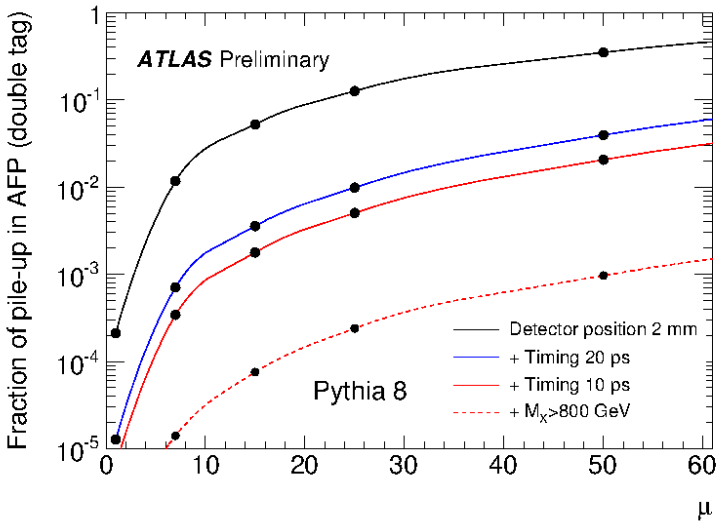

Figure 2.12: The background fraction as a function of pile-up. From [54].

For the LHC Run 3, a new design was implemented to improve the PMT lifetime and prevent electrical failures. This redesign has led to significant improvements in ToF performance. In 2022, during the first high-μ runs (Run 429027, $\mu \approx 33$), the ToF channel efficiencies ranged from 30% to 70% for Side A and 20% to 60% for Side C. In low-μ conditions (Run 428770, $\mu \approx 0.05$), the efficiencies were 45% to 70% for Side A and 20% to 55% for Side C, with some channels showing lower efficiencies compared to high-μ runs.

2.2.6 Trigger and Data Acquisition Systems

As discussed in Section 2.1, the LHC operates with a bunch crossing interval of 25 ns, corresponding to a nominal collision rate of 40 MHz. With each event producing approximately 1.5 MB of raw data, the total data output exceeds current processing and storage capabilities. ATLAS uses a two-level trigger system [57], rapidly identifying and selecting events of particular physics interest. The trigger and data acquisition system underwent significant software and hardware upgrades during LS2 to handle the increased data rates expected in Run 3.
The first stage of the event selection is performed by the Level-1 (L1) trigger. Operating with a latency of 2.5 μs, it reduces the event rate from 40 MHz to around 100 kHz, using the field-programmable gate arrays (FPGAs) to process coarse-granularity data from the calorimeters and muon detectors. The L1 trigger identifies Regions of Interest (RoIs) in the $(\eta - \phi)$ space where significant energy deposits or track segments are detected, corresponding to candidate physics objects. Additionally, the L1 trigger applies the prescale factors (PS_{L1}) to manage the rate, whereby only one in PS_{L1} events meeting the L1 criteria is passed to the next level.
The High-Level Trigger (HLT) constitutes the second and final stage of the ATLAS trigger system. It has access to the full detector granularity within the RoIs identified by L1. Since the HLT runs on a large computing farm, it can perform near-offline-quality reconstruction algorithms. This software-based trigger implements more complex selection algorithms, including tracking information from the Inner Detector, to reduce the event rate to approximately 6 kHz. The HLT decision-making process is steered by the trigger menu, a set of selection criteria configured for the dedicated purpose of data-taking such as various physics analyses, detector performance studies, and calibration needs. Events passing the HLT are fully reconstructed and permanently stored for offline analysis, forming the dataset used in the analyses presented in subsequent chapters of this thesis.

2.2.6.1 AFP Trigger System

The SiT data acquisition is managed by the AFP Trigger and Data Acquisition (TDAQ) system, which is integrated with the central ATLAS TDAQ infrastructure. The system supports both:

- triggered readout, where data is acquired based on ATLAS-wide trigger decisions and
- triggerless operation, where the data are continuously streamed from the detectors.

In the triggerless mode, the SiT can achieve readout rates of up to 40 MHz, limited only by the LHC bunch crossing frequency.

A general scheme of the AFP trigger system is shown in Fig. 2.13. In case a hit is detected in the SiT module, it provides[4] a trigger. These trigger signals are read out by a HitBus chip mounted on the Local Trigger Board (LTB). Due to design properties, for triggering purposes, the LTB[5] can use information from only 3 (out of 4) SiT modules. The choice is made by setting a jumper on LTB. From these 3 signals, the following trigger logic is possible to be used: single plane, AND between all modules, "majority vote" (2 out of 3), OR between all modules. Usually, the "majority vote" option was used since it provides good efficiency together with fair noise (fake signal) suppression.

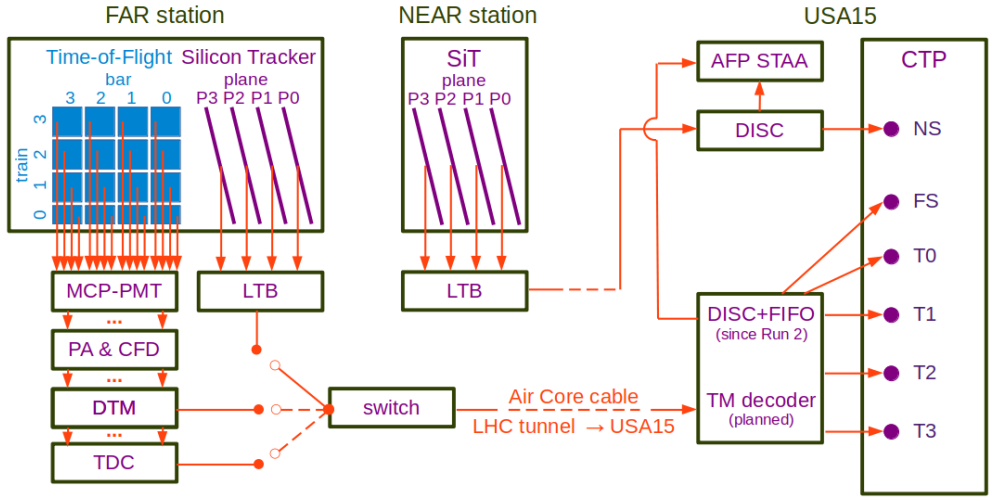

Figure 2.13: Scheme of the AFP trigger system.

In the case of ToF, Cherenkov light produced in each of the 16 quartz bars of the Time-of-Flight system is directed to the Micro-Channel Plate Photo-Multiplier Tube (MCP-PMT). The signal from the MCP-PMT is amplified[6] and processed by the Constant Fraction Discriminator (CFD). In Run 2, such a signal was passed directly to the Time-to-Digital Converter (TDC). In Run 3, it goes first through a Digital Trigger Module (DTM). The trigger logic is built based on information from bars in a train – in the firmware, one can decide how many bars in a train (*e.g.* 1/4 or 4/4) are required for the trigger to fire. The Digital Trigger Module can then encode a signal to send information which the ToF train triggered. The ToF trigger dead time is expected to be below 1 bunch-crossing.

The trigger signal from the AFP NEAR station (LTB) is sent from the LHC tunnel through ultra-fast, low-loss AirCore cable to USA15. This, together with

[4]SiT trigger dead-time is 400 ns – in case of hit no trigger is delivered for the next 16 bunch crossings. Note that SiT readout does not suffer from this dead-time.

[5]Version used during 2016–2023 data-taking.

[6]Since Run 3 amplification is 3-staged: PAa, PAb+PAc.

the shortest possible path, allows the AFP trigger to arrive at the edge but still within the ATLAS latency. In the USA15 cavern, where the majority of the ATLAS electronics is located, the signal goes to the discriminator (DISC), which splits it to the Central Trigger Processor (CTP) and the AFP standalone readout (AFP STAA). The CTP trigger input is named NSA and NSC for the SiT trigger coming from the A and C side, respectively.
The FAR station has 3 sources of trigger: SiT (via LTB), ToF TDC and ToF DTM. Since there is only one Air Core cable available, the decision of which signal is sent to USA15 is made by the remotely controlled switch. The signal arriving to USA15 is sent through the discriminator and Fan-In/Fan-Out (FIFO) through the CTP and AFP STAA. The signal going to CTP is split into 5 inputs: FS (trigger from SiT) and T0–T3 (trigger from ToF). It should be noted that the delay (latency) is different for SiT and ToF – with the switch set to trigger on SiT(ToF) only signals coming to FS(T0–T3) are properly timed-in. Currently, only one trigger bit is sent; thus, the T0–T3 signals are exact copies of each other. The signal encoding done with DTM would allow more detailed information, but before passing it to CTP, decoding would have to be realised using the Trigger Module (TM) decoder. This device, planned to be installed at one point during Run 3, would allow delivering separate signals from each ToF train to different CTP inputs. The naming convention is analogical to the NEAR station: signals from the A/C side are marked by adding the letter A/C in the trigger input name.

2.2.6.2 Data Organization

Up to now, the largest "unit" of the LHC data-taking period – the Run – was mentioned. The LHC Runs have a duration of a few years and, in general, describe LHC colliding protons at certain conditions – after major upgrades of accelerator done during Long Shutdowns and at a given $\sqrt{s}$[7]. A shorter unit is a year when the data are expected to be taken at a given set of magnet settings (optics) and after minor upgrades during the Year End Technical Stops. The smallest unit is a fill – a period between beam dumps. Fill consists of: ramp down, preparation phase (*e.g.* so-called LHC energy cycles), beam injection, energy ramp-up, beam squeeze and adjust, collisions at stable beams and beam dump. Each fill has a unique number.
In the case of ATLAS, the biggest unit is a year[8]. The year is divided into periods (A, B, C, ...), which reflect certain states and configurations of the ATLAS detec-

[7]Except Run 1, when $\sqrt{s} = 7$ and 8 TeV were used.
[8]ATLAS also uses the LHC Run period to describe analysis using the data combined from several years.

tor. Data recording is not continuous – a period between start and stop is called the run. Each run has a unique number. Usually, when LHC starts a new fill, ATLAS records it as a new run. However, an ATLAS run may contain multiple LHC fills, or several ATLAS runs may be recorded during a single LHC fill. The ATLAS run is further divided into the so-called luminosity blocks (LumiBlocks, LB). These usually last 60 seconds but can be shorter (or longer) if a change to the ATLAS configuration happens (*e.g.* change of trigger menu or restart of part of (sub)detector). Each LB has a unique number within a given run. The smallest quanta is an event – data coming from a single bunch crossing. Each event has a unique number within a given run.

An example of the ATLAS run organization, taken from the ATLAS online data browser the so-called *Run Query*, is shown in Fig. 2.14. Run 428770, belonging to period E2, was taken on Wednesday 20/07/2022 and consisted of 2 LHC fills: 8019 (during luminosity blocks 1–27) and 8020 (LB 28–325). There were 590 bunches colliding in ATLAS, organized in 13 trains having 25 ns bunch separation. During the run, a total number of 27,850,350 events was recorded.

						LHC and online luminosity information				
Run	Links	#LB	Start and endtime (local)	#Events	Ready for physics	LHC Fill	Stable beams	Beam energy and intensities	Online del. Luminosity [ATLAS_PREFERRED]	Bunch structure
428770 Period: E2.E AllYear	DS, Rates, BS, AMI, DQ, e-log, DCS:SoR/ EoR, OKS	325 (58 s)	Wed Jul 20 2022 17:40:15 – 22:55:27	27,850,350 (1472.6 Hz)	LB 1 – 3: no LB 4 – 26: yes LB 27 – 197: no LB 198 – 325: yes	LB 1 – 27: 8019 LB 28 – 325: 8020	LB 1 – 27: yes LB 28 – 195: no LB 196 – 326: yes	Maximum intensities: Beam 1: 624 e11 protons Beam 2: 639 e11 protons Maximum beam energy: 6800 GeV [Numbers given for stable beam period (if applies)]	Entire run: 1206 nb^{-1} Stable beams: 701.8 nb^{-1} Peak lumi: 2.8e+03 e30 cm^{-2}s^{-1} Peak <μ>: 33.448	No. of coll. bunches: 590 No. of bunch trains: 13 Bunch dist. in trains: 1 (25 ns) [Mouse over for train configuration. Click for full list of BCIDs]

Figure 2.14: An example of the ATLAS run organization displayed using the ATLAS online data browser – the *Run Query*.

Run 428770 started at 17:40:15 with LB = 1, see Fig. 2.15. The first LumiBlock was 60.12 seconds long. Since the LHC was already colliding at stable beams, 0.241 nb^{-1} of data was delivered to ATLAS. The mean pile-up was about 0.048. It should be noted that luminosity and pile-up are given by the online algorithms, and some, sometimes significant, corrections may be needed in the data analyses.

LB	Start time (CEST)	Duration (sec)	Inst. luminosity (1e30 cm^{-2}s^{-1})	Int. luminosity (nb^{-1})	Cumul. luminosity (nb^{-1})	<μ>	Stable beams
1	17:40:15	60.12	4.008	0.241	0.241	0.0483	T
2	17:41:15	26.04	4.032	0.105	0.346	0.0486	T
3	17:41:41	10.04	4.028	0.04044	0.3865	0.0486	T
4	17:41:51	27.25	4.045	0.1102	0.4967	0.0488	T
5	17:42:18	60.18	4.049	0.2437	0.7404	0.0488	T
6	17:43:18	60.11	4.063	0.2442	0.9846	0.049	T
7	17:44:18	60.13	4.108	0.247	1.232	0.0495	T
8	17:45:18	60.14	3.984	0.2396	1.471	0.048	T
9	17:46:19	60.10	3.992	0.2399	1.711	0.0481	T
10	17:47:19	60.13	3.948	0.2374	1.949	0.0476	T
11	17:48:19	60.14	4.103	0.2467	2.195	0.0495	T

Figure 2.15: Example of basic information about the ATLAS Luminosity Blocks given by the ATLAS online data browser – the *Run Query*.

A typical event recorded by ATLAS is ∼1.5 MB long. In case one would like to

store all events delivered by the LHC, the system should store about 40 TB/second, far beyond current technology. Therefore, ATLAS uses the trigger system mentioned at the beginning of this Section. Another "trick" comes from the observation that certain analyses/performance studies have specific needs – often, only a fragment of ATLAS data needs to be used. Therefore, the recorded ATLAS data are organized into the so-called data streams. In general, one can distinct 3 stream types:

- physics – in which all information needed for "standard" physics analyses are stored, after passing trigger selection,
- express – used for online monitoring and quick offline checks; full information of detector state is available, but events are highly prescaled,
- calibration – information is greatly reduced (often comes from a single subsystem; so-called Partial Event Building, PEB), which greatly reduces event size and allows higher writing rates.

An example of a few ATLAS streams is shown in Fig. 2.16.

Data stream statistics _____ .*										
physics_ Main	physics_ MinBias	physics_ Standby	physics_ ZeroBias	express_ express	calibration_ AFPCalib	calibration_ BeamSpot	calibration_ CostMonitoring	calibration_ IDCalib	calibration_ LArCells	calibration_ LArCellsEmpty	calibration_ LArNoiseBurst
11,528,199 (max: 1571.56 Hz, ave: 1324.10 Hz, 39.4%,, 5.1 TB/ run, 474.2 kB/evt)	16,520,852 (max: 2659.14 Hz, ave: 2023.28 Hz, 56.5%,, 7.0 TB/ run, 453.3 kB/evt)	426,853 (max: 2373.88 Hz, ave: 47.02 Hz, 1.5%,, 429.9 GB/ run, 1.0 MB/evt)	279,789 (max: 2431.58 Hz, ave: 31.96 Hz, 1.0%,, 440.8 GB/ run, 1.6 MB/evt)	8,839 (max: 1.46 Hz, ave: 1.08 Hz, 0.0%,, 4.1 GB/ run, 487.6 kB/evt)	9,914,497 (9.2 GB/run, 994 B/evt)	782,664 (max: 102.06 Hz, ave: 89.88 Hz, , 23.1 GB/run, 30.9 kB/evt)	2,689,754 (26.0 GB/run, 10.1 kB/evt)	12,179 (174.6 MB/run, 14.7 kB/evt)	224,245 (44.8 GB/run, 209.5 kB/evt)	8,759 (184.8 MB/run, 21.6 kB/evt)	228,053 (238.8 GB/run, 1.1 MB/evt)

Figure 2.16: Example of the ATLAS data organization: the data streams (in run 428770).

For the jet-gap-jet analysis, only three of those streams will be directly used:

- calibration_AFPCalib, which contains information about trigger status and full information from AFP; the average event size is smaller than 1 kB, thus about 10M of recorded events takes only 9 GB of space,
- physics_Main to which all jet-based triggers are foreseen to be used in the analysis write data; with 11.5 M events stored during run 428770,
- physics_MinBias with 16.5 M events stored during the above run.

One should note that there is a certain overlap between physics streams – some events are stored in both of them. In the above-mentioned example (*cf.* Fig. 2.16), this fraction is 39.4% and 56.5% in the case of physics_Main and physics_MinBias, respectively. Taking a wrong stream for the analyses would, most probably, result in a reduced number of stored events, making the cross-section measurement incorrect.

Chapter 3

Experimental Data

Studies of jet-gap-jet events have been done in various experiments. The H1 and ZEUS Collaborations conducted the analyses of di-jet photoproduction in electron-proton collisions at HERA (DESY), yielding the gap fractions (f_{CSE}) of about 7–10% [58, 59]. The D0 and CDF Collaborations performed studies in $p\bar{p}$ collisions at the Fermilab Tevatron at $\sqrt{s} = 0.63$ and 1.8 TeV [60]. The D0 experiment defined the rapidity gap between jets and divided the study at $\sqrt{s} = 1.8$ TeV into three sub-samples based on the jet transverse energy (E_T). The CDF experiment results at $\sqrt{s} = 0.63$ TeV and 1.8 TeV can be found in [4, 5]. At the LHC, the CMS Collaboration studied this process at $\sqrt{s} = 7$ TeV in pp collisions [61]. In this study, the pseudorapidity of each of the leading two jets was of $|\eta_{\text{jet1,2}}| > 1.5$ units with $\eta_{\text{jet1}}\eta_{\text{jet2}} < 0$. The second jet's transverse momentum ($p_{T,jet2}$) was divided into three bins and the gap fraction was measured as a function of $\Delta\eta$ in three bins for each bin of $p_{T,jet2}$ which varies between $0.5 - 2\%$. CMS and TOTEM Collaborations jointly performed similar studies using $\sqrt{s} = 13$ TeV data [7] collected during the low luminosity, high β^* LHC run in 2015 with an integrated luminosity of 0.66 pb^{-1}. The gap fraction was measured to be $0.4 - 1.0\%$. Also, results of the measurement of gap fraction in jet-gap-jet events with the intact final state proton detected in the forward region using the TOTEM Roman pot detectors were presented. It was found to be $2.91 \pm 0.70(\text{stat})^{+1.08}_{-1.01}(\text{syst})\%$ for the data of the integrated luminosity of 0.4 pb^{-1}.

ATLAS Collaboration also studies events with a gap between jets. The first approach was to use a veto based on the lack of presence of the reconstructed jet in the gap region [6]. Using 2010 data collected at $\sqrt{s} = 7$ TeV and gap defined as no jets with $p_T > 20$ GeV, the measurement was done for mean di-jet transverse momentum $50 < p_T < 500$ GeV. Notably, such choice of experimental gap definition was argued to be too high, see [62, 63].

Another attempt to measure jet-gap-jet events using 339 nb^{-1} collected by ATLAS during 2010 was done in [64]. The gap was defined as a lack of above-noise activity in the ATLAS tracker and calorimeters. After requiring events to have: one reconstructed vertex, the transverse momentum of the leading jet $p_T > 20$ GeV, two leading jets on the opposite pseudorapidity hemispheres, $|\eta_{jet1}| > 1$ and

$|\eta_{jet2}| > 1$, it was claimed that the distribution of the gap size cannot be properly described without a contribution coming from Jet-Gap-Jet events.

All of these measurements indicate that analysis should be done in relatively "clean" experimental conditions – with pile-up not greater than ∼1. Otherwise, associated minimum-bias events may populate the gap, hence spoiling the measurement.

3.1 Run 2 Low-μ Dataset

During LHC Run 2, ATLAS recorded several runs at low values of the pile-up. Especially interesting was the year 2017, when the full set of AFP detectors was installed, allowing the double-tagged proton measurements. The summary of low-μ runs taken in 2017 is shown in Tab. 3.1.

Table 3.1: An overview of 2017 low-μ runs, including the integrated luminosity for events with protons on the ATLAS A and C sides. From [3].

ATLAS Run Number	**LHC Fill**	**Pile-up μ**	**Int. Luminosity [nb^{-1}] for protons on side A**	**Int. Luminosity [nb^{-1}] for protons on side C**
331020	6019	∼1.0	56.866	510.841
336505	6238	∼0.04	44.751	60.2411
341294	6404	∼2.0	709.542	709.542
341312	6405	∼2.0	18245.492	18234.639
341419	6411	∼2.0	31636.072	31593.050
341534	6413	∼2.0	47663.701	52680.387
341615	6349	∼2.0	31772.631	31772.631
341649	6417	∼2.0	6543.940	6449.680
		∼1.0	3325.167	3325.167

The initial concept was to use these data to search for jet-gap-jet events. Unfortunately, a detailed analysis of single diffractive di-jet production, described in detail in [3], revealed significant difficulties. After the "standard" event selection, the background was still dominating the sample. The data samples were estimated to be only ∼10% pure. In addition, there was no evident correlation between the central system and the forward proton. Such conditions were argued to be due to 1) too high pile-up (∼2) and 2) incorrect settings of ATLAS sub-detectors during the $\mu \approx 0.04$ run.

Considering all the above, and in the light of very promising Run 3 data-taking, the decision was to stop Run 2 analysis and focus on the 2022 data-set.

3.2 Run 3 Low-μ Dataset

Although not finished yet, Run 3, with ATLAS and, especially, AFP refurbished detectors, offers promising low-μ data sets. The list of runs collected by the end of 2024 at $\sqrt{s} = 13.6$ TeV is given in Table 3.2.

Table 3.2: An overview of 2022–2024 low-μ runs.

year	run	# of bunches	pile-up	AT-LAS	AFP SiT	SiT trig.	AFP ToF	recorded data	comments
2022	426140	2	13–20	X	✓	✓	X	330M evt.	BBA
	426201	2	13–20	X	✓	✓	X	250M evt.	BBA
	427929	64	0.005	✓	✓	✓	X	0.6 nb^{-1}	
	428700	590	1	✓	X	?	?	413 nb^{-1}	AFP calibration
	428700	590	0.25	✓	X	?	?	73 nb^{-1}	
	428700	590	1	✓	X	?	?	217 nb^{-1}	
	428700	590	0.05	✓	X	?	?	6 nb^{-1}	
	428747	590	0.05	✓	X	?	?	9 nb^{-1}	
	428759	590	0.05	✓	X	?	?	14 nb^{-1}	
	428770	590	0.05	✓	✓	✓	✓	5.2 nb^{-1}	
	428770	590	0.05	✓	✓	✓	✓	28.4 nb^{-1}	
	STAA	2	2	✓	✓	✓	✓	TBA	“LHCf” BBA
	435229	48	0.02	✓	✓	✓	✓	1 nb^{-1}	“LHCf”
	435229	144	0.02	✓	✓	✓	✓	78.8 nb^{-1}	
	435333	144	0.02	✓	✓	✓	✓	2.9 nb^{-1}	
2023	449548	2	12	X	?	?	X	91M evt.	BBA, calibration
	449553	2	12	X	✓	✓	X	12M evt.	BBA
	455818	386	1	✓	✓	✓	X	223 nb^{-1}	
			0.2					35.7 nb^{-1}	
			0.05					20 nb^{-1}	
	455838	898	0.05	✓	✓	✓	X	39.8 nb^{-1}	
	460096	2	1.2–1.4	✓	?	?	X	18M evt.	“low-B” BBA
	460348	60	0.005	✓	✓	✓	X	1.7 nb^{-1}	“low-B”
2024	478763	2340	1	✓	✓	✓	X	17.9 pb^{-1}	“no magnets”

As one can see, several interesting pp, $\sqrt{s} = 13.6$ TeV data-taking campaigns happened already during Run 3. In addition, in 2024, several runs were taken at $\sqrt{s} = 5.36$ TeV and $2 < \mu < 4.5$. In 2025, proton-oxygen and oxygen campaigns are planned, and in 2026, a week-long $\mu \sim 1$ campaign may take place. All of the above are “inside” the high-μ pp data-taking and $PbPb$ campaign.

Before taking data at given LHC optics, the AFP detectors must be aligned w.r.t. the LHC beam. This procedure, called the Beam Based Alignment, is described in detail later in this Chapter. As one can see, there were several BBA campaigns in the years 2022–2024.

The first special run in 2022 was set to have a pile-up of 0.005. The goal of this run was to collect data for the min-bias analyses, thus, the fill had a low amount of (well separated) bunches and very low-μ, resulting in around 0.6 nb^{-1}

of recorded data. A week later, a set of runs with μ of 1, 0.25 and 0.05 happened. Unfortunately, due to the need for the dedicated AFP calibration, only run taken at $\mu = 0.05$ can be used for proton-tagged analyses. Still, 33.5 nb^{-1} of recorded data looks promising for the jet analyses. All of these runs were taken at low-β^* (1.2–0.6m) "collision" optics. At the end of 2022, a special, $\mu = 0.02$ run was taken with $\beta^* = 19.2$ m optics. This run was requested by the LHCf Collaboration, which took data together with the ATLAS detector, including (part of) the Zero Degree Calorimeter and AFP.
In 2023, μ of 1, 0.2 and 0.05 campaigns were repeated. LHC optics slightly changed w.r.t. 2022, while the ATLAS and AFP detector configurations stayed roughly the same. However, in the case of the AFP SiT detectors, they suffered from slight inefficiency due to radiation damage taken in the high-μ runs. At the end of the 2023 data-taking, another special run took place. This time, the solenoid field was lowered to 40% of its nominal value.
In 2024, only a low-μ run was recorded. It happened "opportunistically" due to problems with ATLAS magnets: both solenoid and toroid were switched off. Similarly, as in the case of the "low-B" run, a dedicated ATLAS track reconstruction should be applied.

3.3 Run 428770

The combined analysis of all of these data-sets is very appealing. Unfortunately, it is far beyond the time scale of my PhD project. Instead, the plan is to focus on a single run, to understand the detector performance well and make the (diffractive) jet-gap-jet measurement. ATLAS run 428770 was chosen for a few reasons:

- it was recorded at the beginning of Run 3 data taking, with AFP detector fully refurbished during LS2, especially SiT system, which had 16 brand new modules,
- pile-up of 0.05 and recorded luminosity of 33.5 nb^{-1} were promising good, low-background data-taking conditions and significant amount of data,
- "regular" settings of LHC optics and ATLAS magnetic field allow to use standard reconstruction algorithms and take advantage from some of "high-μ" performance studies.

3.3.1 Detector Configuration

To not repeat the mistake done during run 336505 (*cf.* [3]), special attention was paid to apply correct "low-μ" settings of the ATLAS detector. The exact changes

are too detailed to be described here. To mention that they include changes in the L1Calo (Digitized Samples Per cell (DSP) and noise thresholds for clustering as well as High Gain in FCal and EMEC Inner Wheel), HLT (Super Master Key (SMK) and correct prescales (PSK)) and tile calorimeter (integrator gains).
As mentioned, AFP had a set of 16 new, non-irradiated SiT modules installed during LS2. The modules and their order were carefully chosen to maximize reconstruction efficiency. The detailed list is given in Table 3.3.

Table 3.3: List of AFP SiT modules installed in a given station in years 2022 – 2023. B3 stands for "batch 3" – a production done during LS2.

Station	Plane	Module
A FAR	0	AFP-B3-M15
	1	AFP-B3-M14
	2	AFP-B3-M13
	3	AFP-B3-M09
A NEAR	0	AFP-B3-M12
	1	AFP-B3-M11
	2	AFP-B3-M10
	3	AFP-B3-M04
C NEAR	0	AFP-B3-M08
	1	AFP-B3-M07
	2	AFP-B3-M05
	3	AFP-B3-M03
C FAR	0	AFP-B3-M19
	1	AFP-B3-M18
	2	AFP-B3-M17
	3	AFP-B3-M06

For efficient data-taking, each of the AFP SiT modules was calibrated. Such an adjustment procedure, called tuning, was done a few times during the Run 3 data-taking campaign. For run 428770, the tune done on 9 July 2022 was used. Global configuration settings were stored in the so-called *top file* from 20 July 2022 15:20:20 [65]. SiT modules were tuned accordingly to settings listed in ASide_AFP_2021___2124.cfg and CSide_AFP_2021___2110.cfg for A and C side, correspondingly. All modules[1] on A side were tuned accordingly to configuration 2124[2]. All modules on side C were tuned accordingly to configuration 2110.
There is a separate mask for readout and a trigger for each SiT plane. In principle,

[1]In the case of this particular run, all module configurations have numbers exactly as in the top file. This is, however, not the rule. In cases of problems with tuning of a given module, one of the older configurations may be used, which will be reflected in the path given in moduleconfig file.

[2]On a computer connected to ATLAS detector internal network the path structure is /det/afp/configs/moduleconfigs/A-SIDE/FAR/AFP-B3-M15/configs/AFP-B3-M15___2124.cfg (example for the A FAR plane 0).

they should be the same. While having the list of masked pixels is important for the performance studies, the details may be too technical for the reader, they are kept in the internal analysis documentation.
The other AFP-related data-taking parameters were as expected:

- SiT LV voltage: stable and between 2.12 and 2.28 V,
- SiT LV current: stable and between 0.4 and 0.48 A depending on plane; within a given plane, the stability was of about 2 mA,
- SiT HV voltage: stable and between -20.06 and -20.11 V; within a given plane, the readout deviations were of about 1 mV,
- SiT HV current: stable and between -0.2 and -0.8 μA depending on plane; within a given plane stability of 0.02 μA,
- heat exchanger (HEX) temperature: stable and between -19.5 and -21 ^{0}C.

One issue that may have an impact on data-taking was the constant recovery (in the readout) of A NEAR plane 0.

3.3.2 Beam Based Alignment

There are several procedures that must be successfully passed in order to have Roman Pots (RP) inserted during the standard LHC operation. The majority of them, like validation of the Beam Interlock System [66], are technical. Since they are not relevant for the data-taking, they will not be described here. Obviously, all of them were successfully done before the 2022 data-taking. The last procedure, called the Beam Based Alignment (BBA), has an impact on data as it defines the actual pot insertion depth. The details of the 2022 BBA are described below.
Before the operation, all Roman Pots at the LHC are positioned w.r.t. the beam. Such procedure must be done for each condition (optics) in which pots are planned to move from the garage position. The procedure, pictured in Fig. 3.1, is as follows:

- low intensity beam (few bunches) is injected and trimmed by the horizontal and vertical primary collimators (TCPs)[3],
- TCPs scrape the beam halo at an aperture $n_1^{TCP} \cdot \sigma^{TCP}$ where:
  - σ^{TCP} is the beam size at collimator calculated for nominal normalized emittance ($\varepsilon = 3.5$ μm·rad) and "design" beam optics,

[3]In case of the AFP BBA the trimming was done always with TCP.C6L7.B1 for beam 1 and TCP.C6R7.B2 for beam 2.

  - n_1^{TCP} is calculated from position of the collimator jaws: $n_1^{TCP} = \left|TCP_1^L - TCP_1^R\right| / \left(2 \cdot \sigma^{TCP}\right)$,

- the scraping by collimator creates a well-defined beam edge,
- Roman pots are slowly (in steps of about 10 μm), one by one, moved towards the beam; the movement stops when signal in the closest Beam Loss Monitor installed after the pot peaks – an indication that beam was touched by pot at distance RP^L,
- afterward the collimator again trims the beam delivering n_2^{TCP}.
- expected beam size at the Roman pot is computed as $n^{RP} \cdot \sigma^{RP}$, where $n^{RP} = \left(n_1^{TCP} - n_2^{TCP}\right)/2$ and σ^{RP} is the nominal beam size at the RP location,
- centre of the beam at the Roman pot position is calculated as $x_{RP}^{beam} = RP^{left} - n^{RP} \cdot \sigma^{RP}$.

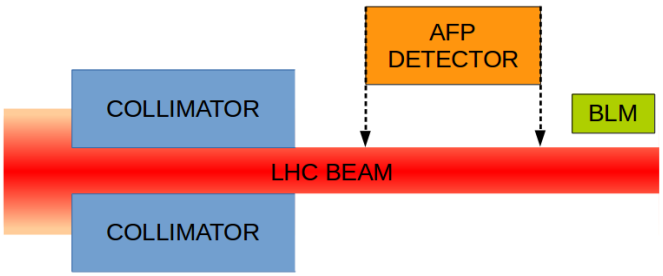

Figure 3.1: Idea of Roman pots alignment: beam is scraped by collimator to a certain width (the assumption is that the position collimator jaws is precisely known), detector approach the beam until they touch it, the beam width is known from simulations, so the position w.r.t. beam centre can be calculated.

The Beam Based Alignment was done each time the Roman pots were significantly touched[4] or when optics was changed. The results for 2022 [67] campaign are summarized in Tab. 3.4.

3.3.3 AFP Data-taking Position

By construction, the Roman pots can be inserted to any position in the range ~2 to about -40 mm, where 0 is the beam-pipe centre. However, positioning the pots very close to the beam (or to the beam itself) may cause them to break physically, stopping the LHC operation (vacuum loss). Therefore, there is a certain minimal beam-detector distance, d_{AFP}, which is considered safe for data taking.

[4]Meaning any intervention more severe than connecting/disconnecting the cables.

Table 3.4: Measured positions of primary collimators (TCP) and Roman pots during the 2022, collision optics, Beam Based Alignment campaigns. Beam sizes were taken from the relevant optics files. See the text for details.

Optics	Station	σ_{TCP}	TCP_1^L	TCP_1^R	n_1^{TCP}	TCP_2^L	TCP_2^R	n_2^{TCP}	σ^{RP}	n^{RP}	RP^L	x_{beam}^{RP}
$\beta^* = 0.6$ m	C FAR	0.263	1.290	-0.785	3.95	1.125	-0.745	3.75	0.081	3.85	0.879	0.568
	C NEAR		1.225	-0.745	3.75	1.200	-0.710	3.64	0.136	3.69	1.492	0.991
$\theta_C = -170$ μrad	A NEAR	0.261	0.955	-1.295	4.31	0.935	-1.145	3.99	0.131	4.15	1.298	0.756
	A FAR		1.165	-1.390	4.90	0.955	-1.295	4.31	0.079	4.60	1.337	0.971

In the language of LHC elements, the Roman pots are treated as collimators. This means that they must follow the collimation hierarchy [68]. Usually, for the low-β^* optics, d_{AFP} is determined w.r.t. opening of the tertiary collimator (TCT).

There was a significant effort from the LHC teams to optimize conditions for Roman pots for Run 3. Besides the optics optimization, a beam-pot distance[5] was minimized. In addition, for the simplicity of the data analyses the pots were decided to be kept in constant positions during the luminosity levelling. In 2022, the collimation hierarchy was preserved by "constant TCT jaw" [69]. This scenario assumes that the TCT collimator jaws openings are kept constant in millimetres. The minimal beam-pot distance is defined by:

$$d_{AFP}(\beta^*) = MAX[(8.5\frac{\sigma_{TCT}(\beta_0^*)}{\sigma_{TCT}(\beta^*)} + 3)\sigma^{RP} + 0.3\ mm, 1.5\ mm], \tag{3.1}$$

where the jaw settings are defined at $\beta_0^* = 30$ cm and σ is the beam size at a given element. One can immediately see two safety margins: one related to the beam size ($3\sigma^{RP}$) and one constant (0.3 mm). In addition, the pot cannot be closer than 1.5 mm from the beam (hard limit).

Taking into account the results of the Beam Based Alignment, the insertion distances were computed. Note that such distance is measured w.r.t. geometrical centre of the beam. To calculate the "true" beam-detector distance, one has to consider the effects like: "true optics" (see Appendix A), pot rotation (Appendix B), *etc.*

The insertion distances for 2022 and 2023 low-β^* data-taking are listed in Table 3.5. For completeness, it should be added that TCL4 and TCL5 were kept open to 15 and 40 σ, respectively.

Table 3.5: AFP data-taking positions (in mm, w.r.t. beam-pipe centre) in 2022.

station	**data-taking distance [mm]**
C FAR	2.079
C NEAR	3.326
A NEAR	3.015
A FAR	2.471

[5]Which impacts the lower limit of AFP acceptance in ξ.

3.3.4 LHC Beam Configuration

Run 428770 was taken with the following settings of the LHC machine:

- centre-of-mass energy: $\sqrt{s} = 13.6$ TeV,
- betatron function at the IP1 (defining optics): $\beta^* = 0.6$ m,
- (vertical) crossing angle: $\theta_C = 170$ μrad,
- horizontal beam separation (to achieve $\mu = 0.05$): ≈ 90 μm.

The filling scheme used by the LHC machine during the run 428770 (LHC fills 8019 and 8020) was 25ns_603b_590_524_542_48bpi_17inj. This means 603 bunches circulating in the LHC and 590 colliding in the ATLAS (and CMS) IP. Trains of 12 and 48 bunch lengths are visible in Tab. 3.6. As well as 2 colliding, isolated bunches: 811 and 2596.

Table 3.6: List of Bunch Crossing IDs (BCIDs) assigned to a given Bunch Group (BGRP) in the run 428770. Only bunch groups relevant to the presented analysis are listed. BCIDs of paired, isolated bunches are in bold.

BGRP	**Name**	**BCID**
1	paired	4–15, 257–304, 336–383, 415–462, **811**, 1151–1198, 1230–1277, 1309–1356, 2045–2092, 2124–2171, 2203–2250, **2596**, 2939–2986, 3018–3065, 3097–3144
3	empty	21–88, 111–116, 139–251, 310–330, 389–409, 468–805, 817–1145, 1204–1224, 1283–1303, 1362–1696, 1711–2039, 2098–2118, 2177–2197, 2256–2590, 2602–2933, 2992–3012, 3071–3091, 3150–3444, 3515–3539, 3561–3562
4	isolated unpaired	94–105 (beam 1), 122–133 (beam 2)
5	non-isolated unpaired	1702 (beam 2), 1705 (beam 1)
6	empty before and after paired	0–3, 16–20, 252–256, 305–309, 331–335, 384–388, 410–414, 463–467, 806–810, 812–816, 1146–1150, 1199–1203, 1225–1229, 1278–1282, 1304–1308, 1357–1361, 2040–2044, 2093–2097, 2119–2123, 2172–2176, 2198–2202, 2251–2255, 2591–2595, 2597–2601, 2934–2938, 2987–2991, 3013–3017, 3066–3070, 3092–3096, 3145–3149, 3563
12	all without Calreq	0–3444, 3515–3539, 3561–3563

3.3.5 Good Run List

During the data-taking, it may happen that a part of the ATLAS detector is malfunctioning. The faults can have a severe impact on the data analysis and thus are intolerable, and such events should be discarded. Or they may only

have an impact on some specific calibrations/performance studies, causing the recorded events to be tolerable for the general studies. All ATLAS subsystems define which types of malfunctions are tolerable and intolerable. The same was done for AFP – the list of defects is shown in Fig. 3.2.
The list of defects is prepared for each run and is used to prepare the Good Run Lists (GRL) – a tool for identifying datasets suitable for physics analysis. A GRL is a compilation of "good runs", referring to luminosity blocks without defects. GRLs in the ATLAS experiment are key to identifying top-quality data samples for physics research, and they play a critical role in ensuring the integrity and precision of scientific outcomes.
For run 428770, the following luminosity blocks passed the quality criteria: 4–26 and 207–325. On top of the standard GRL, additional restrictions may be applied due to the specific needs of a given analysis. In the case of diffractive jet-gap-jet studies, two such requirements were added: the mean pile-up value should be around 0.05, and a proper trigger menu should be used. This restricted the LB range to 4–25 and 210–323.

3.3.6 Luminosity

Online luminosity provided by the ATLAS detector is very useful but has some uncertainties. This may be especially true during the runs taken in non-standard conditions, like low-μ, when "standard" calibrations may not hold. Therefore, a dedicated luminosity analysis was requested for run 428770.
The main ATLAS lumimeter is LUCID-2 [70]. It surrounds the beam pipe on both sides of the interaction point at a distance of 17 m. The detectors consist of 16 + 15 Hamamatsu R760 photomultipliers located in four groups around the beam pipe and one R1635 Hamamatsu photomultiplier positioned on side C. The centre of the photomultipliers is at a distance of 125 mm from the beam line. Charged particles going through the radiation-hard quartz window of the photomultipliers can produce Cherenkov light detected by the photomultipliers. The detector stability response is monitored by Cherenkov light produced by weak ^{207}Bi sources placed on the windows of the photomultipliers. The ^{207}Bi sources give out mono-energetic electrons from internal conversion that have an energy above the Cherenkov threshold in quartz. Single LUCID PMTs act as independent detectors or are combined in global algorithms:

- EventOR – bunch crossing counted if there is at least one hit on either side,
- EventAND – as above, but requires at least one hit on both sides,
- HitOR – number of hits in a given detector is counted.

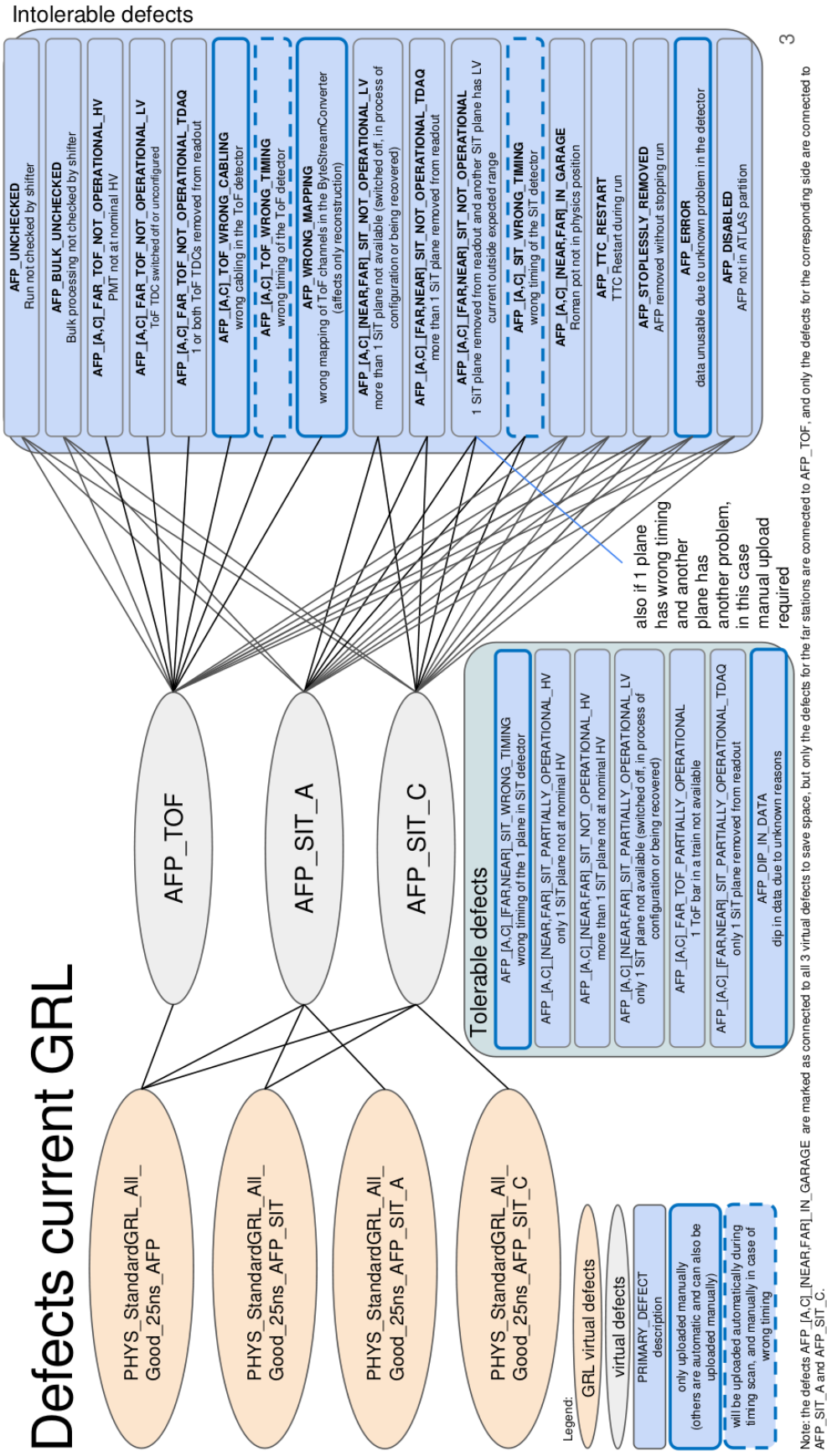

Figure 3.2: AFP Good Run List (GRL) based on the intolerable defects. Tolerable defects are listed as well but do not contribute to GRL.

After the so-called Van der Meer calibration [71], LUCID-2 provides the absolute luminosity measurement. The measurements are cross-checked by other ATLAS lumimeters, for example, the Tile calorimeter. Specialized algorithms, as track counting, can further improve the precision.
Careful, dedicated luminosity calibration of run 428770 included:

- subtraction of ^{207}Bi and beam backgrounds,
- effects due to single-beam background,
- evaluation of crossing-angle effect,
- corrections w.r.t. track counting,
- global uncertainty of VdM calibration (biggest contribution, of 1.45%),
- long-term stability.

The final luminosity estimate for LumiBlock ranges $[4, 25]$ and $[210, 323]$, based on the LUCID HITOR BI2 algorithm, is:

$$L_{428770} = 29647.4 \pm 0.8_{stat} \pm 436.2_{sys}\ \mu b^{-1}. \tag{3.2}$$

Chapter 4

Monte Carlo

High-energy physics experiments provide more and more details on the nature of hadrons and their interactions. This is also reflected in models implemented in the Monte Carlo generators. Phenomena such as the Initial and Final State Radiation (ISR and FSR) or Multi-Parton Interactions (MPI) are widely used (see Ref. [72]) in the modern HEP MC generators, like Pythia 8 [73].
In this thesis, Pythia 8 MC will be used. The choice was based on the fact that the settings of this MC were already well defined for earlier diffractive studies. In addition, the used version of Pythia 8 was tuned to the ATLAS min-bias data, which should provide a more accurate – data-based – description of the diffractive events. In the future, other MC generators, like Herwig [74] and FPMC [75], should be considered.

4.1 Pythia 8 Samples

While depicting diffractive production as shown in Figs. 1.4 – 1.9 is very educational, the models used in the MC generators are much more complicated. An example of a single diffractive di-jet event, where exactly two jets are present in the final state, is shown in Figs. 4.1 and 4.2.
Figure 4.1 shows how particles are produced in the pseudorapidity–azimuthal angle (η, ϕ) plane, *i.e.* as expected to be observed in the detector. Stable particles are shown as green dots of the size proportional to their transverse momentum. Blue points indicate which particles were used to construct a jet (anti-kT algorithm [76] with R=0.4 implemented in the FastJet tool [77]). The jets are marked by the hollow orange circles.
The same event is shown in Fig. 4.2. Here, all particles generated by Pythia 8 MC are shown. This drawing was obtained using the McViz package [78]. The lines represent the "mother-daughter" connections. Colliding protons are shown in light blue. The Pomeron produced from the excited proton state (p^{+}_{diffr}) is visible. The reconstructed jets were added to the picture and are represented as bulbs named "system". The lines connected to jets indicate which final state particles were used for their reconstruction. The spatial placement of particles is "random", *i.e.* it does not reflect their position in the (η, ϕ) plane. A case of SD

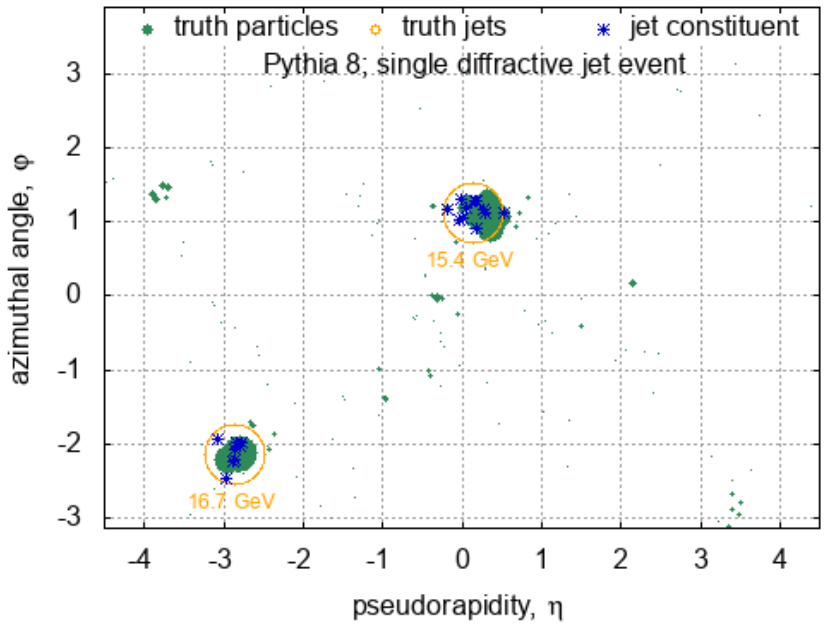

Figure 4.1: Single diffractive di-jet event generated by Pythia 8. Stable particles are shown as green dots with size proportional to their transverse momentum. Blue points indicate which particles were used to construct the jet (anti-kT algorithm with R=0.4). The jets are depicted as hollow orange circles (of arbitrary size) with their transverse momentum printed.

JJ is shown, but the structure of other generated processes has at least the same level of complexity.

4.1.1 Pythia 8 Configuration

For this analysis, two types of Monte Carlo samples were produced:

Single Diffractive Jets the sample was generated using Pythia 8.307 with the A3 tune and NNPDF23_lo_as_0130_qed PDF set. The following key settings were applied:

- `SoftQCD:singleDiffractive = on` – enables single diffractive processes,
- `Diffraction:doHard = on` – enables hard scattering within diffractive events,
- `SigmaDiffractive:PomFlux = 5` – selects the Minimum Bias Rockefeller model for the Pomeron flux,
- `SigmaDiffractive:PomFluxEpsilon = 0.07` – sets the Pomeron trajectory parameter.

Diffractive processes in Pythia 8 are modelled using the Ingelman-Schlein approach, where the Pomeron is treated as having a partonic structure. The hard

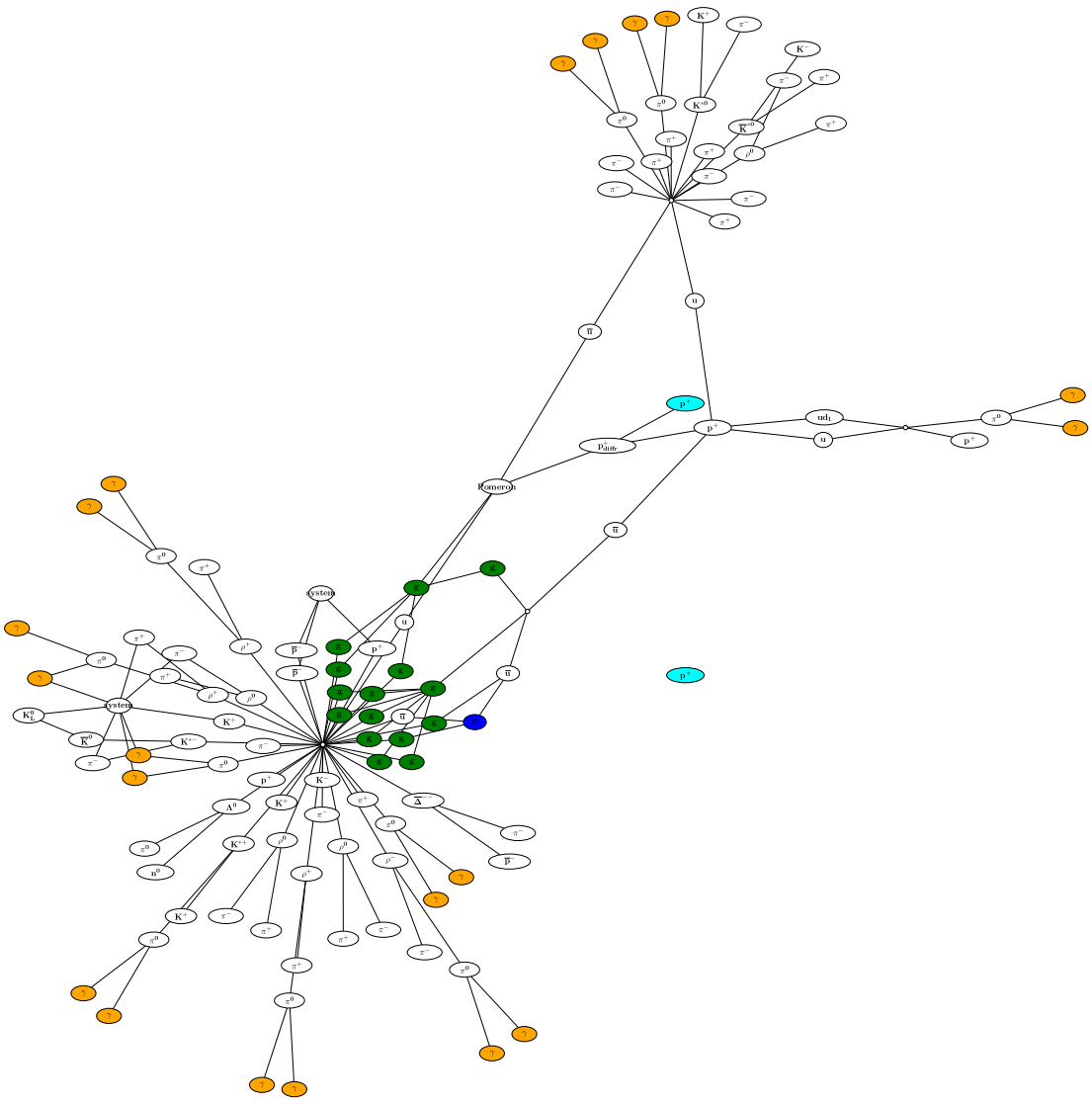

Figure 4.2: Single diffractive di-jet event generated by Pythia 8. All generated particles are shown, with lines indicating the mother-daughter relation. The reconstructed jets are represented as bulbs named “system”; lines directly connected to these bulbs indicate which final state particles were used for their reconstruction.

process occurs between a parton from the Pomeron and a parton from the other proton. For jet production, 2→2 QCD processes are generated according to their respective cross-sections. Multiple parton interactions within the diffractive system are included but are suppressed relative to non-diffractive events. The estimated cross-section for the single diffractive process was 16 mb, divided equally between the two single diffractive modes (8 mb each).

Non-Diffractive Jets the sample was generated using Pythia 8.308 with the A3 tune and NNPDF23_lo_as_0130_qed PDF set. The main setting was:

- `SoftQCD:nonDiffractive = on` – enables non-diffractive processes.

For the non-diffractive processes, Pythia 8 implements a comprehensive model of the underlying event through the multiple parton interactions, which is important for correctly modelling the particle activity in the rapidity gap region. The estimated cross-section for the non-diffractive process was 59 mb.

4.1.2 Event Filtering and Production Statistics

To efficiently produce samples with the desired topologies, filtering was applied during generation:

SD jet sample:

- forward proton filter (`xAODForwardProtonFilter`) selected events with protons within the AFP acceptance,
- Jet filter (`QCDTruthJetFilter`) applied basic quality criteria,
- Multi-jet filter (`QCDTruthMultiJetFilter`) required at least 2 jets with $p_T > 12$ GeV and $|\eta| < 4$.

The application of these criteria resulted in the filter efficiency of $\varepsilon^{SD}_{filter} = 0.024\%$. The low filter efficiency for diffractive jet events underscores their rarity and highlights the importance of dedicated triggers and special running conditions for their experimental study, as described in Chapter 3.

ND jet sample:

- at least 2 jets with $p_T > 12$ GeV and $|\eta| < 4$ (`QCDTruthMultiJetFilter`).

This resulted in a filter efficiency of about $\varepsilon^{ND}_{filter} = 2.4\%$.

4.1.3 Hadronization and Gap Formation

Pythia 8 implements the Lund string fragmentation model for hadronization. In this model, as partons move apart, colour flux tubes (strings) are stretched between them. When the potential energy becomes sufficient, new quark-antiquark pairs are created, breaking the string. This process continues until only on-mass-shell hadrons remain.
For the diffractive events, the colour connection occurs via colour-singlet exchange, leading to regions with suppressed particle production – the rapidity gaps. In the non-diffractive events, gaps can still form due to fluctuations in the hadronization process, but they are exponentially suppressed with increasing gap size.

4.2 ATLAS Reconstruction

The Monte Carlo production in ATLAS is done in 6 steps:

1. **Matrix element calculation.** Some generators, like Pythia 8, are directly embedded in the software, but input from practically any generator can be used as events are accepted in the so-called Les Houches Event format [79].

2. **Parton shower/hadronization.** After this step a list of the "truth" particles generated in the event is stored.

3. **Detector simulation.** The path of "stable" particles through the detector is modelled including their interaction with the detector material and magnetic fields, production of new particles in those interactions and potential decays. The outcome of this step is a list of the energy deposits in various subdetectors of ATLAS.

4. **Digitization.** In this step, the simulated energy deposits are converted into digitized signals. The outcome is equivalent to the raw data that are read from the ATLAS detector, though with additional "truth" information about what happened in the event.

5. **Trigger Simulation.** Provides the trigger decisions corresponding to the ones in the experimental data.

6. **Reconstruction.** The digital signals are reconstructed into physics objects. At this step, the same kind of files as for the actual data, the Analysis Object Data (AOD), are produced. AOD MC files typically store the "truth" record.

To save disk space, not all objects are stored in the AODs. For example, since Run 3, information about the reconstructed jets has not been available. To retain such objects, a dedicated production, called "derivation", has to be made. For diffractive analysis using low-μ data, a derivation called STDM6 was developed. The Run 3 structure of STDM6 is shown in Fig. 4.3.

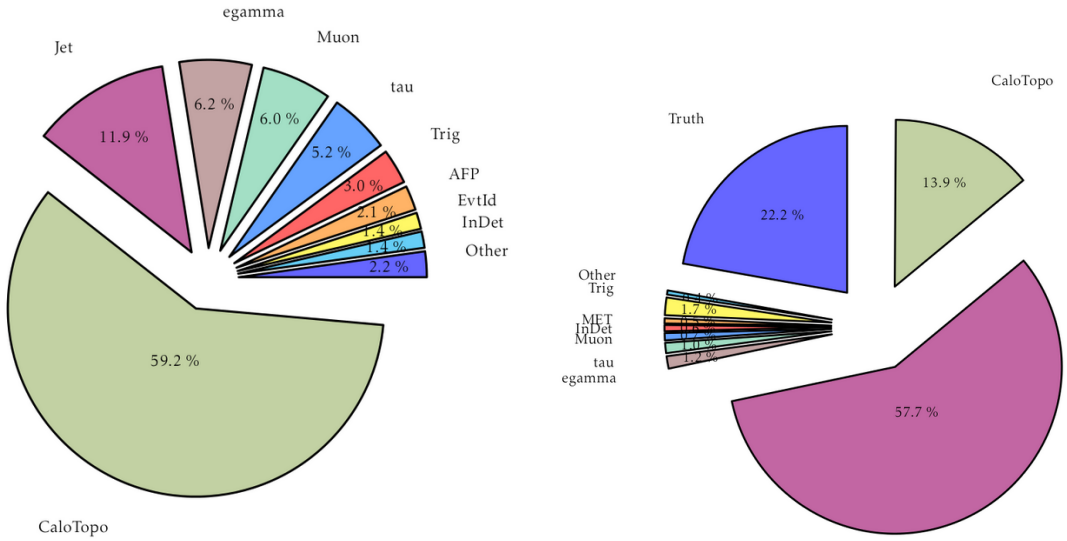

Figure 4.3: Structure of ATLAS STDM6 derivation designed to be used in the low-μ diffractive analyses: the data are on **left** and Monte Carlo on **right**.

4.3 Basic Properties of Generated Jet Events

The transverse momentum of the leading jet is plotted in Fig. 4.4. This sample contains soft single diffractive events that passed the filter requiring the presence of at least 1 jet with transverse momentum greater than 12 GeV. Reconstruction of the truth jets (*i.e.* algorithm running on truth particles) starts from 7 GeV. The ATLAS reconstruction starts from 10 GeV. Both these features are visible in the spectrum. Interestingly, the reconstructed jets tend to have higher p_T than the truth ones (the spectrum is shifted). This indicates a need for the jet calibration, which will be discussed in detail in the next Chapter.

An interesting feature of the ATLAS reconstruction is visible in the pseudorapidity spectrum. The generated jets have smooth distribution falling with pseudorapidity. The reconstructed jets relatively less populate the central region, with pronounced peaks at certain pseudorapidities. These peaks correspond to the sub-detector transition regions, see Section 2.2.3.

The presence of these peaks in the case of the reconstructed jets suggests that p_T order may change, *i.e.* the generated leading jet may become a sub-leading (or third, fourth, ...) one after the reconstruction. This migration is presented

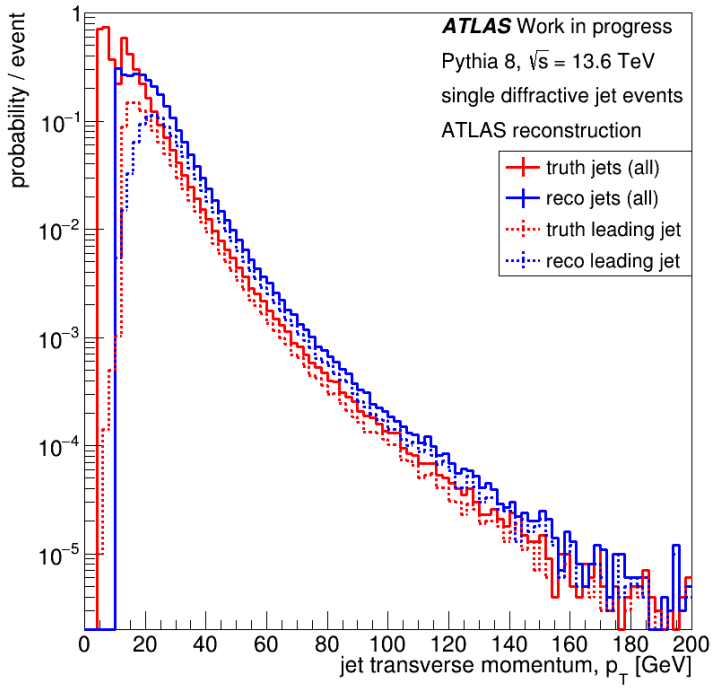

Figure 4.4: Transverse momentum of the truth (red) and reconstructed (blue) jets in Pythia 8 SD JJ MC sample. The solid lines represent all jets generated in the event, whereas dotted lines are for the leading jet only.

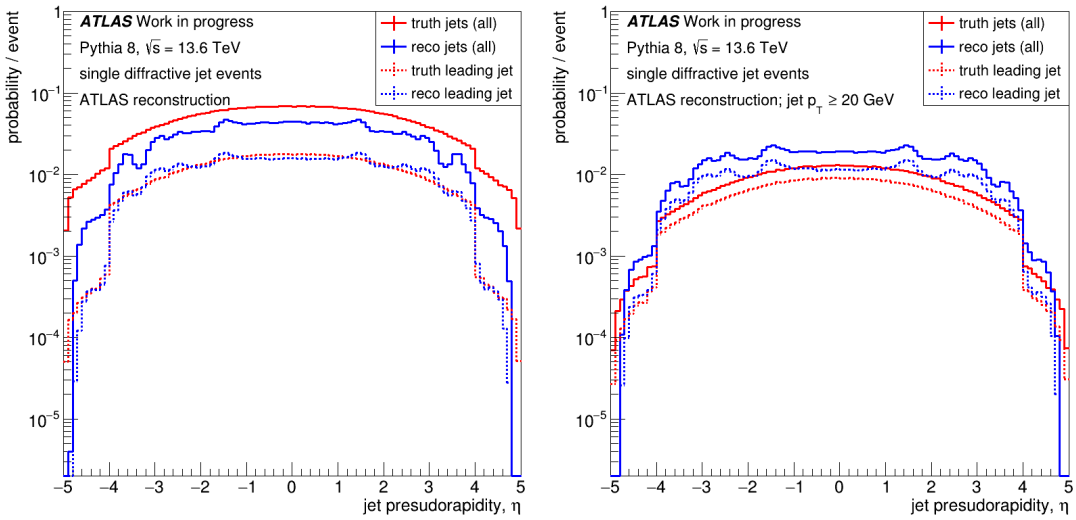

Figure 4.5: Pseudorapidity of the truth (red) and reconstructed (blue) jets in Pythia 8 SD JJ MC sample. The solid lines represent all jets generated in the event, whereas dotted lines are for the leading jet only. **Left** plot shows all generated events while on the **right** only events with truth/reco. jet $p_T \geq 20$ GeV are shown.

in Fig. 4.6. The leading jet has index 0, the sub-leading 1 *etc.* Cases when the reconstructed jets have the negative index (-1) are when the truth jet was not matched to the reconstructed one. The matching criteria required that the "truth" and reconstructed jets are not further than 0.2 units in pseudorapidity and azimuthal angle.

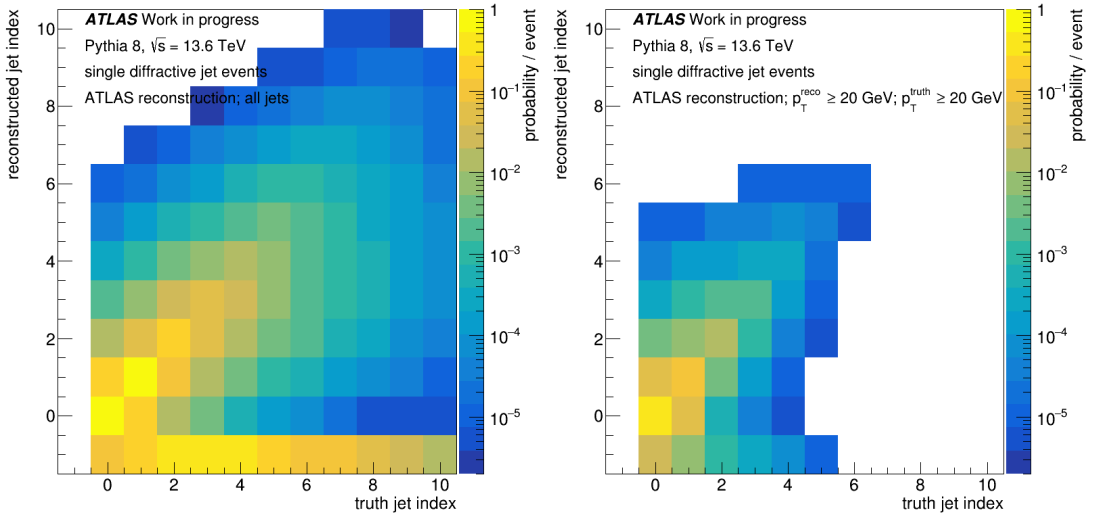

Figure 4.6: Effect of the jet migration for all generated events (**left**) and the ones with leading jet p_T of at least 20 GeV (**right**). Index 0 is for the leading jet, 1 for the sub-leading one *etc.* Cases with negative index are for the truth jet was not matched to any reconstructed one. Matching means that both jets are not further than 0.2 units in pseudorapidity and azimuthal angle.

Since a lot of generated events had $p_T < 20$ GeV (see Fig. 4.4), it is interesting to see the migration when jets with p_T of at least 20 GeV (at the truth and reco level) are compared. This is plotted in Fig. 4.6 (right). Clearly, in the majority of cases, the truth leading/sub-leading/third... jet remains the leading/sub-leading/third jet after the reconstruction. Sometimes there are cases of "swap" between leading and sub-leading jets. All of these should have a minor impact on the analysis. Fortunately, the cases when the leading or sub-leading jet becomes third or higher are relatively rare – they happen for few ‰ of events.
Finally, it is interesting to see the effect of the jet migration. The effect is shown in Fig. 4.7 for events where the jets have $p_T > 20$ GeV. Only the leading jets were considered. While most of the events appear on the diagonal, the migration is clearly visible. As already discussed, it happens a bit more often in the case of calorimeter "transition" regions (*cf.* green horizontal bands).

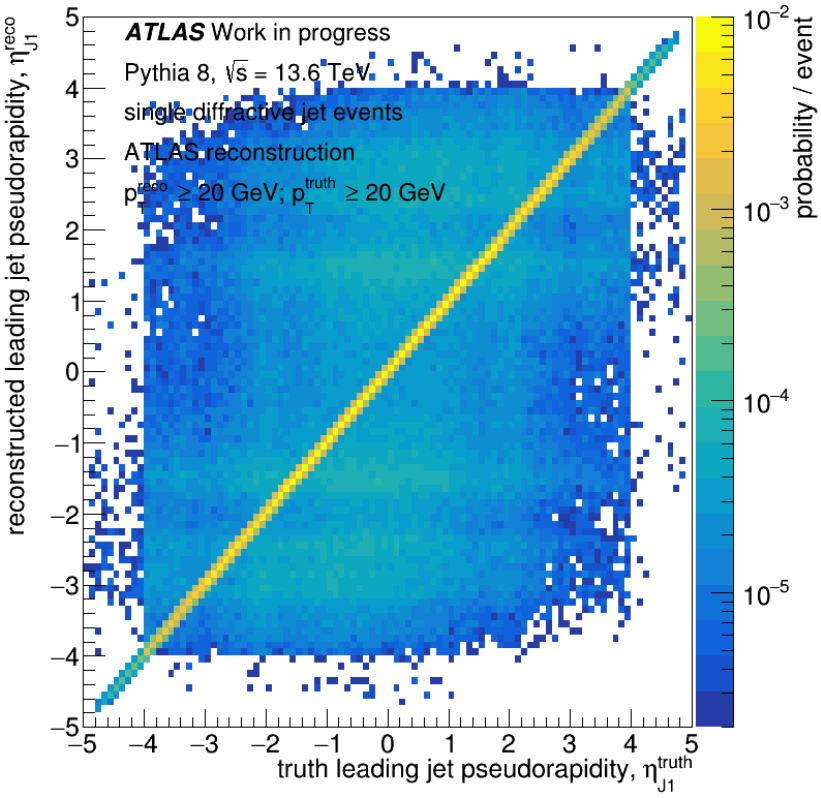

Figure 4.7: Comparison of leading jet generated and reconstructed pseudorapidity. Only events with the leading jet of at least 20 GeV were considered.

Chapter 5

Performance Studies

In this Chapter, the properties of elements and objects needed for the (diffractive) jet-gap-jet analysis will be discussed. First, the performance of the AFP (proton-based) and ATLAS (jet-based) triggers will be described. Next, the reconstruction of the "proton object" would be discussed in quite some detail. Finally, the ATLAS "central" objects will be considered, especially the ones needed for the event selection and gap reconstruction. Also, the jet calibration will be described in detail, as a dedicated procedure was needed for this analysis.

5.1 Trigger Performance

The main concept of the ATLAS trigger system is described in detail in Section 2.2.6, and the AFP trigger system was discussed in Section 2.2.6.1. The "standard" ATLAS jet trigger reconstruction algorithms are used in the present analysis. The concept is described in many ATLAS publications, see *e.g.* [80] or [81].

5.1.1 AFP Trigger Efficiency

Triggers based on a single AFP station are present in the ATLAS trigger menu but, in practice, are used only in the calibration stream or are heavily prescaled. Usually, the four basic AFP trigger signals provided to the Central Trigger Processor (FSA, NSA, NSC, FSC) are used to construct more sophisticated trigger logic, *e.g.* to trigger on a given ATLAS side:

- L1_AFP_A = NSA & FSA,
- L1_AFP_C = NSC & FSC.

These triggers are mainly used to store events in the AFP calibration stream, but since full L1 trigger decision is available in AOD, this information can be also used in analyses to distinguish which AFP side triggered.
For physics analyses, one should use either:

- logical OR between sides: L1_AFP_A_OR_C = (NSA & FSA) | (NSC & FSC)

- or logical AND: L1_AFP_A_AND_C = NSA & FSA & NSC & FSC.

5.1.1.1 Single Station

The efficiency of FSA, NSA, NSC and FSC triggers was studied using two methods. The first one, called **direct**, was based on counting the number of events with the trigger fired and relating them to the number of events in which the trigger signal was expected. Following the logic described in Sect. 2.2.6.1, the AFP trigger should fire if there is at least 1 hit in at least two SiT planes used for triggering[1].
The second method, called **tag-and-probe**, assumed that the scattered proton would leave a signal in both NEAR and FAR stations. Therefore, by requiring a "signal quality" criteria in one (tag) station, the trigger signal in the other one (probe) can be checked. The following tag requirements were applied:

- a "good hit" in a plane, defined as exactly 1 or 2 hits to reduce the impact of events with showers,
- each hit must be in $15 < row < 321$ and $3 < col < 78$ to reduce the "edge effects" (due to non-zero proton trajectory slope and staggering of the SiT planes) and account for the differences in the data-taking positions (see Sect. 3.3.3),
- at least 3 planes with a "good hit" to resemble AFP track reconstruction.

The results based on the run 428770 data (obtained with the AFP calibration stream) are listed in Table 5.1. The efficiencies obtained by both methods are in agreement. Also, there are no large differences between the results obtained for fills 8019 and 8020.
One obvious issue is high inefficiency, especially on side C. The discussion about its source is ongoing within the community, with the following effects pointed as culprits:

- SiT trigger dead-time,
- SiT trigger jitter,
- "malfunction of electronics": issues with passing the trigger signal to CTP by LTB or with generating clock by VLDB.

Fortunately, there is no dependence on BCID, LumiBlock or (x, y) AFP position, thus proton's ξ. The latter is shown in Fig. 5.1 for the AFP C NEAR station. This means a single efficiency value per station can be used for run 428770.

[1] In the run 428770 case, it was SiT P0, P1 and P2 for all stations.

Table 5.1: AFP single station trigger efficiency in run 428770.

Station	**Method**	**Efficiency Fill 8019** [%]	**Efficiency Fill 8020** [%]
A FAR	direct	96.75 ± 0.22	97.59 ± 0.08
	tag&probe	97.93 ± 0.22	98.27 ± 0.08
A NEAR	direct	91.18 ± 0.38	91.77 ± 0.16
	tag&probe	90.73 ± 0.42	90.47 ± 0.18
C NEAR	direct	60.71 ± 0.56	61.39 ± 0.24
	tag&probe	57.77 ± 0.69	58.88 ± 0.31
C FAR	direct	71.60 ± 0.46	70.38 ± 0.20
	tag&probe	74.66 ± 0.71	74.44 ± 0.30

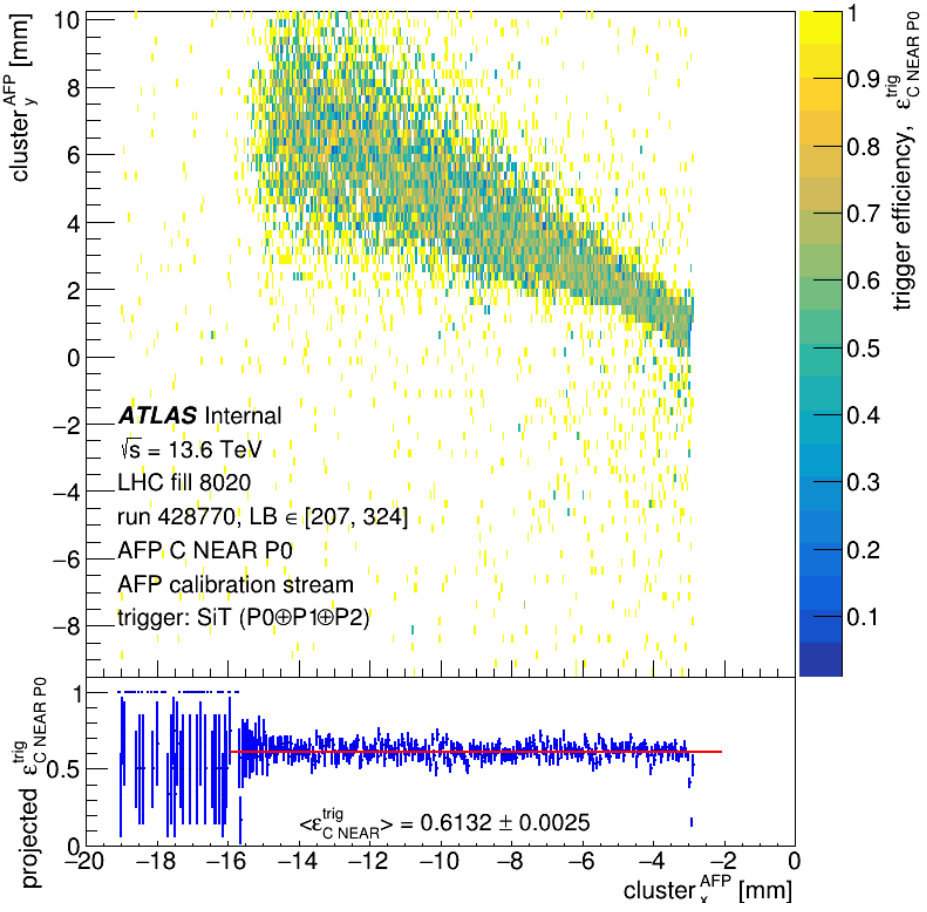

Figure 5.1: **Top panel**: The AFP C NEAR trigger efficiency as a function of the proton (x, y) position. **Bottom panel**: the trigger efficiency as a function of x_{AFP} indicating no dependence as a function of the proton relative energy loss (ξ).

5.1.1.2 Single Side

The *tag-and-probe* method cannot be used to determine the single-side efficiency. Fortunately, this can be performed using the *direct* method, cf. previous Section. In addition, one can use the "usual" definition of efficiency:

$$\varepsilon^{trig}_{AFP\ side} = \frac{N^{trig}_{evt}\ \&\ N^{track}_{evt}\ \&\ is\_ref\_trig}{N^{track}_{evt}\ \&\ is\_ref\_trig}, \tag{5.1}$$

where N^{trig}_{evt} is the number of events with the trigger fired at L1 before the prescale under a condition that event was stored by the reference trigger (is_ref_trig). N^{track}_{evt} is the number of events fulfilling the following requirements:

- at least one reconstructed track in both – NEAR and FAR – stations on a given side,
- taken under condition that event was stored by a reference trigger,
- reconstructed by the default algorithm (no extra quality requirements).

Several reference triggers were considered:

- HLT_noalg_mb_L1RD0_FILLED – purely random as it triggers on every filled bunch and no reconstruction algorithm is requested at the HLT; usually heavily prescaled,
- HLT_mb_sp_L1RD0_FILLED – as above, but at least one space-point (hit) at the HLT level in the inner detector should be present,
- HLT_mb_sptrk_pt2_L1RD0_FILLED – as above, but at least one track with $p_T \geq 2$ GeV must be reconstructed at the HLT level,
- HLT_noalg_mb_L1MBTS_2 – at least 2 Minimum Bias Trigger Scintillator (MBTS) tiles should fire at L1; no algorithm on HLT,
- HLT_noalg_L1EM3 – at least one cluster with energy greater than 3 GeV reconstructed in the electromagnetic part of the calorimeter must be present; no algorithm at HLT.

The computed efficiencies are listed in Table 5.2. As one can see, there are no differences between fills 8019 and 8020. Also, the results obtained using different methods are compatible with each other.

Table 5.2: AFP single side trigger efficiency in run 428770.

trigger	**reference trigger or method**	**stream**	**Efficiency Fill 8019** [%]	**Efficiency Fill 8020** [%]
L1_AFP_A	"direct"	AFP calibration	90.27 ± 0.40	91.06 ± 0.16
	HLT_noalg_mb_L1RD0_FILLED	physics_MinBias	92.89 ± 1.71	92.82 ± 0.76
	HLT_mb_sp_L1RD0_FILLED	physics_MinBias	92.63 ± 1.25	92.27 ± 0.56
	HLT_mb_sp-trk_pt2_L1RD0_FILLED	physics_MinBias	91.19 ± 0.98	91.29 ± 0.42
	HLT_noalg_mb_L1MBTS_2	physics_MinBias	91.28 ± 0.35	91.41 ± 0.20
	HLT_noalg_L1EM3	physics_Main	91.57 ± 2.16	92.32 ± 0.91
L1_AFP_C	"direct"	AFP calibration	45.43 ± 0.58	46.05 ± 0.25
	HLT_noalg_mb_L1RD0_FILLED	physics_MinBias	43.72 ± 3.67	44.38 ± 1.67
	HLT_mb_sp_L1RD0_FILLED	physics_MinBias	43.27 ± 2.54	44.52 ± 1.18
	HLT_mb_sp-trk_pt2_L1RD0_FILLED	physics_MinBias	46.58 ± 1.88	46.18 ± 0.84
	HLT_noalg_mb_L1MBTS_2	physics_MinBias	45.85 ± 0.65	46.11 ± 0.39
	HLT_noalg_L1EM3	physics_Main	47.86 ± 4.22	44.56 ± 1.91

5.1.1.3 Single Tag

As mentioned at the beginning of this Chapter, in the trigger menu, the single station and the single side trigger items are heavily prescaled (or even prescaled out) when writing to physics streams. Therefore, for the single tag physics analyses, the triggers based on L1_AFP_A_OR_C are expected to be used. Similarly to the single station case, the efficiency for a single tag can be defined as:

$$\varepsilon^{trig}_{AFP\ single\ tag} = \frac{N^{trig}_{evt}\ \&\ N^{track}_{evt}\ \&\ is\_ref\_trig}{N^{track}_{evt}\ \&\ is\_ref\_trig}, \tag{5.2}$$

where N^{track}_{evt} counts the tracks reconstructed in both stations on side A or both stations on side C. The resulting efficiencies are listed in Tab. 5.3.

5.1.1.4 Double Tag

The double-tagged events are expected to be triggered by the L1_AFP_A_AND_C. The efficiency is defined as:

$$\varepsilon^{trig}_{AFP\ double\ tag} = \frac{N^{trig}_{evt}\ \&\ N^{track}_{evt}\ \&\ is\_ref\_trig}{N^{track}_{evt}\ \&\ is\_ref\_trig}, \tag{5.3}$$

where N^{track}_{evt} means at least 1 reconstructed track in all four stations. The results are given in Table 5.4. Unfortunately, the chance to have a double-tagged event in the independent, "randomly" triggered event is small. Therefore, due to the limited statistics, the uncertainty on the obtained results is very high.
Fortunately, an alternative method, based on the assumption that the AFP A and C sides are independent, was used. Here, the efficiency is defined as:

$$\varepsilon^{trig}_{AFP\ double\ tag} = \varepsilon_{L1\_AFP\_A} \times \varepsilon_{L1\_AFP\_C}. \tag{5.4}$$

The results are listed in Table 5.4. Clearly, due to the significant inefficiency of the C side, the L1_AFP_A_AND_C trigger efficiency is only $41.85 \pm 0.12\%$.
The situation can be improved if the events triggered by the L1_AFP_A_OR_C are not prescaled more than L1_AFP_A_AND_C. This is indeed the case for run 428770, where:

- L1_AFP_A_OR_C had PS of: 2 in LBs 4–16 and 1 in LBs 17-20 and 210-325,
- L1_AFP_A_AND_C had PS of 1 for all LBs mentioned above.

Such efficiency is defined as in Eq. 5.3, and the results are listed in Table 5.4.

Table 5.3: AFP single tag trigger efficiency in run 428770.

trigger	**reference trigger**	**stream**	**Efficiency Fill 8019** [%]	**Efficiency Fill 8020** [%]
L1_AFP_A_OR_C	HLT_noalg_mb_L1RD0_FILLED	physics_MinBias	70.94 ± 2.25	71.92 ± 1.00
	HLT_mb_sp_L1RD0_FILLED	physics_MinBias	69.63 ± 1.62	71.65 ± 0.71
	HLT_mb_sp-trk_pt2_L1RD0_FILLED	physics_MinBias	71.17 ± 1.16	71.56 ± 0.51
	HLT_noalg_mb_L1MBTS_2	physics_MinBias	69.87 ± 0.42	71.42 ± 0.24
	HLT_noalg_L1EM3	physics_Main	71.71 ± 2.58	71.28 ± 1.16

Table 5.4: AFP double tag trigger efficiency in run 428770 computed using 3 different methods.

trigger	**reference trigger**	**stream**	**Efficiency Fill 8019** [%]	**Efficiency Fill 8020** [%]
L1_AFP_A_AND_C direct method	HLT_noalg_mb_L1RD0_FILLED	physics_MinBias	50.00 ± 35.36	56.25 ± 12.40
	HLT_mb_sp_L1RD0_FILLED	physics_MinBias	66.67 ± 27.22	55.56 ± 9.56
	HLT_mb_sp-trk_pt2_L1RD0_FILLED	physics_MinBias	33.33 ± 15.71	44.83 ± 6.53
	HLT_noalg_mb_L1MBTS_2	physics_MinBias	36.42 ± 3.92	46.48 ± 2.55
	HLT_noalg_L1EM3	physics_Main	50.00 ± 35.36	71.43 ± 17.07
L1_AFP_A_AND_C method: L1_AFP_A × L1_AFP_C	"direct"	AFP calibration	41.01 ± 0.55	41.93 ± 0.24
	HLT_noalg_mb_L1RD0_FILLED	physics_MinBias	40.61 ± 3.49	41.20 ± 1.58
	HLT_mb_sp_L1RD0_FILLED	physics_MinBias	40.08 ± 2.42	41.08 ± 1.12
	HLT_mb_sp-trk_pt2_L1RD0_FILLED	physics_MinBias	42.48 ± 1.78	42.16 ± 0.79
	HLT_noalg_mb_L1MBTS_2	physics_MinBias	41.85 ± 0.61	42.15 ± 0.37
	HLT_noalg_L1EM3	physics_Main	43.82 ± 4.00	41.14 ± 1.81
L1_AFP_A_OR_C double tagged events method: L1_AFP_A or L1_AFP_C	HLT_noalg_mb_L1RD0_FILLED	physics_MinBias	96.00 ± 1.00	96.01 ± 0.44
	HLT_mb_sp_L1RD0_FILLED	physics_MinBias	95.82 ± 0.74	95.71 ± 0.32
	HLT_mb_sp-trk_pt2_L1RD0_FILLED	physics_MinBias	95.29 ± 0.55	95.31 ± 0.24
	HLT_noalg_mb_L1MBTS_2	physics_MinBias	95.28 ± 0.20	95.37 ± 0.11
	HLT_noalg_L1EM3	physics_Main	95.60 ± 1.18	95.74 ± 0.52

Indeed, the usage of logical OR "restores" the efficiency of triggering the double-tagged events to the level of $95.41 \pm 0.06\%$.

5.1.1.5 Summary

Since the obtained results are indifferent[2] for both LHC fills and various considered reference triggers, a single efficiency per trigger item can be used. Such values, obtained by computing the means from the results listed in previous Sections, are given in Table 5.5.

Table 5.5: Final trigger efficiencies for the AFP "physics" triggers in run 428770.

Trigger	**Efficiency** [%]
L1_AFP_A	91.25 ± 0.29
L1_AFP_C	45.92 ± 0.13
L1_AFP_A_OR_C	71.16 ± 0.21
L1_AFP_A_AND_C	41.85 ± 0.12
L1_AFP_A_OR_C (double tag)	95.41 ± 0.06

5.1.2 Jet Trigger Efficiency

The ATLAS trigger menu used during run 428770 contains several triggers suitable for the jet analysis. The most promising ones are:

- HLT_j20_L1J12 – at least 1 jet with a threshold of 12 GeV is required at L1, and at least 1 jet with $p_T > 20$ GeV is required at HLT,
- HLT_j20_L1MBTS_2 – an event is triggered at L1 if at least 2 MBTS tiles were activated (meaning particles being produced in $2.1 < |\eta| < 3.8$ region) followed by the HLT jet requirement,
- HLT_j20_L1AFP_A_OR_C – a presence of the AFP proton is required at L1 and at least 20 GeV HLT jet.

For L1_J12, the mid-point of the turn-on curve is expected to be at around 40 GeV for the offline (reconstructed) jets – *cf.* Fig. 5.2 (left). HLT_j20 algorithm is expected to be fully effective for the offline jets having p_T of around 25 GeV – *cf.* Fig. 5.2 (right).
It is interesting to see how many jet events are stored when a certain trigger is required. This is shown for run 428770 in Fig. 5.3 for events with at least 1

[2] *i.e.* they are compatible within the statistical uncertainty.

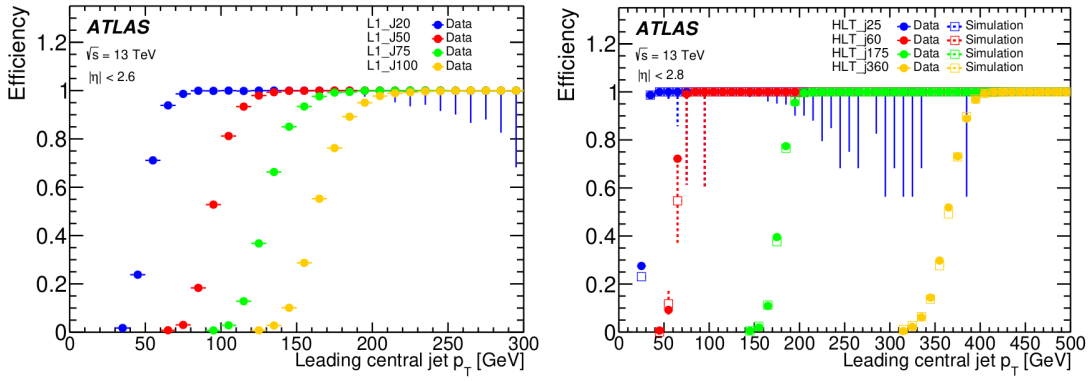

Figure 5.2: L1 and HLT jet trigger efficiency measured using ATLAS Run 2 data.

reconstructed jet (left) and an additional requirement of a proton tag (right). In the former case, the HLT_j20_L1J12 stores the highest number of events if the leading jet has $p_T > 30$ GeV. For events with the leading jets having lower p_T, the HLT_j20_L1MBTS_2 saves the highest number of events. In case of additional requirement of the AFP proton tag, the situation changes – the HLT_j20_L1AFP_A_OR_C stores the highest number of events except for the region of the leading jet $p_T > 50$ GeV where the HLT_j20_L1J12 performs slightly better.

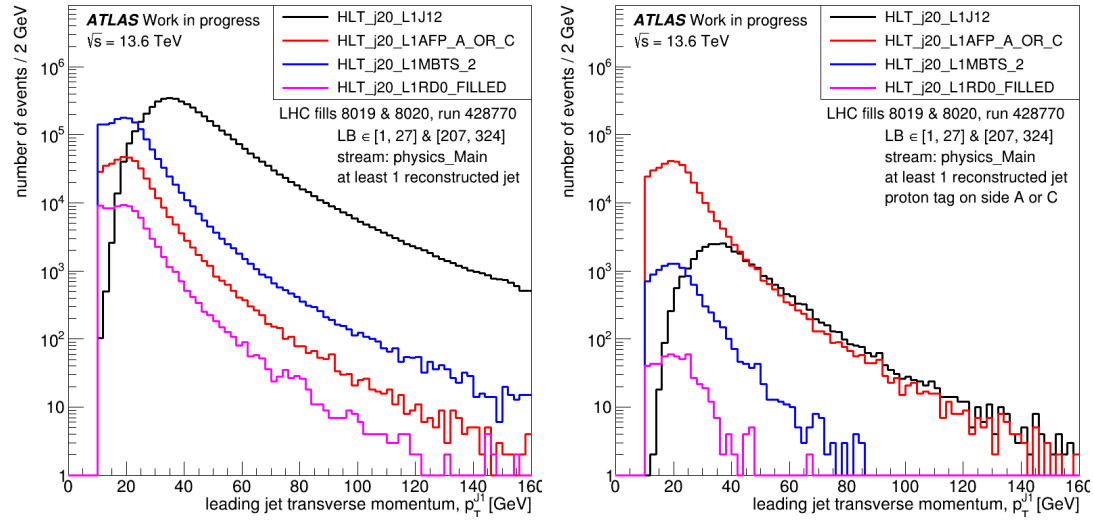

Figure 5.3: The number of events in run 428770 containing at least 1 reconstructed jet (**left**) and jet plus proton tag (**right**).

The differences in the number of stored events, besides the algorithm efficiency, are due to the trigger prescales. As was mentioned in the previous Section, the L1_AFP_A_OR_C had the PS of 2 in LBs 4–16, 1 in LBs 17-20 and 210-325. The L1_MBTS_2 had the prescale of 25, L1_RD0_FILLED of 1000 and L1_J12 was unprescaled. Once the event passed the L1 trigger, there was no prescale at HLT for events passing the j20 algorithm.

5.1.2.1 The L1_J12 Trigger

The jet efficiency is computed as a function of leading jet transverse momentum:

$$\varepsilon = \frac{N_{evt}^{trig} \ \& \ N_{evt}^{jet} \ \& \ is\_ref\_trig}{N_{evt}^{jet} \ \& \ is\_ref\_trig}, \tag{5.5}$$

where N_{evt}^{trig} is the number of events with trigger fired under the condition that the event was stored by the reference trigger (is_ref_trig) and N_{evt}^{jet} is the number of events with offline reconstructed jets of a given p_T. The reference triggers used in the efficiency analysis are as described in Section 5.1.1.2, with the addition of one AFP-based item – the HLT_noalg_L1AFP_A_OR_C.
The efficiency of the L1_J12 algorithm as a function of the leading jet transverse momentum is shown in Fig. 5.4. The example of three reference triggers is shown. The fitted sigmoid curve confirms the turnover midpoint to be around 40 GeV.

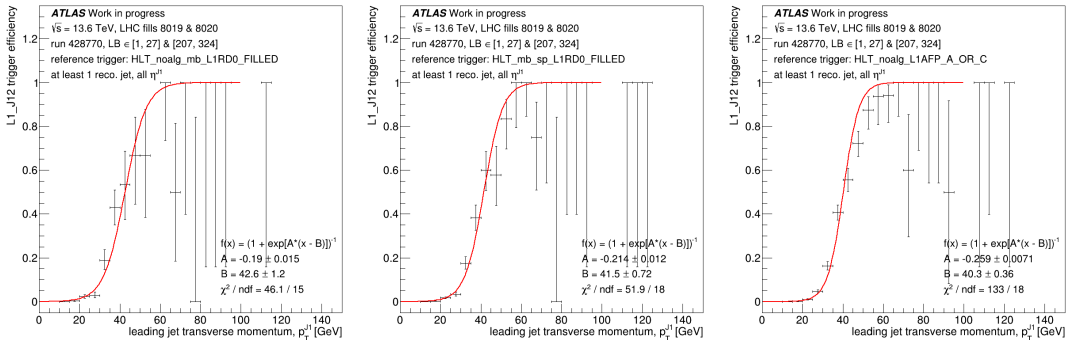

Figure 5.4: The efficiency of the L1_J12 algorithm as a function of the leading jet transverse momentum for various reference triggers. At least 1 reconstructed jet was required to be present in the event.

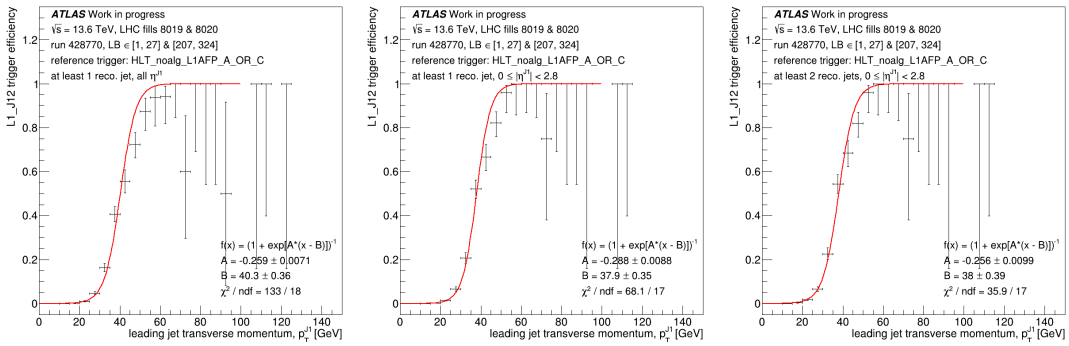

Figure 5.5: The efficiency of L1_J12 algorithm in a function of leading jet transverse momentum for events triggered by HLT_noalg_L1AFP_A_OR_C. In the **left** plot at least 1 reconstructed jet was required to be present in the event, in the **middle** this jet had to be in $|\eta| < 2.8$ and in the **right** at lest 2 jets in mentioned η range were required.

The usual ATLAS trigger efficiency studies (*cf.* Fig. 5.2) restrict the recon-

structed jets to be within a certain pseudorapidity region. In addition, one could expect a bit higher efficiency if two jets are present in the event, which would be, anyway, the analysis requirement. These cases are shown in Fig. 5.5 for the example of events stored by the HLT_noalg_L1AFP_A_OR_C trigger. Indeed, small improvements are visible (*cf.* χ^2/ndf).
From all these studies, one can conclude that the L1_J12 algorithm becomes fully effective for events having at least one (reconstructed) jet with $p_T \gtrsim 55$ GeV.

5.1.2.2 The HLT_j20 Trigger

Similarly, the HLT_j20 efficiency was checked. Several reference triggers were investigated, from which the HLT_noalg_L1AFP_A_OR_C is presented in this thesis. The results are shown in Fig. 5.6. The midpoint of the turnover curve is around 19 GeV, and the algorithm becomes fully effective for the di-jet events with the leading jet of at least 30 GeV.

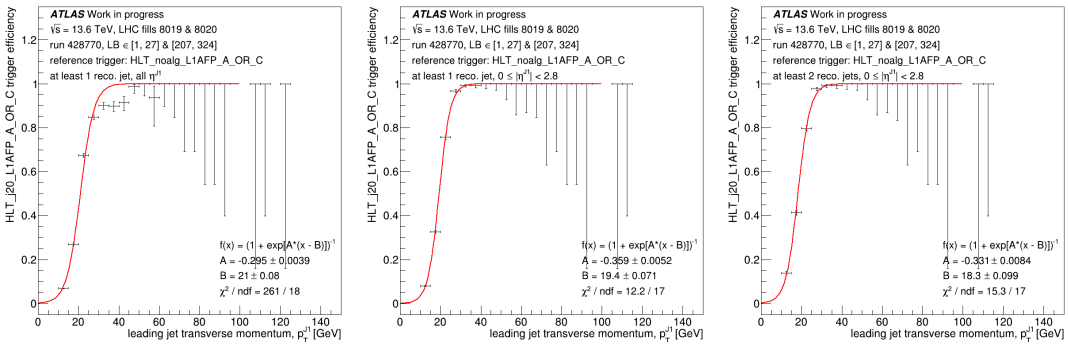

Figure 5.6: The efficiency of the HLT_j20 algorithm in a function of the leading jet transverse momentum for events triggered by HLT_noalg_L1AFP_A_OR_C. In the **left** plot at least 1 reconstructed jet was required to be present in the event, in the **middle** this jet had to be within $|\eta| < 2.8$ and in the **right** at lest 2 jets in mentioned η range were required.

The efficiency of the HLT_j20 algorithm was also checked for the events with at least 1 proton tag. Comparing Fig. 5.7 and Fig. 5.6, one may conclude that no bias nor change in the efficiency occurred.

5.1.3 Summary

Several algorithms can be used for the (diffractive) jet-gap-jet analysis. In the case of jets without a proton tag, one can use events triggered by HLT_j20_L1J12. This trigger is fully effective for events having at least one (reconstructed) jet with $p_T \gtrsim 55$ GeV. A "combined" two-trigger analysis, with the addition of HLT_j20_L1MBTS_2, can be considered to lower the jet p_T threshold to 30 GeV.

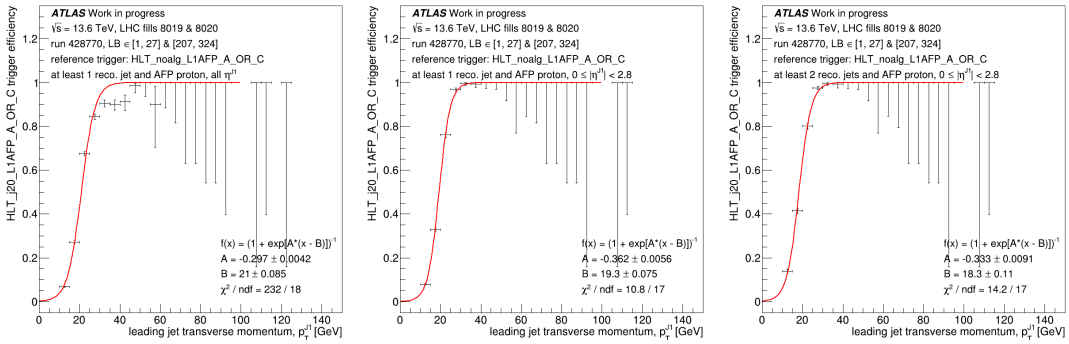

Figure 5.7: The efficiency of the HLT_j20 algorithm as a function of the leading jet transverse momentum for events triggered by HLT_noalg_L1AFP_A_OR_C. In the **left** plot at least 1 proton should be present and at least 1 reconstructed jet was required to be present in the event, in the **middle** this jet had to be in $|\eta| < 2.8$ and in the **right** at lest 2 jets in mentioned η range were required.

In the case of diffractive analysis, when the proton is required to be measured in the AFP, one should use HLT_j20_L1AFP_A_OR_C, which will be fully effective for events containing a leading jet of at least 30 GeV. Due to the inefficiency of the L1AFP_A_OR_C algorithm, the "combined" two-trigger analysis with HLT_j20_L1J12 used for events with a jet of at least 55 GeV can be considered.

5.2 Proton Reconstruction Performance

The reconstruction of proton kinematics is a complex process that requires several intermediate steps and corrections. First, to effectively register protons, the SiT detectors must be tuned. This calibration step, briefly described in Section 3.3.1, was done by the experts before the data-taking.

Protons passing the AFP leave "hits" in the Silicon Tracker. These hits are used to reconstruct clusters which, by using the information about deposited charge, allow for a more precise determination of proton trajectory position. Before combining the clusters into a track, SiT planes must be aligned w.r.t. each other (the so-called *local alignment*). To reconstruct the proton trajectory from NEAR and FAR stations, their position w.r.t. the LHC beam must be determined. This procedure is called *the global alignment*. Finally, a dedicated unfolding procedure (see Ref. [82]) is employed to reconstruct the proton kinematics. The reconstruction chain is pictured in Fig. 5.8.

5.2.1 Hits

The initial stage of the proton reconstruction begins with the identification and characterization of "hits" in the silicon tracking detectors. Each "hit" represents

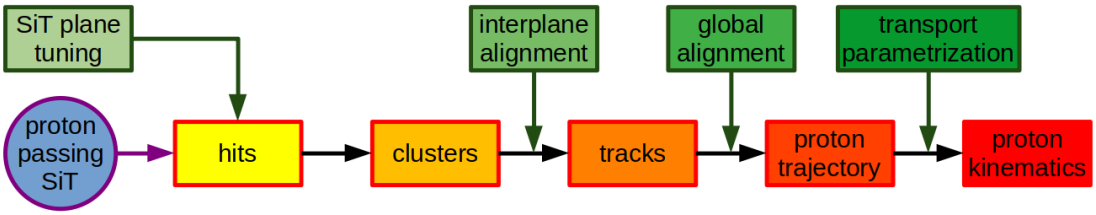

Figure 5.8: General scheme of the forward proton kinematics reconstruction chain.

an interaction between the charged particle and the sensor material, producing a signal that exceeds the predetermined threshold. The spatial distribution of hits across the detector planes provides information about the detector's performance. Figure 5.9 presents the hit distribution for the example of plane 3 in AFP C NEAR station, revealing regions of varying response characteristics. The hitmap analysis indicates specific regions where the pixels do not respond, primarily due to radiation exposure or electronic noise considerations. These masked regions are predominantly localized, suggesting isolated detector effects rather than systematic limitations.

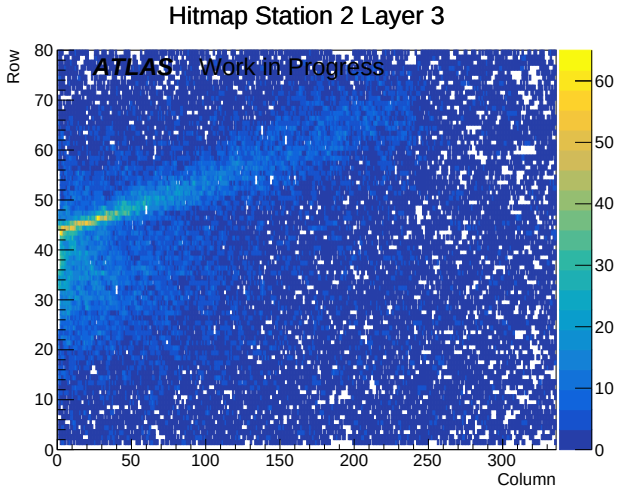

Figure 5.9: Pixel hitmap in run 428770 for the example of AFP C NEAR (station #2) plane (layer) 3. The characteristic diffractive pattern is visible. White areas, especially in the highly populated region of the diffractive pattern, are due to individual pixels being masked out in the readout.

The efficiency of each detector plane was studied. An exceptional uniformity across all planes, with efficiencies consistently above 98%, was found.

Finally, it is interesting to check the hit multiplicity distributions since they provide additional characterization of the detector response. Two primary regions of interest were considered: a low-multiplicity domain dominated by single-particle interactions and a high-multiplicity regime due to shower development.

In the high-multiplicity domain, shown in Fig. 5.10, the distribution exhibits a characteristic exponential decrease. This behaviour is attributed to the development of electromagnetic and hadronic showers within the detector material. The shower formation process initiates when incident protons undergo interactions with the detector material, producing secondary particles through various mechanisms, including bremsstrahlung and nuclear interactions. The exponential nature of the multiplicity decrease reflects the successive particle generation and energy-sharing processes inherent in the shower development.

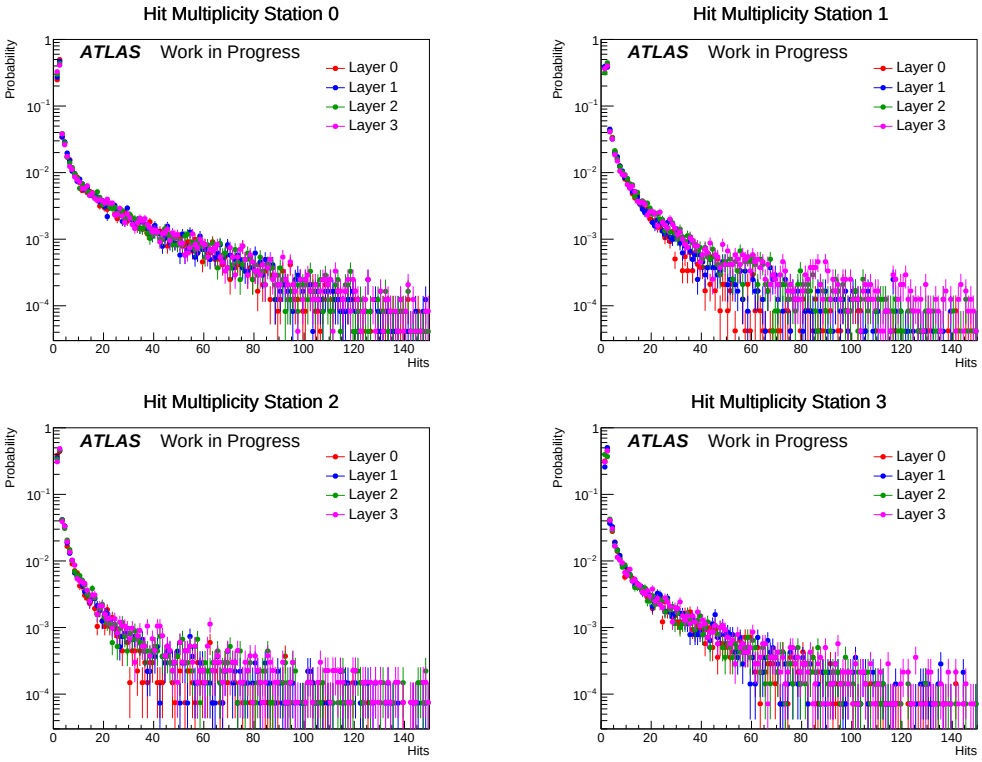

Figure 5.10: Hit multiplicity distribution for all detector stations and planes in a wide multiplicity range to demonstrate the shower development regime.

In the low-multiplicity region, detailed in Figure 5.11, a pronounced peak at the multiplicity of 2 is visible. This characteristic structure primarily results from the geometric configuration of the sensor planes *i.e.* their 14^0 tilt angle relative to the incident proton trajectory. The tilted geometry enhances the probability of the charge sharing between adjacent pixels, leading to the observed multiplicity pattern.

The Time-over-Threshold (ToT) measurement quantifies the energy deposition in each pixel. Figure 5.12 displays the ToT distribution for all SiT planes, exhibiting a characteristic shape with a peak around 4, set during the detector tuning.

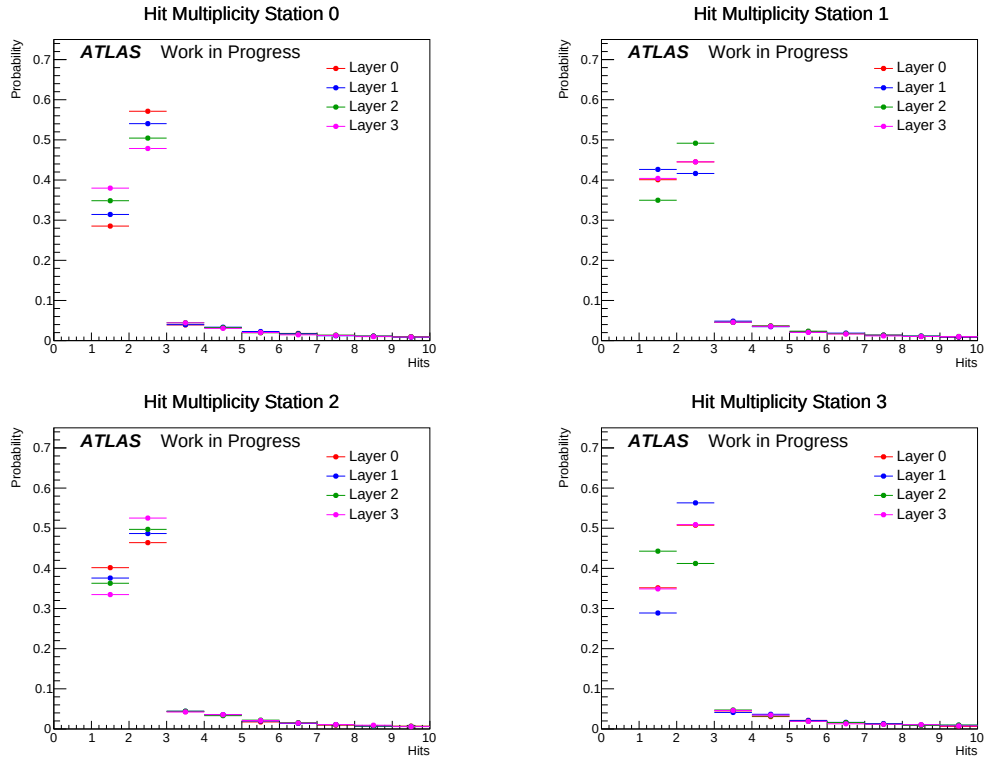

Figure 5.11: Hit multiplicity distribution for all detector stations and planes focused on the range 0-10 to highlight the peak at 2 expected due to the 14^0 tilt of the detector planes.

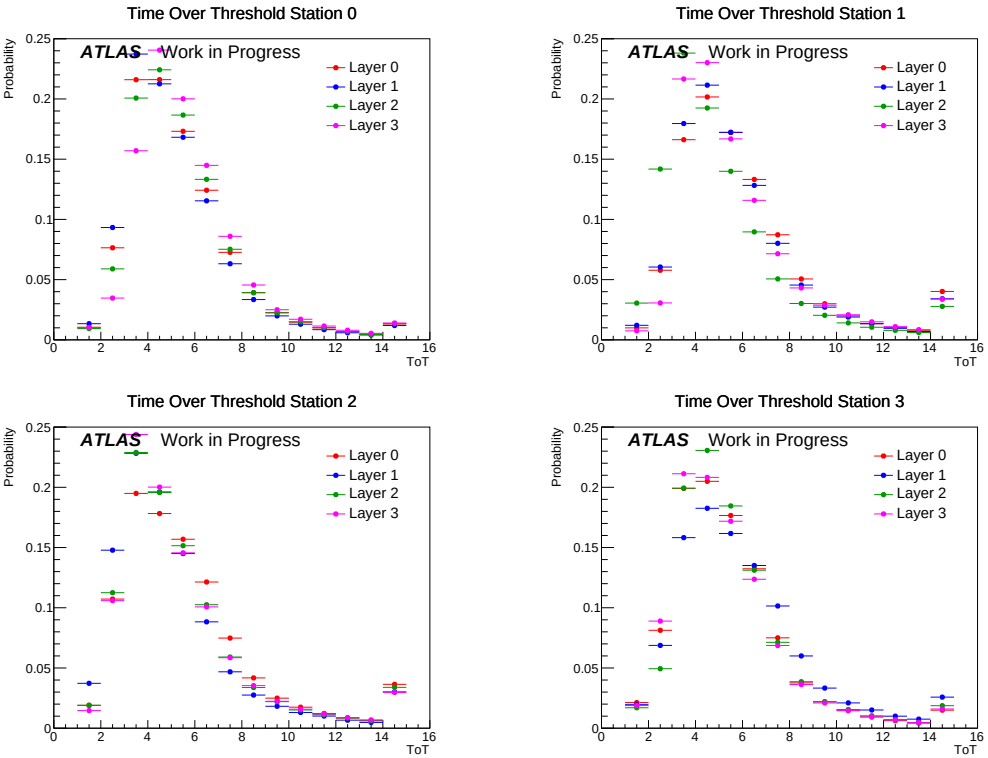

Figure 5.12: Time-over-Threshold distributions across all detector stations, illustrating the characteristic energy deposition patterns in each of the four silicon layers.

5.2.2 Clusters

The next phase of the proton trajectory reconstruction in the AFP detector involves the formation of clusters from the individual pixel hits within each plane of each station. The process begins with identifying the cluster seeds from the individual pixel hits within each detector plane. Adjacent hits along the x-direction are iteratively incorporated into the cluster, with the cluster position determined via the charge(ToT)-weighted calculation of the constituent pixel centres. This approach optimizes the spatial resolution.

The number of clusters per event (cluster multiplicity) is shown in Figure 5.13. Clearly, the majority of events contain exactly one cluster.

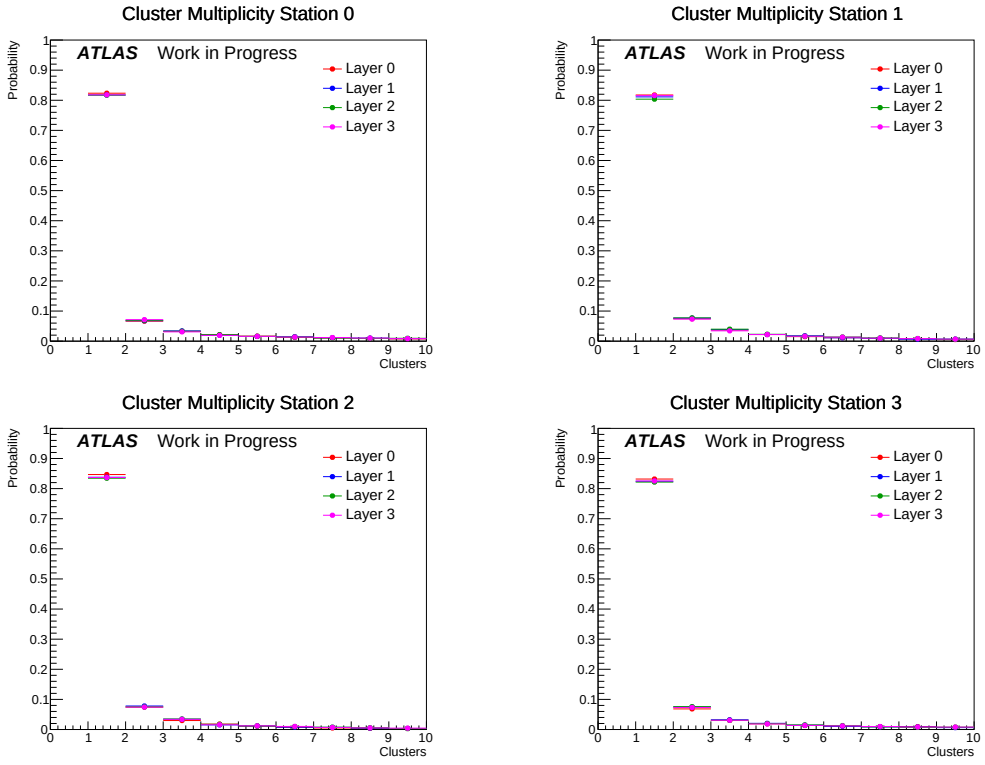

Figure 5.13: The cluster multiplicity distributions for all AFP planes.

The cluster reconstruction efficiency was measured using the *tag-and-probe* method, which provides an unbiased measurement across all detector planes. Valid *tag* event was requested to have exactly 1 cluster in 3 planes, except the one being *probed*, in a given station. Clusters were requested to be within a 2 mm radius of each other. The *probe* was checked for the presence of a cluster in the radius of 2 mm around the mean position of tag clusters. Results listed in Table 5.6 show exceptional reconstruction performance, with efficiencies consistently exceeding 98% across all stations and planes.

Table 5.6: The cluster reconstruction efficiency in run 428770.

Station	Tag Plane 0	Tag Plane 1	Tag Plane 2	Tag Plane 3
Station 0	99.04 ± 0.01%	99.24 ± 0.01%	99.50 ± 0.01%	99.14 ± 0.01%
Station 1	98.85 ± 0.01%	98.95 ± 0.01%	98.66 ± 0.01%	99.25 ± 0.01%
Station 2	99.14 ± 0.01%	99.70 ± 0.01%	99.39 ± 0.01%	98.19 ± 0.01%
Station 3	99.45 ± 0.01%	99.79 ± 0.00%	99.25 ± 0.01%	99.38 ± 0.01%

5.2.3 Local Alignment

The transformation between the measured cluster position vector ($\vec{r}_m$) and the true position vector ($\vec{r}$) is characterized by a rotation matrix R and the translation vector $\delta\vec{r}$:

$$\vec{r}_m = R(\alpha, \beta, \gamma)\vec{r} + \delta\vec{r}. \tag{5.6}$$

For small angular rotations, the rotation matrix can be approximated to first order by:

$$R(\alpha, \beta, \gamma) \approx \begin{pmatrix} 1 & -\alpha & \beta \\ \alpha & 1 & -\gamma \\ -\beta & \gamma & 1 \end{pmatrix} \tag{5.7}$$

The alignment procedure uses an iterative algorithm that minimizes residuals between cluster positions and reconstructed tracks. To eliminate ambiguity on the whole-detector rotation, the tracks are constrained to be parallel to the beam axis during the alignment process. The first plane (P0) of each station serves as the reference, effectively reducing the number of free parameters per station to: three translational (δx, δy, δz) and three rotational (α, β, γ) parameters for each of the remaining three planes.

Analysis of the run 427929 data, described in detail in [83], demonstrate the effectiveness of the local alignment method. The width of the x-residuals improves from 29.3 μm to 6.2 μm after approximately 25 iterations, with x-translations for planes 1-3 ranging from 60 to 165 μm, as shown in Figure 5.14.

SiT planes are expected to be tightly attached to the pot, thus, the local alignment is expected to be kept as long as the detector packages are not exchanged. Since the detectors installed before Run 3 were extracted only after 2023 data-taking, the results obtained in one run are expected to be valid for a full data-taking period.

The 2022–2023 local alignment parameters are listed in Table 5.7. The translational corrections exhibit sub-millimetre magnitudes, with the maximum displacement observed in station 1, plane 3, reaching 277 μm in the x-direction. Rotational corrections around the z-axis extend to 6.923 mrad while maintaining

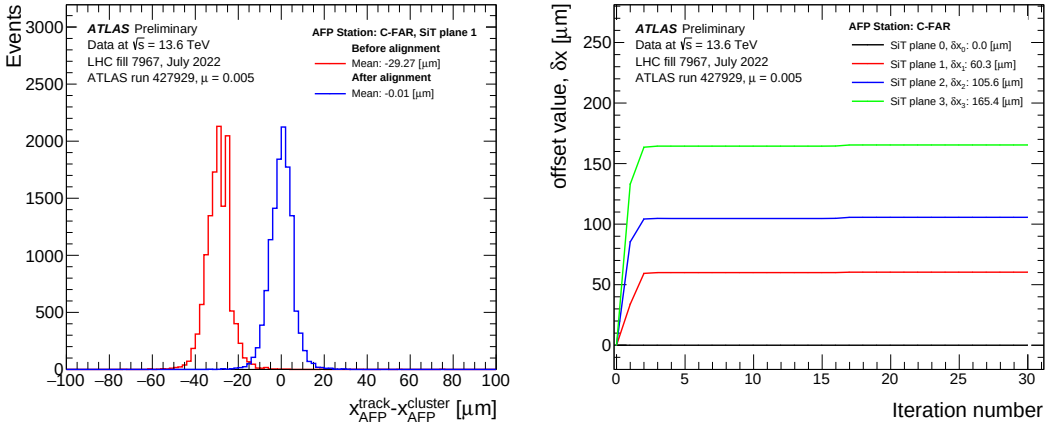

Figure 5.14: **Left:** the difference between the x-positions of a reconstructed track and a cluster in SiT Plane 1 of the AFP C-FAR station. **Right:** progression of the offset value (δx) as a function of the alignment iteration step. From [83].

null corrections in the β and γ parameters due to the geometric constraints of the detector system.

Table 5.7: Local alignment parameters for years 2022–2023. Planes are aligned w.r.t. P0.

Station	Plane	δx [mm]	δy [mm]	δz [mm]	α [mrad]	β [mrad]	γ [mrad]
A FAR	1	-0.123	-0.031	0.000	-0.324	0.000	0.000
	2	-0.039	-0.009	0.000	-3.694	0.000	0.000
	3	-0.207	-0.077	0.000	-2.514	0.000	0.000
A NEAR	1	-0.159	0.005	0.000	-2.518	0.000	0.000
	2	-0.193	-0.072	0.000	1.226	0.000	0.000
	3	-0.277	-0.063	0.000	-0.943	0.000	0.000
C NEAR	1	-0.060	0.086	0.000	-5.555	0.000	0.000
	2	0.034	0.156	0.000	-6.923	0.000	0.000
	3	-0.041	0.204	0.000	-6.243	0.000	0.000
C FAR	1	0.000	0.058	0.000	-1.761	0.000	0.000
	2	-0.145	0.102	0.000	-1.198	0.000	0.000
	3	-0.188	0.162	0.000	-2.053	0.000	0.000

5.2.4 Tracks

The AFP tracks are reconstructed using a dedicated algorithm; see Ref. [84]. The track reconstruction efficiency in run 428770 was checked using the *tag-and-probe* method. Only the cases requiring exactly one reconstructed track in one station of the AFP arm (*tag*) were considered. The reconstructed track was requested to be in the expected overlap region of both NEAR and FAR stations to remove bias

due to the edge effects. The results are presented in Table 5.8. For all stations, the track reconstruction efficiency is ∼99%.

Table 5.8: The AFP track reconstruction efficiency measured using the tag-and-probe method. For each side, both NEAR and FAR stations were used alternately as tag-and-probe.

Side	TAG Station	PROBE Station	Efficiency (%)
A	NEAR	FAR	98.45 ± 0.07
	FAR	NEAR	98.90 ± 0.07
C	NEAR	FAR	99.07 ± 0.09
	FAR	NEAR	98.81 ± 0.09

The track multiplicity distribution is shown in Fig. 5.15. Some interesting features are visible. First, the events with exactly one reconstructed track dominate. The higher track multiplicities, which are expected due to showers, occur in less than 10% of cases. Second, the AFP trigger inefficiency can also be observed – stations on side C (2&3) contain much fewer events than the ones on side A, which is expected since quite a large fraction of the events is stored due to the L1_AFP_A_OR_C trigger.

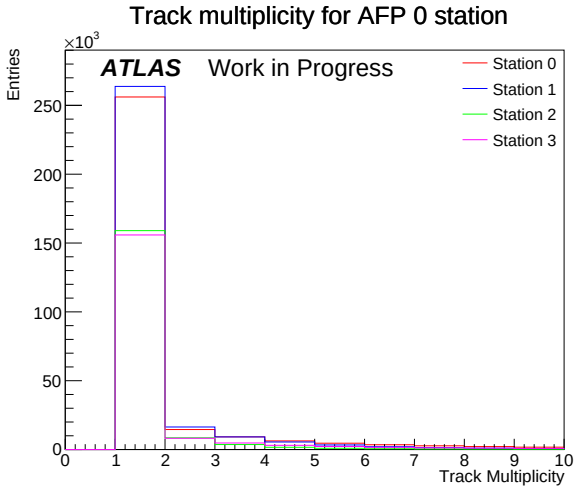

Figure 5.15: The track multiplicity for each AFP station.

5.2.5 Global Alignment

A precise determination of the proton trajectory is linked to the accurate spatial alignment of the AFP stations. Therefore, a deep understanding of the detector alignment relative to the LHC beam is essential for ensuring a reliable proton kinematics reconstruction. The alignment framework integrates multiple complementary methodologies.

The global alignment process is initiated through the Beam-Based Alignment (BBA), see Section 3.3.2. This procedure results in the positioning accuracy of approximately 20 μm w.r.t. the LHC beam but accounts neither for the position of the SiT detectors inside the Roman pot nor the effective LHC optics (see Appendix A).

5.2.5.1 SiT-Beam Distance

The spatial alignment methodology incorporates a series of coordinate transformations defined by the relation:

$$x(s,r) = x_{\text{pre-align}} + x_{\text{tracker}} - x_{\text{beam}}(s) + x_{\text{RP}}(r,s) + \delta x_{\text{corr}}(s), \tag{5.8}$$

where s represents the station identifier ($s \in \{\text{FSA, NSA, NSC, FSC}\}$) and r denotes the run number. Various terms used in this equation correspond to pre-alignment parameters, tracker positions, beam coordinates, Roman Pot positions and empirically derived corrections, respectively. The concept is visualized in Fig. 5.16.

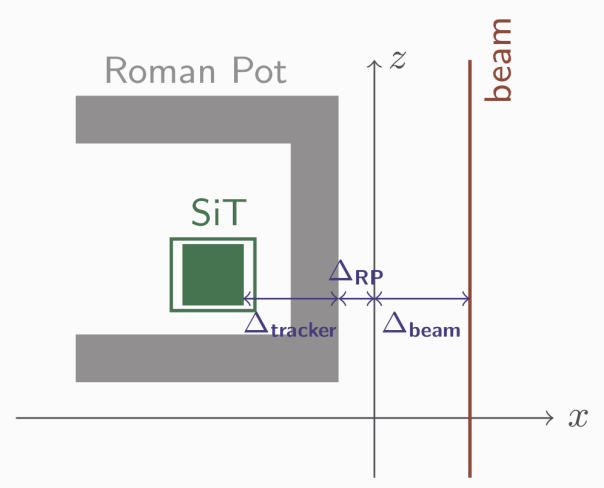

Figure 5.16: Various contributions to the final SiT–beam distance.

Some of the parameters of Eq. 5.8, determined with the 2022 data, are listed in Table 5.9. The tracker position was fixed at -0.5 mm for all stations, representing the assumed offset between the active detector region and the Roman pot edge. The beam positions, varying between -0.556 mm and -1.000 mm, reflect variations of the LHC beam orbit position in the AFP region. The Roman pot positions ranging from -2.080 mm to -3.330 mm were obtained during the BBA (*cf.* Section 3.3.3). Final corrections, derived through the physics-based validation, compensate for the residual misalignments.

Table 5.9: Global alignment parameters in year 2022.

Parameter [mm]	A FAR	A NEAR	C NEAR	C FAR
Tracker position	-0.500	-0.500	-0.500	-0.500
Beam position	-1.000	-0.782	-0.995	-0.556
Roman pot position	-2.471	-3.015	-3.326	-2.079
Final correction	-0.940	-0.703	-0.558	-0.350

5.2.5.2 Di-lepton Alignment

The absolute position of the AFP detectors can be calibrated using the data-driven methods based on the analysis of the exclusive processes. In the exclusive type of event, the energy of the central system is expected to match the energy lost by scattered protons. The first analysis of the exclusive lepton production using the AFP for the proton tagging was published in [85]. The Run 3 results were recently published by ATLAS [86]. The concept is demonstrated in Fig. 5.17.

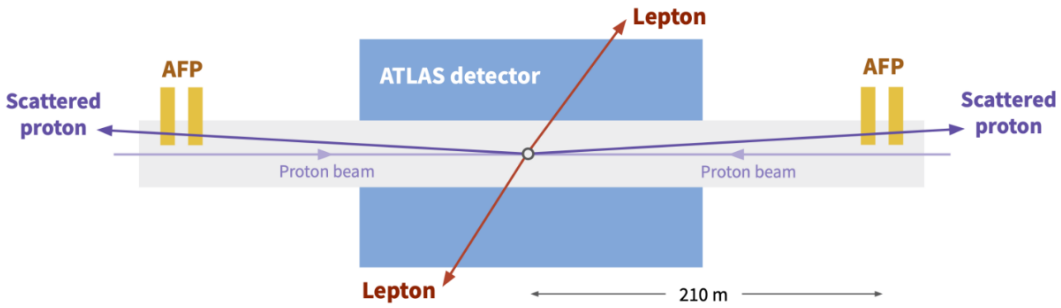

Figure 5.17: Scheme of the exclusive lepton production: both leptons are measured in the ATLAS central detector while proton(s) are tagged in the AFP. No other particle is produced in the event, thus the energy of the lepton pair matches the energy lost by protons. From [87].

For the exclusive di-lepton production, the fractional momentum loss of the proton is given by:

$$\xi_{ll} = \frac{m_{ll}}{\sqrt{s}} e^{(\pm) y_{ll}}, \tag{5.9}$$

where m_{ll} and y_{ll} denote the invariant mass and rapidity of the di-lepton system, respectively. The transport functions utilize polynomial expansions to relate the detector-delivered coordinates to the proton kinematics:

$$x_{\text{det}} = \sum_{i,j,k} c_{ijk} \xi^i p_x^j p_y^k. \tag{5.10}$$

The exact values of the transport coefficients used in the analysis are summarized in Table 5.10.

Table 5.10: Transport parametrization coefficients used for di-lepton alignment.

Component	Order	c_0	c_1	c_2	c_3
x_{det}	3	1.97×10^{-6}	-0.128	-0.148	-0.263
y_{det}	2	-3.993	-4.511	5.012	-
$\Delta x/\Delta z$	2	-1.45×10^{-7}	5.15×10^{-5}	-3.73×10^{-4}	-

The situation before applying the alignment correction for the example of C NEAR station is shown in Fig. 5.18. The black dots represent the signal while the red ones mark the background: di-muons combined with uncorrelated protons. On the right side, the background was extracted from the signal, and the Gaussian distribution was fitted. One can observe a 107 ± 30 μm shift.

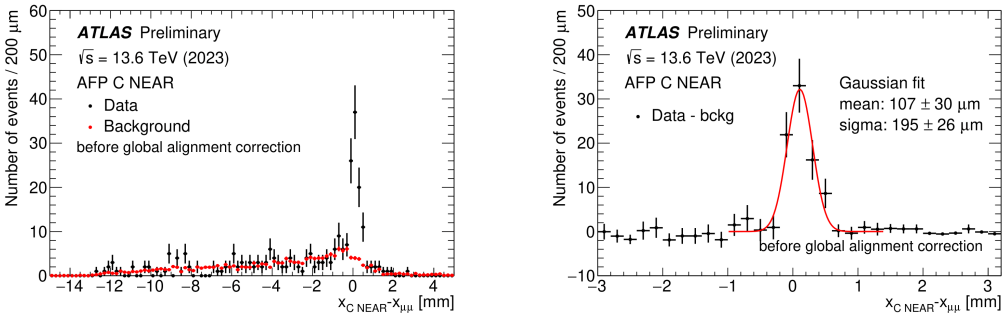

Figure 5.18: **Left**: the distribution of the difference of the x positions measured in AFP and calculated from the di-muon events. The di-muon candidates are marked in black, while combinatorial background events are in red. **Right**: the distribution after the background subtraction with Gaussian function fitted (red line). From [86].

Application of the global alignment corrections brings the centre of the distribution to be close to 0, within the uncertainty – see Fig. 5.19. The alignment results obtained using di-muons (left) were checked with the di-electron events (right). No discrepancy was observed. Table 5.11 contains the full set of the obtained corrections.

Systematic uncertainties were evaluated by varying the event selection criteria and demonstrating stability across all measurements. The achieved global alignment precision resulted in the relative proton energy reconstruction resolution of $\delta\xi/\xi \approx 1\%$.

5.2.6 Proton Trajectories

After applying the local and global alignments, it is interesting to discuss features of the tracks reconstructed in the AFP. The x-position of the reconstructed tracks is shown in Fig. 5.20. With the LHC beam located around 0, one can see that

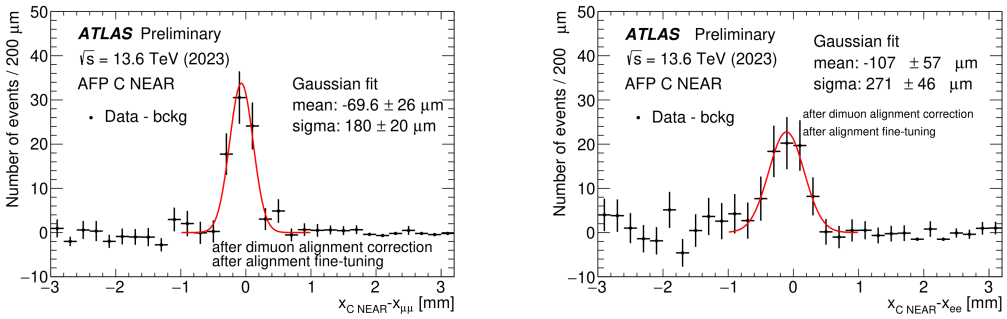

Figure 5.19: The difference of the x positions measured in the AFP and calculated from the di-muon (**left**) and di-electron (**right**) events after applying the global alignment corrections. From [86].

Table 5.11: Global alignment corrections obtained using ee and $\mu\mu$ channels for the 2023 dataset.

Station	Channel	Before Correction		After Correction	
		Mean [μm]	σ [μm]	Mean [μm]	σ [μm]
A-Near	ee	337 ± 41	173 ± 33	20.5 ± 32	150 ± 32
	$\mu\mu$	333 ± 48	216 ± 24	3.1 ± 31	185 ± 19
A-Far	ee	1420 ± 93	164 ± 88	446 ± 120	216 ± 97
	$\mu\mu$	726 ± 150	538 ± 140	-18.6 ± 110	477 ± 120
C-Near	ee	48.1 ± 62	302 ± 48	-107 ± 57	272 ± 47
	$\mu\mu$	138 ± 27	186 ± 20	-69.6 ± 26	180 ± 20
C-Far	ee	392 ± 83	449 ± 81	13.2 ± 70	397 ± 66
	$\mu\mu$	401 ± 42	274 ± 43	13.1 ± 29	226 ± 30

the FAR stations take data closer to the beam than the NEAR ones. This is due to the LHC machine optics and was already observed in other AFP analyses. On the high-x side, an effect of the collimators is visible: if a single track is requested, the probability of observing a proton steeply falls starting from around -15 mm. Finally, one can clearly see that more showers are registered in the FAR station than in the NEAR one.

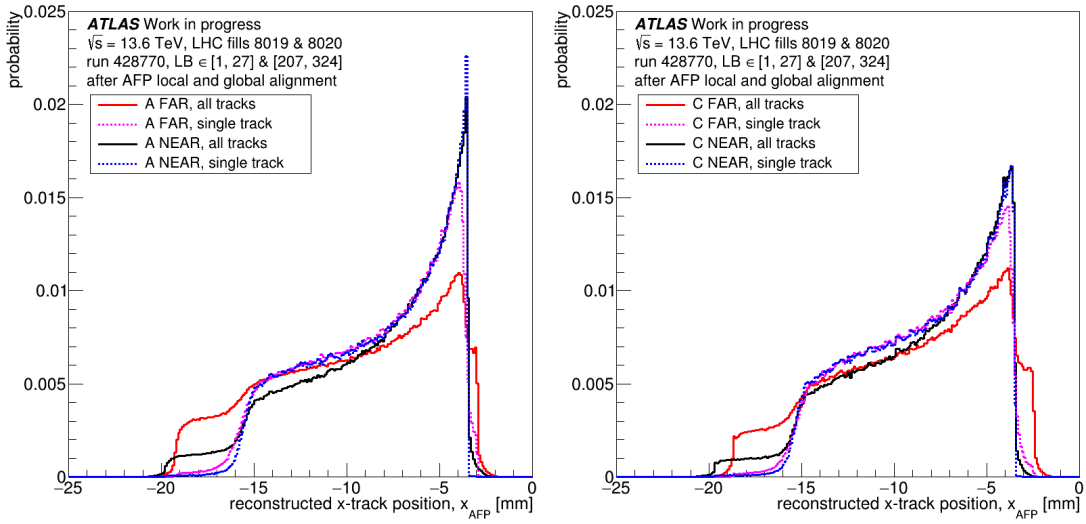

Figure 5.20: Horizontal x-position of the tracks reconstructed in AFP on side A (**left**) and C (**right**) after considering corrections due to the local and global alignments.

To complete the picture, a relation between the track reconstructed in the NEAR and FAR station is shown in Fig. 5.21. Only cases when exactly one track is reconstructed in NEAR and FAR stations on a given side are plotted. As expected, a strong correlation between the sides is visible.

5.2.7 Proton Kinematics

Finally, after considering all the alignment corrections and LHC optics, the proton kinematics can be reconstructed. This is shown in Fig. 5.22 for both AFP sides. One can see that the acceptance starts from ξ of about 0.02, but the full efficiency seems to be achieved for the protons with ξ of at least 0.03. At the high energy loss end, the collimators start to cut out protons with ξ of about 0.09. The entries with $\xi \gtrsim 0.11$ are most probably due to the "unphysical" reconstructed position in the NEAR and FAR stations. As one can see, such events are considerably filtered out when exactly one track is required in both NEAR and FAR stations, pointing to their shower origin.

The relation between the proton x-position reconstructed in the NEAR station and the proton ξ for events with exactly one reconstructed track in the NEAR

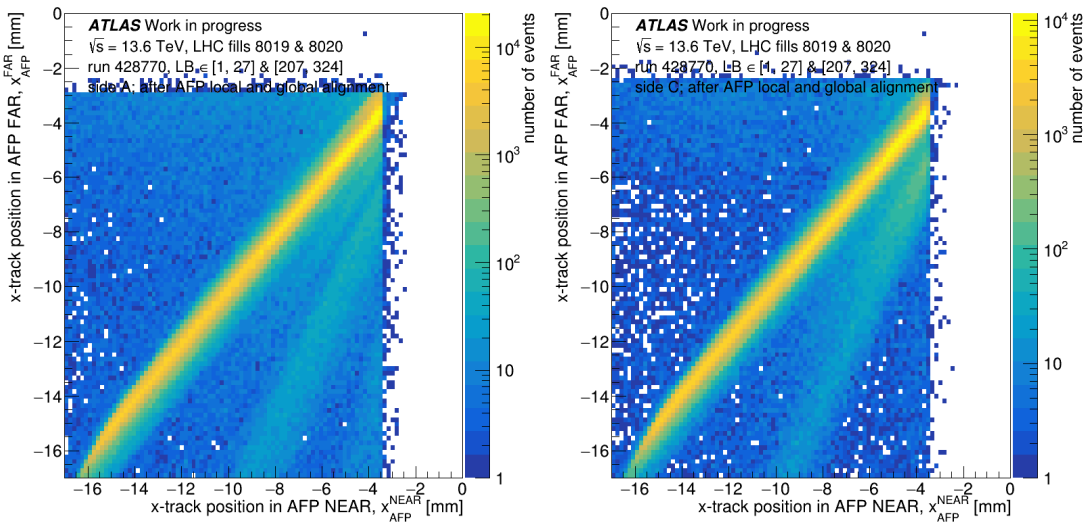

Figure 5.21: Correlation between x-position of the tracks reconstructed in AFP NEAR and FAR station on side A (**left**) and C (**right**) after considering corrections due to the local and global alignments.

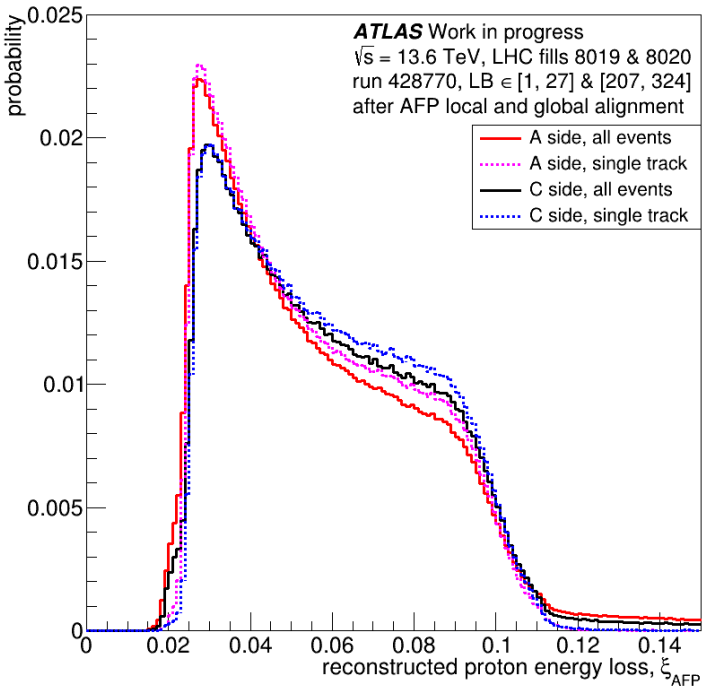

Figure 5.22: The reconstructed proton energy loss.

and FAR stations is presented in Fig. 5.23. As expected, these variables are strongly correlated. The "smearing" is due to the proton p_x momentum – *cf.* Sect. A.4.

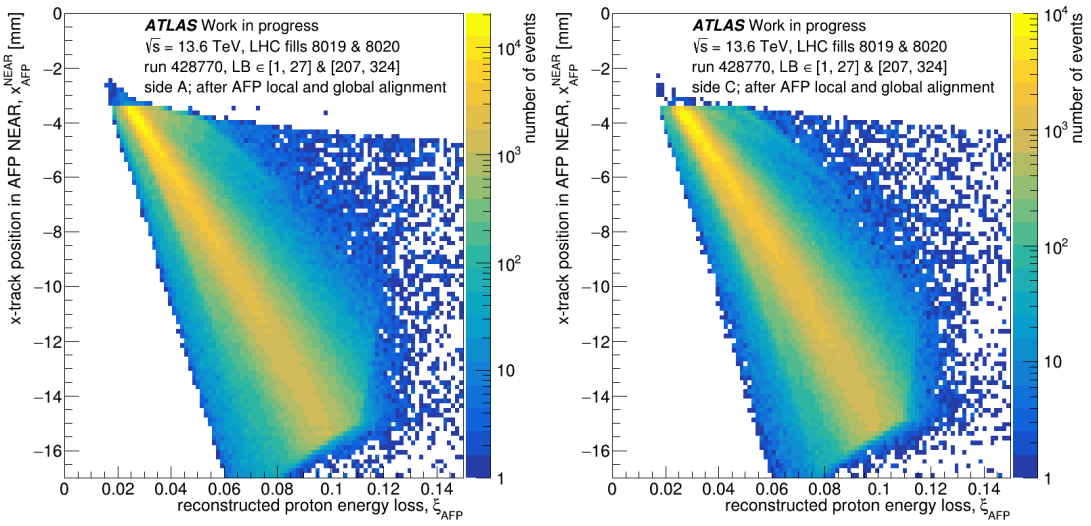

Figure 5.23: The correlation between x-position of the track reconstructed in the AFP NEAR station and the reconstructed proton energy loss. Side A is shown on **left** and side C on **right**. Corrections due to the local and global alignment were applied, and only events with exactly one track reconstructed in the NEAR and FAR stations on a given side were considered.

5.3 "Central" Objects

5.3.1 Tracks

Studies of the track reconstruction performance were based on the Monte Carlo sample. Below, only plots for the single diffractive jet production generated by Pythia 8 are shown, but the results are the same for other MC samples.

5.3.1.1 Reconstruction Efficiency

To investigate the track reconstruction efficiency, stable particles generated by Pythia 8, the so-called truth particles, were considered. In addition, the following requirements were implied:

- generated particle should have the charge of $q^{truth} = \pm 1$,
- be within the expected pseudorapidity range of the ATLAS tracker: $|\eta^{truth\ charged}| < 2.4$,

- the matching reconstructed track should be close to the position of the generated particle: $|\eta^{truth\ charged} - \eta^{reco}| < 0.02$ and $|\phi^{truth\ charged} - \phi^{reco}| < 0.02$.

The track reconstruction efficiency as a function of the charged particle transverse momentum is shown in Fig. 5.24 (left). The track reconstruction starts to be efficient at about 500 MeV, a typical value for a "standard" ATLAS reconstruction algorithm. In the future, for the data reprocessing, one should strongly consider employing a dedicated, so-called *low p_T tracking* algorithm.

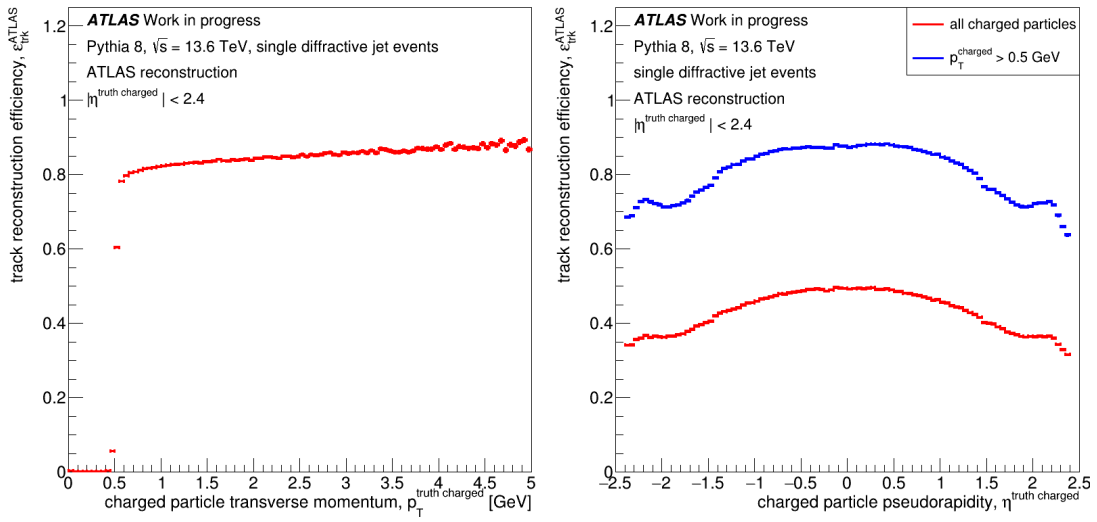

Figure 5.24: The ATLAS track reconstruction efficiency as a function of the charged particle transverse momentum (**left**) and pseudorapidity (**right**).

The reconstruction efficiency as a function of charged particle pseudorapidity is shown in Fig. 5.24 (right). Both p_T and η distributions have characteristic shapes expected to be observed in ATLAS – see [88].
It is interesting to check for any non-uniformities in the (p_T, η) and (η, ϕ) phase space. As can be seen in Fig. 5.25, the distributions are smooth. Small inefficiency region in $(\eta, \phi) \approx (2.5, -0.5)$ should not be problematic for the jet-gap-jet measurement.
Finally, a relation between the transverse momentum of the truth particle and the matched reconstructed track was studied. Figure 5.26 shows that these are indeed strongly correlated, as expected (*cf.* [88]).

5.3.1.2 MC-Data Comparison

The reconstructed MC tracks were compared to the experimental data. First, their spatial coordinates – pseudorapidity and azimuthal angle – were checked. In the experimental data case, two sets were considered: all recorded events (black

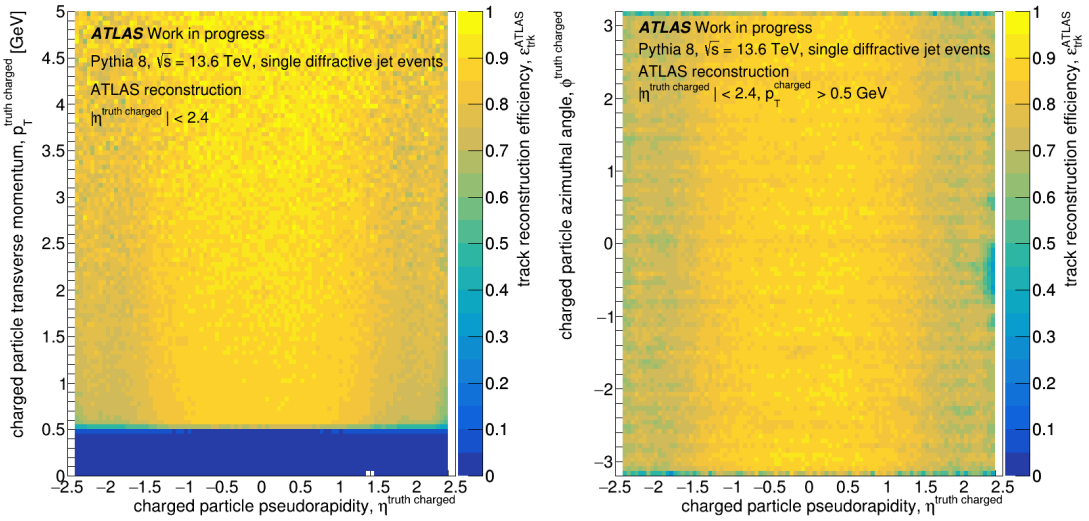

Figure 5.25: The ATLAS track reconstruction efficiency as a function of the charged particle pseudorapidity and: **left** – transverse momentum and **right** azimuthal angle.

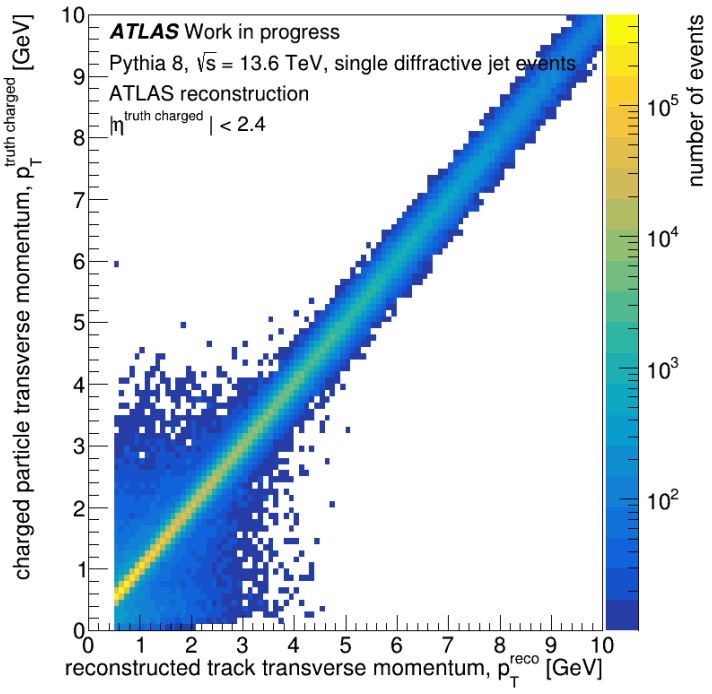

Figure 5.26: The correlation between the transverse momentum of the generated particle and that of the matched reconstructed track. See the text for the matching criteria.

points) and those triggered by the HLT_j20_L1MBTS_2 trigger (red points). As one can see from Fig. 5.27, MC very well describes the reconstructed data.

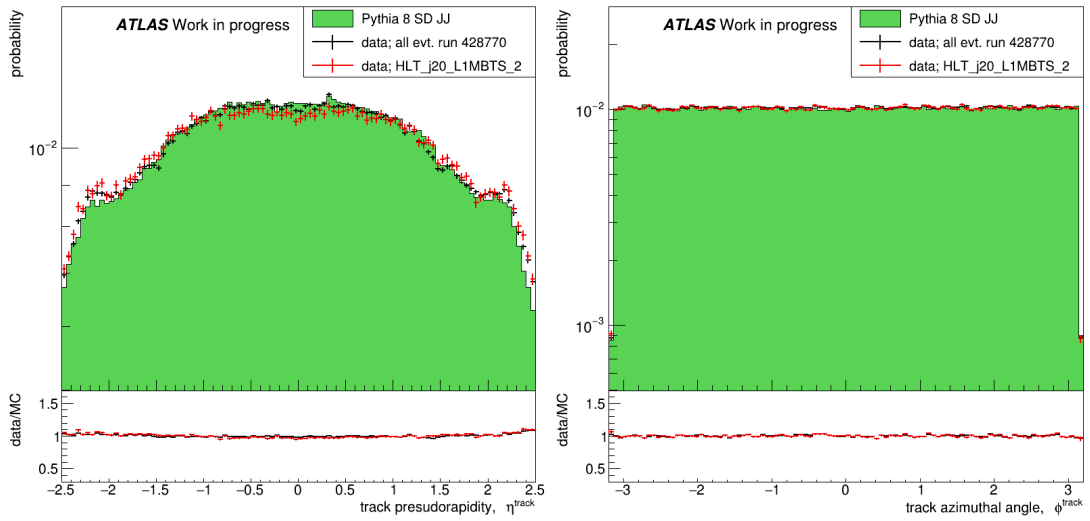

Figure 5.27: Comparison between the tracks reconstructed in MC and data samples: pseudorapidity (**right**) and azimuthal angle (**left**).

The reconstructed vertex position – see Fig. 5.28 – is also in agreement with the data. As usual in ATLAS, the z track position was corrected for its polar angle.

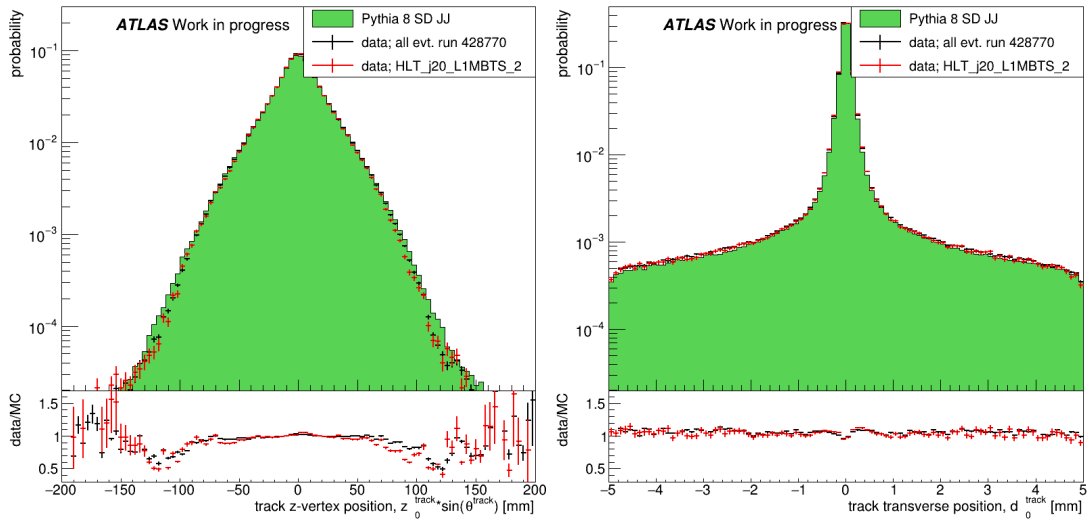

Figure 5.28: Comparison between the tracks reconstructed in MC and data samples: longitudinal (**right**) and transverse (**left**) vertex position.

A small discrepancy is visible in the track transverse momentum spectrum – see Fig. 5.29 (left). It gets more and more pronounced as the track momentum rises. Clearly, this may be the subject of the MC tuning, but it should not significantly affect the jet measurement. Finally, the fit quality is shown in Fig. 5.29 (right).

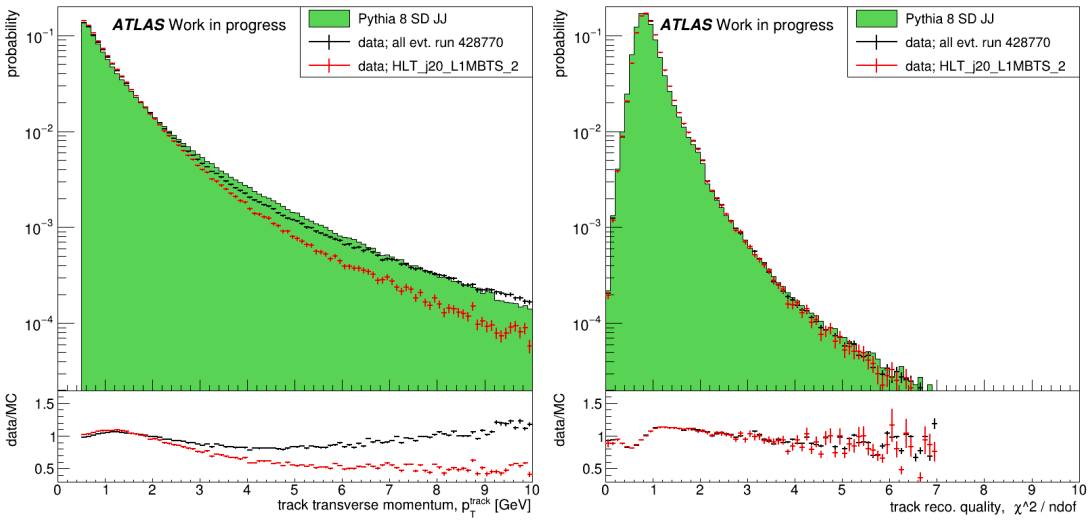

Figure 5.29: Comparison between the tracks reconstructed in MC and data samples: the transverse momentum (**right**) and the reconstruction quality (χ^2 divided by the number of degrees of freedom, **left**).

5.3.2 Vertex

The interaction vertex reconstruction in ATLAS begins with tracks reconstructed in the Inner Detector, utilizing signals from the Pixel, SCT and TRT sub-detectors within the pseudorapidity range $|\eta| < 2.5$. The tracks passing the quality requirements serve as inputs to the vertex reconstruction algorithms, which determine the spatial coordinates of the interaction point.

The vertex reconstruction proceeds through an iterative process comprising three principal stages: (i) the vertex finding through the track clustering in z, (ii) the vertex fitting to determine precise spatial coordinates and associated uncertainties and (iii) the vertex classification based on the topological and kinematic properties.

Several distinct categories of vertices are defined in ATLAS:

- **Primary Vertices (PriVtx):** represent the principal proton-proton interaction points where the hard-scatter interaction occurs. Primary vertices are identified through the analysis of the associated track multiplicities and $\sum p_T^2$ of the constituent tracks.
- **Pile-up Vertices (PileUpVtx):** Their reconstruction is particularly crucial for the high-luminosity operations where multiple interactions per bunch crossing are prevalent.
- **Secondary Vertices (SecVtx):** arise from the decays of long-lived particles at positions displaced from the primary interaction point. The reconstruction algorithm implements specialized criteria to identify them,

including requirements on the radial displacement and the track impact parameters.

- **Conversion Vertices (ConvVtx):** result from photon conversions to electron-positron pairs in the detector material. Their identification utilizes distinct topological signatures and the electromagnetic nature of the pair particles.
- **V0 Vertices (V0Vtx):** correspond to neutral hadron decays (K^0_S, Λ^0, *etc.*) and are characterized by two oppositely charged tracks forming a displaced vertex with specific invariant mass constraints.
- **Kink Vertices (KinkVtx):** are characterized by abrupt changes in track trajectory, typically associated with particle decays producing a single charged and neutral particles.

In the run 428770 dataset, only primary and pile-up vertices are present, as shown in Figure 5.30.

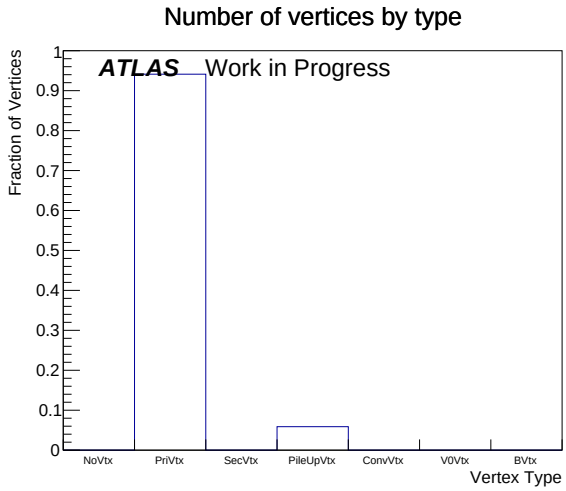

Figure 5.30: Types of the interaction vertices reconstructed in run 428770 dataset. See the text for details.

For run 428770, where the mean pile-up was set to 0.05, one would expect the probability of having more than 1 collision (*i.e.* vertex) of about 1.2‰. The trigger may disrupt this number since the stored events, usually containing high p_T objects, are expected to have a reconstructed vertex. One can also compare the expected ratio of the number of events with exactly 1 to the number of events with more than 1 vertex. For μ of 0.05, this ratio is about 40. Figure 5.30 suggests a factor of 20 – much more pile-up vertices are reconstructed than expected.
To investigate this effect, the correlation between primary and pile-up vertex positions, shown in Figure 5.31, was investigated. The plot reveals a clear diagonal

structure where the z position of the primary vertex is very close to the z position of the pile-up vertex. This suggests that in such events, with closely spaced interactions, the vertex reconstruction algorithm may artificially separate what should be a single vertex into two distinct vertices – a primary vertex and a pile-up one. This potential over-splitting of vertices necessitates a detailed study of the vertex reconstruction performance and may result in the need for the data reconstruction reprocessing.

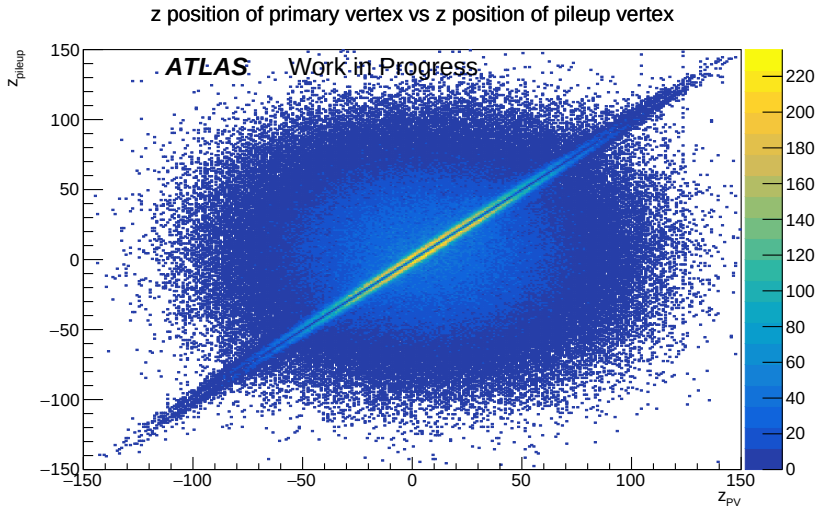

Figure 5.31: Relation between the longitudinal z-position of primary and pile-up vertices for cases when at least 1 pile-up vertex was reconstructed in the event.

The z-coordinate of the ATLAS beam spot is shown in Fig. 5.32. Four parametric models were tried to describe its shape adequately:

- Gaussian plus exponential function,
- double Gaussian function,
- Student's t-distribution,
- Crystal Ball function.

Analysis of the fit quality based on the $\chi^2/\texttt{ndf}$ established that both the double Gaussian and Crystal Ball functions provide the best description of the beam spot z-shape ($\chi^2/\texttt{ndf} = 5.08$ in both cases). These models demonstrated a superior description of the data compared to the Gaussian plus exponential ($\chi^2/\texttt{ndf} = 9.43$) and the Student's t-distribution ($\chi^2/\texttt{ndf} = 35.34$). Results of all fits, in both linear and logarithmic scales, are shown in Figure 5.32. The double Gaussian function was selected for a subsequent analysis based on its properties: an accurate data description and analytical tractability for random number generation.

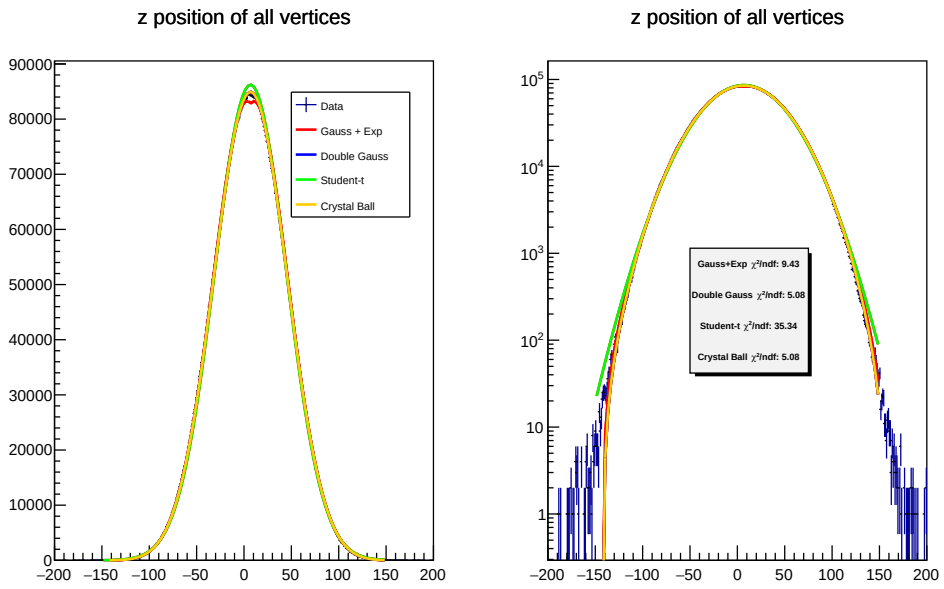

Figure 5.32: The ATLAS beam-spot: the longitudinal z-position of the reconstructed vertices. Various functions were fitted to obtain the analytical description of the beam spot distribution shape.

To investigate the vertex separation issue, a set of the z-positions was randomly generated according to the double Gaussian fit function. The expected distribution was then compared to the data – see Figure 5.33.
The distribution of the vertex-to-vertex distances (Δz) reveals distinct features requiring a detailed investigation. The experimental distribution is two-modal. It steeply falls toward zero for $\Delta z \lesssim 2$ mm, and it also decreases rapidly for $\Delta z \gtrsim 4$ mm and for $\Delta z \gtrsim 13$ mm flattens out. The generated distribution is approximately flat in the whole considered region.
The deficit at small Δz can be attributed to the vertex reconstruction algorithm's resolution limitations. When two vertices are separated by less than 2 mm, the algorithm is unable to distinguish them reliably as separate entities, leading to their reconstruction as a single vertex. This effect leads to a reduction of the observed number of vertex pairs at small separations.
The excess observed in the intermediate separation range (2-13 mm) represents a compensatory effect: a single vertex is artificially split in two (or more). This behaviour is consistent with the diagonal enhancement observed in Fig. 5.31.
To quantify these effects, the simulated distribution required normalization to the data in the high Δz region. The normalization region 10 mm $< \Delta z <$ 50 mm was selected based on three key criteria:

- sufficient separation from the resolution effects observed at low Δz,
- large enough statistics to minimise statistical uncertainties,

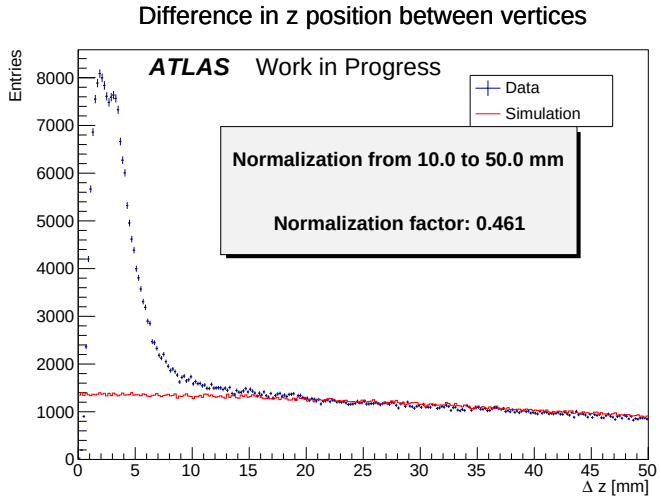

Figure 5.33: The difference between the z positions of the primary and pile-up vertices as seen in run 428770 (blue points) and as expected from the simulation (red line). The simulated events were normalized to the large-distance tail of the data. The huge excess in region 2–13 mm indicates issues with vertex reconstruction. The drop to 0 for the very small Δz values is expected due to a finite detector reconstruction resolution.

- avoidance of potential systematic effects at very large separations.

Based on these studies, the single vertex requirement intended to be used in the analysis cannot be too strict in order to preserve the signal. Judging from Fig. 5.33, the value of 13 mm is proposed to be used. The issue of artificial vertex splitting should be investigated and addressed in future data-reprocessing campaigns.

5.3.3 Calorimeter Clusters

The reconstruction of the calorimeter clusters in ATLAS uses the so-called topo-clustering algorithm, which processes signals from individual calorimeter cells. As detailed in the ATLAS documentation [89], the algorithm identifies the seed cells based on their signal significance, which is defined as:

$$\varsigma_{\text{cell}}^{\text{EM}} = \frac{E_{\text{cell}}^{\text{EM}}}{\sigma_{\text{noise, cell}}^{\text{EM}}}, \tag{5.11}$$

where $E_{\text{cell}}^{\text{EM}}$ is the energy deposited (reconstructed) in the calorimeter cell and $\sigma_{\text{noise, cell}}^{\text{EM}}$ is known[3] noise level of this cell.
The cluster formation implements a three-threshold approach with the following parameters:

$$|\varsigma_{\text{cell}}^{\text{EM}}| > S \text{ (primary seed threshold, S = 4)}, \tag{5.12}$$

[3]Measured during the test-beam experiments, *etc.*

$$|\varsigma_{\text{cell}}^{\text{EM}}| > N \text{ (growth control threshold, N = 2)}, \tag{5.13}$$

$$|\varsigma_{\text{cell}}^{\text{EM}}| > P \text{ (principal cell filter, P = 0)}. \tag{5.14}$$

A key feature of the topo-clustering algorithm is its treatment of the transition regions; see Section 2.2.3. Particularly, at $|\eta| \sim 0.8$–1.0, $|\eta| \sim 1.4$, and $|\eta| \sim 3.2$, the changes in the detector granularity affect the cluster formation. The algorithm also handles negative energy deposits, which play an important role in pile-up suppression through the statistical cancellation of out-of-time energy deposits.

5.3.3.1 Reconstruction Efficiency

Similarly to the track case, the cluster reconstruction efficiency was computed. For these studies, stable particles generated by Pythia 8 fulfilling the conditions listed above were considered:

- generated particle should have charge of $q^{truth} = 0$,
- be in the expected ATLAS calorimeter pseudorapidity: $|\eta^{truth\ neutral}| < 4.9$,
- matching reconstructed cluster should be close to position of generated neutral particle: $|\eta^{truth\ neutral} - \eta^{reco}| < 0.02$ and $|\phi^{truth\ neutral} - \phi^{reco}| < 0.02$.

Figure 5.34 (left) shows the cluster reconstruction efficiency as a function of the neutral particle energy. The turnover curve results in a plateau starting from around 50 MeV, but the overall reconstruction efficiency does not exceed 15%. Such a small efficiency will have to be considered in the gap reconstruction definition. The reconstruction efficiency as a function of neutral particle pseudorapidity is shown in Fig. 5.34 (right).
The two-dimensional (E, η) and (η, ϕ) dependencies are shown in Fig. 5.35 and the relation between the energy of the truth particle and the matched reconstructed calorimeter cluster is shown in Fig. 5.36.

5.3.3.2 MC-Data Comparison and Quality Criteria

First glance at the experimental (η, ϕ) distribution of clusters reveals the presence of "hot clusters" – see Fig. 5.37. This is not surprising and was studied in detail in *e.g.* Ref. [3].
Following the detailed studies from the mentioned reference, a few cleaning criteria were applied:

- rejection of high timestamps, to remove the out-of-time clusters; such clusters are due to the neighbouring bunch-crossing collisions (previous or next); $|cl_t| < 10$ ns was used; pictured in Fig. 5.38 (left),

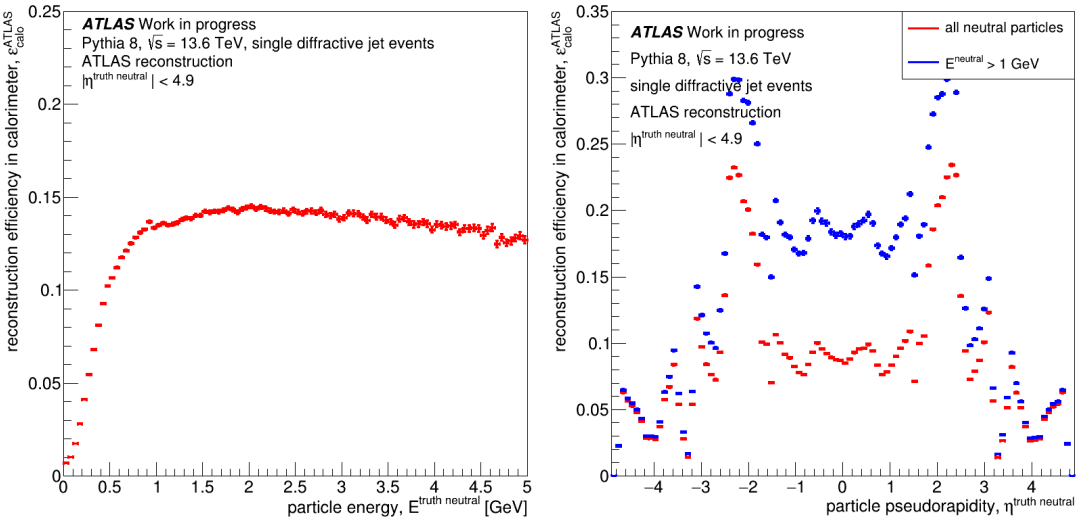

Figure 5.34: The cluster reconstruction efficiency as a function of the neutral particle energy (**left**) and pseudorapidity (**right**).

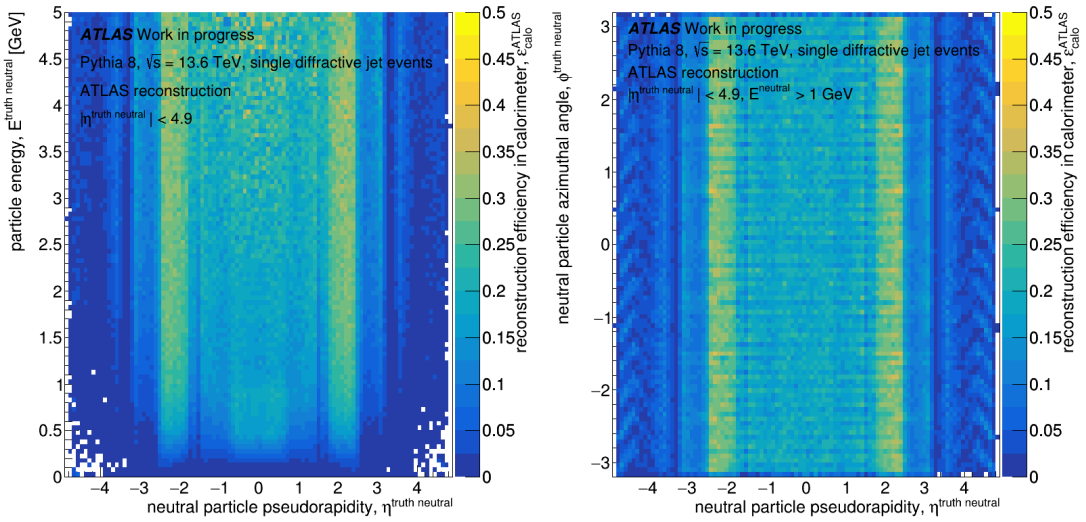

Figure 5.35: ATLAS track reconstruction efficiency as a function of the neutral particle pseudorapidity and: **left** – energy and **right** azimuthal angle.

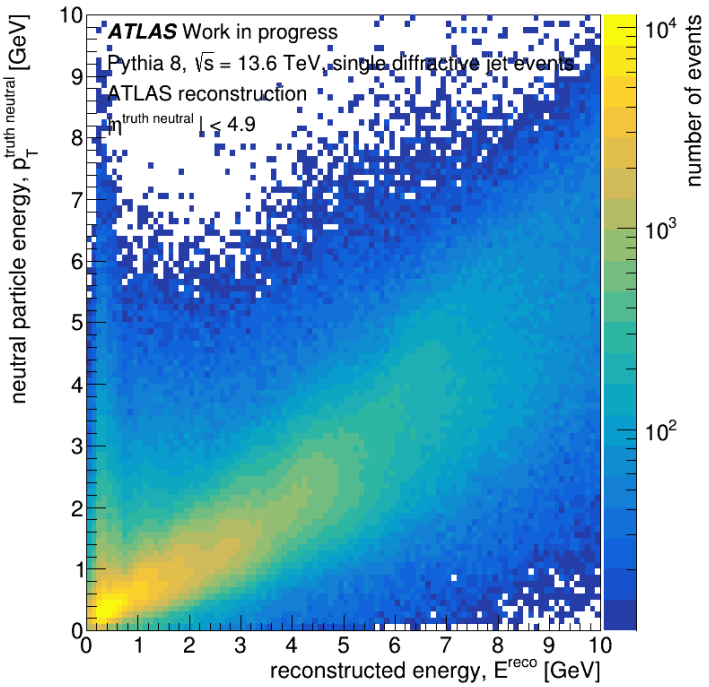

Figure 5.36: Correlation between the energy of the generated particle and corresponding reconstructed calorimeter cluster. See the text for the matching criteria.

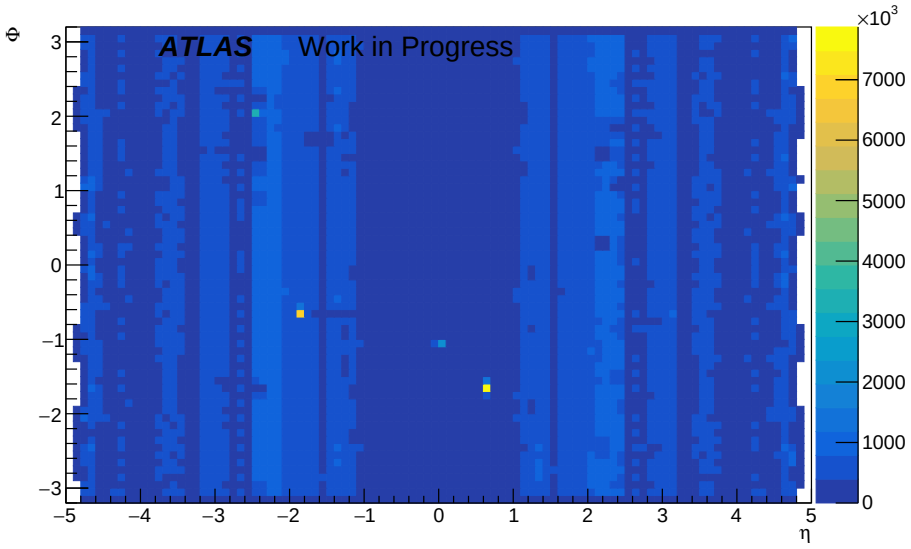

Figure 5.37: Experimental distribution of the calorimeter clusters in the (η,ϕ) plane, showing the detector acceptance patterns and occupancy variations. "Hot clusters" are visible.

- removal of clusters containing majority of energy in a single cell; $cl_{EngFracMax} < 0.8$,
- rejection of clusters with raw energy greater than 250 MeV; see Fig. 5.38 (right).

In addition, a few (η, ϕ) regions had to be excluded due to the presence of noisy cells. The (η, ϕ) map after the cleaning is shown in Fig. 5.39. The Monte Carlo (noiseless) sample is shown on the right, whereas the data distribution is on the left side of the plot.

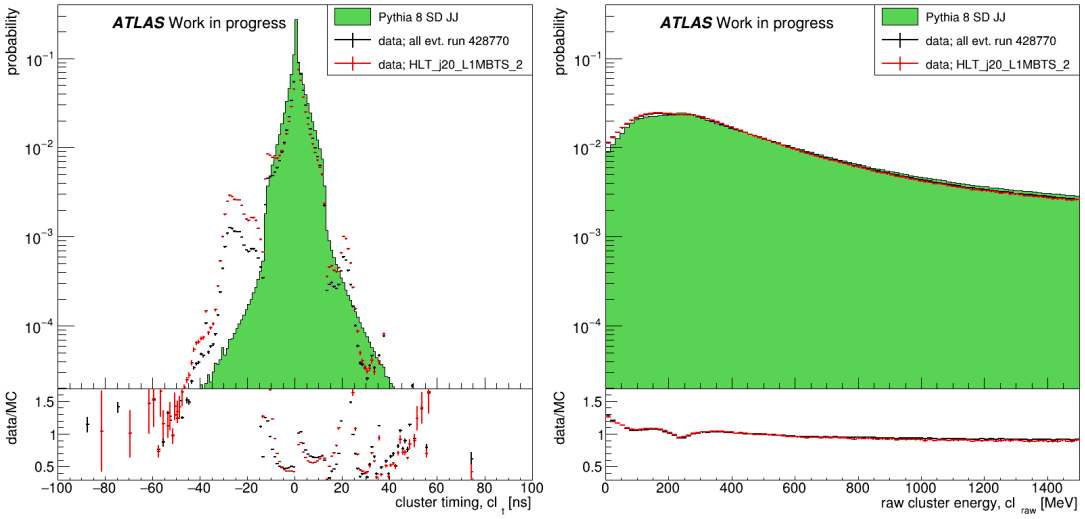

Figure 5.38: Distributions of the clusters timing (**left**) and the ear energy (**right**) for data (black and red points) and Pythia 8 SD JJ MC (green area).

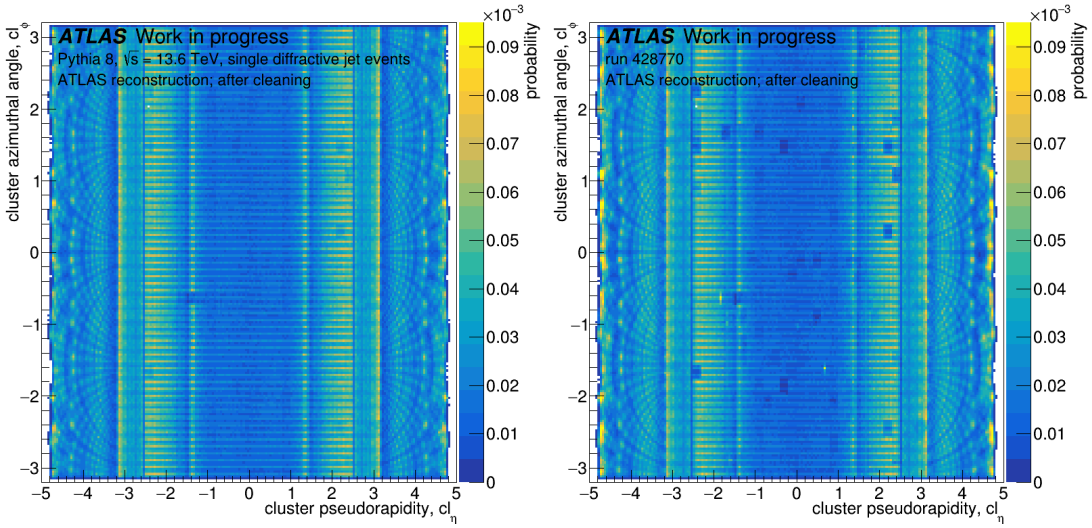

Figure 5.39: Distribution of calorimeter clusters in the (η, ϕ) plane after the cell cleaning (see text for details). Pythia 8 SD JJ MC is shown on the **right** side, whereas run 428770 data are on the **left**.

5.3.4 Jets

Jets used in this analysis are reconstructed using the anti-kt [76] algorithm with a radius parameter of $R = 0.4$ from either the calorimeter topological clusters or the combined tracker-calorimeter particle flow objects. The anti-kt algorithm iteratively merges input objects based on their relative distances in (η, ϕ) space. For the EMtopo jets, only the calorimeter signals that pass the noise thresholds provide inputs to the jet reconstruction. The particle flow reconstruction combines tracking and calorimeter measurements, with charged hadron tracks replacing their calorimeter deposits. This improves the low-p_T jet response compared to the calorimeter-only jets.
Due to special settings of the ATLAS calorimeter for the low-μ run resulting in *e.g.* changes of pedestals, a dedicated jet calibration was needed. However, before deriving the Jet Energy Scale (JES) corrections, a systematic jet quality selection has to be applied to ensure reliable inputs for the calibration.

5.3.4.1 Cleaning

The quality assessment of reconstructed jets implements the ATLAS JetCleaningTool framework with the *LooseBad* configuration level. The cleaning process evaluates the key jet quality variables, including:

- **EMFrac:** Electromagnetic energy fraction.
- **HECFrac:** Hadronic Endcap energy fraction.
- **LArQuality:** Quality factor of LAr calorimeter cells.
- **AverageLArQF:** Average quality factor of LAr cells.
- **HECQuality:** Quality factor of HEC calorimeter cells.
- **ChF:** Charged particle fraction derived from tracking.
- **Timing:** Jet timing information.

The "LooseBad" criteria are designed to remove the jets arising from non-collision backgrounds or calorimeter noise. They reject the jets with the following conditions:

- EMFrac < 0.05 and ChF < 0.05 for $|\eta| < 2$,
- EMFrac < 0.05 for $|\eta| \geq 2$,
- Maximum energy fraction > 0.99 for $|\eta| < 2$,

- EMFrac > 0.95 with $|\text{LArQuality}| > 0.8$ for $|\eta| < 2.8$,
- HECFrac > 0.5 with $|\text{HECQuality}| > 0.5$ and AverageLArQF > 0.8.

This selection is supplemented by a timing requirement ensuring that the jets coincide with the nominal bunch crossing within $|\Delta t| \leq 12.5$ ns.
In addition, the jets categorized as "ugly" are excluded from the selection process to maintain the purity of the final jet population. Such jets correspond to the real energy depositions in regions where the energy measurement is not accurate, *e.g.* the transition region between barrel and end-cap and problematic calorimeter regions.
The impact of the "good jet" event selection is shown in Fig. 5.40 (left), where the jet multiplicity is plotted. The black points are for all events recorded in physics_main stream in run 428770. The red points represent di-jet events passing GRL (see Sect. 3.3.5) and fulfilling trigger criteria:

- HLT_j20_L1MBTS_2 for events with leading jet transverse momentum $30 < p_T^{J1} < 55$ GeV,
- HLT_j20_L1J2 for $p_T^{J1} > 55$ GeV.

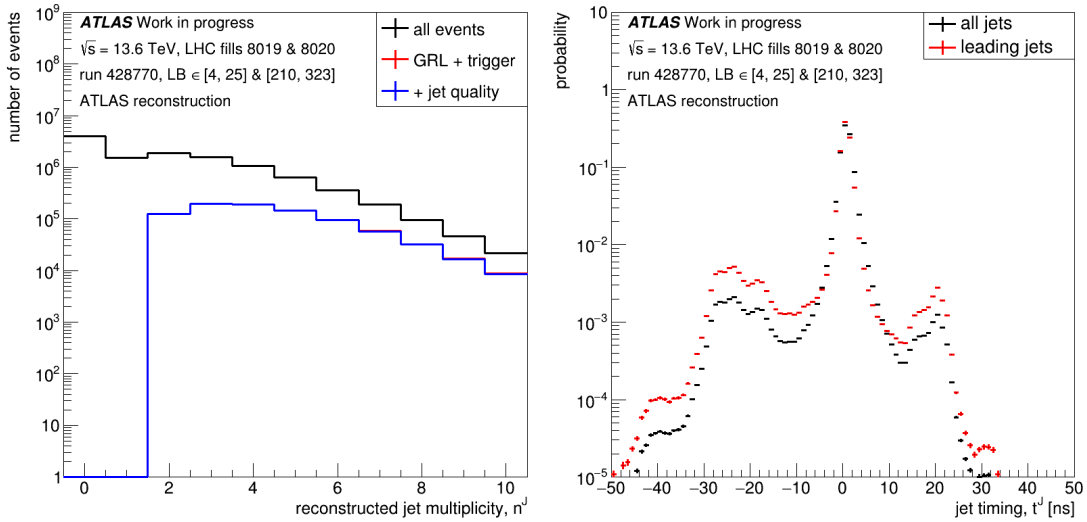

Figure 5.40: **Left:** the jet multiplicity distribution for: all events (black line), events passing Good Run List and the trigger requirements (red) and, additionally, passing the cleaning criteria (blue). **Right:** the distribution of the jet timing.

Blue points show events after additional requirement of jets being of good quality. As one can see, these quality criteria remove a relatively small percentage of events. Still, their usage is very important for the proper jet calibration [90].
An example of one of the jet quality criteria – the jet timing – is shown in Fig. 5.40 (right). The majority of events are in-time with the collision, but a few ‰

tails around ±1 bunch crossing (25 ns) are present. The timing requirement effectively suppresses the out-of-time backgrounds while maintaining high efficiency for genuine hadronic jets from collision events. The "LooseBad" requirement provides optimal performance characteristics, ensuring a balance between background rejection and signal retention.

Figures 5.41 present the fundamental kinematic distributions before and after the mentioned trigger and quality selection application. The transverse momentum spectrum is due to "dual" trigger selection – events with $p_T > 55$ GeV were unprescaled, whereas the ones with smaller p_T had a prescale of 25 at L1. The pseudorapidity distributions demonstrate a uniform cleaning efficiency across the central detector region $|\eta| < 2.5$, with slightly enhanced impact in the forward regions. The azimuthal angle distributions, not shown in this thesis, maintain their expected uniformity post-selection, confirming the absence of geometrical biases in the cleaning procedure.

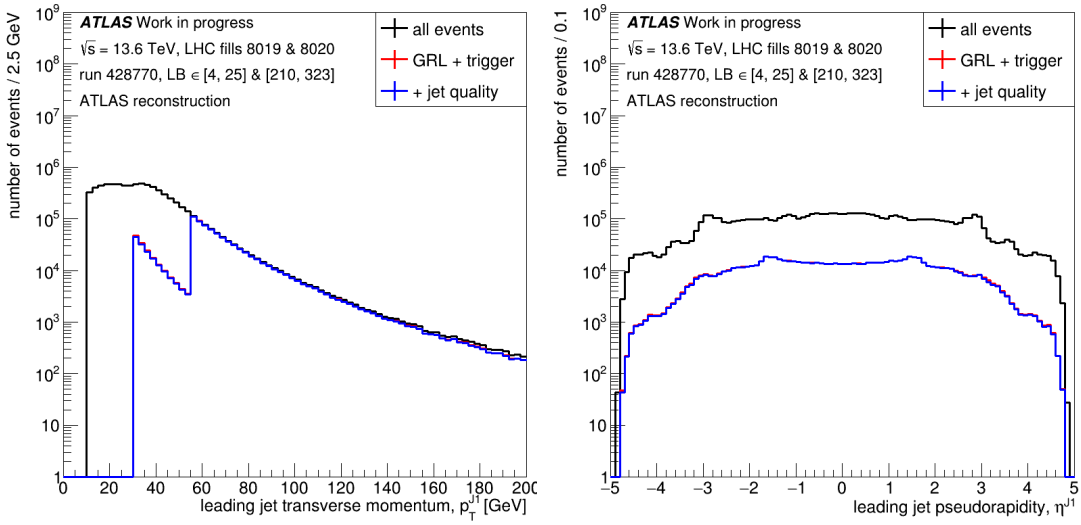

Figure 5.41: Kinematic distributions of the leading jets for: all events (black line), events passing Good Run List and trigger (red) and, additionally, passing the cleaning criteria (blue). **Left:** the jet transverse momentum distribution, **right:** the pseudorapidity. Note that only a few events do not pass the quality criteria, thus, the red line usually coincides with the blue one.

This cleaning process ensures that the jet calibration is derived using only well-measured jets with reliable calorimeter signals while maintaining high efficiency for real jets originating from the hard-scattering interaction.

5.3.4.2 Calibration

The reconstruction process introduces systematic deviations between the measured and particle-level jet properties due to the detector effects. These arise from the calorimeter non-compensation, dead material losses, shower leakage,

noise thresholds and out-of-cone radiation. The magnitude of these effects varies significantly with jet p_T and η, necessitating a precise calibration to establish the jet energy scale.

The standard ATLAS jet calibration, provided by the Jet/ETmiss Performance Group, addresses these effects for nominal high pile-up conditions ($\mu \approx$ 30-60). However, the AFP diffractive data were collected in run 428770 at $\mu = 0.05$ with modified calorimeter settings optimized for the low pile-up running. This necessitates a dedicated calibration procedure accounting for the specific detector response under these conditions.

The jet calibration is quite a complex procedure, encompassing several steps as shown in Fig. 5.42. The calibration methodology begins with the truth-to-reconstruction matching in the Monte Carlo simulation applying the following criteria:

- spatial matching within $\Delta R < 0.3$ between the reconstructed and truth jets,
- isolation requirement: the jet has to be separated by $\Delta R > 0.6$ from other reconstructed jets with $p_T > 7$ GeV,
- truth jet isolation: the truth jets have to be separated by $\Delta R > 1.0$.

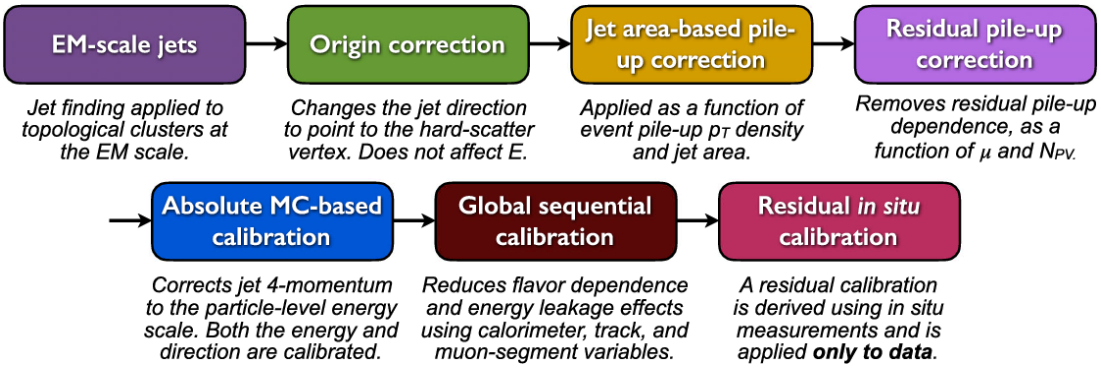

Figure 5.42: Scheme of the ATLAS jet calibration procedure. From [91].

Jet Energy Scale The jet response, defined as $R = p_{Treco}/p_{Ttrue}$, quantifies the detector effects requiring correction. First, the pseudorapidity dependence is investigated – see Fig. 5.43. The η-dependent response exhibits pronounced variations across different p_T ranges, with maxima at $|\eta| \sim 1.5$ and $|\eta| \sim 3.0$ corresponding to the calorimeter transition regions. Very low-p_T jets (10–20 GeV) show response variations between 1.1 and 1.4, while higher-p_T jets (above 60 GeV) demonstrate a more stable response at around 1.0–1.1. The p_T-dependent

response reveals a characteristic non-linearity below 30 GeV, particularly pronounced in the forward regions. The central jets show smoother p_T dependence, while the forward ones exhibit enhanced response variations from material and containment effects. These distributions establish the baseline for deriving the p_T and η-dependent calibration factors.

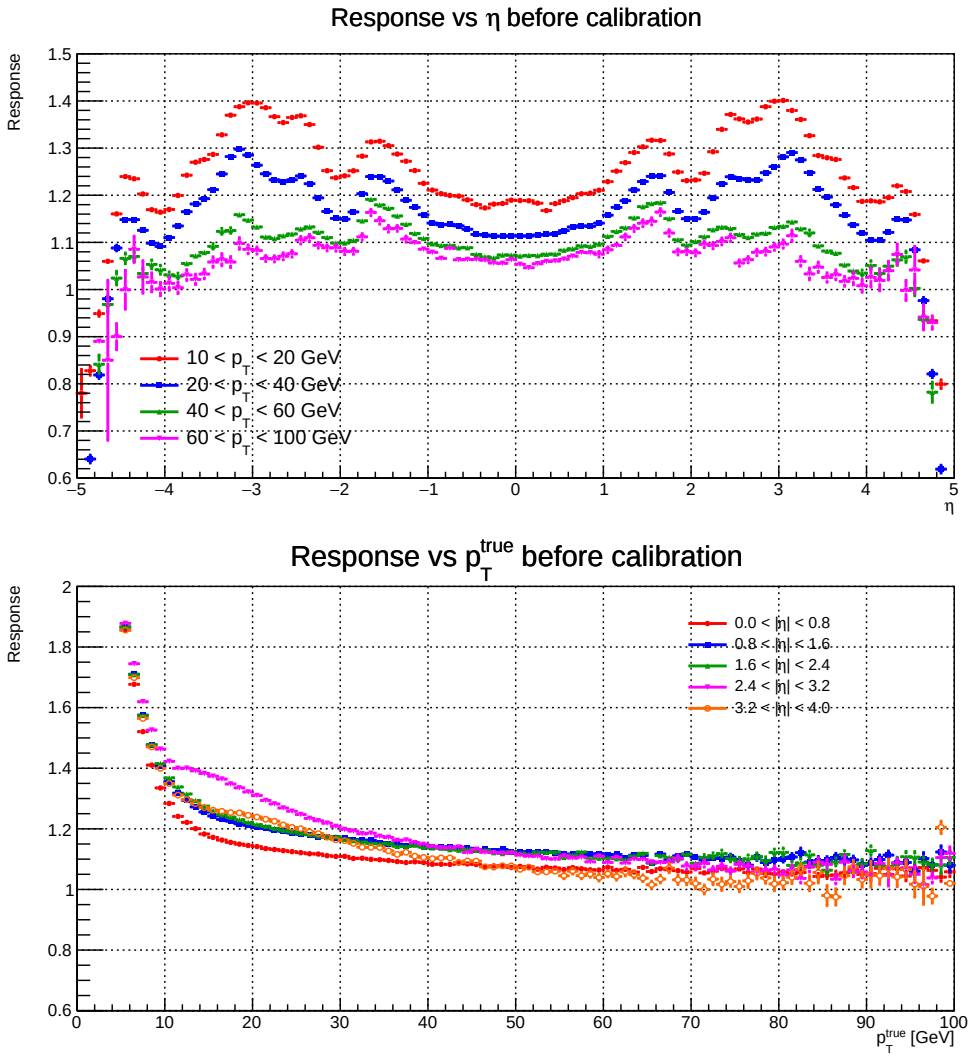

Figure 5.43: The et response as a function of its pseudorapidity (**top**) and transverse momentum (**bottom**).

The next step is the determination of the correction as a function of jet pseudorapidity. It is calculated using the matched MC truth and reconstructed jets and shown in Fig. 5.44. The shape is similar for all considered p_T ranges, but for lower p_T jets corrections in the transition regions, ± 0.02 near $|\eta| \sim 1.5$ and $|\eta| \sim 3.0$, are relatively higher. The η-dependent correction addresses response variations in calorimeter transition regions like the systematic shift between reconstructed and truth jet pseudorapidity.

Having the pseudorapidity correction, the correlation between the reconstructed

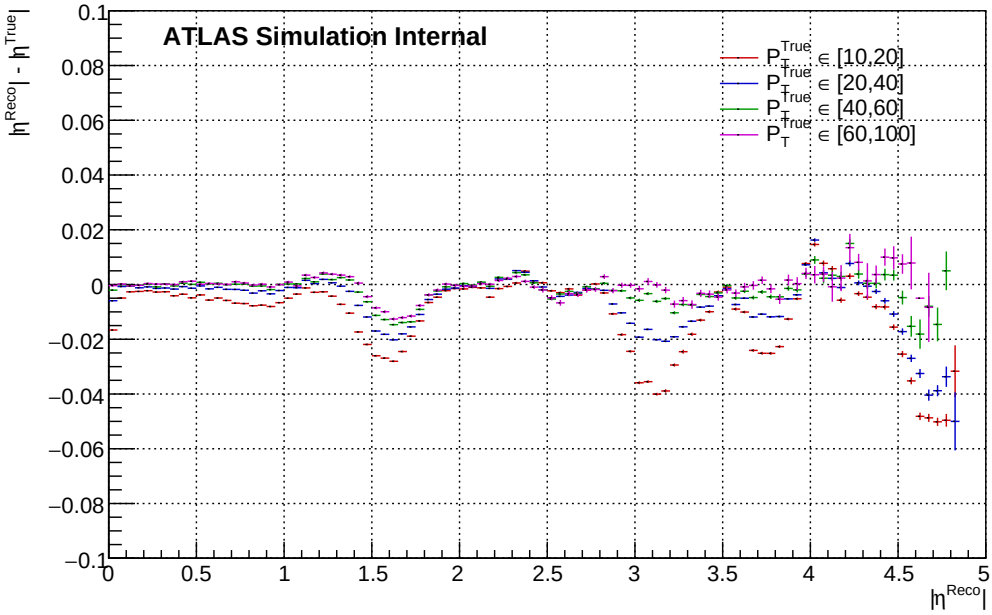

Figure 5.44: The difference between the reconstructed and truth jet pseudorapidity for various p_T ranges.

and truth jet transverse momenta can be investigated for various pseudorapidity ranges. For each such range, the relationship is parametrized using a function that captures both the linear response and low-p_T non-linearities:

$$\tilde{p}_T^{\text{reco}} = A \times p_T^{\text{true}} + B + \frac{C}{p_T^{\text{true}}}, \tag{5.15}$$

where A represents the linear response coefficient, B accounts for the reconstruction offsets and C characterizes the low-p_T non-linearity.

As an example, the transverse momentum correlation with fitted parametrization for the pseudorapidity region ($|\eta| < 0.4$) is shown in Figure 5.45. The fit parameters obtained for all considered pseudorapidity regions are listed in Table 5.12.

The calibration factor, c_{JES}, is derived as the inverse of the parametrized response:

$$p_T^{\text{corr}} = c_{\text{JES}}(p_T^{\text{reco}}, \eta^{\text{reco}}) \times p_T^{\text{reco}}, \tag{5.16}$$

$$\eta^{\text{corr}} = \eta^{\text{reco}} + \Delta\eta. \tag{5.17}$$

The calibrated response after these corrections demonstrates significant improvement in uniformity across phase space, as shown in Fig. 5.46. Residual variations in η are contained within $\pm 3\%$ for all p_T ranges. The p_T-dependent response shows a deviation from unity below 2% for $p_T > 10$ GeV across the entire η

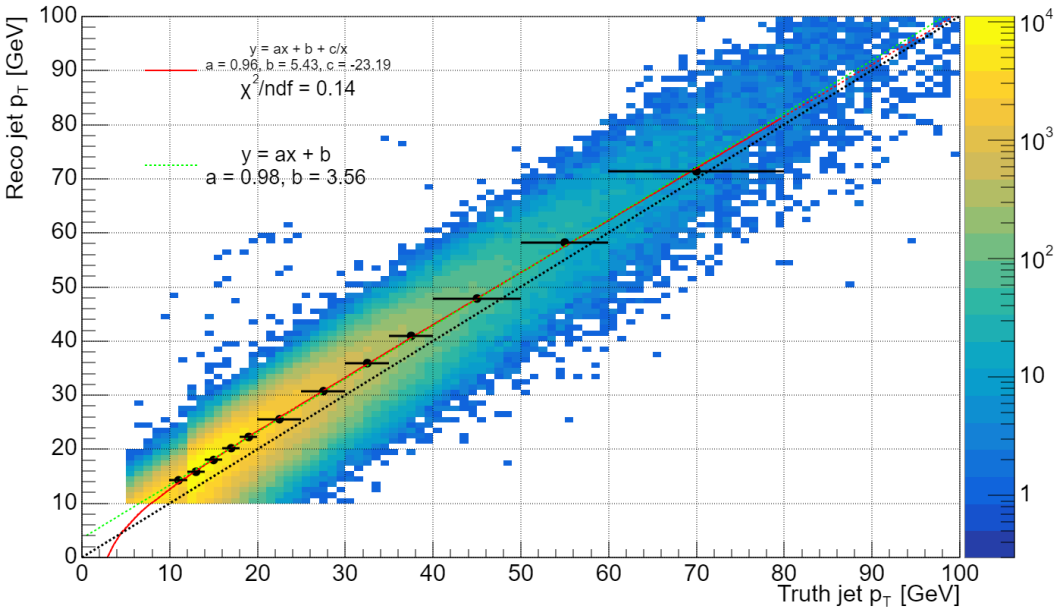

Figure 5.45: Correlation between the reconstructed and truth jet p_T for $0.0 < |\eta| < 0.4$. The black points show the mean reconstructed p_T in the truth p_T bins. The red curve shows the fitted response function used for the JES calibration derivation above 15 GeV. The green dashed line indicates an alternate linear parametrization.

Table 5.12: Fit parameters obtained for different η regions.

η Range	A	B	C
0.0–0.4	0.955166	5.42711	-23.1852
0.4–0.8	0.964382	5.70485	-26.7876
0.8–1.2	0.976892	6.11253	-29.4645
1.2–1.6	1.00279	7.48785	-39.2368
1.6–2.0	0.9886	6.86141	-31.9317
2.0–2.4	0.959046	7.39692	-31.7339
2.4–2.8	0.887591	11.3627	-51.6818
2.8–3.2	0.893779	11.6042	-53.1509
3.2–3.6	0.833215	14.0556	-87.7993
3.6–4.0	0.80902	12.7637	-91.944

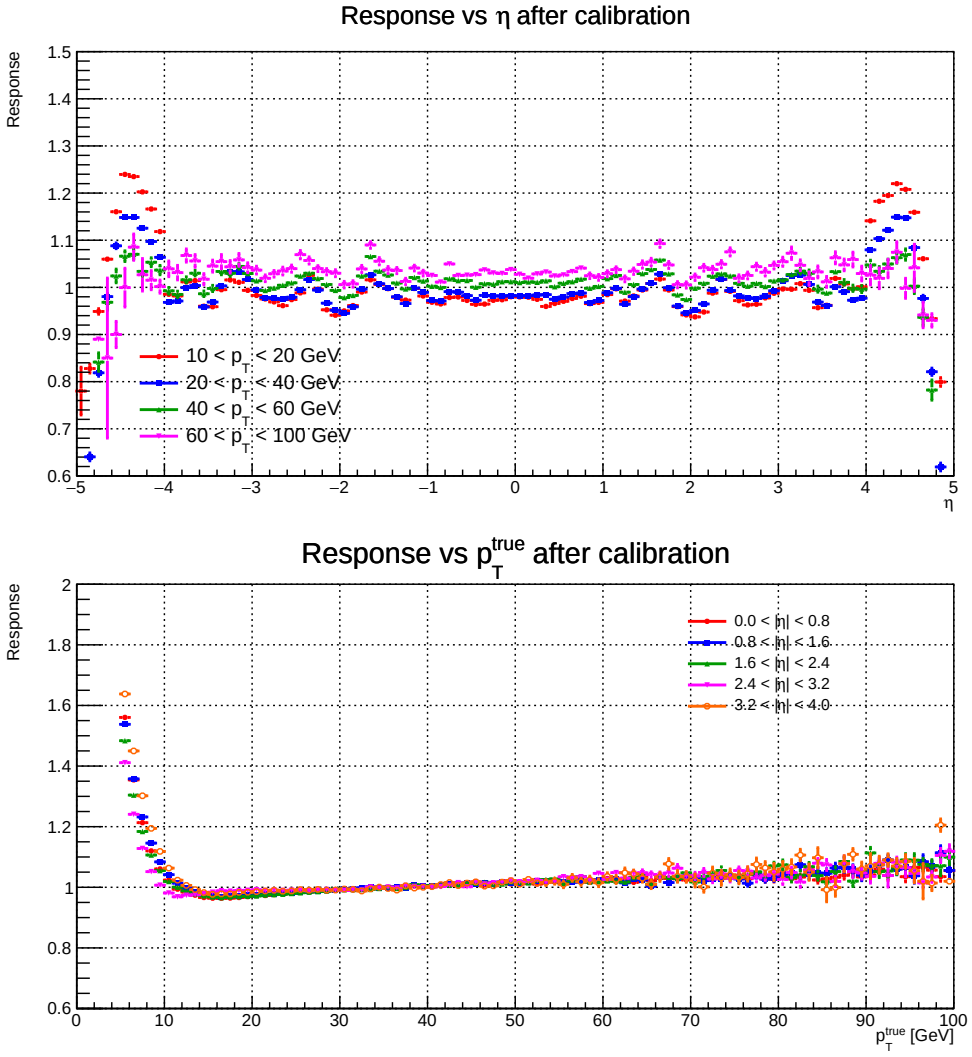

Figure 5.46: The calibrated jet response as a function of the jet pseudorapidity (**top**) and transverse momentum (**bottom**).

acceptance, with the largest residual non-uniformity in the forward regions, for $|\eta| > 3.2$.

Jet Energy Resolution The Jet Energy Resolution (JER) quantifies the detector's ability to measure the jet energies and is essential for understanding and mitigating resolution effects in physics analyses. In this study, the JER is determined using the di-jet asymmetry method. This asymmetry, A, is defined as:

$$A = \frac{p_T^{\text{probe}} - p_T^{\text{ref}}}{p_T^{\text{avg}}}, \tag{5.18}$$

where p_T^{probe} and p_T^{ref} are the transverse momenta of the probe and reference jets, respectively. The p_T^{avg} is their arithmetic mean:

$$p_T^{\text{avg}} = \frac{p_T^{\text{probe}} + p_T^{\text{ref}}}{2}. \tag{5.19}$$

The standard deviation of the asymmetry distribution, σ_A, is used to derive the relative resolution in different pseudorapidity regions. For jets in the reference region, defined as $|\eta| < 0.8$, the relative resolution is given by:

$$\frac{\sigma_{p_T}^{\text{ref}}}{p_T^{\text{ref}}} = \frac{\sigma_A^{\text{ref}}}{\sqrt{2}}. \tag{5.20}$$

For jets in the probe region, $|\eta| > 0.8$, the relative resolution is determined as:

$$\frac{\sigma_{p_T}^{\text{probe}}}{p_T^{\text{probe}}} = \sqrt{\left(\sigma_A^{\text{probe}}\right)^2 - \left(\frac{\sigma_A^{\text{ref}}}{\sqrt{2}}\right)^2}. \tag{5.21}$$

The di-jet asymmetry method assumes a minimal contribution from additional jets, ensuring the p_T balance between the two leading jets is preserved. To select events with the "di-jet topology", the following criteria are applied:

- the azimuthal angle between the two leading jets satisfies $\Delta\phi(j_1, j_2) > 2.5$ radians,
- the transverse momentum of the third jet, if present, is constrained to $p_T^{\text{jet3}} < 0.4 \times p_T^{\text{avg}}$,
- the transverse momentum of each considered jet is greater than 20 GeV.

These criteria ensure a clean di-jet sample with a minimal contamination from multi-jet events or mismeasured jets.
The measured di-jet asymmetry, σ_A^{Reco}, includes contributions from the detector and intrinsic physics effects. To isolate the detector resolution, the true asymmetry, σ_A^{True}, is determined from the Monte Carlo simulation:

$$\sigma_A^{\text{Det}} = \sqrt{\left(\sigma_A^{\text{Reco}}\right)^2 - \left(\sigma_A^{\text{True}}\right)^2}. \tag{5.22}$$

The corrected σ_A^{Det} is then used to derive the JER. The resolution as a function of average di-jet transverse momentum is shown in Fig. 5.47. The red points are for the "ideal" resolution obtained using the truth jets. The colour bands represent the fit uncertainty. The black and blue points mark the jet resolution obtained for data and MC sample, correspondingly.

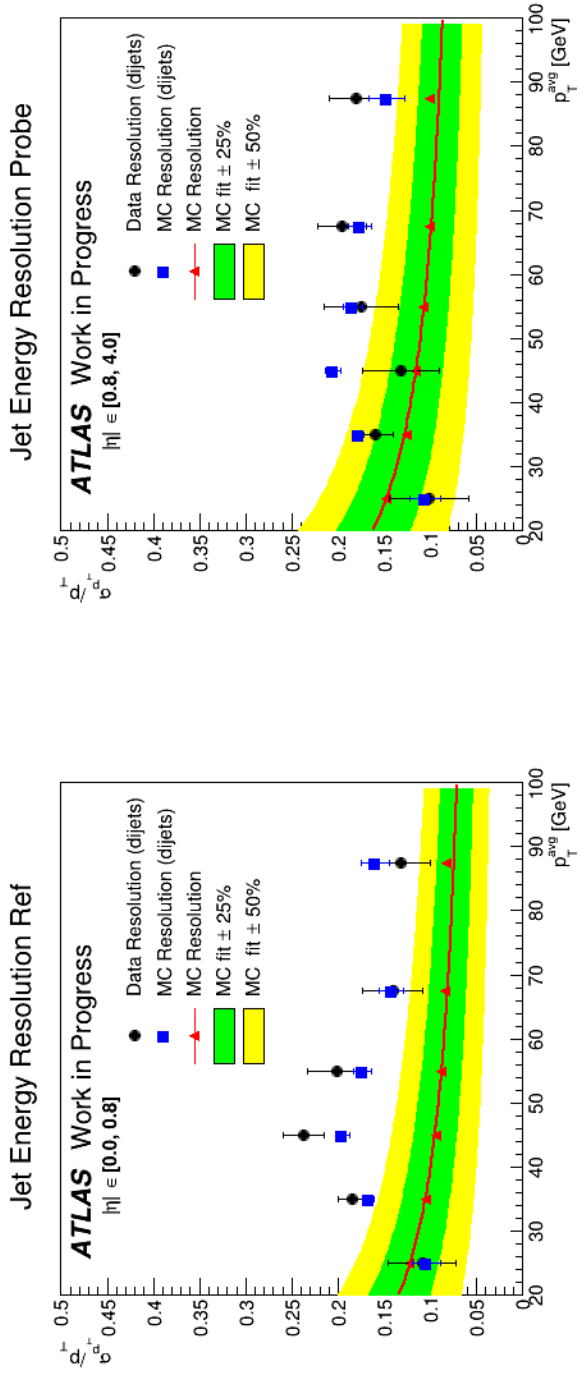

Figure 5.47: The Jet Energy Resolution for the low-μ run 428770. The red points are for the "ideal" resolution obtained using the truth jets. The colour bands represent the fit uncertainty. The black and blue points show the jet resolution obtained for data and MC sample, correspondingly.

Chapter 6

Data Analysis

In this chapter, the search for the diffractive jet-gap-jet production will be discussed. At first, the search for the non-diffractive jet-gap-get events is described, including the "experimental" gap definition. Next, the identification of the single diffractive events is given. Finally, the search for the single diffractive jet-gap-jet candidates is presented.

6.1 Search of the Non-Diffractive Jet-Gap-Jet Events

As discussed in the introductory chapter, jet-gap-jet events differ from the non-diffractive jet production ones by the presence of a rapidity gap between the jets. The first step is, therefore, gap identification.

6.1.1 Monte Carlo Studies

As mentioned in Section 1.4.3, a gap may appear due to fluctuations in non-diffractive jet events. This can be evaluated using the Pythia 8 non-diffractive jet sample. Since the data are expected to be efficiently triggered by events containing at least one jet with p_T of 30 GeV, *cf.* Sect. 5.1.2, the reconstructed leading jet was requested to have at least such transverse momentum. To consider the jet reconstruction efficiency and effects connected to the energy calibration, the sub-leading jet was requested to have $p_T > 20$ GeV. Since the gap is expected to occur between the jets and the analysis intends to use the ATLAS tracker, two leading jets were requested to be distant in pseudorapidity, $|\eta^{J1}| > 1.5$ and $|\eta^{J2}| > 1.5$, and belong the opposite hemispheres: $\eta^{J1} \times \eta^{J2} < 0$.
Figure 6.1 shows the probability distribution of the appearance of events with a gap defined as a space in rapidity between:

1. particle generated in the negative pseudorapidity hemisphere, closest to $\eta = 0$ and

2. particle closest to $\eta = 0$ belonging to the positive hemisphere.

The black line shows such distance – the gap – considering all generated, stable particles. As one can see, the distribution is steeply falling – the situation when the gap between particles is greater than 1 rapidity unit occurs in less than 1‰ of cases. Unfortunately, such a gap would be reconstructed only by the "ideal" detector. If only charged particles are considered (red line), the average gap size is slightly larger – the "below 1‰-fluctuation-chance" would require asking for distances of at least 1.5 rapidity unit. The situation when only particles with p_T of at least 250 MeV are considered (blue line) does not considerably change the picture. Unfortunately, "relaxing" the reconstruction request to p_T of at least 500 MeV results in a "random" gap probability of a few permille even for the gap size of 2 (magenta line). This shows the importance of having the low-p_T tracking present in the event reconstruction. Unfortunately, as discussed in Section 5.3.1.1, this is not the case for the currently available data samples, where only tracks with at least 0.5 GeV are effectively reconstructed.

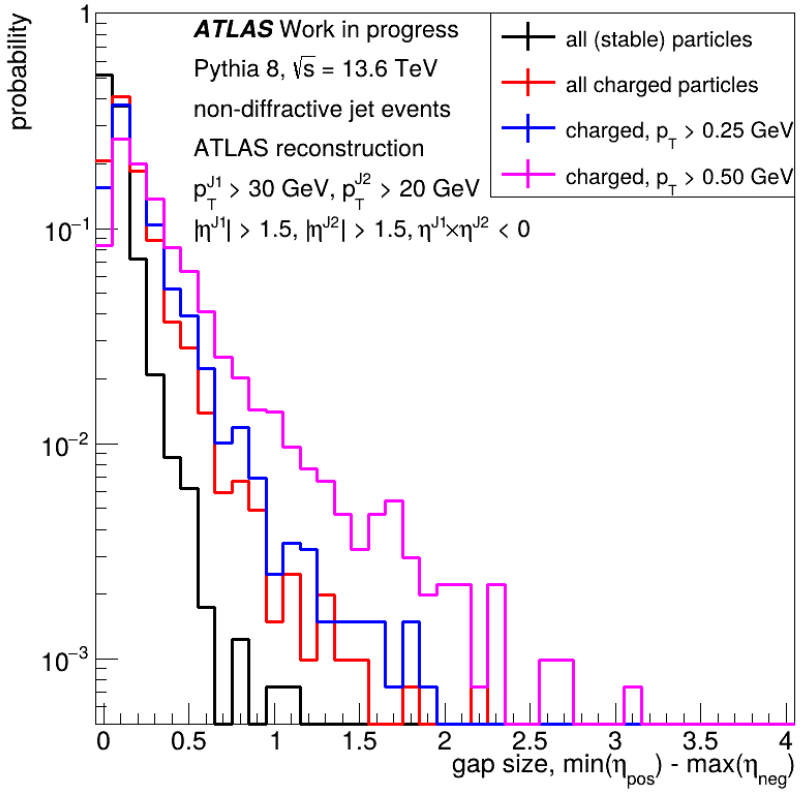

Figure 6.1: Properties of the non-diffractive jet sample: the gap size from fluctuations. The black line represents the "true" gap – reconstructed from all generated, stable particles. The red line is for a gap when only charged particles are considered. Blue and magenta lines show situations when the charged particles should have transverse momentum of at least 250 and 500 MeV/c, respectively.

The number of particles present in a given pseudorapidity region is shown in Fig. 6.2 (left). The chance to have a few particles is smaller than one permille for the pseudorapidity region of 2 units (blue line). Unfortunately, the situation gets

"worse" when the detector is not ideal (*cf.* Fig. 6.2 right) – in the case that only particles with $p_T > 0.5$ GeV are considered (magenta line), a chance of the multiplicity equal to 0 is around 4‰. This results in a non-reducible background for the jet-gap-jet events.

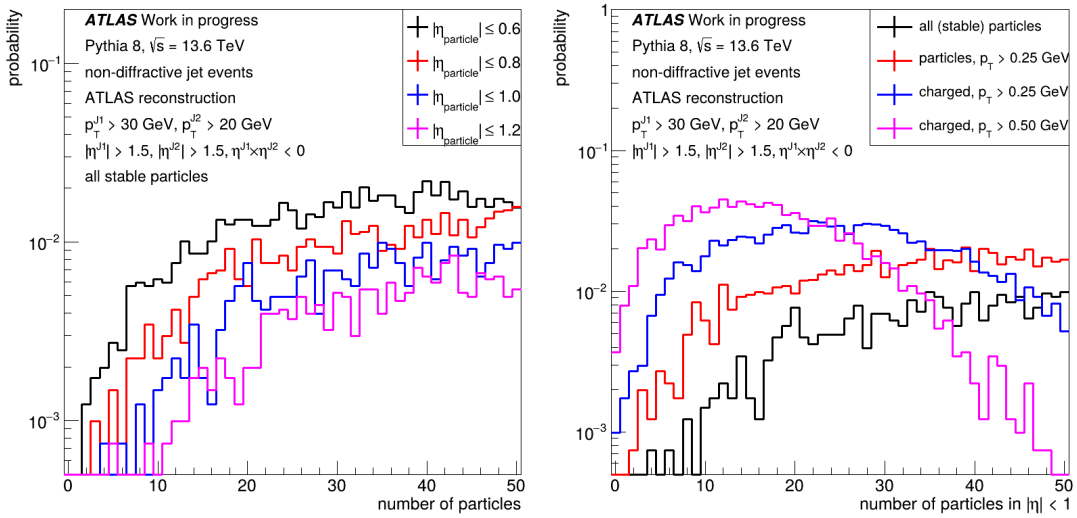

Figure 6.2: **Right:** the number of particles present within a certain pseudorapidity region.**Left:** the number of particles in $|\eta| < 1$.

So far, only the truth particles were considered. Experimentally, the gap can be defined as a pseudorapidity region devoid of the charged particle tracks. Switching to tracks requires using the reconstruction algorithms, which may be prone to the detector effects. The comparison of the gap size reconstructed using the truth charged particles with $p_T > 0.5$ GeV to a gap obtained with reconstructed tracks is shown in Fig. 6.3. In the majority of cases, the gaps are of the same size. Sometimes the "track gap" is larger than the "true gap" – this is expected due to the track reconstruction inefficiency.
The cases when the "true gap" is smaller are due to fake tracks. Such a situation should be avoided since it may reduce the jet-gap-jet signal. Dedicated performance studies, resulting in the "analysis-tailored" quality criteria, were performed to address this issue. The goal was to reduce the fake rate while keeping the maximum number of "good tracks". For this reason, two classes of events were identified:

- **matched**: the reconstructed track matching the "truth" particle in its vicinity defined as $|\eta^{track} - \eta^{truth}| < 0.05$ and $|\varphi^{track} - \varphi^{truth}| < 0.05$,
- **not matched** if no truth particle was present in the particle vicinity.

In addition, the *matched* tracks were required to have no other truth particle within $|\eta^{track} - \eta^{truth}| < 0.1$ and $|\varphi^{track} - \varphi^{truth}| < 0.1$. Such tracks were named **matched isolated**.

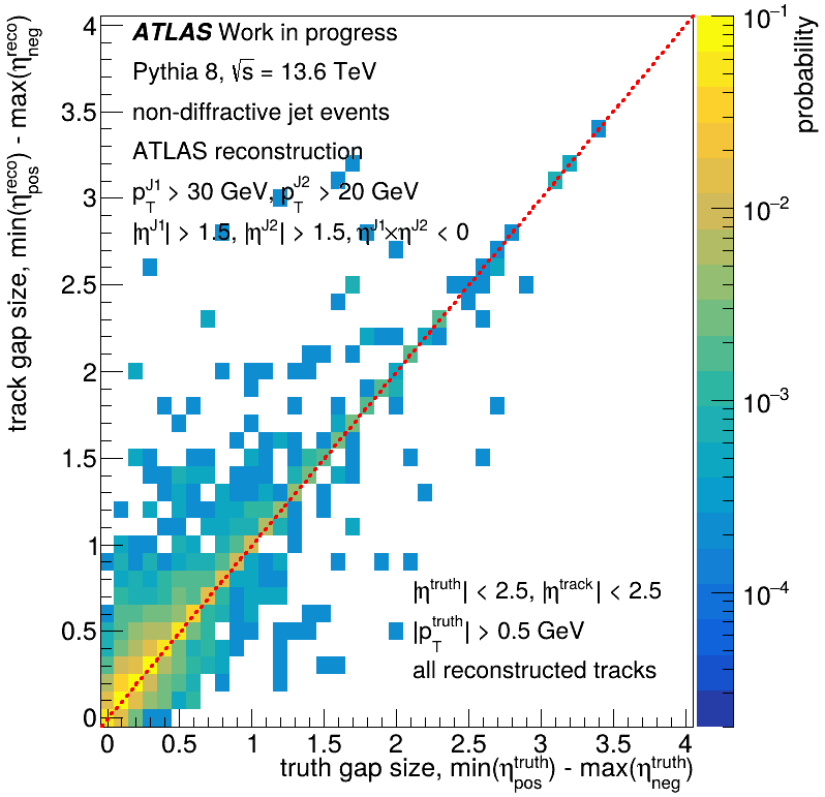

Figure 6.3: Relation between the gap obtained by using the truth charged particles with $p_T > 0.5$ GeV and the one obtained for the reconstructed tracks.

The ATLAS dataset provides multiple information on properties of the reconstructed tracks: their kinematics, trajectory, vertex position, and the number of detector layers used in the reconstruction *etc.* After careful studies of all of them, three were identified to differentiate between *not matched* (fake) and *matched isolated* (good) tracks:

- distance of the closest approach to the vertex in the transverse plane: $|d_0| < 0.3$ mm,
- distance of the closest approach to the vertex along the z-axis: $|\Delta z \times \sin(\theta)| < 0.35$ mm,
- number of hits in the first layer of the ATLAS pixel detector (the so-called B-Layer), in case such hit was expected due to track trajectory: $n_{BL} > 0$.

The distributions of these variables for the *matched isolated* and *not matched* tracks are shown in Fig. 6.4.
After applying the above selection, the number of "fake" tracks is significantly reduced. As one can see from Fig. 6.5, the selection criteria reduced "fake" gaps while only mildly increasing the size of the "reconstructed" ones.
The impact of the "fake" track removal procedure on the number of the charged particle tracks between the jets is demonstrated in Fig. 6.6 (left). In addition, the

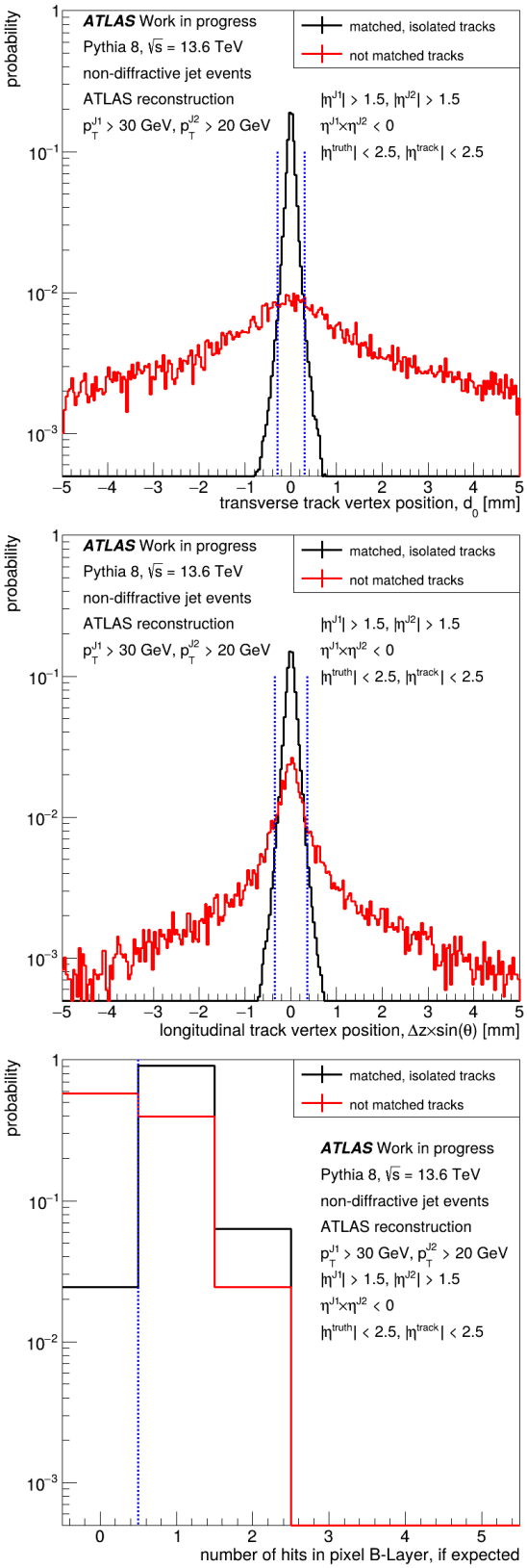

Figure 6.4: The fake track identification. **top:** the track transverse position w.r.t. the vertex, **middle:** the track longitudinal position w.r.t. the vertex, **bottom:** the number of hits in the first layer of the ATLAS pixel detector in case such a hit was expected due to the track trajectory. The dashed blue lines indicate the selection criteria.

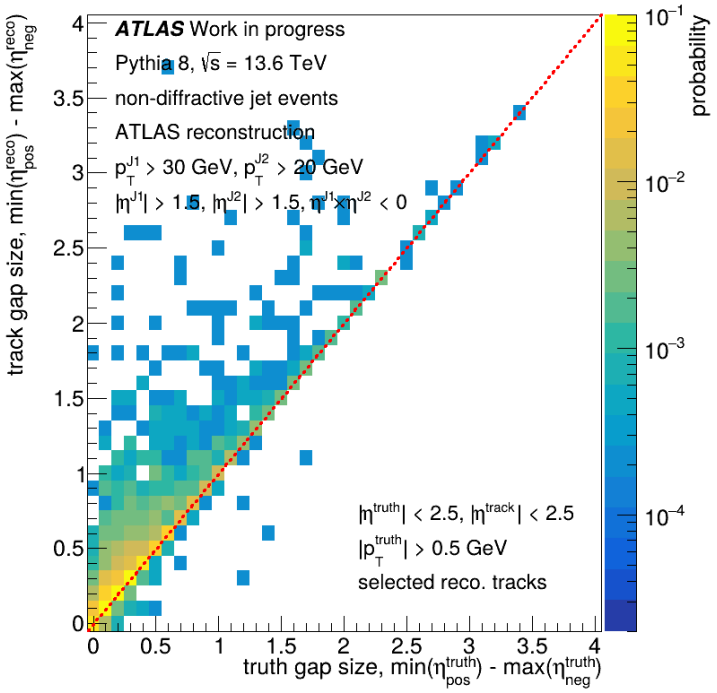

Figure 6.5: Relation between the gaps obtained by using the truth level charged particles with $p_T > 0.5$ GeV and the one obtained from the reconstructed tracks after the "fakes" removal.

track multiplicity distribution for the pseudorapidity region of $|\eta| < 1$ is shown in Fig. 6.6 (right).

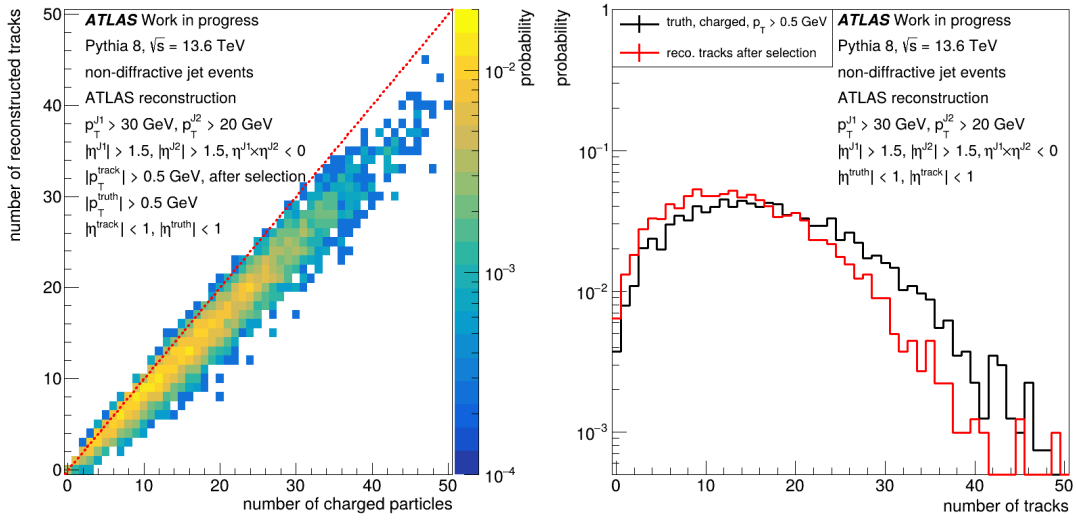

Figure 6.6: **Left:** the correlation between the truth (charged, $p_T > 0.5$ GeV) and reconstructed (after the "fakes" cleaning) tracks in an event. **Right**: the number of the "truth" and "reconstructed" tracks in pseudorapidity region $|\eta| < 1$.

The cleaning criteria resulted in an increased probability of having the "zero-track" events to around 6‰. Such an increase may result in a high background contamination since the cross-section for the jet-gap-jet events is expected to be

at least 2 orders of magnitude smaller [92, 30, 33, 34] than that for the non-diffractive jets (having the corresponding jet kinematics). An improvement may come from the inclusion of the calorimeter clusters into the gap definition. As one can see from Fig. 6.7 (left), the amount of energy is correlated to the number of the charged particles, but for the low track multiplicities, the expected energy spread is quite large.

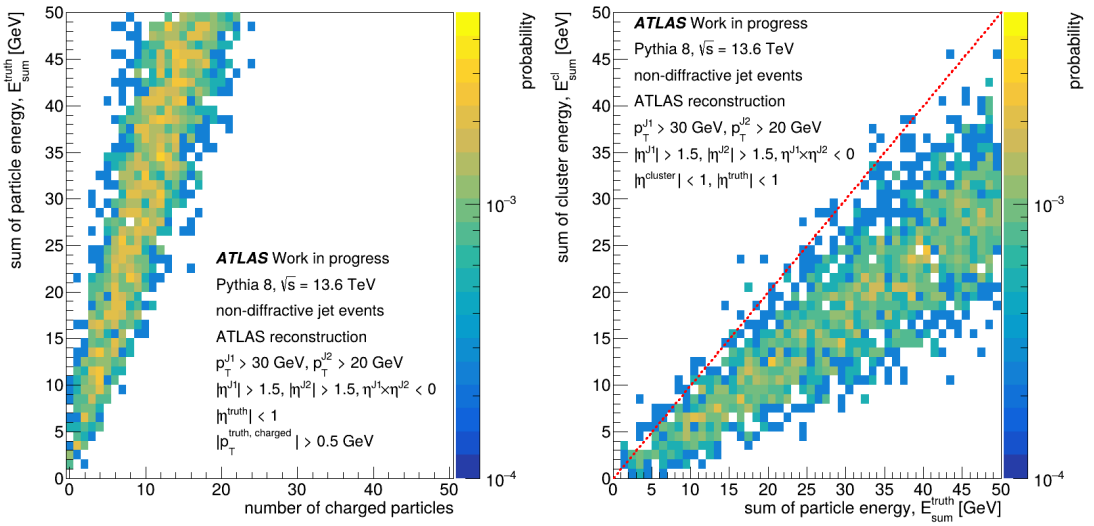

Figure 6.7: **Left:** correlation between the number of the truth charged, $p_T > 0.5$ GeV particles and the truth energy in the pseudorapidity region $|\eta| < 1$. **Right**: correlation between the truth and reconstructed energy deposited in the pseudorapidity region $|\eta| < 1$ in a given event.

The presence of the solenoid field, the ATLAS reconstruction efficiency and application of the quality criteria (see Section 5.3.3) result in the energy reconstructed in the region of $|\eta| < 1$ smaller than that expected from the truth particles – see Fig. 6.7 (right). Still, the energy criterion may be used to define a gap.
A combination of the track multiplicity and calorimeter energy present between the jets in the pseudorapidity region of $|\eta| < 1$ is shown in Fig. 6.8. The situation improves w.r.t. to the "track-only" criterion – considering the deposited energy smaller than 2 GeV, the gap in the case of non-diffractive jets is present only in ∼1‰ of cases. Unfortunately, due to the available size of the generated Monte Carlo sample, the uncertainty on this value is quite high – about 50%. Considering the expected cross-section, after application of the generation filter efficiency, the jet event selection and the above gap definition, the estimated fiducial background cross-section is $\sigma^{fid}_{ND\ JJ,\ gap} = 0.06 \pm 0.03$ nb.

6.1.2 Data

The data sample was selected in the following way:

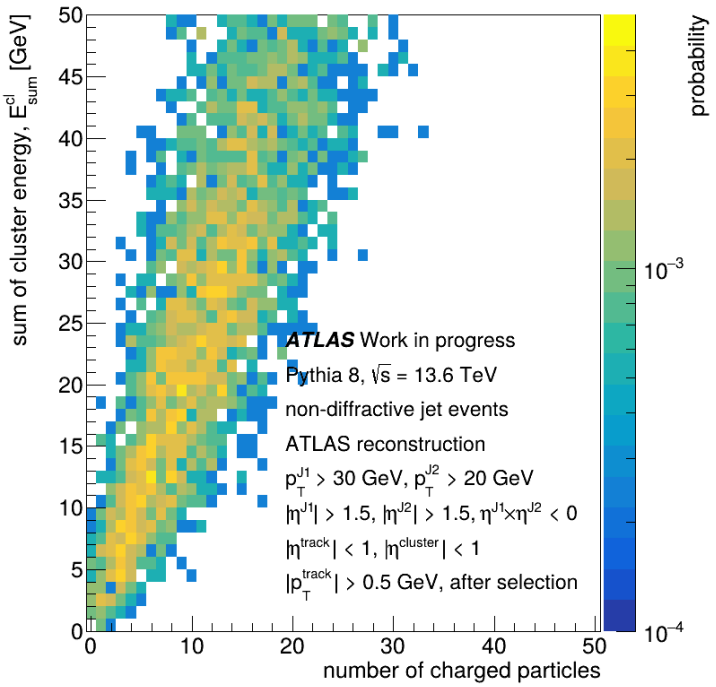

Figure 6.8: The gap identification: non-diffractive jet events with a given number of the reconstructed tracks and a certain energy deposited in the calorimeter in the pseudorapidity region $|\eta| < 1$.

- each event must pass the Good Run List and be accepted by either HLT_j20_L1J12 (for leading jet $p_T^{J1} \geq 55$ GeV) or $HLT\_j20\_L1MBTS\_2$ ($30 \leq p_T^{J1} \leq 55$ GeV) trigger,

- the transverse momentum of the leading (subleading) jets, after considering the Jet Energy Scale corrections, must be of at least 30 (20) GeV,

- both leading jets must belong to the opposite pseudorapidity hemispheres and have $|\eta| \geq 1.5$,

- a "combined gap", *i.e.* no tracks and the sum of the cluster energy smaller than 2 GeV in the pseudorapidity region $|\eta| \leq 1$.

After applying the above criteria, 234 events were left. These should be considered as the **jet-gap-jet** candidates. Since the integrated luminosity is 29.65 ± 0.44 nb^{-1}, the fiducial cross-section is estimated to be:

$$\sigma^{fid}_{ND\ JGJ} = 7.9 \pm 0.5 \text{ nb}.$$

Besides the cross-section, it is interesting to see the kinematics of the events. The "basic distributions": the transverse momentum and pseudorapidity of the two leading jets are shown in Fig. 6.9 and 6.10, correspondingly. As expected, the

jet p_T spectrum is steeply falling. Finally, the pseudorapidity difference between both leading jets is shown in Fig. 6.11.

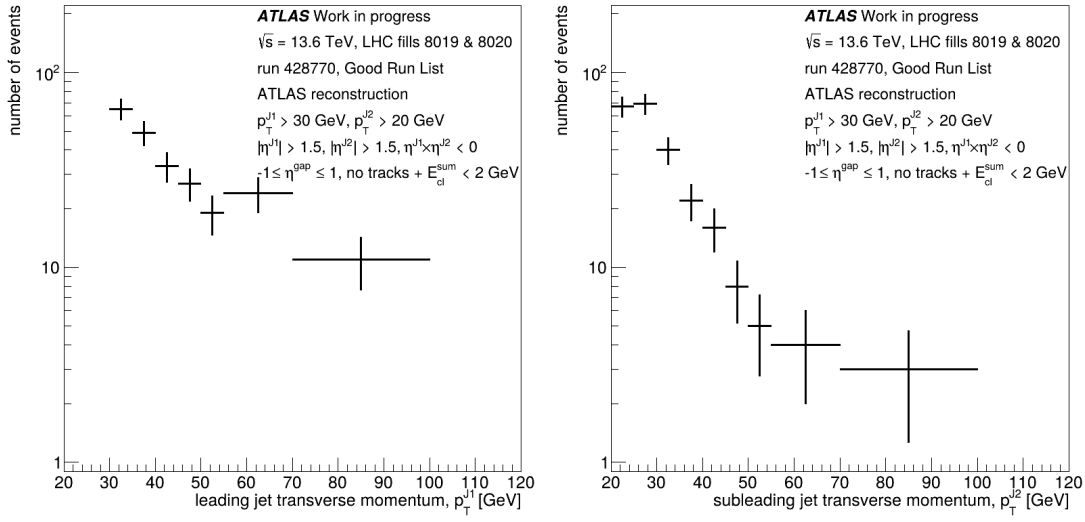

Figure 6.9: The transverse momentum of the leading (**left**) and subleading (**right**) jet for events passing the gap selection criteria. The ATLAS run 428770 data.

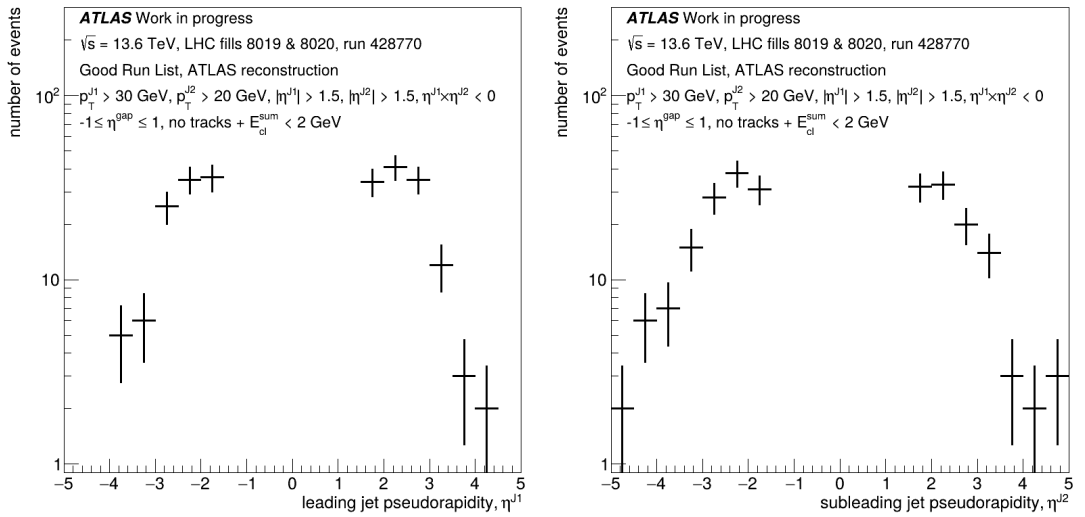

Figure 6.10: The pseudorapidity of the leading (**left**) and subleading (**right**) jet for events passing the gap selection criteria. The ATLAS run 428770 data.

6.2 Single Diffractive Di-jets

Single diffractive jet production is a very interesting process to study on its own. However, in the scope of this PhD thesis, it is used as an "intermediate" step between the non-diffractive and single diffractive jet-gap-jet analysis. Therefore, despite a few interesting features visible in the data, only the ones leading to the

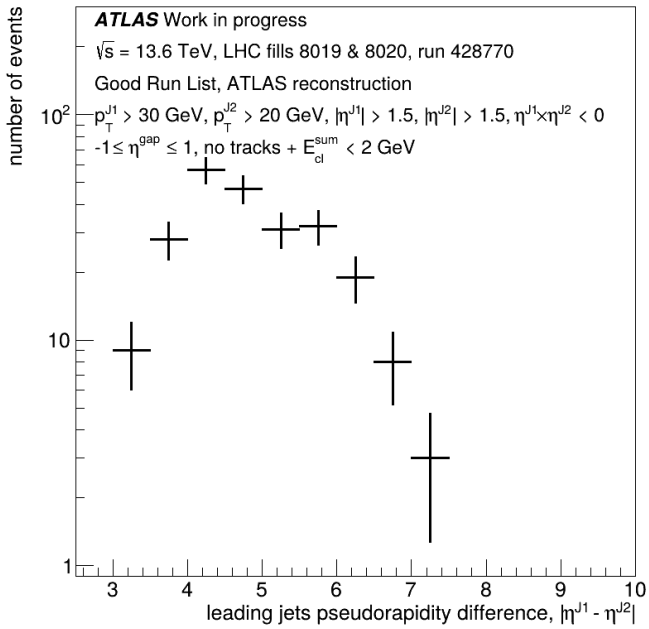

Figure 6.11: The difference of the pseudorapidities of the leading and subleading jet for events passing the gap selection criteria. The ATLAS run 428770 data.

SD JGJ identification will be discussed. However, it should be noted that the single diffractive di-jet analysis is expected to be published in the coming months by the ATLAS Collaboration.
The single diffractive di-jet events are characterised by two jets in the "central detector" and one intact proton. The intact proton loses a small fraction of its initial momentum and is scattered at a very small angle, allowing its detection in the AFP station. The lost energy is available to produce the di-jet system and possibly additional particles from the Pomeron remnants. For the event topology, *cf.* Fig. 1.5.

6.2.1 Event Selection

The selection of the single diffractive di-jet events follows a series of requirements, summarised in Table 6.1. The initial **trigger** selection requires both the AFP proton candidate and a jet in the central detector, based on `HLT_j20_L1AFP_A_OR_C`. The **di-jet** requirement selects events with the leading jet $p_T > 30$ GeV and subleading jet $p_T > 20$ GeV. The **proton** requirement indicates if a tag was on side A or C. The double tag events are not considered at this step.
Events were required to have either exactly one reconstructed primary **vertex** or, in the case of two vertices, the distance between them in the z direction had to be smaller than 13 mm. This requirement ensures that the measured proton and jets originate from the same interaction, reducing the background due to the coincidental proton-jet combinations by a factor of 7.

Table 6.1: Number of events passing given selection criteria.

Selection	**A Side**	**C Side**
trigger	443748	
di-jets	16323	
proton	10837	5227
vertex	9351	4507
max. ξ cut	6607	3127
ξ range	4011	1328

To ensure that the proton momentum fraction remains within the AFP detector's acceptance range, a constraint on the energy recorded in the calorimeter (**max. ξ cut**) was imposed, requiring $\xi < 0.09$. This constraint removes events with "unphysical" kinematics, which is possible in the combinatorial background case[1]. The requirement follows from the detector acceptance studies of Section 5.2.7.

An interesting first observation can be done already at the trigger-level analysis. Figure 6.12 shows the distribution of energy deposited in the ATLAS calorimeters, $\log_{10}(\xi_{cal})$, for events triggered by `HLT_j20_L1AFP_A_OR_C` (signal-like signature, green line) and by `HLT_j20_L1J12` (expected to be background dominated, black line). The distributions are normalised in the high-ξ tail region: $\log_{10}(\xi_{cal}) > -0.5$, as this region is expected to be dominated by the non-diffractive (background) events in both samples.

An excess at lower ξ values is visible in the signal-like sample. As supported by the Pythia 8 MC (blue line), it corresponds to the single diffractive contribution. This indicates that the proton requirement (assured by the trigger) selects diffractive events from the bulk of non-diffractive ones (red line). In addition, one can make an estimate of the expected sample purity by looking at the ratio between signal-like and background-like events.

Returning to the Table 6.1, an asymmetry in the proton detection between the A and C sides is evident. This difference primarily reflects the AFP trigger efficiency between the two sides of the detector (see Section 5.1.1.2), with the A side showing approximately twice as many events as the C side.

The correlation between the AFP-measured proton momentum loss (ξ_{AFP}) and the calorimeter-based estimation (ξ_{cal}) provides important information on the single diffractive event kinematics. To gain an insight into how such distribution may look like, one may use the Pythia 8 MC sample. The results in Figure 6.13 show a clear correlation, with some smearing towards the lower values of ξ_{cal} reflecting the fact that not all particles are reconstructed, *e.g.* due to the acceptance or inefficiency.

[1] Or, in some rare cases, due to wrong reconstruction of the proton kinematics.

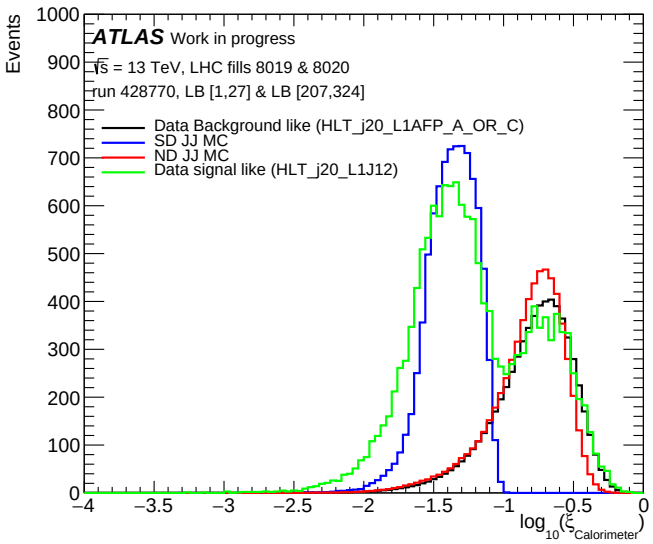

Figure 6.12: The combined relative energy loss distribution for A and C sides compared to the non-diffractive background. The distributions are normalised in the tail region $\log_{10}(\xi_{cal}) > -0.5$.

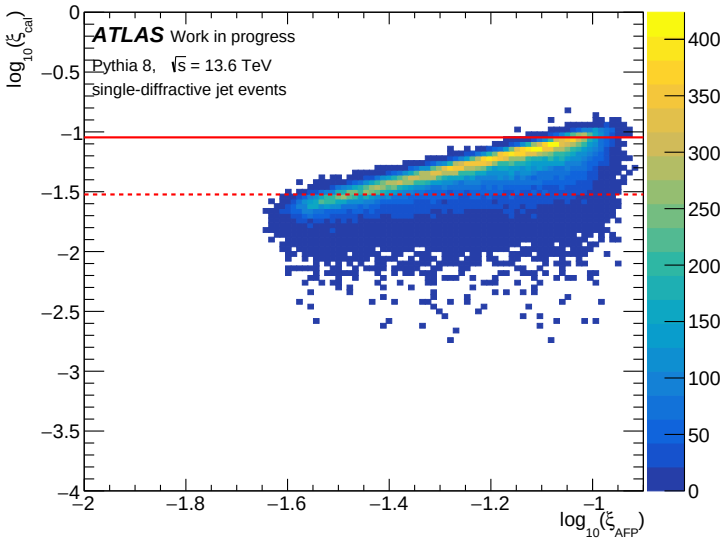

Figure 6.13: The correlation between the energy loss ξ_{cal} (calculated from the energy reconstructed in the ATLAS calorimeter) and that reconstructed from the proton measured in AFP, ξ_{AFP}. Pythia 8 single diffractive jet sample. The red lines indicate the AFP acceptance region.

Figure 6.14 shows this correlation for the data. Two cases are considered: before (left) and after (right) applying the vertex requirements. The red lines indicate the AFP high-acceptance region. The effect of the vertex requirement is particularly visible for points outside the AFP acceptance region (high-ξ_{cal}), as they are expected to be dominated by background events: non-diffractive jet + pile-up proton. Within the AFP acceptance region, the correlation pattern remains largely unchanged after the vertex cut, indicating that these events are predominantly due to the single diffractive interactions.

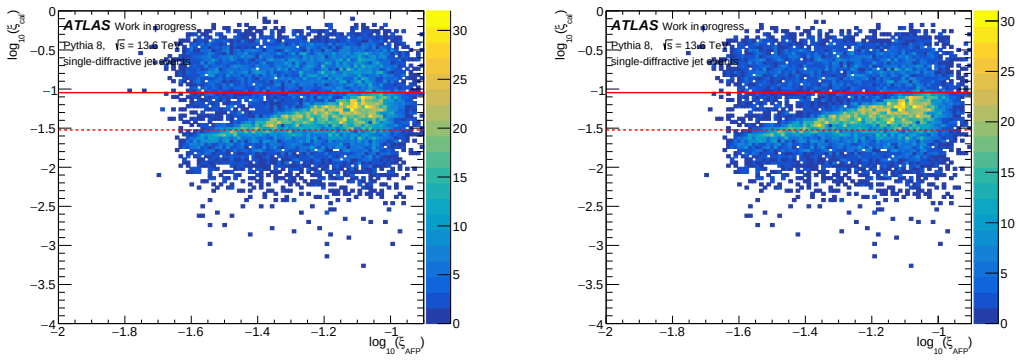

Figure 6.14: The correlation between the relative energy loss reconstructed with the ATLAS calorimeter, ξ_{cal}, and the one from the proton measured in AFP, ξ_{AFP}, before (**left**) and after (**right**) the single vertex requirement. The red lines indicate the AFP acceptance region.

Comparing the data (Fig. 6.14) and MC (Fig. 6.13) distributions, one observes that the MC reproduces the core correlation pattern seen in the data, with a majority of events following the expected relationship where $\xi_{\text{cal}} \lesssim \xi_{\text{AFP}}$. However, the data show a broader distribution with more events populating the region where $\xi_{\text{cal}} > \xi_{\text{AFP}}$. The fact that many of such events pass the single vertex requirement indicates that the applied selection criteria are not strict enough. Indeed, the 13 mm criterion used in the current selection reduces background contribution by a factor of 7, *cf.* Sec. 5.3.2. Once the "vertex miss-reconstruction feature" is fixed, application of the 2 mm cut should result in further reduction by the factor of 7 (thus ~ 50 in total).
This "feature" motivates the application of more stringent selection on kinematics relation, causing an additional background removal. The difference between the proton energy loss, $\Delta\xi = \xi_{\text{AFP}} - \xi_{\text{cal}}$ is shown in Figure 6.15 for both data (green line for all events passing ethe vertex requirement and blue for additional $\xi < 0.09$ criterion) and Monte Carlo simulation (magenta). The data show a peak centred slightly below zero, which is well described by the Monte Carlo prediction for single diffractive events, but with much longer tails. Based on this, a requirement of $-0.03 < \Delta\xi < 0.01$ is imposed for further sample purification.

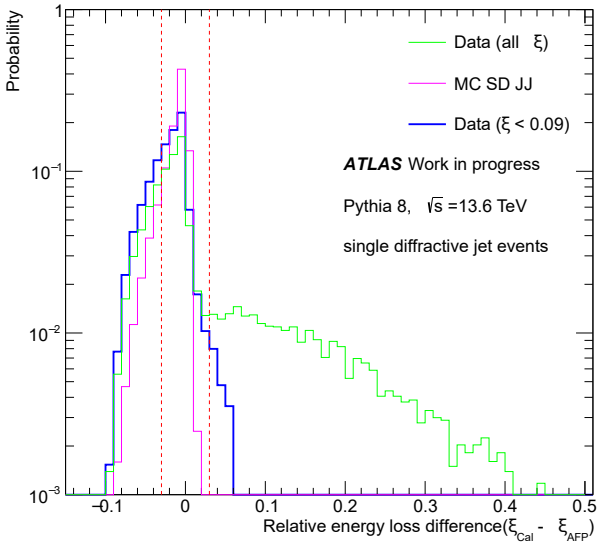

Figure 6.15: The difference $\Delta\xi = \xi_{\text{cal}} - \xi_{\text{AFP}}$ for data (green) compared to single-diffractive Monte Carlo simulation (magenta) – see text. The data events with $\xi_{cal} < 0.09$ are shown in blue. All distributions are normalised to unity. The vertical dashed red lines indicate the selection criteria: $-0.03 < \Delta\xi < 0.01$.

6.2.2 Data-MC Comparison

The kinematics of the selected events were compared with predictions from a single diffractive Monte Carlo model. The data had to pass all selection criteria, including the "ξ-range". The same criteria were applied for the MC samples. It should be noted that, due to the reconstruction "features" (cf. Chapter 5), there is still quite a significant contribution of the non-diffractive events in the data. This is visible in the example of the leading jet transverse momentum – see Fig. 6.16 – where data passing the selection (black points) are shown together with single diffractive (blue area) and non-diffractive (green area) MC events. From this figure, one can also conclude that there is enough statistics in the ATLAS run 428770 sample to effectively measure single diffractive jet events with the leading jet p_T reaching up to about 100 GeV. Finally, it should be mentioned that events having the scattered protons on either side of ATLAS are shown together on a single plot. In the MC case, the distribution was weighted[2] accordingly to appropriate trigger prescale depending if the proton was on side A or C.

Another interesting distribution is the pseudorapidity of leading jets, shown in Fig. 6.17. It shows an interesting asymmetry: events with a proton tag on side A(C) have the leading jet located more often in the opposite hemisphere.

[2]Obviously, the MC events which passed the selection criteria are weighted to the expected number of events in data, *i.e.* by considering the generated cross-section, generation filter efficiency, collected luminosity and, as already mentioned, the trigger efficiency.

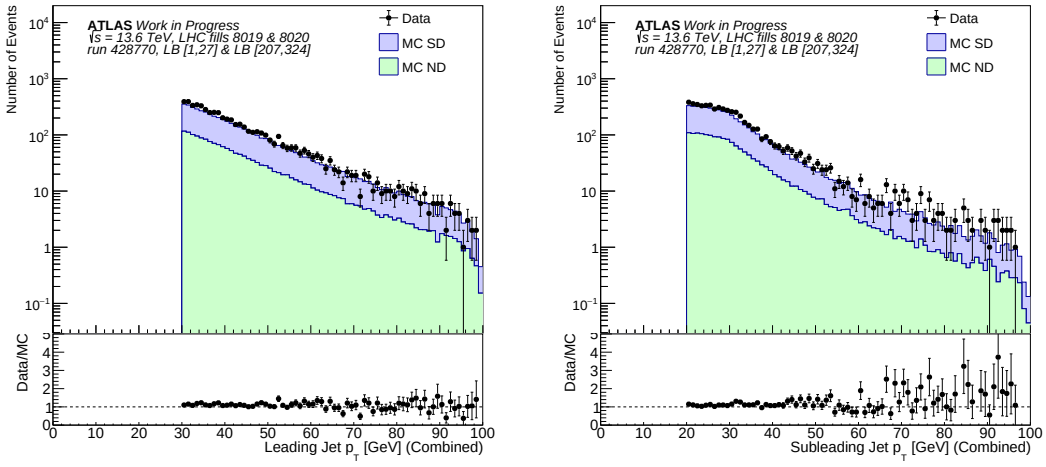

Figure 6.16: The measured and MC-predicted p_T distributions for the leading (**left**) and subleading (**right**) jet after diffractive event selection (see text).

Such a feature was already observed in the data collected by the AFP, see *e.g.* [93]. Notably, also in this case, MC describes data quite well, except for some small mismatches in the very forward region, probably due to the MC generation settings.

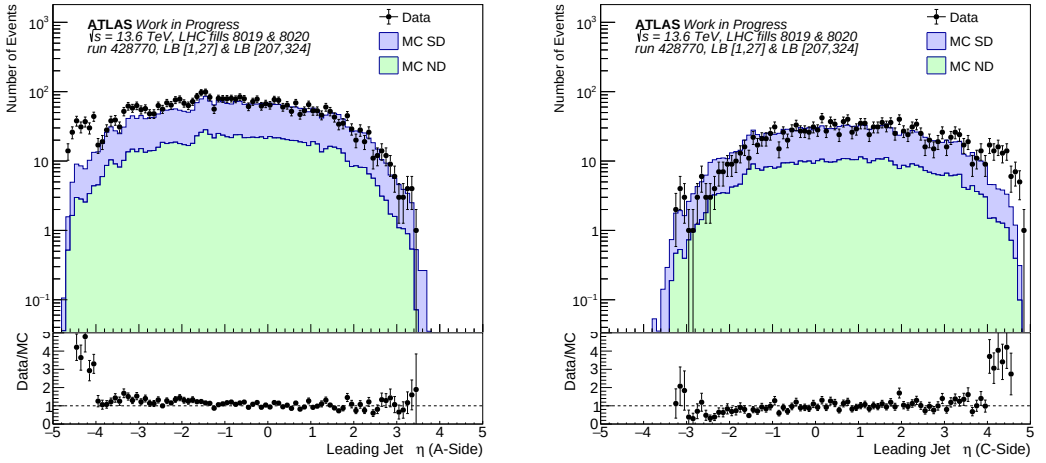

Figure 6.17: The measured and MC-predicted leading jet η distributions for A side (**left**) and C side (**right**) after diffractive event selection (see text).

6.3 Single Diffractive Jet-Gap-Jet Events

The application of the merged selection of events – non-diffractive jet-gap-jet and single diffractive jet production – results in the identification of the single diffractive jet-gap-jet candidates. The data sample of 29.6 nb^{-1} collected during the

ATLAS run 428770 contains 7 such events: 5(2) with proton on side A(C). Based on the Pythia 8 diffractive jet sample, the random gap configuration contributes to the cross-section by $\sigma^{fid}_{bkg,\ gap,\ proton} = 0.0015$ nb, which implies 0.5 expected background events.

The single diffractive jet-gap-jet events are presented using event displays in the form of pseudorapidity-azimuthal angle maps, see Figs. 6.18 – 6.20.

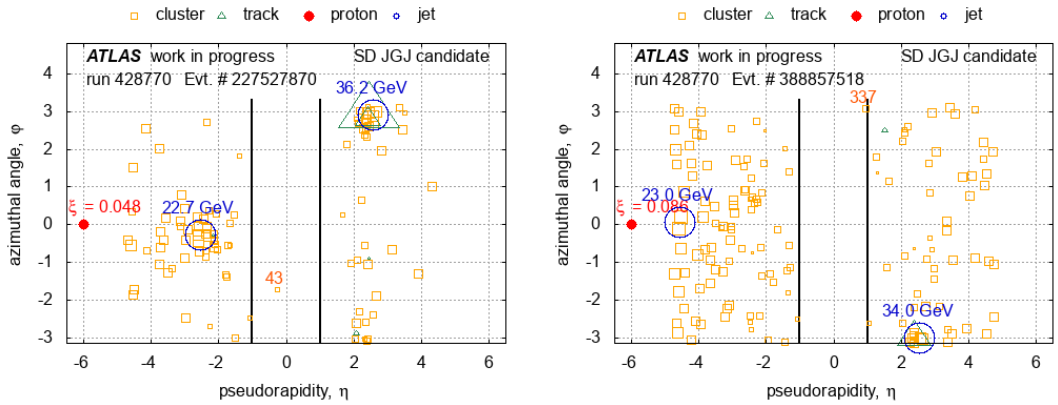

Figure 6.18: Single diffractive jet-gap-jet candidates. Two events with proton on side A and almost energy-empty gap region.

In these plots, jets are represented by circles of constant, arbitrary radius centred at the reconstructed jet η and φ. The blue numbers above the circles refer to the jet transverse momentum in GeV. Only leading and subleading jets are shown. The red dots, arbitrarily placed at $|\eta| = 6$ and $\varphi = 0$, represent proton(s) on a given side (-6 in case of A and $+6$ for C). The red number above refers to the reconstructed proton ξ. The green triangles mark the tracks. Their size is proportional to track p_T. The orange squares are for clusters. Their size is proportional to $\log_{10}(E_{cl})$. In case a cluster is within the gap region ($|\eta| < 1$, represented by vertical black lines), its energy is explicitly given (in MeV).

Figure 6.18 shows two candidates with an almost empty gap region. In one case, there is only one cluster with energy of 43 MeV. In the other, the 337 MeV cluster is located very close to the gap "border". In both cases, there is a significant activity outside a gap.

Figure 6.19 shows both cases with the proton tagged on side C. In one case, both leading jets are within the tracker region. The energy within the gap sums to about 1-1.5 GeV. The remaining 3 candidates are shown in Fig. 6.20 for completeness.

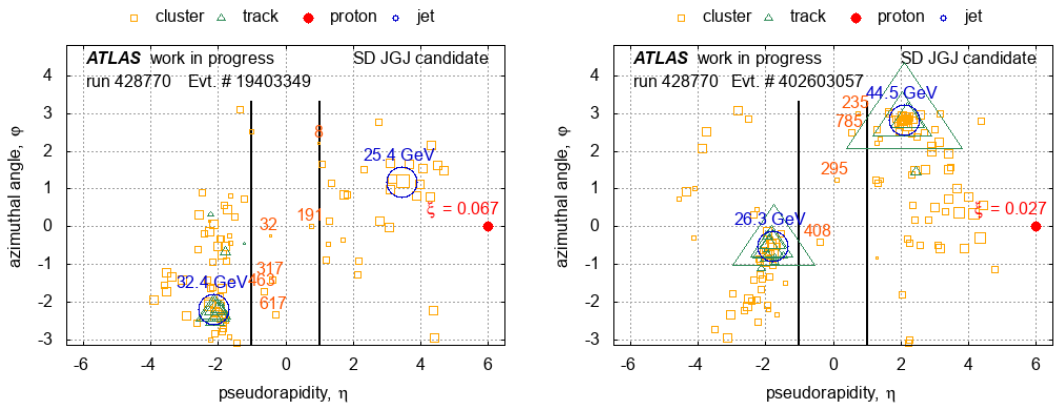

Figure 6.19: Single diffractive jet-gap-jet candidates. Two events with proton on side C.

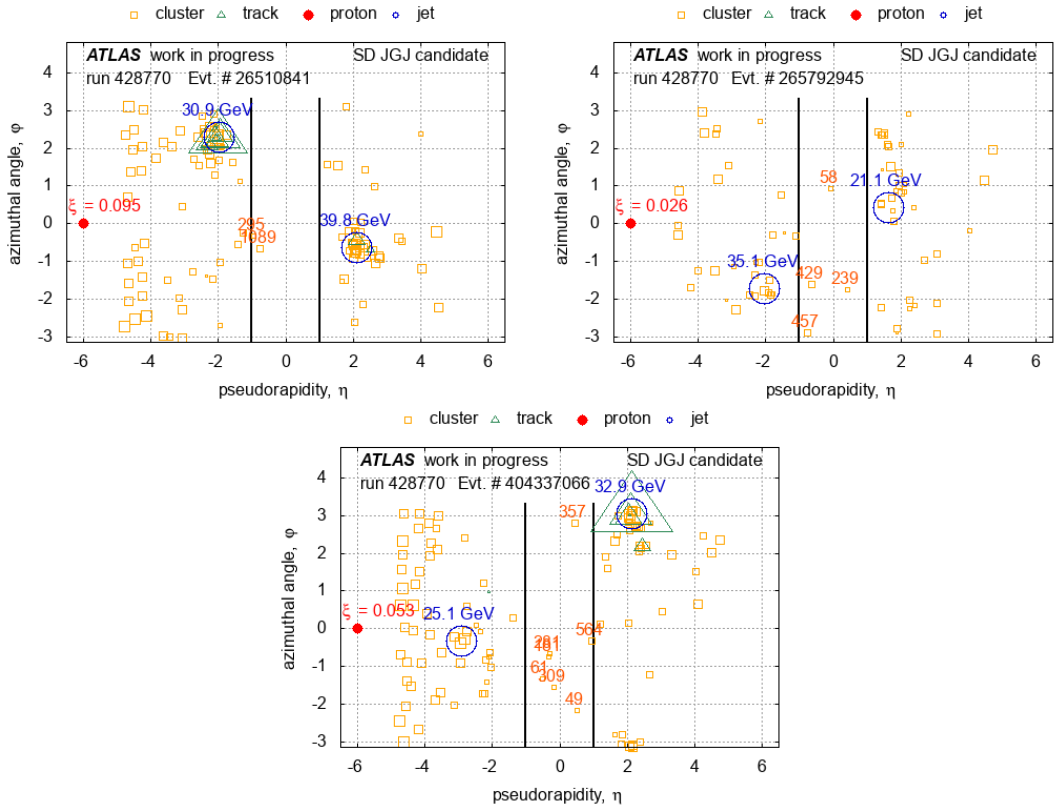

Figure 6.20: Single diffractive jet-gap-jet candidates. Events with a proton on side A and some (small) energy reconstructed in the gap region are shown.

Considering the HLT_j20_L1AFP_A_OR_C trigger efficiency, the estimated cross-section in the fiducial region is:

- $\sigma^{fid}_{SD\ JGJ,\ A} = 0.19 \pm 0.08$ nb for proton on side A,
- $\sigma^{fid}_{SD\ JGJ,\ C} = 0.15 \pm 0.10$ nb for proton on side C.

Unfortunately, a direct comparison of these results with the measurements reported by CMS Collaboration [7] is not feasible due to differences in the experimental phase space. The CMS study applied higher jet p_T thresholds ($p_T^{jet} > 40$ GeV) compared to 30/20 GeV in this analysis. Additionally, the gap definitions are not equivalent.

Chapter 7

Summary

Jet-gap-jet production is a very interesting process to be studied. It is well-suited for tests of the Quantum Chromodynamics, in particular the test of the so-called BFKL Pomeron. Therefore, precise measurements of this process provide a valuable platform for further development.

Following the first observation at the Tevatron, this signature was searched for using the LHC data. The first ATLAS analysis employed a veto on the presence of a third jet to select interesting events. An unpublished analysis of low-μ Run 1 ATLAS data indicated the presence of such events even with a more stringent gap definition. Subsequently, the first evidence of the diffractive jet-gap-jet events with a single forward proton tag was published by the CMS Collaboration. It is worth stressing that all these measurements have significant uncertainties on the cross-section. Moreover, the double Pomeron exchange jet-gap-jet process has not been observed to date.

After taking lessons from 2017 data analysis, one of the Run 3 datasets, run 428770 with $\mu = 0.05$, was chosen to search for the jet-gap-jet events. The integrated luminosity of the data sample is 29.65 ± 0.44 nb^{-1}. Since this was a non-standard data-taking run, dedicated performance studies had to be performed. This includes both ATLAS "central" objects like tracks, clusters and jets as well as the forward scattered protons.

The analysis started with determining the most suitable triggers for the analysis. From all trigger items, the combination of HLT_j20_L1MBTS_2 and HLT_j20_L1J12 proved to be the most effective for selecting non-diffractive jet-gap-jet events. The former one was fully efficient (although prescaled by a factor of 20), hence used for the events containing (offline) leading jets having $30 \leq p_T^{J1} < 55$ GeV, whereas the latter one was the best for $p_T^{J1} \geq 55$ GeV.

For the single diffractive jet-gap-jet events, the most efficient unprescaled trigger was HLT_j20_L1AFP_A_OR_C. This trigger is fully efficient for events with $p_T^{J1} \geq 30$ GeV. The AFP efficiency was measured to be 91.25 ± 0.29 and 45.92 ± 0.13 for protons tagged on side A and C, respectively.

Unlike the trigger, the AFP track reconstruction efficiency is very high – approximately 99%. In addition, the precision of the scattered proton energy reconstruction also remains high, $\sim \delta\xi/\xi \approx 1\%$. The data-taking position, determined by

the LHC optics, resulted in a lower limit on the AFP proton acceptance $\xi \sim 0.03$. The upper limit of $\xi \approx 0.09$ on the acceptance was imposed by the LHC collimators.

A dedicated analysis of ATLAS track reconstruction efficiency showed that the so-called low-p_T tracking was not employed in the data processing. As a result, decent efficiency was achieved only for tracks having the transverse momentum of at least 500 MeV. Fortunately, contrary to the 2017 low-μ data-taking, the calorimeter appeared to be properly configured, with no reconstruction issues detected in the forward region. Finally, performing a dedicated Jet Energy Scale calibration enabled the commencement of the jet-gap-jet events search.

In the first step, a "gap" was defined using Monte Carlo samples. To suppress "random" gaps originating from fluctuations, a combined "track veto" and "2 GeV energy limit" were applied in the region of $|\eta| < 1$. After applying the trigger-based event selection and requesting the presence of the leading (subleading) jet p_T of 30 (20) GeV with $|\eta^{J1,J2}| > 1.5$, $\eta^{J1} \times \eta^{J2} < 0$ and that of the gap, the background contribution was estimated to be $\sigma^{fid}_{ND\ JJ,\ gap} = 0.06 \pm 0.03$ nb. The same selection criteria applied to the experimental data result in a sample of 234 events. Considering the integrated luminosity of the analysed data sample, the fiducial cross-section for the non-diffractive jet-gap-jet process was estimated to be:

$$\sigma^{fid}_{ND\ JGJ} = 7.9 \pm 0.5 \text{ nb}.$$

As an "intermediate" step, a single diffractive analysis was performed. The selection considered the presence of the forward proton, minimal jet p_T threshold, single vertex requirement, and kinematic relation between the energy reconstructed in the ATLAS calorimeter and that of the scattered proton. After this selection, 4011 and 1328 di-jet events with protons on side A and C, respectively, remained. These events are still expected to contain a significant amount of non-diffractive background. It should be noted that, in the future analysis, the selection should be improved, especially after addressing the "vertex splitting" feature. Additionally, a proper analysis of systematic effects, as well as extrapolation to the full phase space, should be carried out.

Finally, a combination of the above analyses resulted in the identification of 7 single diffractive jet-gap-jet candidates. Considering the HLT_j20_L1AFP_A_OR_C trigger efficiency, the estimated cross-section in the fiducial region is:

- $\sigma^{fid}_{SD\ JGJ,\ A} = 0.19 \pm 0.08$ nb for proton on side A,
- $\sigma^{fid}_{SD\ JGJ,\ C} = 0.15 \pm 0.10$ nb for proton on side C.

A direct comparison of the above result with the measurements reported by CMS Collaboration [7] is not feasible. The two studies largely differ in the considered

phase space. The CMS study applied higher jet p_T thresholds ($p_T^{jet} > 40$ GeV) compared to 30/20 GeV in this analysis. Additionally, the gap definitions are not equivalent.

The analyses described above are the first of their kind using ATLAS Run 3 data. During the studies, several problems were identified, resulting in a list of recommendations to the analysis/performance groups to improve/fix issues related to the reconstructed data and Monte Carlo. On the other hand, the above analyses clearly show that non-diffractive jet-gap-jet and single di-jet events are present in the data. Enhancing the dataset with other low-μ runs collected by ATLAS during Run 3 should allow for a significant single diffractive jet-gap-jet analyses with the hope of observing a few of double Pomeron exchange jet-gap-jet events. The obtained cross-sections may be especially useful for planning further low-μ, potentially to be realized before the end of LHC Run 3.

Appendices

Appendix A

Optics Studies

Knowledge of the settings of the LHC elements, especially magnets and collimators between collision point and forward proton detectors, is crucial for analysis using the forward scattered protons. A good description of the LHC optics between IP1 and the AFP stations is essential to understanding the AFP detector's acceptance and accurately reconstruct the proton kinematics. Below, a part of my studies towards understanding the LHC optics is described.

A.1 LHC Magnetic Lattice from IP1 to AFP

The magnetic lattice between IP1 and AFP comprises several distinct sections:

1. Inner Triplet: Three quadrupole magnets (Q1, Q2, Q3) that provide strong focusing at the IP. For the nominal collision optics ($\beta^* = 30$ cm), these magnets generate β-functions of up to 5 km.

2. Separation Dipoles: D1 (normal conducting) and D2 (superconducting) join/separate the two beams before/after the collision.

3. Matching Section: Quadrupoles Q4 to Q7 match the optics between the inner triplet and the arc.

The placement of these elements along the LHC beam-line is shown in Fig. A.1. The figure also shows the proton trajectories for the Run 2 LHC collision optics: $\sqrt{s} = 13$ TeV, $\beta^* = 0.4$ m and $\theta_C = -185$ μrad.

A.2 Simplified Transport Model

The LHC uses a very sophisticated tool – Methodical Accelerator Design (MAD-X) [95] – for the optics studies. However, due to its complexity, the tool is relatively slow. In addition, introducing modifications needed for the AFP feasibility studies is difficult and time-consuming. Therefore, for the fast optics studies, a stand-alone transport model was developed. It tracks the protons element-by-element through the magnetic lattice. It should be noted that this code was successfully cross-checked and validated with the MAD-X transport.

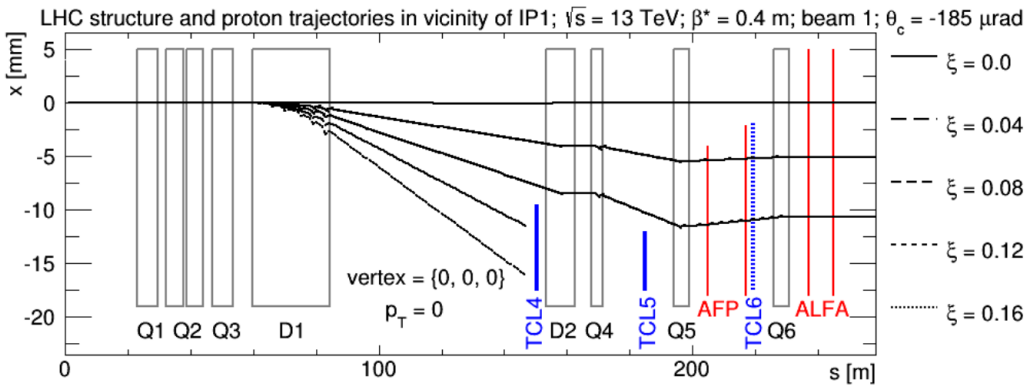

Figure A.1: The LHC beam-line in the vicinity of the ATLAS collision point. Proton trajectories are plotted for LHC Run 2 optics: $\sqrt{s} = 13$ TeV, $\beta^* = 0.4$ m and $\theta_C = -185$ μrad. From [94].

In the model, a right-handed coordinate system is used where s is the longitudinal coordinate along the ideal orbit (beam direction), x is the horizontal (bending plane, pointing outside of the LHC ring) coordinate, and y is the vertical coordinate (pointing upward).
The particle state is represented by the vector (x, x', y, y', δ), where x' and y' are the angles in the horizontal and vertical planes, and $\delta = (p - p_0)/p_0$ is the relative momentum deviation from the reference beam momentum p_0.

A.3 Proton Trajectories for 2022 Optics

Two key kinematic variables, the fractional energy loss ξ and the transverse momentum p_T, are particularly relevant in describing the proton transport. The fractional energy loss ξ is defined as:

$$\xi = \frac{E_{\text{beam}} - E_{\text{proton}}}{E_{\text{beam}}}. \tag{A.1}$$

Protons with larger ξ experience greater horizontal deflection due to the LHC lattice dispersion, while their vertical displacement depends primarily on the initial vertical angle at the interaction point (IP), which is related to p_T.
As protons traverse the magnetic lattice, they encounter various aperture restrictions and collimators. The LHC magnetic lattice strongly influences the proton trajectories; see Fig. A.2. The figure shows the proton trajectories for optics used during the 2022 data-taking: $\sqrt{s} = 13.6$ TeV, $\beta^* = 0.6$ m and $\theta_C = 160$ μrad.
In this plot, the beam ($\xi = 0$) is shown as the thick black line. Trajectories of protons with ξ ranging from 1% to 19% are shown as the dashed and dotted blue lines. The greater the ξ value, the larger the deflection from the nominal trajectory is. Eventually, such protons will be stopped by the beam pipe aperture

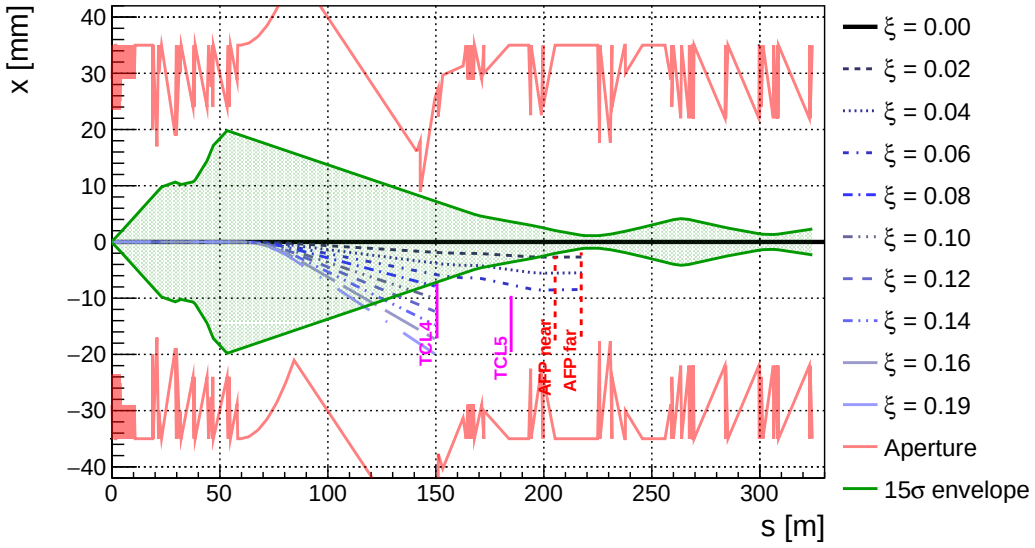

Figure A.2: Comparison of the proton trajectories from IP1 to the AFP stations for 2022 optics configuration: $\sqrt{s} = 13.6$ TeV, $\beta^* = 0.6$ m and $\theta_C = 160$ μrad. The horizontal position (x) relative to the nominal beam is shown as a function of the distance from IP1 (s). The blue lines represent protons with different momentum losses (ξ). The 15σ beam envelope (green shaded area), machine aperture (red lines) and positions of TCL4/5 collimators and AFP stations are indicated.

or collimators. The former is shown with a red line, while the latter is depicted with pink vertical bars. The green area marks the 15σ beam envelope.

A.4 Proton Kinematics–Position Relation

The configuration of the LHC lattice impacts the proton trajectory. In consequence, the proton position at a given location in the LHC is due to:

- its kinematics (p_x, p_y, p_z),
- position of the collision vertex (x_0, y_0, z_0) and
- machine optics.

Since the beam width at the collision point is small (~ 15 μm), the position of the collision vertex has the smallest impact and is often neglected. As shown in Fig. A.3, the characteristic hit pattern in AFP is, in practice, due to optics and kinematics.

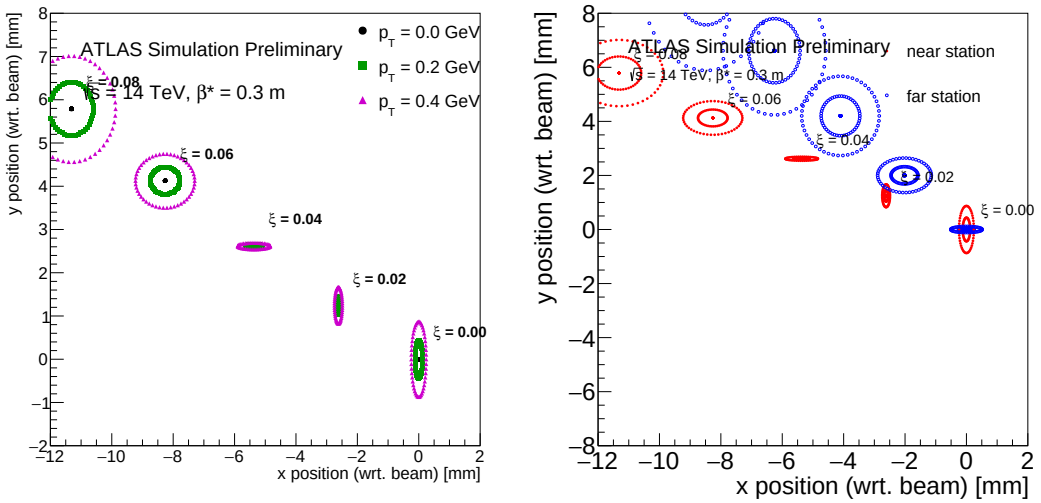

Figure A.3: Hit patterns at the AFP detector stations for $\beta^* = 0.3$ m optics. The proton position for various energy losses (xi) and transverse momentum (p_T) are shown. **Left:** figure shows position for NEAR station with p_T in various colours. On the **right:** hit patterns for the same proton, but registered in the AFP NEAR and FAR stations are shown.

A.5 AFP Insertion Distance

To protect the LHC components (especially superconducting magnets) from particles scattered from the beam, a collimation system is used. For effective operation, it keeps a certain hierarchy – elements must not be placed closer to the beam (in σ) than a certain collimator. This directly impacts the AFP, as the closest position to which Roman pot can be inserted is determined by the (tertiary, TCT) collimator:

$$d_{XRP}[mm] = MAX((n_{TCT} + 3) \cdot \sigma_{XRP} + 0.3\ mm, 1.5\ mm), \tag{A.2}$$

where n_{TCT} is the distance, expressed in the multiplicity of beam widths, at which TCT jaws are closed and σ_{XRP} is beam width at the location of AFP. There are 2 safety margins: relative to the beam size (3σ) and constant (0.3 mm). In addition, there is a hard limit of 1.5 mm below which the pot cannot be inserted. During Run 3, two operation scenarios were used: "constant TCT position" and "minimal Roman pot distance". The former was used in 2022, while the latter was used during 2023 and 2024 data-taking campaigns.

A.5.1 Constant TCT Position

The β of TCT collimator will change with β^*, to keep constant distance, *i.e.* there will be no collimator movement. Since the opening is defined at $\beta^* = 0.3$

m, the following scaling was used for other values of β^*:

$$n(\beta^*) = \frac{\sigma_{TCT}(\beta_0^*)}{\sigma_{TCT}(\beta^*)} n(\beta_0^*). \tag{A.3}$$

The minimum distance at which the Roman Pot can approach the beam is defined as in Eq. A.2, thus, with the TCT jaw constant in mm, it will be:

$$d_{XRP}(\beta^*) = MAX[(8.5\frac{\sigma_{TCT}(\beta_0^*)}{\sigma_{TCT}(\beta^*)} + 3)\sigma_{XRP} + 0.3\ mm, 1.5\ mm]. \tag{A.4}$$

The exact numbers for relevant β^* values are given in Table A.1. As one can see, the FAR station is expected to hit the "hard limit" for $\beta^* \leq 0.6$ m.

Table A.1: Minimal distances of AFP pots for the "constant TCT position" used during the 2022 data-taking.

β^*	d_{XRP}^{NEAR} [mm]	d_{XRP}^{FAR} [mm]
30	2.251	1.500
36	2.238	1.500
43	2.241	1.500
51	2.260	1.500
60	2.299	1.500
71	2.362	1.632
84	2.456	1.815
100	2.591	2.045
120	2.784	2.334

Opening of the TCL collimators is defined at $\beta^* = 30cm$ optics: TCT/TCL4/TCL5 = $8.5\sigma/15\sigma/40\sigma$. The exact values for relevant β^* values are given in Table A.2.

Table A.2: The TCT and TCL collimator positions for β^* values for the "constant TCT position" scenario.

β^*	$n_{TCT}[\sigma]$	$n_{TCL4}[\sigma]$	$n_{TCL5}[\sigma]$
30	8.5	15	40
36	9.309	16.427	43.686
43	10.173	17.946	47.546
51	11.076	19.534	51.489
60	12.009	21.173	55.438
71	13.057	23.009	59.679
84	14.192	24.991	63.996
100	15.468	27.212	68.434
120	16.917	29.718	72.850

A.5.2 Minimal Roman Pot Distance

In this scenario, all Roman Pots are assumed to be at the closest distance of 1.5 mm unless it does not break the collimation hierarchy. From the machine protection rule, the maximum TCT jaw opening is:

$$n_{TCT} \leq \frac{1.2mm}{\sigma_{XRP}} - 3. \tag{A.5}$$

As shown in Tab. A.3, such a setting is not possible for the NEAR station as it would mean the TCT breaking the 8.5σ limit.

Table A.3: A hypothetical closure of the TCT jaws in case a given pot is kept at a 1.5 mm distance.

β^*	d_{XRP}^{NEAR} [mm]	d_{XRP}^{FAR} [mm]
30	2.251	1.500
36	2.238	1.500
43	2.241	1.500
51	2.260	1.500
60	2.299	1.500
71	2.362	1.632
84	2.456	1.815
100	2.591	2.045
120	2.784	2.334

Using Eq. A.2 the minimum assuming fixed TCT half gap at 8.5σ was computed: $d_{XRP}[\sigma] = \frac{d_{XRP}[mm]}{\sigma_{XRP}}$, see Tab. A.4. The TCL4 and TCL5 openings are listed in Tab. A.5.

Table A.4: Minimal distances of the AFP pots for the "minimal Roman pot distance" used during the 2023 data-taking.

β^*	d_{XRP}^{NEAR} [mm]	d_{XRP}^{FAR} [mm]
30	2.251	1.500
36	2.238	1.500
43	2.241	1.500
51	2.260	1.500
60	2.299	1.500
71	2.362	1.632
84	2.456	1.815
100	2.591	2.045
120	2.784	2.334

Table A.5: TCT and TCL collimator positions for β^* values for the "minimal Roman pot distance" scenario.

β^*	TCT [mm]	TCL4 [mm]	TCL5 [mm]
30	9.545	9.943	13.099
36	8.714	9.079	11.994
43	7.975	8.310	11.020
51	7.325	7.635	10.177
60	6.756	7.044	9.452
71	6.214	6.482	8.780
84	5.717	5.968	8.188
100	5.245	5.481	7.657
120	4.796	5.019	7.193

A.6 AFP Geometric Acceptance

These collimators and aperture restrictions limit the range of proton kinematics, particularly in terms of ξ and p_T, that can be detected, directly impacting the physics reach of the AFP measurements. The AFP geometric acceptance measures what fraction of protons with given kinematics can be detected:

$$A(\xi, p_T) = \frac{\text{number of protons reaching the AFP detector with given } \xi \text{ and } p_T}{\text{number of the generated protons with given } \xi \text{ and } p_T}. \tag{A.6}$$

The AFP geometric acceptance varies significantly with beam optics parameters, as illustrated in Fig. A.4. Generally, higher β^* values provide larger acceptance for low-p_T protons.

A.7 Towards "True Optics" Determination

So far, in all feasibility studies and data analysis, the "ideal" description of the LHC magnetic field was used. Unfortunately, these settings, stored in the MAD-X files [95], may not reflect reality. First, the laser surveys indicate that the LHC elements are not perfectly aligned with the ideal beam centre. As can be seen in Fig. A.5, the survey done in 2022 shows offsets up to 3 mm in vertical and up to 2 mm in horizontal (radial) direction. Second, the collision point is determined by the data-driven approach during the LHC "adjust" phase, meaning that the strengths of magnets and kickers are being effectively determined.

As was shown earlier in this Chapter, the settings of the LHC elements directly influence the proton trajectories, thus their position in the AFP. A deviation from the "ideal" description may introduce systematic shifts in the reconstruction of the scattered proton kinematics. This gives a motivation to search for the "true"

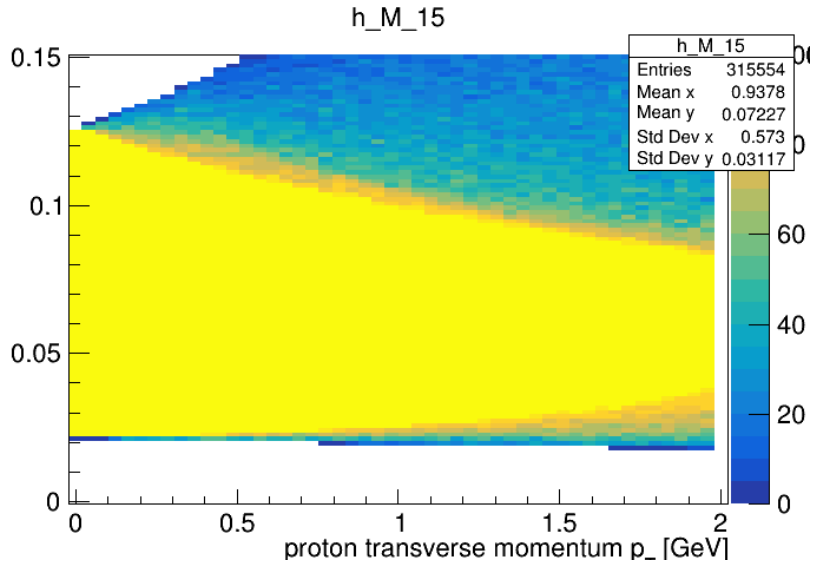

Figure A.4: The AFP geometric acceptance for 2022 LHC optics – $\sqrt{s} = 13.6$ TeV, $\beta^* = 0.6$ m and $\theta_C = 160$ μrad – as a function of proton transverse momentum (p_T) and its relative energy loss (ξ). The colour scale indicates the acceptance percentage.

optics.

As mentioned in Section A.1, several elements between ATLAS IP and AFP may change proton trajectory. For simplicity, one can assume that each such element has four[1] degrees of freedom: (x, y, z) position and the magnet strength K. The stand-alone transport tool (see Sec. A.2) allows easy modification of these variables to check their influence on the proton trajectory.

Besides the proton position registered in both AFP stations, there are several more constraints which can be used:

- data about the shifts of the elements (measurements of positions over years) stored in the *Geode* database,
- information about the beam centre as measured by the Beam Position Monitors (BPMs); stored in *TIMBER* database,
- real pot position: rotation (survey), thin window bulkiness, *etc.* (see Chapter B),
- beam-spot position as measured by ATLAS.

[1]Other degrees of freedom, as *e.g.* tilt, or effects as *e.g.* fringe fields are expected to be of 2^{nd} order correction, thus are not considered.

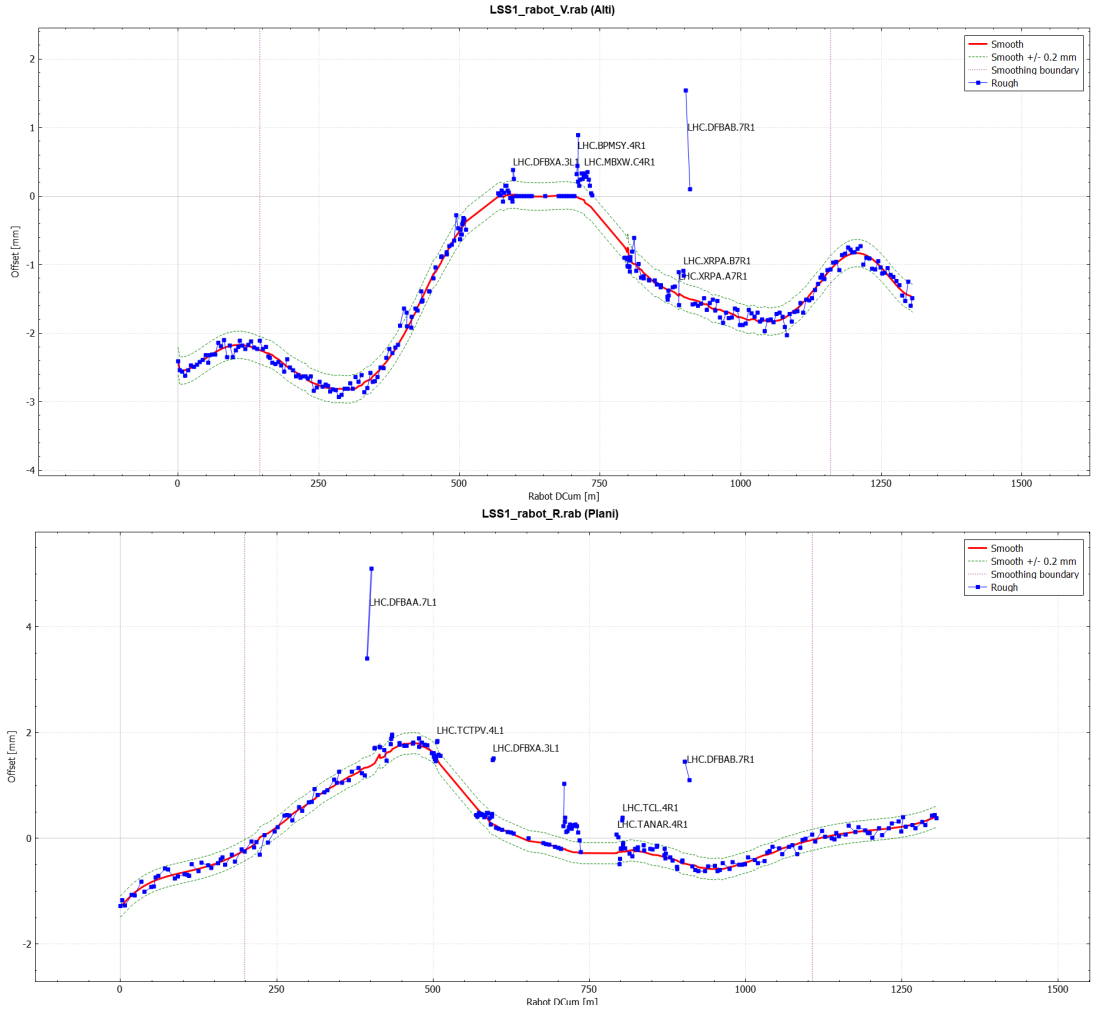

Figure A.5: Vertical (**top**) and horizontal (**bottom**) positions of LHC elements as measured during the 2022 laser survey campaigns. ATLAS collision point is located around 650 m.

A.7.1 LHC Laser Surveys

Positions of the LHC elements are periodically measured. During Run 3, the measurements are performed yearly – every Year End Technical Stop (YETS). However, not all elements are measured each time. This is especially true for the inner triplet region, where high radiation prevents the work.
For the data taken in 2022, the last survey of the full straight section (with the exceptions mentioned above) was done in February 2023. The measured positions of magnets on the C side of ATLAS (beam 1) are listed in Table A.6.
It should be mentioned that the elements seem to drift during the year. This is visible when data from various survey campaigns are considered – see Fig. A.6. It is interesting to see if and how these shifts impact the proton trajectory. The concept is shown in Fig. A.7. Figure A.8 (left) shows "ideal" proton trajectories (no shifts). Fig. A.8 (right) was done assuming that:

- (x, y, z) position of all dipoles and quadrupoles changed accordingly to the 2023 survey measurement,
- kickers' positions were unchanged,
- no variation in the magnet strength was applied.

The effect is evident. However, one can expect that since the LHC machine managed to keep the beam orbit closed despite such large deviations, the shifts are effectively corrected by adjusting the magnetic fields and switching on the correctors (kickers).

A.7.2 Beam Position Monitors

Before discussing the effect of field modification, it is worth considering additional useful constraints coming from the Beam Position Monitors (BPMs). All such elements located in the LHC straight section on ATLAS side C are listed in Table A.7.
The BPM measurement is expected to be quite stable and precise (relative precision is expected to be $O(20\ \mu m)$). This can be seen in Fig. A.9, where the readouts taken for about 2 hours are presented. During that time, the beams were colliding in ATLAS. Unfortunately, the absolute beam position is expected to be less known – of the order of 200 μm.

A.7.3 Real Magnet Strengths

"Real" settings of the LHC magnets' currents are also stored. Since the access to the values is not as straightforward as in the BPMs case, those listed in Table

Table A.6: Positions of LHC beam 1 magnets in the vicinity of the ATLAS collision point measured during the February 2023 survey campaign.

Element	Element name	Z [m]	shift in x [mm]	shift in y [mm]	shift in z [mm]
Quadrupole	MQXA.1R1.E:	22.965	-0.009	0.007	3.036
	MQXB.A2R1.E:	29.602	0.021	-0.003	3.036
	MQXB.B2R1.E:	29.617	0.021	-0.003	3.036
	MQSX.3R1.E:	32.05	0.019	0.016	-0.585
	MQXA.3R1.E:	37.779	0.049	0.023	-0.585
	MQY.4R1.E:	37.794	0.049	0.023	-0.585
	MQML.5R1.E:	38.55	0.053	0.024	-0.585
Dipole	MBXW.A4R1.E:	46.4965	0.113	0.001	1.051
	MBXW.B4R1.E:	46.965	0.115	0.001	1.051
	MBXW.C4R1.E:	53.574	0.147	0.004	1.051
	MBXW.D4R1.E:	53.589	0.147	0.004	1.051
	MBXW.E4R1.E:	59.622	0.223	-0.038	-0.374
	MBXW.F4R1.E:	63.888	0.308	0.042	0.218
	MBRC.4R1.E:	68.154	0.247	-0.016	-0.164
Kickers	MCBXH.1R1.E:	72.42	0.292	0.001	0.678
	MCBXV.1R1.E:	76.686	0.178	-0.071	1.112
	MCBXH.2R1.E:	80.952	0.252	-0.099	0.779
	MCBXV.2R1.E:	153.175	0.152	-0.74	1.78
	MCBXH.3R1.E:	163.99	0.411	-0.927	-4.108
	MCBXV.3R1.E:	165.286	0.369	-0.985	-4.108
	MCBYV.A4R1.E:	166.582	0.327	-1.043	-4.108
	MCBYH.4R1.E:	167.853	0.286	-1.1	-4.108
	MCBYV.B4R1.E:	192.996	0.219	-1.225	-1.224
	MCBCH.5R1.E:	194.09	0.222	-1.241	-1.224

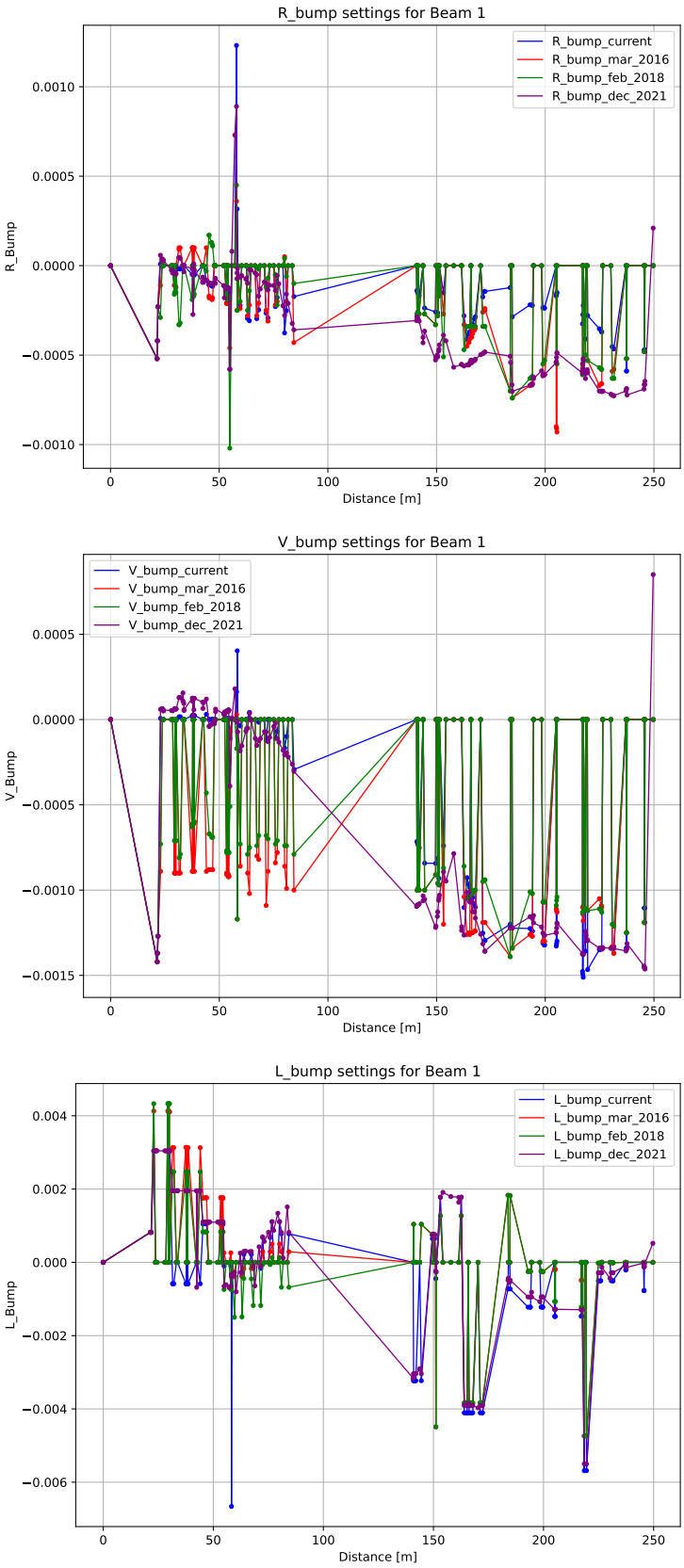

Figure A.6: Positions of the elements measured during various survey campaigns: 2016 (red line), 2018 (green), 2021 (magenta) and 2023 (blue). **Top** figure shows horizontal (radial), **middle** vertical and **bottom** longitudinal displacement. ATLAS collision point is at 0.

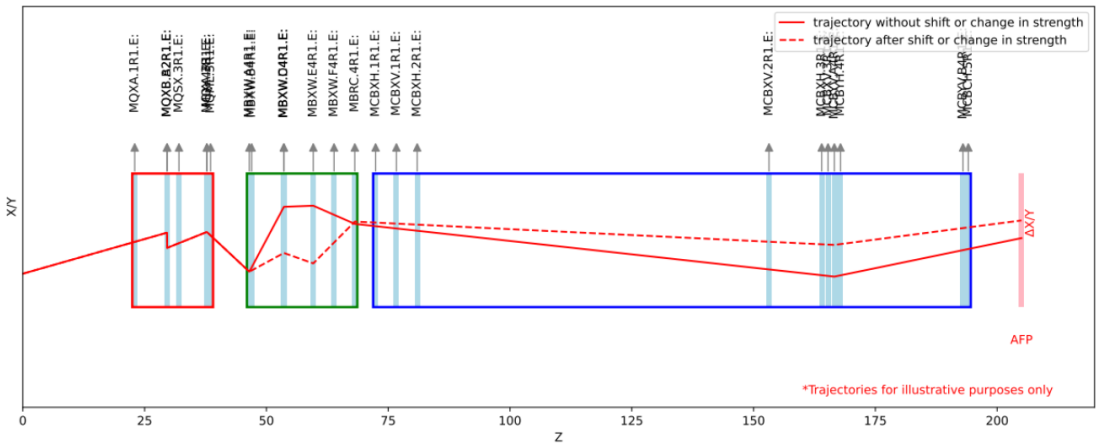

Figure A.7: Illustration of the influence of magnet shift on the proton trajectory.

Table A.7: List of BPMs installed on a beam 1 in the vicinity of the ATLAS IP. Readouts (mean readout in period 23/09/22 12:58:32 – 22:02:23) were taken from the TIMBER database. One of them could not be located, and its data should be read out using the ATLAS COOL database.

BPM name Twiss	z-position [m]	In Timber	$\bar{x}$ [mm]	$\bar{y}$ [mm]
BPMSW.1R1.B1_DOROS	21.564	✓	-0.322	-2.743
BPMWF.A1R1.B1	21.697	✓	0.982	3.866
BPMS.2R1.B1	31.529	✓	-0.322	-5.329
BPMSY.4R1.B1	58.2545	✓	-0.322	-4.297
BPMWB.4R1.B1	151.095	✓	0.478	-3.187
BPMYA.4R1.B1	172.227	✓	0.101	-1.357
BPM.5R1.B1	199.635	✓	-0.459	-1.579
BPMSA.A6R1.B1	217.6105	**X**	-	-
BPMR.6R1.B1	231.535	✓	-0.143	-0.424

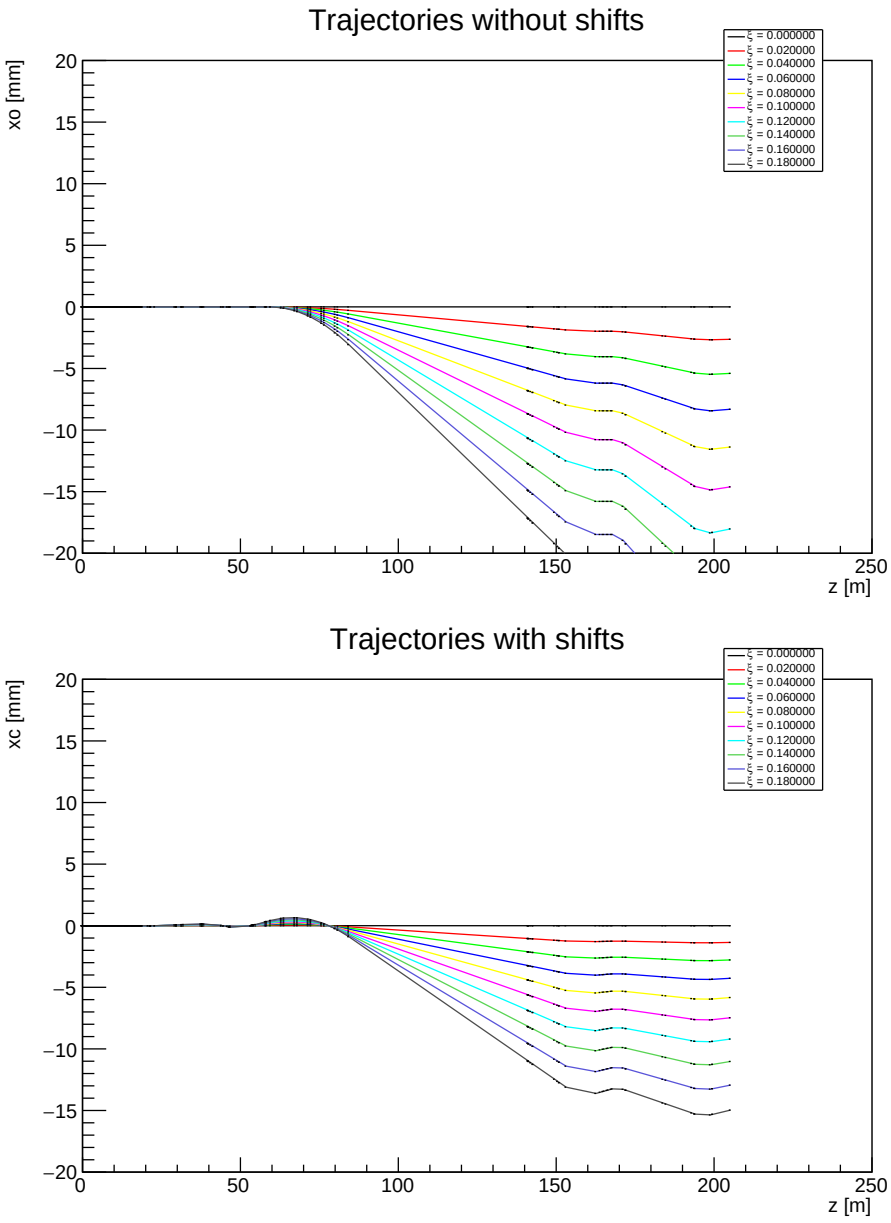

Figure A.8: Proton trajectories: "ideal" (no shifts, **left**) and assuming shifts of dipoles and quadrupoles (but no change in the field strength; **right**).

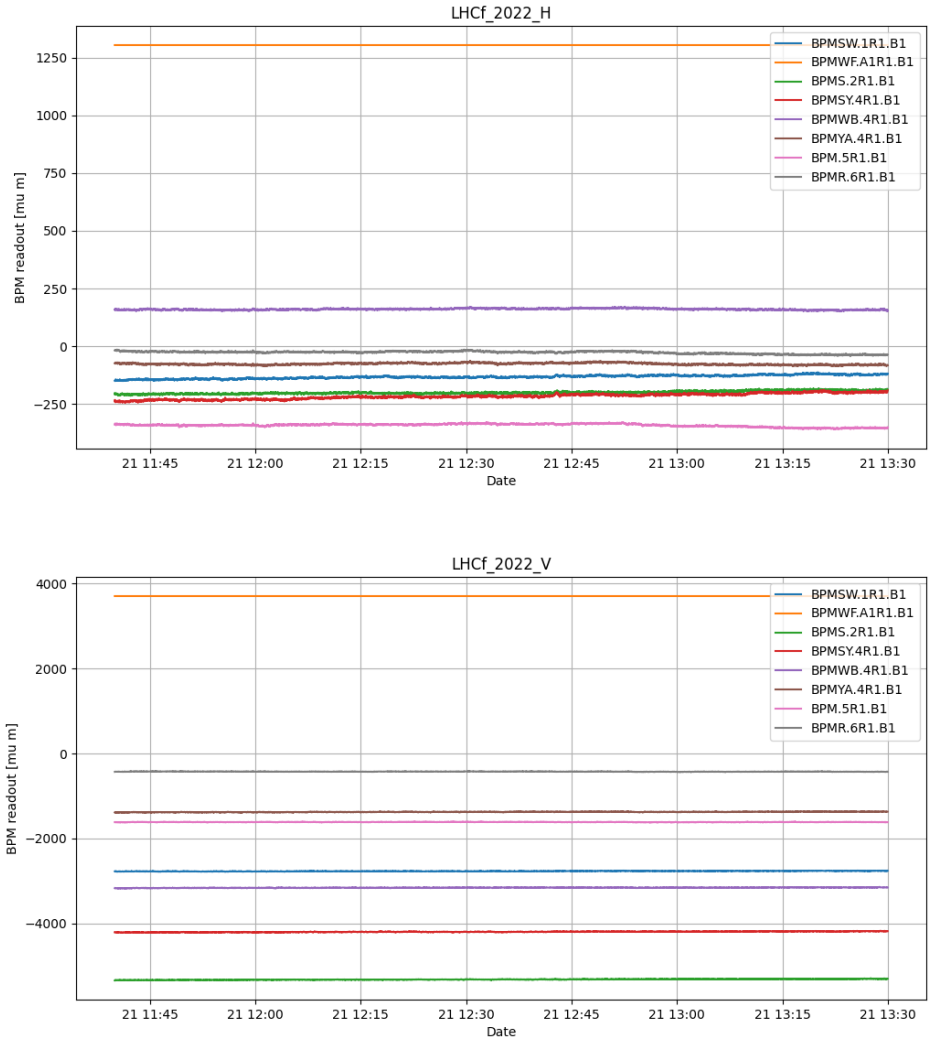

Figure A.9: Position of the beam measured by various BPMs located in the vicinity of the ATLAS collision point during the period of proton collisions.

A.8 were provided by the LHC machine experts. Unfortunately, these values were delivered with the advice against using them in any analysis since they have been tuned to correct local magnetic field errors. Indeed, it was checked that usage of these values for the proton transport resulted in much larger deviations from the "true optics" than using the MAD-X design ones.

Table A.8: "Real" strengths of LHC magnets as provided by the machine experts. "Ideal" MAD-X values are listed for comparison.

Element	Real Values	MADX Values
MQXA1.R1	0.008716056391	0.05552
MQXA3.R1	0.008749034449	0.05591
MQXB2.R1	-0.008774017907	-0.04820
MQY.4R1.B1	-0.003486105265	-0.01185
MQML.5R1.B1	0.001995968302	0.00958
MCBXH.1R1	5.55E-06	1.15E-21
MCBXV.1R1	-1.64E-05	6.27E-6
MCBXH.2R1	3.27E-06	1.15E-21
MCBXV.2R1	-1.29E-05	6.27E-6
MCBXH.3R1	1.26E-05	1.15E-21
MCBXV.3R1	-2.25E-05	6.27E-6
MCBYV.A4R1	3.87E-06	-1.77E-5
MCBYH.4R1	-5.90E-07	-7.82E-21
MCBYV.B4R1	-1.44E-05	0

A.7.4 First Attempt of the "True Optics" Determination

Having information about the possible range of the LHC elements shifts and beam position measured by BPMs, one can try to determine a set of values of the magnetic field which will describe the data. This can be done by minimizing $\Sigma(calculated\,x\,position - BPM\,x\,position)^2 + \Sigma(calculated\,y\,position - BPM\,y\,position)^2$, where:

- (x, y, z) position of each magnet is randomly generated within the range coming from the laser survey,
- field strength of each magnet is randomly generated with $\pm 5\%$ of the "ideal" value.

After the simulation of 10000 cases, 117 "true optics" candidates (*i.e.* the ones which had $\chi^2 \approx 1$) were identified. The difference between "ideal" and "true" optics in predicting x and y position in the AFP NEAR and FAR stations is shown in Fig. A.10.

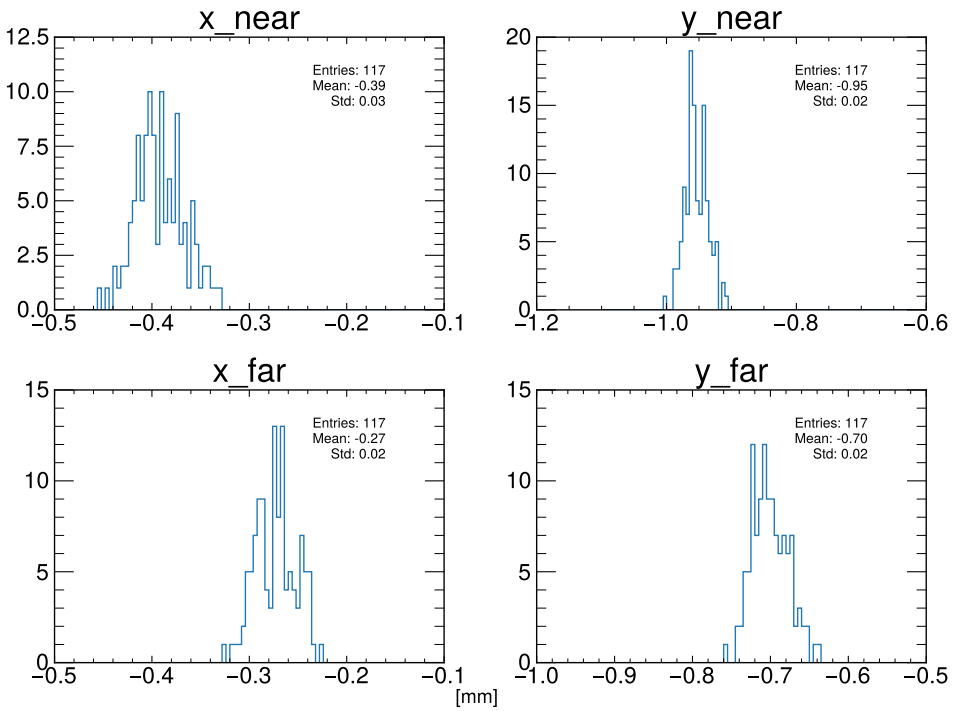

Figure A.10: The difference between "ideal" and "true" optics predictions of x (**left**) and y (**right**) positions in the AFP NEAR (**top**) and FAR (**bottom**) stations.

Many of the above solutions were found for quite large variations of magnet strengths (O(5%)). From past analyses performed (see *e.g.* [96]), the magnets are expected not to vary more than a few ‰. Restricting the generation criteria to 5‰ resulted in fewer solutions, from which 3 exemplary are listed in Table A.9. The Proton trajectories for these solutions are plotted in Fig. A.11.

A.7.5 Summary and Outlook

The first approach to determine the "true" optics was encouraging: combining information about the magnet position as measured during the laser surveys with the infraction coming from the BPMs allowed for the selection of a few optics candidates. Unfortunately, in the light of clear deviations from the BPMs values leading to rather high χ^2 values (especially in the case of y), there are several points to be addressed. To mention:

- positions of BPMs seem to indeed have some systematic shifts $\rightarrow$ their straightforward usage, as was done in the above studies, may not be a good approach; a dedicated study to determine better their absolute position should be done,

Table A.9: Strengths of the magnets for solutions best matching the BPM readouts.

element	$\chi_x^2 = 0.913, \chi_y^2 = 4.287$	$\chi_x^2 = 0.879, \chi_y^2 = 4.118$	$\chi_x^2 = 0.873, \chi_y^2 = 4.249$
MQXA.1	0.999113	0.999886	0.996377
MCBXH.1	0.998485	1.00016	0.997472
MCBXV.1	1.00389	1.00245	1.00122
MQXB.A	0.999174	0.996996	0.995982
MCBXH.2	1.00281	0.999389	1.00049
MCBXV.2	0.998642	0.995412	1.00355
MQXB.B	0.996697	0.995763	0.996311
MQSX.3	1.00464	1.00336	1.00074
MQXA.3	1.00346	0.998373	1.00204
MCBXH.3	1.00068	1.00472	1.00027
MCBXV.3	0.997718	1.00156	1.00013
MBXW.A	1.00272	1.00448	1.00291
MBXW.B	0.999406	1.00359	0.999741
MBXW.C	1.00366	1.00333	1.00262
MBXW.D	1.00476	1.0004	1.00321
MBXW.E	1.00086	1.00291	1.00353
MBXW.F	1.00208	1.00454	1.00492
MBRC.4	0.996608	0.996038	0.996261
MCBYV.A4	0.996874	0.998025	1.00249
MCBYH.4	0.996138	0.99819	1.00041
MCBYV.B4	0.996761	1.00185	1.00089
MQY.4	1.00171	0.996187	1.00129
MCBCH.5	1.00159	0.995407	0.999947
MQML.5	0.995391	0.997161	0.996548

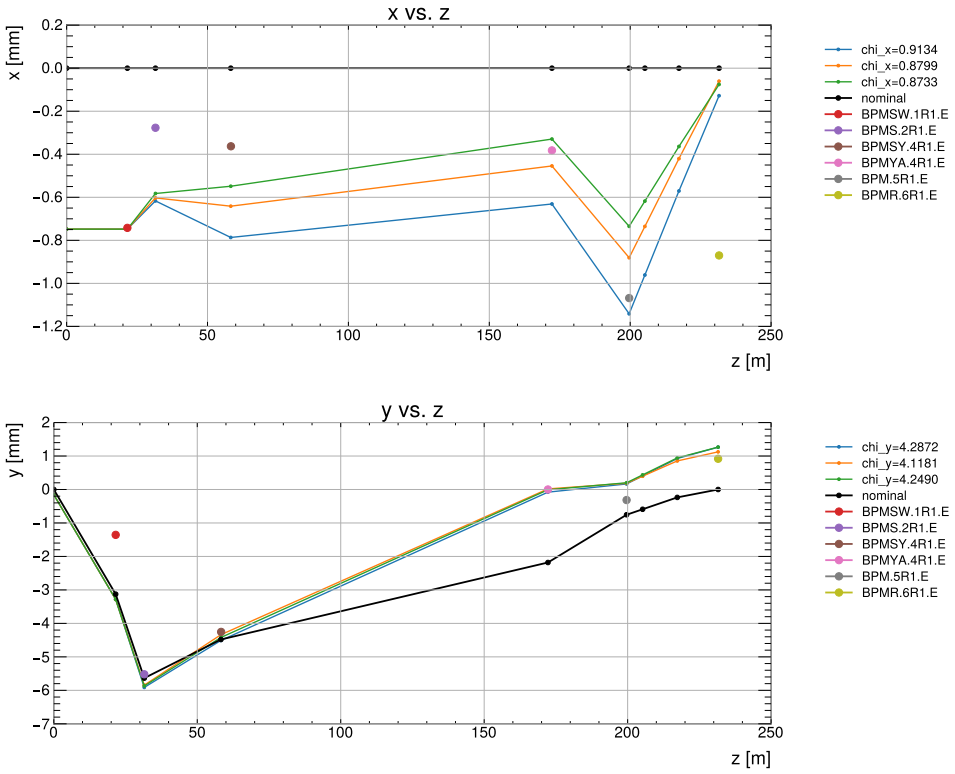

Figure A.11: Proton trajectories: "ideal" optics in black, "true" optics candidates in green, orange and blue. The BPM readouts are shown as colour dots.

- information from various data-taking periods, especially from BBA, should be commonly considered to obtain better precision as the optics is not expected to change during the year,
- properties of optics visible in the AFP, like diffractive hotspot, should be used,
- the information about the beam-spot position should be considered.

Unfortunately, addressing the above points was beyond the timescale of my PhD project. These studies are continued by other Colleagues from the AFP Proton Combined Performance group.

Appendix B

Pot Rotation

The mechanical complexity of the Roman Pot system introduces several challenges that must be thoroughly understood and quantified. The primary concern stems from the potential rotation of these detector vessels during their insertion movement, which can significantly impact the effective distance between the detector components and the beam. This rotation effect, if not properly accounted for, introduces systematic uncertainties in the measurement of proton trajectories and their kinematic properties.

Furthermore, the global displacement of the entire detector stations relative to their designed positions represents another critical aspect requiring detailed investigation. These displacements can arise from various sources, including installation procedures, mechanical stress and environmental factors. The cumulative effect of these positioning variations directly influences the detector acceptance and the precision of physics measurements.

Traditional beam-based alignment procedures, while providing operational reference points, may not fully account for the complex mechanical effects of the pot movement. The discrepancies observed between different alignment techniques necessitate a comprehensive investigation of the underlying mechanical behaviour of the detector system.

Understanding the long-term stability of the detector positioning and potential systematic effects is crucial for maintaining consistent measurement quality throughout extended data-taking periods. Moreover, the mechanical behaviour of the Roman Pot system during insertion and retraction cycles may evolve in time due to various factors such as mechanical wear, thermal effects or radiation exposure. Quantifying these effects and their impact on the detector positioning provides an essential input for both operational procedures and physics analyses.

B.1 Measurement Methodology

The first systematic measurements of the pot rotation during the movement were conducted in 2017 using survey laser techniques. In these measurements, the reference markers were positioned at the Right Top (RT) position of each pot (see Fig. B.2). While these measurements provided initial insights into the pot

behaviour, they were limited by the single-point measurement approach.
A significant advancement in the measurement methodology was implemented in 2018/2019, where three distinct measurement positions were selected, see Fig. B.1: E (positioned slightly above the Left Top), M (middle position on top) and S (positioned slightly above the Right Top). The survey methodology incorporated precise tracking of the motor positions and LVDT readings, stored in the LHC TIMBER and ATLAS DCS databases. This approach was particularly significant as it established the movement calibration from the initial motor position, referred to as the 0^{th} motor step.

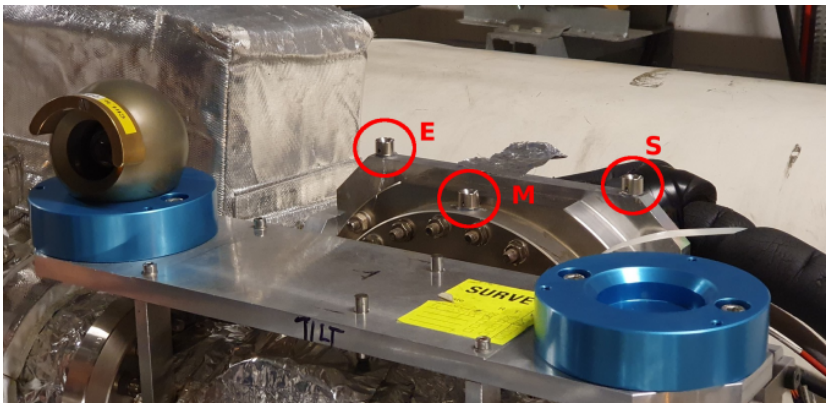

Figure B.1: Survey measurement of the positions implemented in 2019: inlet (E – *fr.* entrée), middle (M – milieu) and outlet (S – sortie) reference points positioned along the top surface of the Roman Pot. This configuration enabled precise tracking of pot rotation through multiple measurement positions, with coordinates recorded relative to the beam pipe centre.

In parallel with the survey measurements, dedicated studies were conducted in 2019 and 2020 using a calibrated SICK laser system. This measurement campaign established four precise reference points on each pot's surface: Left Top (LT), Right Top (RT), Left Bottom (LB) and Right Bottom (RB) B.2. These measurements were performed while the pots were moved through their operational range, enabling a detailed analysis of the position-dependent effects.
The measurement program continued with refined survey campaigns in 2021 and 2023. These surveys maintained the four-point reference system established during the SICK laser measurements but incorporated improved calibration procedures, see Fig. B.3. The 2021 survey, conducted after the installation of the detector packages for Run 3, established the baseline measurements for the new operational period. The November 2023 campaign provided comparative data to assess temporal stability and systematic changes in the mechanical system.
The comprehensive nature of these measurements, spanning multiple years and employing various technical approaches, provided the foundation for a detailed analysis of the pot rotation effects and their impact on the physics measurements.

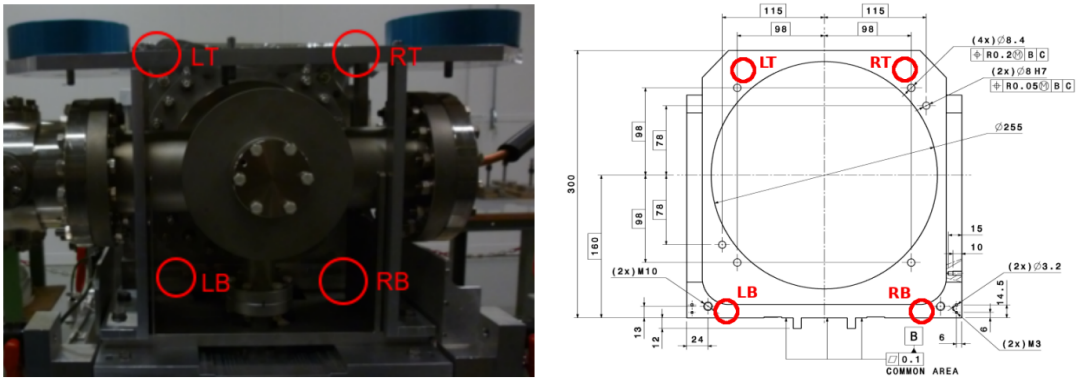

Figure B.2: The measurement reference points for the pot rotation analysis: Left Top (LT), Right Top (RT), Left Bottom (LB) and Right Bottom (RB) positions shown on the Roman Pot mechanical assembly (left) and technical drawing (right). These points were established during the 2019–2020 SICK laser measurement campaign to characterize the pot rotation effects during the insertion movements.

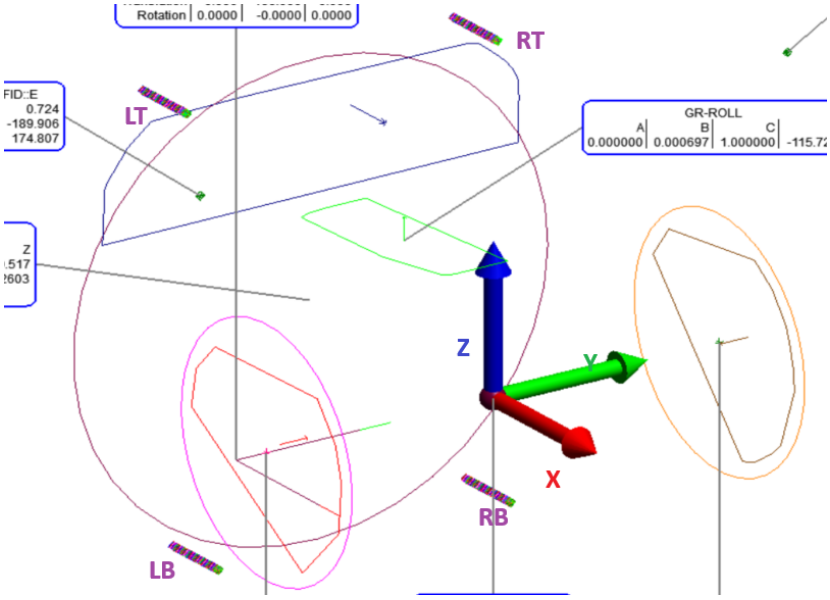

Figure B.3: Standardized coordinate system used for the pot rotation measurements: x-axis aligned with pot movement direction (radial), y-axis parallel to beam direction (longitudinal) and z-axis oriented vertically. The measurement reference points (LT, RT, LB, RB) are indicated in purple and positioned at the corners of the pot flange surface. This coordinate convention was consistently maintained across all survey campaigns to ensure measurement compatibility and facilitate comparative analyses.

The evolution from initial single-point surveys to comprehensive multi-point analyses reflects the increasing sophistication in understanding pot mechanical behaviour and its implications for detector positioning accuracy.

B.2 Indication of Pot Rotation

Upon the installation in the tunnel, the pot was expected to move in parallel to the beam. This should have been ensured by the precise roll system [54]. Unfortunately, the first physics results [85] indicated the difference between the expected and measured position of the Roman pots. The effect might have come from several sources, like different-than-assumed LHC optics (see Section A.7), thermal extensions or pot rotation. Indeed, dedicated studies of the pot behaviour during its insertion, see Fig. B.4, indicated that the pot does not slide completely parallelly. This was caused by the significant force due to the spring-extraction system – see Fig. B.5.

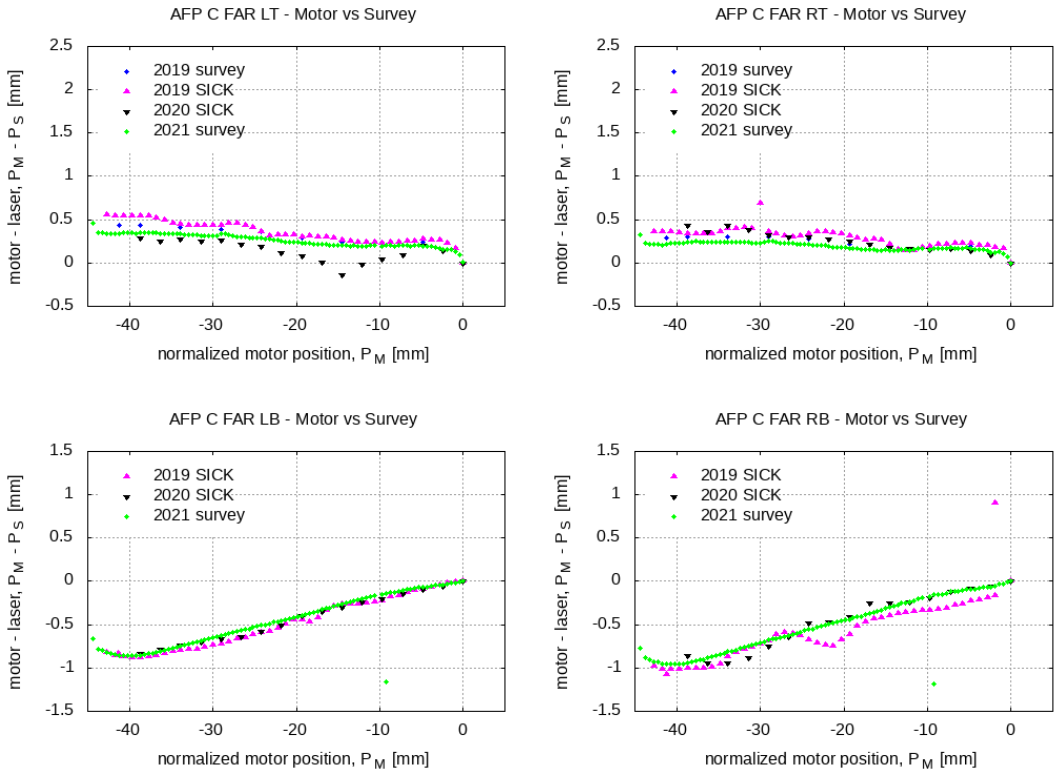

Figure B.4: The difference between the expected (motor) and measured (laser) position of the Roman pot as a function of the motor position. The data from the 2019–2021 survey campaigns are plotted for various reference points on pot. The C FAR station was taken as an example. See text for details.

In Fig. B.4, a difference between the expected (motor) and measured (laser) positions of the Roman pot as a function of the motor position is plotted using

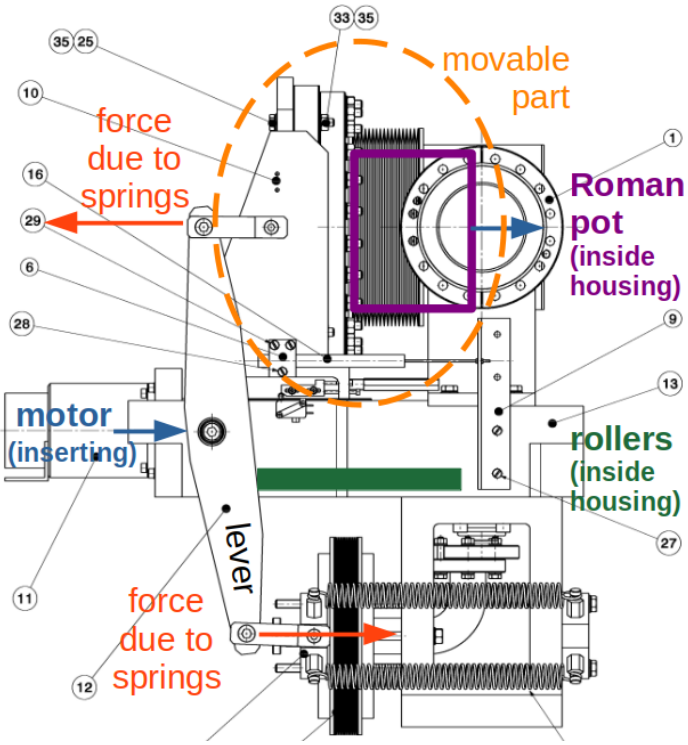

Figure B.5: Drawing of the AFP Roman pot station as viewed from the side. The force due to the emergency spring extraction system acts oppositely to that created by the motor for the pot insertion. The points of the force application may cause the pot rotation during the insertion.

data from the 2019–2021 survey campaigns. The value $P_M = 0$ indicates that the pot is fully extracted, *i.e.* it should be a situation where there is no (or very small) force from extraction springs. The laser readout is normalized in such a way that at $P_M = 0$, it matches the motor. It is evident that the more pot is inserted, the higher the deviation between the motor and laser is. Moreover, the difference becomes positive for both top points and negative for both bottom ones. This means that, as being inserted, the top part of the pot is further from the beam than the bottom part – a clear sign of pot rotation.

In the first approximation, the dependence seems to be linear, with an exception at the $P_M > 40$ mm when some non-linear effect seems to happen. These non-linearities are explained to originate from the fact that at this point, the top pot bellow is highly compressed, which may create additional forces. The linear fit results, for the example of the Left Top (LT) point for all stations, are listed in Table B.1.

Table B.1: The linear fit results for the Left Top (LT) point for all AFP stations for data taken during 2019 – 2921 survey campaigns.

Station	Campaign	Intercept	Slope
A NEAR	2019 Surv	0.028 ± 0.017	-0.00457 ± 0.00078
	2019 SICK	0.029 ± 0.010	-0.00533 ± 0.00044
	2020 SICK	-0.162 ± 0.108	-0.01409 ± 0.00462
	2021 Surv	0.052 ± 0.004	-0.00544 ± 0.00016
A FAR	2019 Surv	0.084 ± 0.034	-0.00084 ± 0.00159
	2019 SICK	0.095 ± 0.078	-0.00326 ± 0.00326
	2020 SICK	0.095 ± 0.024	-0.00228 ± 0.00105
	2021 Surv	0.123 ± 0.005	0.000277 ± 0.00020
C NEAR	2019 Surv	0.046 ± 0.020	-0.00233 ± 0.00085
	2019 SICK	0.201 ± 0.085	-0.00244 ± 0.00339
	2020 SICK	-0.050 ± 0.018	-0.00547 ± 0.00078
	2021 Surv	0.165 ± 0.007	-0.00480 ± 0.00029
C FAR	2019 Surv	0.106 ± 0.034	-0.00936 ± 0.00147
	2019 SICK	0.156 ± 0.013	-0.00928 ± 0.00055
	2020 SICK	0.004 ± 0.044	-0.00681 ± 0.00196
	2021 Surv	0.106 ± 0.024	-0.00666 ± 0.00105

B.3 Pot Rotation Analysis

The analysis of the pot rotation effects was conducted using two distinct methodological approaches. This section details both the initial methodology used for determining the left-right and top-bottom differences and the refined approach developed for determining the true beam touching point. A fundamental aspect of the analysis framework was the establishment of a consistent coordinate system across all measurement campaigns. The spatial coordinates of the reference points were recorded in a three-dimensional system where x represents the pot movement direction, y aligns with the beam direction, and z corresponds to the vertical axis, as shown in B.3.

The initial analytical approach focused on two primary aspects of the pot rotation: left-right and top-bottom differences. Figure B.6 presents a schematic view of the left-right rotation measurement methodology across all four AFP stations relative to the interaction point (IP), while Figure B.7 demonstrates the top-bottom rotation measurement in the $x - z$ plane.

For the left-right rotation analysis, the differences between x- coordinates of the left (LT/LB) and right (RT/RB) points were computed. The results are listed in the Table B.2. A positive value indicates that the left side of the pot (when viewed from the ring centre) was positioned closer to the beam. This is the C FAR

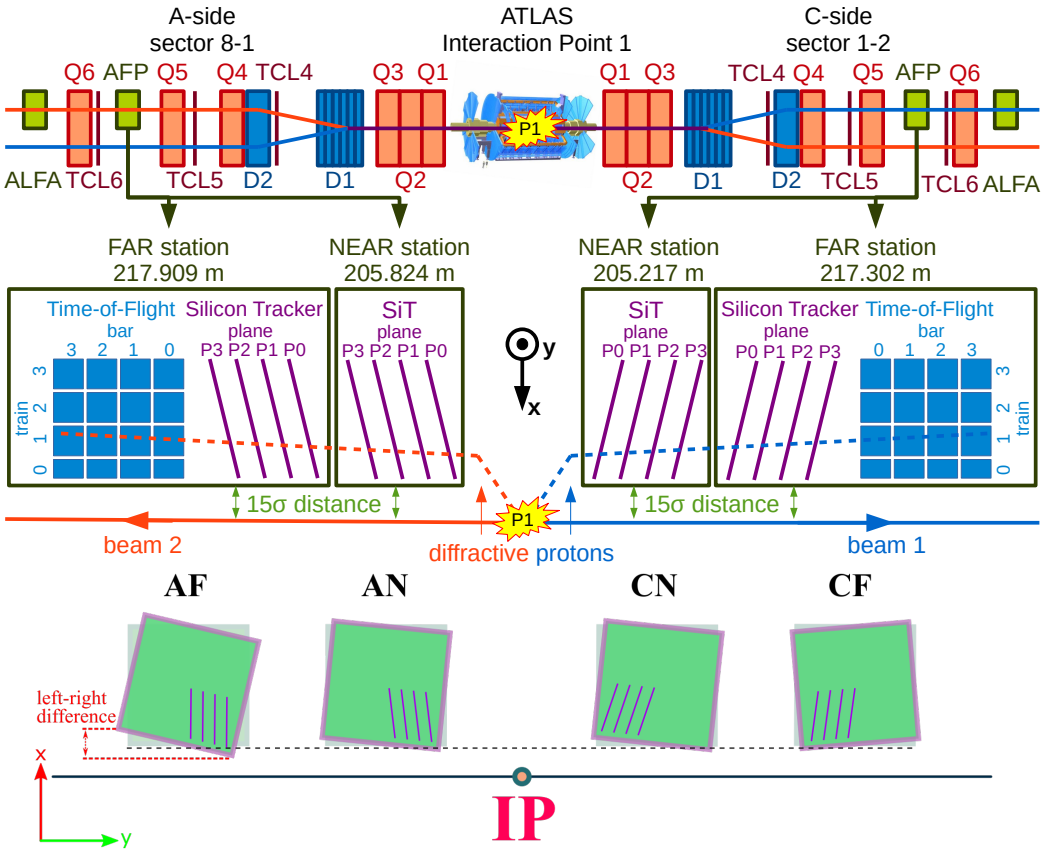

Figure B.6: **Top**: a sketch of the AFP placement around ATLAS. **Bottom:** a schematic representation of the left-right rotation measurement for all four Roman Pot stations (AF: A Far, AN: A Near, CN: C Near, CF: C Far) relative to the interaction point (IP). The (x, y) coordinate system and measurement reference points are shown, with the left-right difference indicated by the red dotted lines. The green rectangles represent the detector planes, and the vertical purple lines indicate 4 planes of SiT.

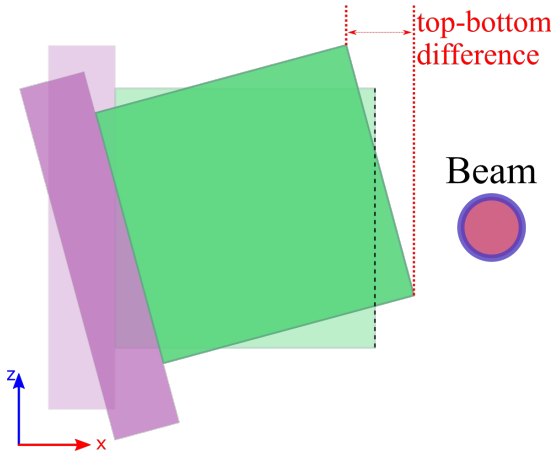

Figure B.7: The $x-z$ cross-section showing the top-bottom rotation measurement methodology. The difference between the top and bottom positions (indicated by red dotted lines) is measured relative to the beam position. The green rectangle represents the detector plane in its rotated state. The coordinate system demonstrates the radial (x) and vertical (z) measurement axes.

(CF) station case. In the other cases, the right side is closer to the beam. This rotation may affect the proton reconstruction for the C NEAR station – the SiT detectors are further from the beam compared to what would be expected from the Beam Based Alignment (and no rotation). This implies effectively smaller acceptance – an effect at the level of 5–10 SiT pixels. For the other stations, the part of the pot where SiT detectors are located would touch the beam first.
Differences between the "top" and "bottom" for a given year are small – at the level of 10 μm, which seems to be a reasonable effective precision of the survey. Except for the C NEAR (CN), for which it is about 60 μm in 2023. The differences between 2021 and 2023 for the A NEAR (AN) station are of the order of 10 μm (although in 2023, it seems to be slightly more rotated). For the A FAR (AF) and C FAR (CF) stations, these are about 40 μm and C NEAR of about 120 μm, respectively. This seems not to be an effect of the station's "global" rotation but points to the real change of the pot movement while inserted.

Table B.2: The left-right rotation measurements expressed as differences between the x-coordinates of the left (LT/LB) and right (RT/RB) points in mm for all stations in 2021 and 2023. Positive values indicate that the left side is further from the beam.

Survey		AF [mm]	AN [mm]	CN [mm]	CF [mm]
2021	Top	-0.193	-0.044	-0.245	0.080
	Bottom	-0.180	-0.034	-0.243	0.068
2023	Top	-0.140	-0.053	-0.441	0.025
	Bottom	-0.136	-0.057	-0.379	0.037

The top-bottom rotation analysis was performed in the same manner. The difference between the x-coordinates of the top (RT/LT) and bottom (RB/LB) points were calculated. The results are listed in Table B.3.

Table B.3: The top-bottom rotation measurements showing differences between the x-coordinates of the top (RT/LT) and bottom (RB/LB) points in mm for all stations in 2021 and 2023. Positive values demonstrate the bottom side's positioning nearer to the beam relative to the top. Negative values, while not observed in the presented data, would indicate the top side being closer to the beam.

Survey		AF [mm]	AN [mm]	CN [mm]	CF [mm]
2021	Left	0.595	0.547	0.656	0.646
	Right	0.604	0.554	0.657	0.638
2023	Left	0.547	0.521	0.749	0.684
	Right	0.549	0.519	0.791	0.693

Positive values indicate that the bottom side is positioned closer to the beam. This is the case for all pots. For each station, the differences between the left and right are of about 10 μm. The difference between years is at the level of 50 μm; except for the C NEAR where it is around 100 μ (similar remarks as in the "left-right" discussion). Assuming that the beam is in the middle of the pot, the value has to be divided by 2 to obtain the touching point.

B.4 "True" Beam Touching Point

The Beam Based Alignment procedure (see Section 3.3.2) is based on a pot touching the precisely-known beam. To investigate how the rotation would impact the BBA, a three-dimensional spatial analysis of the pot surface when moving in was performed.

The methodology employs a mathematical construction of the pot plane using three measurement points. This approach begins with the fundamental assumption that the pot surface can be represented as a plane in three-dimensional space. The selection of three points from the available four reference points (LT, RT, LB, RB) defines this plane uniquely. To validate this approach, multiple combinations of three points were tested, with the resulting variations in plane definition not exceeding 10 μm, confirming the robustness of the method.

For determining the true beam touching point, a simulation framework was developed incorporating realistic parameter ranges:

- x-coordinate (pot movement direction): -38.0 to -44.0 mm,

- y-coordinate (beam direction): $\pm$(71 to 74) mm, with sign depending on the station,
- z-coordinate (vertical): -2.0 to 2.0 mm.

A crucial aspect of this methodology is its ability to account for the non-uniform insertion of pots, where different parts of the pot surface may reach the beam at different nominal positions. This effect is particularly significant for understanding the true beam centre position during the BBA procedures and its implications for detector acceptance calculations.
The simulation systematically explored the above parameter space to determine potential beam-pot intersection points. This analysis revealed that while the range of possible touching points depends on initial conditions, the standard deviation remains consistently around 50 μm for each pot and BBA configuration. As an example, the result of the analysis of the A NEAR station is shown in Fig. B.8.

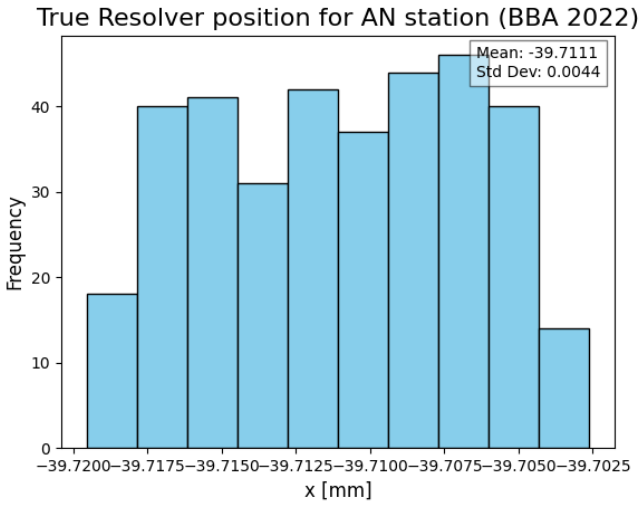

Figure B.8: The "true" touching point analysis: position of the resolver (motor) for cases when the A NEAR would touch the beam during the 2022 BBA, assuming the rotation effect.

Using this method, all the AFP Beam-Based Alignments done in 2022 and 2023 were evaluated. Table B.4 shows the result obtained using the 2021 survey data, while in Table B.5, 2023 measurements are shown.

B.5 Uncertainty Discussion

Several sources of uncertainty were identified. The primary contribution to the measurement precision comes from the top-bottom rotation uncertainties for a

Table B.4: Determination of the "true" touching point for various AFP Beam-Based Alignment campaigns using the 2021 laser survey data.

BBA Name	Station	BBA Resolver position	True Resolver position	BBA resolver - True resolver	BBA beam center x	True beam center x	beam x diff	Uncertainty
BBA_2022	CF	0.879	0.0827141	0.796286	0.568	-0.229136	0.797136	0.00554711
BBA_2022	CN	1.492	0.931369	0.560631	0.991	0.429529	0.561471	0.00598457
BBA_2022	AF	1.337	0.862391	0.474609	0.971	0.498991	0.472009	0.00495027
BBA_2022	AN	1.298	0.959714	0.338286	0.756	0.416064	0.339936	0.00420332
BBA_2023	CF	0.992	0.197562	0.794438	0.517	-0.277718	0.794718	0.00560159
BBA_2023	CN	1.532	0.97087	0.56113	0.973	0.41207	0.56093	0.00567649
BBA_2023	AF	1.288	0.812591	0.475409	0.778	0.301711	0.476289	0.00505321
BBA_2023	AN	1.273	0.934843	0.338157	0.831	0.492843	0.338157	0.004415
BBA_2023_mu_005	CF	1.83	1.04314	0.786863	0.465	-0.323013	0.788013	0.00518017
BBA_2023_mu_005	CN	2.4	1.85116	0.548836	0.811	0.263864	0.547136	0.00576991
BBA_2023_mu_005	AF	2.094	1.62986	0.464141	0.64	-0.106441	0.746441	0.00475016
BBA_2023_mu_005	AN	2.268	1.93877	0.329227	0.568	0.513773	0.054227	0.00438438
BBA_2022_LHCf	CF	1.87	1.08415	0.78585	0.418	-0.36796	0.78596	0.00532539
BBA_2022_LHCf	CN	2.498	1.95022	0.547776	0.776	0.229724	0.546276	0.00568786
BBA_2022_LHCf	AF	2.134	1.67038	0.463622	0.708	0.245378	0.462622	0.00482305
BBA_2022_LHCf	AN	2.239	1.91004	0.328958	0.578	0.248922	0.329078	0.00443491

Table B.5: Determination of the "true" touching point for various AFP Beam-Based Alignment campaigns using the 2023 laser survey data.

BBA Name	Station	BBA Resolver position	True Resolver position	BBA resolver - True resolver	BBA beam center x	True beam center x	beam x diff	Uncertainty
BBA_2022	CF	0.879	0.108144	0.770856	0.568	-0.203706	0.771706	0.00548502
BBA_2022	CN	1.492	1.05549	0.436514	0.991	0.553646	0.437354	0.00719677
BBA_2022	AF	1.337	0.848673	0.488327	0.971	0.485273	0.485727	0.00465511
BBA_2022	AN	1.298	0.960413	0.337587	0.756	0.416763	0.339237	0.00441287
BBA_2023	CF	0.992	0.222717	0.769283	0.517	-0.252563	0.769563	0.00586873
BBA_2023	CN	1.532	1.09556	0.436443	0.973	0.536757	0.436243	0.00691825
BBA_2023	AF	1.288	0.799585	0.488415	0.778	0.288705	0.489295	0.00489177
BBA_2023	AN	1.273	0.935163	0.337837	0.831	0.493163	0.337837	0.0044378
BBA_2023_mu_005	CF	1.83	1.07095	0.759054	0.465	-0.295204	0.760204	0.00558691
BBA_2023_mu_005	CN	2.4	1.97343	0.426569	0.811	0.386131	0.424869	0.00695638
BBA_2023_mu_005	AF	2.094	1.61622	0.477782	0.64	-0.120082	0.760082	0.00452827
BBA_2023_mu_005	AN	2.268	1.93928	0.328725	0.568	0.514275	0.0537249	0.00435238
BBA_2022_LHCf	CF	1.87	1.11121	0.758788	0.418	-0.340898	0.758898	0.00574904
BBA_2022_LHCf	CN	2.498	2.07231	0.425691	0.776	0.351809	0.424191	0.00690497
BBA_2022_LHCf	AF	2.134	1.65677	0.477225	0.708	0.231775	0.476225	0.00452387
BBA_2022_LHCf	AN	2.239	1.91055	0.328454	0.578	0.249426	0.328574	0.00412147

given year ($\sigma_{TB}^{year}(left-right)$), which established a baseline precision of approximately 10 μm for all stations, representing the fundamental limit of the survey methodology.

The left-right rotation uncertainties ($\sigma_{LR}^{year}(top-bottom)$) demonstrated similar characteristics, typically maintaining 10 μm precision for most of the stations. However, the C NEAR one exhibited notably different behaviour, with uncertainties reaching approximately 60 μm in the 2023 measurements.

Variations between the 2021 and 2023 measurement campaigns were observed. The left-right rotation variations ($\sigma_{LR}(year)$) showed the station-dependent behaviour, with the A NEAR maintaining exceptional stability at 10 μm, while the A FAR and C FAR exhibited moderate changes of 40 μm. The C NEAR station demonstrated the most substantial temporal evolution, with variations reaching 120 μm.

The top-bottom rotation variations ($\sigma_{TB}(year)$) showed more uniform behaviour across the stations, with the A FAR, A NEAR and C FAR exhibiting approximately 50 μm variation. Again, the C NEAR station demonstrated larger variations, approaching 100 μm.

The plane definition uncertainty (σ_{plane}), derived by comparing different three-point combinations, remained consistently below 10 μm for all stations, validating the robustness of the plane-fitting methodology. The fiducial region uncertainty ($\sigma_{fiducial}$), determined through simulation of the beam touching points, maintained approximately 50 μm for each pot and BBA configuration.

The total rotational uncertainty, σ_{ROT}, was calculated using a comprehensive formula incorporating all identified uncertainty components:

$$\begin{aligned}\sigma_{ROT}^2 = &(\sigma_{LR}^{year}(top-bottom))^2 + (\sigma_{TB}^{year}(left-right))^2 \\ &+ (MAX(\sigma_{LR}(year), \sigma_{TB}(year)))^2 + \sigma_{plane}^2 + \sigma_{fiducial}^2.\end{aligned} \tag{B.1}$$

The obtained uncertainties for each station are listed in Table B.6.

Table B.6: The uncertainty components and the total rotational uncertainty for each station.

Uncertainty Component	A FAR	A NEAR	C NEAR	C FAR
$\sigma_{LR}^{year}(top-bottom)$	10	10	60	10
$\sigma_{LR}(year)$	40	10	120	40
$\sigma_{TB}^{year}(left-right)$	10	10	10	10
$\sigma_{TB}(year)$	50	50	100	50
σ_{plane}	10	10	10	10
$\sigma_{fiducial}$	50	50	50	50
σ_{ROT} [μm]	73	73	144	73

B.6 Global Displacement

As discussed in Section A.7.1, the position of all LHC elements are almost regularly measured by the survey team. This is also true for the AFP stations – during Run 3, the survey campaigns were usually carried out at the same time when the pot rotation was measured. The results are listed in Tab. B.7 and B.8 for the 2021 and 2023 surveys, respectively. On each station, two survey markers, named inlet and outlet, are placed. They are visible in Fig. B.1 – see blue "bowls" with a laser ball placed on the left one (inlet). The discussion on how to include observed significant differences for radial measurements (pot movement direction) between 2021 and 2023 is ongoing.

Table B.7: AFP position as measured during the laser survey on 13-Nov-2021.

Station	Radial [mm]	Vertical [mm]	Tilt [rad]	Longitudinal [mm]
C NEAR (inlet)	-0.537	-1.247	-0.000008	-1.283
C NEAR (outet)	-0.489	-1.196	-0.000008	-1.283
C FAR (inlet)	-0.584	-1.373	-0.000068	-1.293
C FAR (outet)	-0.520	-1.377	-0.000068	-1.293
A FAR (inlet)	1.264	-1.520	-0.000068	0.067
A FAR (outlet)	1.278	-1.511	-0.000039	0.067
A NEAR (inlet)	1.210	-1.437	-0.000039	-0.132
A NEAR (outlet)	1.172	-1.447	-0.000039	-0.132

Table B.8: AFP position as measured during the laser survey on 15-Feb-2023.

Station	Radial [mm]	Vertical [mm]	Tilt [rad]	Longitudinal [mm]
C NEAR (inlet)	-0.169	-1.328	0.000092	-1.476
C NEAR (outet)	-0.15	-1.299	0.000092	-1.476
C FAR (inlet)	-0.325	-1.477	0.000052	-1.469
C FAR (outet)	-0.223	-1.511	0.000052	-1.469
A FAR (inlet)	1.937	-1.529	0.000311	0.008
A FAR (outlet)	1.963	-1.516	0.000311	0.008
A NEAR (inlet)	1.802	-1.386	0.000211	-0.209
A NEAR (outlet)	1.776	-1.386	0.000211	-0.209

Using the mentioned above survey data, one can calculate the "global" station rotation. The results are given in Tab. B.9. Comparison of these to the results of the pot rotation analysis (*cf.* Tab. B.2, from now called "local") leads to the following conclusions:

- for each station the "global" rotation is either smaller than the "local" one or it goes in the same direction meaning that the "side" of pot-beam touching point remains the same,

- due to rotation the AFP BPM (not considered in this thesis) on the IP1 A/C side will be closer/further to/from the beam.

Table B.9: The "global" rotation of the AFP stations obtained using the 2021 and 2023 laser survey data. The sign convention is the same as in Tab. B.2.

Survey	A FAR	A NEAR	C NEAR	C FAR
2021 [mm]	0.014	-0.038	0.048	0.064
2023 [mm]	0.026	-0.026	0.019	0.102

While the "left-right" rotation is interesting as it may impact the SiT distance from the beam, the major rotation is the "top-bottom" one (*cf.* Tab. B.3). It is connected to the radial displacement[1] of the station. The results are listed in Table. B.10. It should be noted that the radial deviations are positive outward of the LHC ring, meaning that the A/C side is further/closer from/to the designed beam centre.

Table B.10: Radial displacement of the AFP stations.

year	**A FAR**	**A NEAR**	**C NEAR**	**C FAR**
2021	1.28	1.19	-0.51	-0.58
2023	1.95	1.79	-0.16	-0.27

Based on this information, the true resolver (motor) positions for various BBA campaigns in 2022 and 2023 were calculated – see Table B.11 for the summary.

Table B.11: The "true" resolver (motor) positions (in mm) during the 2021 and 2023 BBA campaigns.

BBA	**A FAR**	**A NEAR**	**C NEAR**	**C FAR**
low-β^* 2022	0.849 ± 0.073	0.960 ± 0.073	1.056 ± 0.144	0.108 ± 0.073
low-β^* 2023	0.799 ± 0.073	0.936 ± 0.073	1.095 ± 0.144	0.223 ± 0.073
$\beta^* = 19.2$ m 2022	1.656 ± 0.073	1.910 ± 0.073	2.073 ± 0.144	1.111 ± 0.073
low-B field 2023	1.616 ± 0.073	1.940 ± 0.073	1.974 ± 0.144	1.071 ± 0.073

Finally, the beam centre position (see Sect. 3.3.2 and Tab. 3.4) can be corrected for the "global" displacement. These results are detailed in Table B.12. It should be noted that the positive value of the beam centre coordinate means that the beam is shifted outside the ring w.r.t. the nominal position.

[1] In the pot movement direction.

Table B.12: The "true" beam centre positions measured at the AFP pot station location during the 2021 and 2023 BBA campaigns.

Configuration	**A FAR**	**A NEAR**	**C NEAR**	**C FAR**
low-β^* 2022	0.485 ± 0.073	0.417 ± 0.073	0.554 ± 0.144	-0.204 ± 0.073
low-β^* 2023	0.288 ± 0.073	0.494 ± 0.073	0.537 ± 0.144	-0.253 ± 0.073
$\beta^* = 19.2$ m 2022	0.231 ± 0.073	0.249 ± 0.073	0.352 ± 0.144	-0.341 ± 0.073
low-B field 2023	-0.120 ± 0.073	0.515 ± 0.073	0.386 ± 0.144	-0.295 ± 0.073

Appendix C

Roman Pots at HL-LHC – Feasibility Studies

The High-Luminosity Large Hadron Collider (HL-LHC) represents a significant advancement in accelerator technology, necessitating sophisticated beam optics configurations to achieve an unprecedented luminosity target while maintaining precise detection capabilities. The recent version of the HL-LHC optics (1.5; used in the studies presented below) has been optimised to accommodate both the machine constraints and physics requirements. The analysis results were published in [2].
The HL-LHC centre-of-mass energy is expected to be $\sqrt{s} = 14$ TeV. The normalised beam emittance is designed to be of $\varepsilon_n = 2.5$ μm·rad, meaning a reduction from the previous operational value of 3.5 μm·rad. The minimal betatron function at the interaction points is intended to be reduced to around 10–15 cm, enabling the achievement of peak luminosities reaching $5 - 7.5 \times 10^{34}$ cm^{-2}s^{-1}. These parameters collectively result in an average pile-up multiplicity of $\langle\mu\rangle = 140 - 200$ interactions per bunch crossing.

C.1 ATLAS Case

The studies utilized the HL-LHC ver. 1.5 optics files with $\sqrt{s} = 14$ TeV, $\beta^* = 15$ cm and a reduced normalized emittance of 2.5 μm·rad. A systematic analysis of four distinct crossing angle phases was conducted to evaluate their impact on proton trajectories and detector acceptance comprehensively:

- $\phi = 0°$: horizontal crossing with $p_x = -250 \times 10^{-6} \times 7000 =$ -1.75 GeV,
- $\phi = 180°$: horizontal crossing with $p_x = 1.75$ GeV,
- $\phi = 90°$: vertical crossing with $p_y = 1.75$ GeV,
- $\phi = 270°$: vertical crossing with $p_y = -1.75$ GeV.

Unfortunately, at the end of the day, only the option of $\phi = 0$ will be possible for the ATLAS experiment in Run 4. This is because, due to the overall stability of the accelerator optics, the crossing plane should differ by 90^0 between the ATLAS

and CMS. Also, the $\phi = 180^0$ is not feasible since it might create multiple "beam collision points" inside the ATLAS detector.

C.1.1 Proton Trajectories

The beam-line in the vicinity of the ATLAS interaction point is much more dense for the HL-LHC (see Fig. C.1) configuration than the current one (*cf.* Fig. A.1).

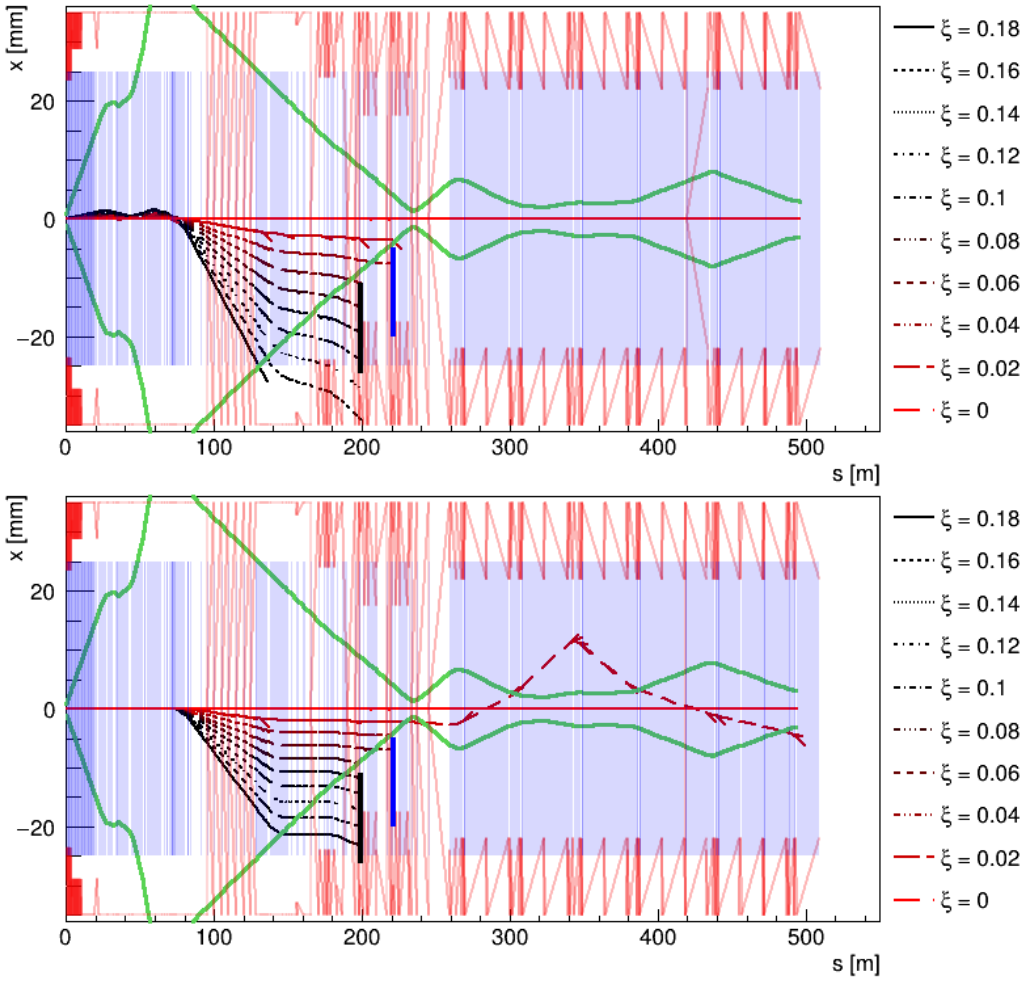

Figure C.1: Proton trajectories in the (s, x) plane for the relative energy losses ξ ranging from 0 to 0.18, calculated with the horizontal crossing angle $\phi = 0$ (**top**) and vertical one $\phi = 90$ (**bottom**). The blue-shaded regions represent the LHC magnets with apertures marked by red lines, while the green line indicates the 15σ beam envelope.

After detailed discussions with machine experts and comprehensive evaluation of the accelerator lattice constraints, three potential Roman Pot (RP) locations were identified within the machine layout in v1.5:

- RP1: 195.5 and 198.0 m (fixed 2.5 m separation),
- RP2: 217.0 and 219.5 m (fixed 2.5 m separation),

- RP3: 234.0–245.0 m (variable separation: 3–11 m; in these studies case of pot as 237 m was considered).

Similarly to the earlier described LHC optics studies (*cf.* Fig. A.3), the hit pattern for protons of certain energy loss and transverse momentum can be computed for a desired location of the forward detector. Such plots for $\phi = 0$ optics are shown in Figure C.2. From these plots, one can immediately conclude that this optics causes diffractive protons to be very close to the beam.

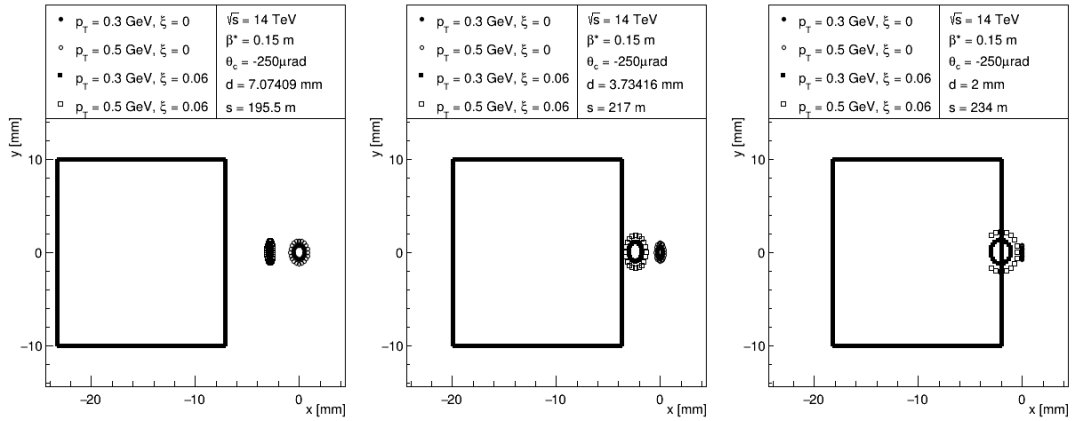

Figure C.2: Hit patterns for the three hypothetical AFP detector locations: 195.5 (**left**), 217 (**middle**) and 234 m (**right**) for $\phi = 0$ HL-LHC optics ver. 1.5. The proton positions for various energy losses (xi) and transverse momentum (p_T) values are shown.

C.1.2 Geometrical Acceptance

The acceptance of the forward proton detector depends on multiple experimental constraints and primarily is dominated by three collimators (TCL4/TCLPX.4, TCL5, and TCL6) positioned in the vicinity of the detector locations. The TCLPX.4 collimator, situated at 136.114 m from the interaction point, affects the acceptance for all Roman pot positions (RP1–RP3). The TCL.5 collimator at 199.51 m influences only the acceptance of RP2 and RP3, while TCL.6 at 221.057 m impacts exclusively the RP3 configuration. These collimators are configured with symmetric jaw positions at 14.2σ from the beam centre, with studies also considering a potential relaxation to 16.4σ with σ being the beam width at the collimator location.

The beam-detector distance represents another crucial parameter affecting the acceptance. As discussed in Section A.5, the minimum approach distance ($d_{\min}$) is governed by the TCT collimator setting through the relation:

$$d_{\min} = MAX[(TCT_{\text{setting}} + 3)\sigma_{RP} + 0.3\ 1.5]\text{mm}, \tag{C.1}$$

where σ_{RP} represents the beam width at the Roman pot location. The analysis implements an optimistic yet realistic assumption for $d_{\min}$, resulting in smaller detector-beam distances compared to the conventional "15σ" approach. For the RP3 case, the calculations demonstrate that the hard limit of 1.5 mm becomes the determining factor. Additionally, the acceptance analysis incorporates a 0.5 mm allowance for dead material, encompassing the pot-thin floor, detector-pot gap, and detector dead area.

Geometric acceptances for all considered locations and $\phi = 0$ optics are shown in Fig. C.3. The detectors located closer to the IP1 offer higher acceptance for higher ξ, thereby facilitating the detection of higher masses within the central system. Assuming particles not being blocked by the collimators, the RP1 station allows for accessing protons with $0.17 < \xi < 0.35$, RP2 with $0.11 < \xi < 0.18$ and RP3 with $0.07 < \xi < 0.09$.

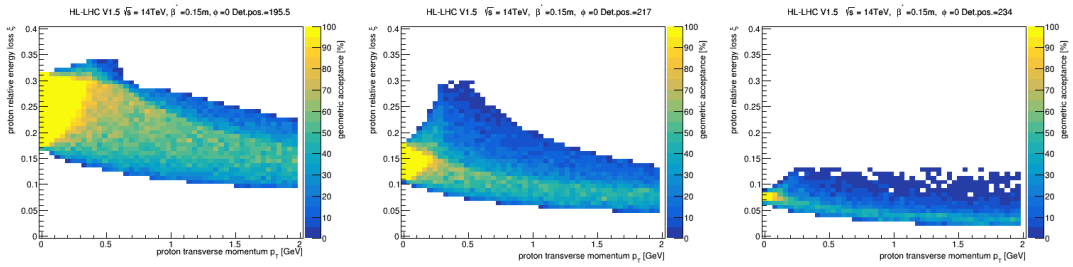

Figure C.3: Geometric acceptance for stations near IP1 and the horizontal crossing angle ($\phi = 0$) for pots at: 195.5 (**left**), 217 (**middle**) and 234 m (**right**).

C.1.3 Mass Acceptance

A single set of stations would limit the accessible acceptance region, see Fig. C.3. Therefore, a scenario of multiple Roman pots was considered. This is shown in Fig. C.4, where the mass acceptance, computed as $M = \sqrt{s \cdot \xi_1 \cdot \xi_2}$, is shown. Based on the above results, the idea of having Roman pots around IP1 was considered by the ATLAS Collaboration [97]. Contrary to CMS [98], the decision was to not install such devices for Run 4, with an open possibility for Run 5 and beyond.

C.2 ALICE Case

Similar studies were conducted for the ALICE experiment located at IP2. The crossing angle was assumed to be 270 μrad (in the vertical plane), and β^* was set to 10 m [99]. The vicinity of IP2, up to 350 m, is shown in Fig. C.5. It should be noted that here, the region with negative values of x is in between beam pipes.

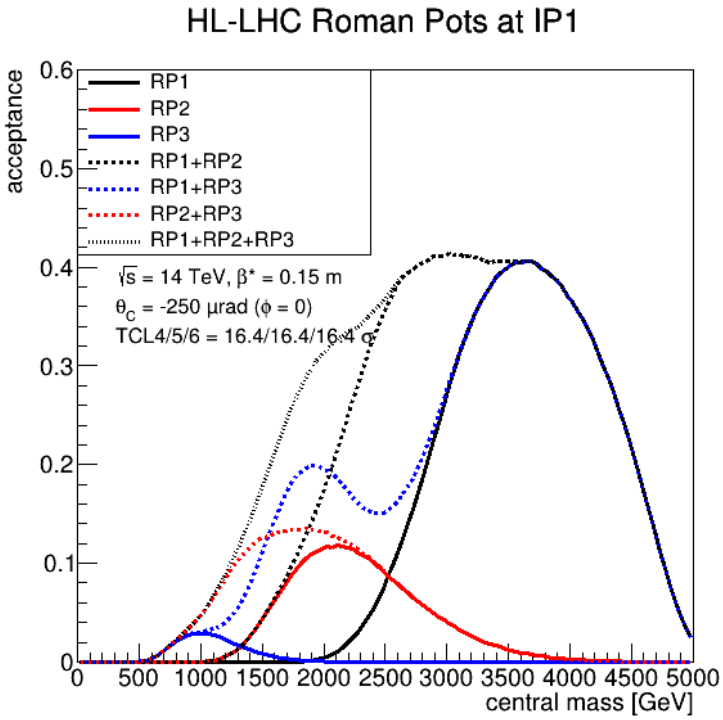

Figure C.4: Mass acceptance for various combinations of stations near IP1 for the horizontal crossing angle with ϕ=0.

As previously, various proton trajectories are shown as dashed/dotted red/black lines. Similarly to IP1, the low-ξ region is accessible for detectors located after 300 m. For the high-ξ studies, the best location for the Roman pots is around 150 m.

The proton hit-map is shown in Figure C.6 (left), whereas the corresponding geometric acceptance is on the right side. For the detector–beam distance of 15σ, the station at 150 m allows access to a proton with $0.05 < \xi < 0.15$.

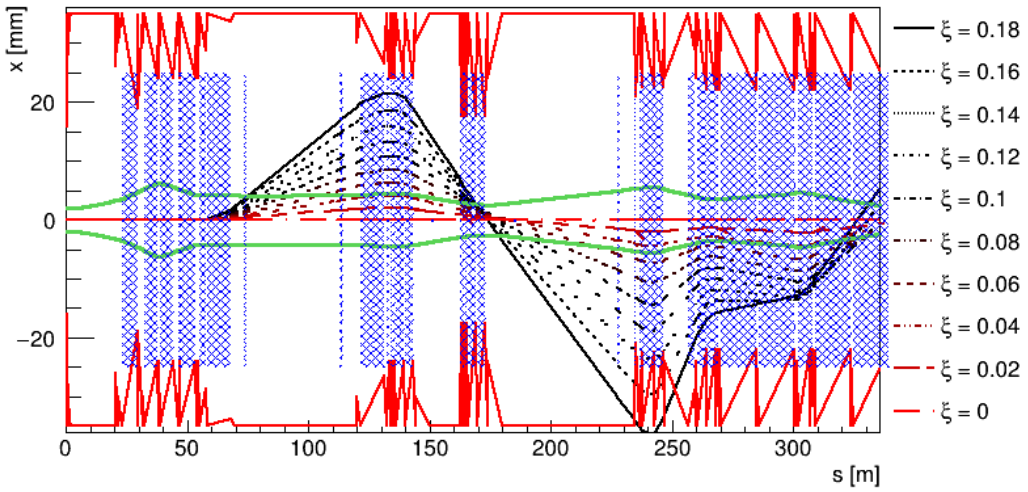

Figure C.5: Proton trajectories in the vicinity of the ALICE collision point.

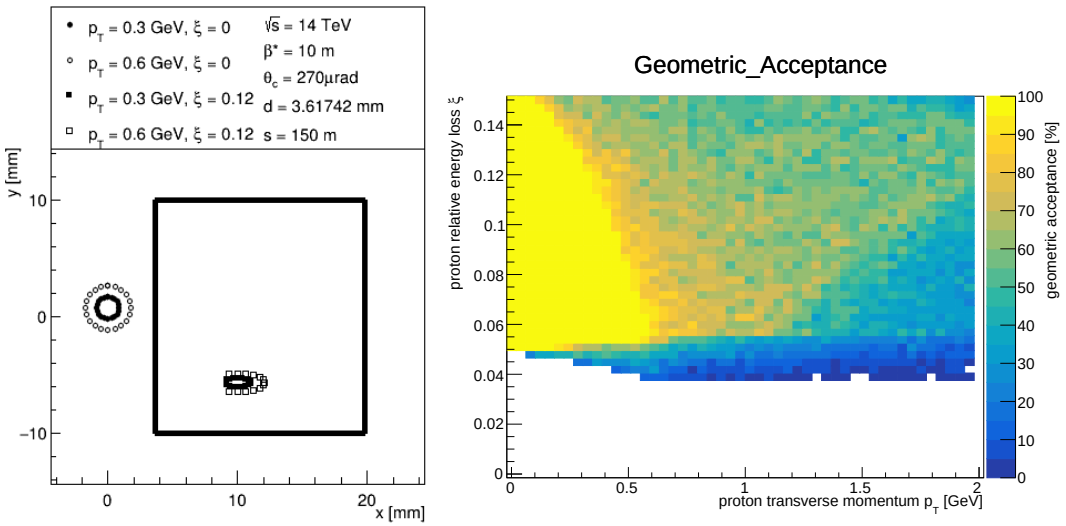

Figure C.6: Proton trajectories in the vicinity of the ALICE collision point.

Bibliography

[1] ATLAS Collaboration, https://twiki.cern.ch/twiki/bin/view/AtlasPublic/LuminosityPublicResults.

[2] P. Patel, M. Trzebinski, "High Luminosity LHC Optics Feasibility Studies for: ATLAS, ALICE, and LHCb," Acta Phys. Pol. B Proc. Suppl. 17, 5-A30 (2024).

[3] P. Erland, "Evidence of the Exclusive Jet Production Using the ATLAS Detector," PHD Thesis. [Online]. Available: https://ifjpan.bip.gov.pl/fobjects/download/1522293/rozprawa-doktorska-paula-erland-pdf.html

[4] F. Abe *et al.*, "Events with a rapidity gap between jets in $\bar{p}p$ collisions at $\sqrt{s} = 630$ GeV," *Phys. Rev. Lett.*, vol. 81, pp. 5278–5283, 1998.

[5] F. Abe *et al.*, "Dijet production by color - singlet exchange at the Fermilab Tevatron," *Phys. Rev. Lett.*, vol. 80, pp. 1156–1161, 1998.

[6] ATLAS Collaboration, "Measurement of dijet production with a veto on additional central jet activity in pp collisions at $\sqrt{s} = 7$ TeV using the ATLAS detector," *JHEP*, vol. 2011, no. 9, Sep. 2011. [Online]. Available: http://dx.doi.org/10.1007/JHEP09(2011)053

[7] TOTEM, CMS Collaboration, "Hard color-singlet exchange in dijet events in proton-proton collisions at $\sqrt{s} = 13$ TeV," *Phys. Rev. D*, vol. 104, p. 032009, 2021.

[8] C. Marquet, C. Royon, M. Trzebiński, and R. Žlebčík, "Gaps between jets in double-pomeron-exchange processes at the lhc," *Phys. Rev. D*, vol. 87, no. 3, Feb. 2013. [Online]. Available: http://dx.doi.org/10.1103/PhysRevD.87.034010

[9] Atlas Collaboration, "Observation of a new particle in the search for the Standard Model Higgs boson with the ATLAS detector at the LHC," *arXiv preprint arXiv:1207.7214*, 2012.

[10] S. Chatrchyan *et al.*, "Observation of a New Boson at a Mass of 125 GeV with the CMS Experiment at the LHC," *Phys. Lett. B*, vol. 716, pp. 30–61, 2012.

[11] [Online]. Available: https://commons.wikimedia.org/wiki/File:Standard_Model_of_Elementary_Particles.svg

[12] H. D. Politzer, "Asymptotic freedom: An approach to strong interactions," *Phys. Rep.*, vol. 14, no. 4, pp. 129–180, 1974.

[13] A. Deur, S. J. Brodsky, and G. F. de Teramond, "The QCD running coupling," *Prog. Part. Nucl. Phys.*, vol. 90, pp. 1–74, 2016.

[14] R. P. Feynman, "Very high-energy collisions of hadrons," *Phys. Rev. Lett.*, vol. 23, no. 24, p. 1415, 1969.

[15] J. Pumplin, D. R. Stump, J. Huston, H. L. Lai, P. M. Nadolsky, and W. K. Tung, "New generation of parton distributions with uncertainties from global QCD analysis," *JHEP*, vol. 07, p. 012, 2002.

[16] A. D. Martin, W. J. Stirling, R. S. Thorne, and G. Watt, "Parton distributions for the LHC," *Eur. Phys. J. C*, vol. 63, no. 2, pp. 189–285, 2009.

[17] R. D. Ball, V. Bertone, S. Carrazza, L. Del Debbio, S. Forte, A. Guffanti, N. P. Hartland, J. Rojo, N. Collaboration *et al.*, "Parton distributions with QED corrections," *Nucl. Phys. B*, vol. 877, no. 2, pp. 290–320, 2013.

[18] F. D. Aaron *et al.*, "Combined Measurement and QCD Analysis of the Inclusive e+- p Scattering Cross Sections at HERA," *JHEP*, vol. 01, p. 109, 2010.

[19] P. D. B. Collins, *An introduction to Regge theory and high energy physics*. Cambridge University Press, 1977.

[20] N. Cartiglia, "Measurement of the proton-proton total, elastic, inelastic and diffractive cross sections at 2, 7, 8 and 57 TeV," *arXiv preprint arXiv:1305.6131*, 2013.

[21] G. Ingelman and P. E. Schlein, "Jet Structure in High Mass Diffractive Scattering," *Phys. Lett. B*, vol. 152, pp. 256–260, 1985.

[22] UA8 Collaboration, "Evidence for Transverse Jets in High Mass Diffraction," *Phys. Lett. B*, vol. 211, p. 239, 1988.

[23] UA8 Collaboration, "Cross-section measurements of hard diffraction at the SPS collider," *Phys. Lett. B*, vol. 421, pp. 395–404, 1998.

[24] CDF Collaboration, "Diffractive Dijets with a Leading Antiproton in $\bar{p}p$ Collisions at $\sqrt{s} = 1800$ GeV," pp. 5043–5048, 2000.

[25] G. Watt, "MSTW PDFs and impact of PDFs on cross sections at Tevatron and LHC," Nucl. Phys. Proc. Suppl. 222-224 (2012) 61-80.

[26] H.-L. Lai, M. Guzzi, J. Huston, Z. Li, P. M. Nadolsky, J. Pumplin, and C. P. Yuan, "New parton distributions for collider physics," *Phys. Rev. D*, vol. 82, p. 074024, 2010.

[27] P. Jimenez-Delgado and E. Reya, "Dynamical NNLO parton distributions," *Phys. Rev. D*, vol. 79, p. 074023, 2009.

[28] ZEUS Collaboration, "Deep inelastic scattering with leading protons or large rapidity gaps at HERA," *Nucl. Phys. B*, vol. 816, pp. 1–61, 2009.

[29] H1 Collaboration, "Measurement and QCD analysis of the diffractive deep-inelastic scattering cross-section at HERA," *Eur. Phys. J. C*, vol. 48, pp. 715–748, 2006.

[30] A. Kaidalov, V. A. Khoze, A. D. Martin, and M. Ryskin, "Probabilities of rapidity gaps in high energy interactions," *Eur. Phys. J. C*, vol. 21, pp. 521–529, 2001.

[31] A. H. Mueller and W.-K. Tang, "High energy parton-parton elastic scattering in QCD," *Phys. Lett. B*, vol. 284, no. 1-2, pp. 123–126, 1992.

[32] J. D. Bjorken, "Rapidity gaps and jets as a new-physics signature in very-high-energy hadron-hadron collisions," *Phys. Rev. D*, vol. 47, no. 1, p. 101, 1993.

[33] O. Kepka, C. Marquet, and C. Royon, "Gaps between jets in hadronic collisions," *Phys. Rev. D*, vol. 83, no. 3, p. 034036, 2011.

[34] F. Chevallier, O. Kepka, C. Marquet, and C. Royon, "Gaps between jets at hadron colliders in the next-to-leading BFKL framework," *Phys. Rev. D*, vol. 79, no. 9, p. 094019, 2009.

[35] A. Ekstedt, R. Enberg, and G. Ingelman, "Hard color singlet BFKL exchange and gaps between jets at the LHC," *arXiv:1703.10919*, 3 2017.

[36] I. Babiarz, R. Staszewski, and A. Szczurek, "Multi-parton interactions and rapidity gap survival probability in jet–gap–jet processes," *Phys. Lett. B*, vol. 771, pp. 532–538, 2017.

[37] L. Evans and P. Bryant, "LHC Machine," *JINST*, vol. 3, p. S08001, 2008.

[38] ATLAS Collaboration, "The ATLAS Experiment at the CERN Large Hadron Collider," *JINST*, vol. 3, p. S08003, 2008.

[39] ALICE Collaboration, "The ALICE experiment at the CERN LHC," *JINST*, vol. 3, p. S08002, 2008.

[40] CMS Collaboration, "The CMS Experiment at the CERN LHC," *JINST*, vol. 3, p. S08004, 2008.

[41] LHCb Collaboration, "The LHCb Detector at the LHC," *JINST*, vol. 3, p. S08005, 2008.

[42] E. Lopienska, "The CERN accelerator complex, layout in 2022," 2022. [Online]. Available: https://cds.cern.ch/record/2800984

[43] P. Grafström and W. Kozanecki, "Luminosity determination at proton colliders," *Prog. Part. Nucl. Phys.*, vol. 81, pp. 97–148, 2015. [Online]. Available: https://www.sciencedirect.com/science/article/pii/S0146641014000878

[44] O. Aberle et.al., *High-Luminosity Large Hadron Collider (HL-LHC): Technical design report*, ser. CERN Yellow Reports: Monographs. Geneva: CERN, 2020. [Online]. Available: https://cds.cern.ch/record/2749422

[45] ATLAS Collaboration, "ATLAS experiment schematic or layout illustration," 2022, general Photo. [Online]. Available: http://cds.cern.ch/record/2837191

[46] ATLAS Collaboration, *ATLAS inner detector: Technical design report. Vol. 1*, 4 1997. [Online]. Available: https://cds.cern.ch/record/331063

[47] ATLAS Collaboration, "ATLAS inner detector: Technical design report. Vol. 2," 4 1997.

[48] ATLAS Collaboration, "ATLAS Insertable B-Layer Technical Design Report," 2010. [Online]. Available: https://cds.cern.ch/record/1291633

[49] ATLAS Collaboration, "Technical Design Report for the ATLAS Inner Tracker Pixel Detector," CERN, Geneva, Tech. Rep., 2017. [Online]. Available: https://cds.cern.ch/record/2285585

[50] ATLAS Collaboration, "Technical Design Report for the ATLAS Inner Tracker Strip Detector," CERN, Geneva, Tech. Rep., 2017. [Online]. Available: https://cds.cern.ch/record/2257755

[51] ATLAS Collaboration, "AtlFast3: The Next Generation of Fast Simulation in ATLAS," *Comput. Softw. Big Sci.*, vol. 6, no. 1, p. 7, 2022.

[52] ATLAS Collaboration, "ATLAS muon spectrometer: Technical Design Report," 6 1997. [Online]. Available: https://cds.cern.ch/record/331068

[53] T. Kawamoto *et al.*, "New Small Wheel Technical Design Report," 2013, aTLAS New Small Wheel Technical Design Report. [Online]. Available: https://cds.cern.ch/record/1552862

[54] L. Adamczyk *et al.*, "Technical Design Report for the ATLAS Forward Proton Detector," 5 2015. [Online]. Available: https://cds.cern.ch/record/2017378

[55] ATLAS Collaboration, "Beam tests of an integrated prototype of the ATLAS Forward Proton detector," *JINST*, vol. 11, no. 09, p. P09005, 2016.

[56] L. Chytka *et al.*, "Timing resolution studies of the optical part of the AFP Time-of-flight detector," *Opt. Express*, vol. 26, no. 7, pp. 8028–8039, 2018. [Online]. Available: https://cds.cern.ch/record/2667193

[57] ATLAS Collaboration, "Operation of the ATLAS trigger system in Run 2," *JINST*, vol. 15, no. 10, p. P10004, 2020.

[58] H. Collaboration and C. Adloff, "Energy flow and rapidity gaps between jets in photoproduction at HERA," *Eur. Phys. J. C*, vol. 24, no. 4, pp. 517–527, 2002.

[59] M. Derrick *et al.*, "Rapidity gaps between jets in photoproduction at HERA," *Phys. Lett. B*, vol. 369, no. 1, pp. 55–68, 1996.

[60] B. Abbott *et al.*, "Probing Hard Color-Singlet Exchange in $p\bar{p}$ Collisions at $\sqrt{s} = 630$ GeV and 1800 GeV," *Phys. Lett. B*, vol. 440, pp. 189–202, 1998.

[61] A. M. Sirunyan and other, "Study of dijet events with a large rapidity gap between the two leading jets in pp collisions at $\sqrt{s} = 7$ TeV," *Eur. Phys. J. C*, vol. 78, no. 3, p. 242, 2018, [Erratum: Eur. Phys. J. C 80, 441 (2020)].

[62] Y. Hatta, C. Marquet, C. Royon, G. Soyez, T. Ueda, and D. Werder, "A QCD description of the ATLAS jet veto measurement," *Phys. Rev. D*, vol. 87, no. 5, Mar. 2013. [Online]. Available: http://dx.doi.org/10.1103/PhysRevD.87.054016

[63] R. M. D. Delgado, J. R. Forshaw, S. Marzani, and M. H. Seymour, "The dijet cross section with a jet veto," *JHEP*, vol. 2011, no. 8, Aug. 2011. [Online]. Available: http://dx.doi.org/10.1007/JHEP08(2011)157

[64] M. Trzebinski, "Study of QCD and Diffraction with the ATLAS detector at the LHC," 2013, presented 20 Sep 2013. [Online]. Available: https://cds.cern.ch/record/1616661

[65] [Online]. Available: https://gitlab.cern.ch/atlas-tdaq-oks/p1/tdaq-09-04-00/-/blob/fa3ae2f1cefebc252783b43a60405accdb2114ce/afp/segments/AFP_Top_Segment.data.xml

[66] M. Trzebinski, "The ATLAS Roman Pots Interlock Logic in 2022: Test Results," EDMS 2729054 v.1, AT1-UR-OR-0001 v.1. [Online]. Available: https://edms.cern.ch/document/2729054/

[67] [Online]. Available: https://twiki.cern.ch/twiki/bin/view/Atlas/AFPFirstBBA2022

[68] R. Bruce, R. W. Assmann, and S. Redaelli, "Calculations of safe collimator settings and β^* at the CERN Large Hadron Collider," *Phys. Rev. ST Accel. Beams*, vol. 18, p. 061001, Jun 2015. [Online]. Available: https://link.aps.org/doi/10.1103/PhysRevSTAB.18.061001

[69] F. V. D. Veken, "Overview of Run 3 collimation scenarios," LHC Collimation Working Group #256. [Online]. Available: https://indico.cern.ch/event/1049387

[70] G. Avoni *et al.*, "The new LUCID-2 detector for luminosity measurement and monitoring in ATLAS," *JINST*, vol. 13, no. 07, p. P07017, 2018.

[71] ATLAS Collaboration, "Preliminary analysis of the luminosity calibration of the ATLAS 13.6 TeV data recorded in 2022," CERN, Geneva, Tech. Rep., 2023, all figures including auxiliary figures are available at https://atlas.web.cern.ch/Atlas/GROUPS/PHYSICS/PUBNOTES/ATL-DAPR-PUB-2023-001. [Online]. Available: https://cds.cern.ch/record/2853525

[72] M. H. Seymour and M. Marx, "Monte Carlo Event Generators," 2013. [Online]. Available: https://arxiv.org/abs/1304.6677

[73] T. Sjostrand, S. Mrenna, and P. Skands, "A Brief Introduction to PYTHIA 8.1," Comput. Phys. Commun. **178** (2008).

[74] J. Bellm *et al.*, "Herwig 7.0/Herwig++ 3.0 release note," *Eur. Phys. J. C*, vol. 76, no. 4, p. 196, 2016.

[75] M. Boonekamp, V. Juranek, O. Kepka, and C. Royon, "Forward Physics Monte Carlo," in *HERA and the LHC: 4th Workshop on the Implications of HERA for LHC Physics*, 3 2009, pp. 758–762.

[76] M. Cacciari, G. P. Salam, and G. Soyez, "The anti-ktjet clustering algorithm," *JHEP*, vol. 2008, no. 04, p. 063–063, Apr. 2008. [Online]. Available: http://dx.doi.org/10.1088/1126-6708/2008/04/063

[77] M. Cacciari, G. Salam, and G. Soyez, "Fastjet user manual: (for version 3.0.2)," *Eur. Phys. J. C*, vol. 72, no. 3, Mar. 2012. [Online]. Available: http://dx.doi.org/10.1140/epjc/s10052-012-1896-2

[78] P. Waller and J. Ebke, "MCViz – Visualize HEP Monte Carlo Events," https://github.com/mcviz/mcviz.

[79] J. Alwall *et al.*, "A Standard format for Les Houches event files," *Comput. Phys. Commun.*, vol. 176, pp. 300–304, 2007.

[80] ATLAS Collaboration, "The performance of the jet trigger for the ATLAS detector during 2011 data taking," *Eur. Phys. J. C*, vol. 76, no. 10, Sep. 2016. [Online]. Available: http://dx.doi.org/10.1140/epjc/s10052-016-4325-0

[81] ATLAS Collaboration, "The ATLAS trigger system for LHC Run 3 and trigger performance in 2022," *Journal of Instrumentation*, vol. 19, no. 06, p. P06029, Jun. 2024. [Online]. Available: http://dx.doi.org/10.1088/1748-0221/19/06/P06029

[82] M. Trzebinski, R. Staszewski, and J. Chwastowski, "LHC High β* Runs: Transport and Unfolding Methods," *ISRN High Energy Phys.*, vol. 2012, p. 491460, 2012.

[83] F. Ozturk, "Alignment of the ATLAS-AFP Detectors," CERN, Geneva, Tech. Rep., 2024. [Online]. Available: https://cds.cern.ch/record/2894034

[84] ATLAS Collaboration, "Performance of the ATLAS Forward Proton Spectrometer during High Luminosity 2017 Data Taking," CERN, Geneva, Tech. Rep., 2024, all figures including auxiliary figures are available at https://atlas.web.cern.ch/Atlas/GROUPS/PHYSICS/PUBNOTES/ATL-FWD-PUB-2024-001. [Online]. Available: https://cds.cern.ch/record/2890974

[85] ATLAS Collboration, "Observation and Measurement of Forward Proton Scattering in Association with Lepton Pairs Produced via the Photon Fusion Mechanism at ATLAS," *Phys. Rev. Lett.*, vol. 125, no. 26, p. 261801, 2020.

[86] ATLAS Collaboration. [Online]. Available: https://twiki.cern.ch/twiki/bin/view/AtlasPublic/ForwardDetPublicResults

[87] T. Mroz, "Global Alignment of ATLAS Forward Proton Detectors," talk given during the XXXI Cracow Epiphany Conference on the recent LHC Results.

[88] ATLAS Collaboration, "Charged particle multiplicities in pp interactions for track $pT > 100$ MeV at $sqrts = 0.9$ and 7 TeV measured with the ATLAS detector at the LHC," CERN, Geneva, Tech. Rep., 2010, all figures including auxiliary figures are available at https://atlas.web.cern.ch/Atlas/GROUPS/PHYSICS/CONFNOTES/ATLAS-CONF-2010-046. [Online]. Available: https://cds.cern.ch/record/1281296

[89] ATLAS Collaboration, "Topological cell clustering in the ATLAS calorimeters and its performance in LHC Run 1," Eur. Phys. J. C, 77:490, 2017.

[90] ATLAS Collaboration, "Selection of jets produced in 13TeV proton-proton collisions with the ATLAS detector," CERN, Geneva, Tech. Rep., 2015, all figures including auxiliary figures are available at https://atlas.web.cern.ch/Atlas/GROUPS/PHYSICS/CONFNOTES/ATLAS-CONF-2015-029. [Online]. Available: https://cds.cern.ch/record/2037702

[91] G. A. Gram, "Jet energy scale measurements and their systematic uncertainties in proton-proton collisions at root s = 13 tev with the atlas detector," 2018. [Online]. Available: https://api.semanticscholar.org/CorpusID:260784017

[92] O. Kepka, C. Marquet, and C. Royon, "Gaps between jets in hadronic collisions," p. 034036, 2011.

[93] S. Czekierda, "Hadronic final states in diffractive pp scattering at $\sqrt{s}$=13 TeV using the ATLAS detector," PhD Thesis. [Online]. Available: http://rifj.ifj.edu.pl/handle/item/299

[94] M. Trzebinski, "Prospects for Proton-Proton Measurements with Tagged Protons in ATLAS," in *International Conference on the Structure and the Interactions of the Photon*, 2019, pp. 144–149.

[95] F. Schmidt, "MAD-X User's Guide," CERN 2005.

[96] ATLAS Collaboration, "Measurement of the total cross section from elastic scattering in pp collisions at $sqrts = 7TeV$ with the ATLAS detector," *Nucl. Phys. B*, vol. 889, p. 486–548, Dec. 2014. [Online]. Available: http://dx.doi.org/10.1016/j.nuclphysb.2014.10.019

[97] M. Trzebiński, "Overview of ATLAS forward proton detectors for LHC Run 3 and plans for the HL-LHC," *Nucl. Instr. Meth. A*, vol. 1050, p. 168187, 2023. [Online]. Available: https://www.sciencedirect.com/science/article/pii/S0168900223001778

[98] CMS Collaboration, "The CMS Precision Proton Spectrometer at the HL-LHC – Expression of Interest," CERN-CMS-NOTE-2020-008.

[99] R. D. Maria, R. Bruce, D. Gamba, M. Giovannozzi, and F. Plassard, "High Luminosity LHC Optics and Layout HLLHCV1.4," *Journal of Physics: Conference Series*, vol. 1350, no. 1, p. 012001, nov 2019. [Online]. Available: https://dx.doi.org/10.1088/1742-6596/1350/1/012001